nagra.

Arbeitsbericht NAB 20-09 Rev. 1

TBO Trüllikon-1-1: Data Report

Dossier IX Rock-mechanical and Geomechanical Laboratory Testing

March 2023

E. Crisci, L. Laloui & S. Giger

National Cooperative
for the Disposal of
Radioactive Waste

Hardstrasse 73
P.O. Box
5430 Wettingen
Switzerland
Tel. +41 56 437 11 11

nagra.ch

nagra.

Arbeitsbericht NAB 20-09

TBO Trüllikon-1-1: Data Report

Dossier IX Rock-mechanical and Geomechanical Laboratory Testing

March 2023

E. Crisci[1], L. Laloui[1] & S. Giger[2]

[1] Ecole polytechnique fédérale de Lausanne
Laboratory for Soil Mechanics, EPFL ENAC IIC LMS,
Station No. 18

[2] Nagra

Keywords:
TRU1-1, Zürich Nordost, TBO, deep drilling campaign, geomechanics, geomechanical laboratory testing, triaxial tests, oedometric tests

National Cooperative for the Disposal of Radioactive Waste

Hardstrasse 73
P.O. Box 280
5430 Wettingen
Switzerland
Tel. +41 56 437 11 11

www.nagra.ch

Nagra Arbeitsberichte ("Working Reports") present the results of work in progress that have not necessarily been subject to a comprehensive review. They are intended to provide rapid dissemination of current information.

This NAB aims at reporting drilling results at an early stage. Additional borehole-specific data will be published elsewhere.

In the event of inconsistencies between dossiers of this NAB, the dossier addressing the specific topic takes priority. In the event of discrepancies between Nagra reports, the chronologically later report is generally considered to be correct. Data sets and interpretations laid out in this NAB may be revised in subsequent reports. The reasoning leading to these revisions will be detailed there.

This Dossier was prepared by a project team consisting of:
E. Crisci (test coordination, formal analysis and QC, writing)
S. Giger (project administration, conceptualisation, writing)
L. Laloui (review, supervision)

The present report was prepared based on numerous contractor reports, to which many people from different laboratories contributed, namely B. Bohloli, K. Halvorsen, J. Stenebråten, R. Stankovic, V. Vajdova, R. Ewy, A. Ferrari, M. Rosone, H. Baumgartner, S. Louis and J. Szech.

Editorial work: P. Blaser and M. Unger

The Dossier has greatly benefitted from technical discussions with external and internal experts. Their input and work are very much appreciated.

NAB 20-09, March 2023: Revision 1
The main reason for the revision are corrections in tables E-2 and E-3. In addition, other minor adjustments were made in the text in chapters 4.2.3 and 6.2.1.3, in table 6-2, and in figures 6-5, 6-11 and 6-13b.

Table of Contents

List of Tables

List of Figures

1 Introduction

1.1 Context

To provide input for site selection and the safety case for deep geological repositories for radioactive waste, Nagra has drilled a series of deep boreholes in Northern Switzerland. The aim of the drilling campaign is to characterise the deep underground of the three remaining siting regions located at the edge of the Northern Alpine Molasse Basin (Fig. 1-1).

In this report, we present the results from the Trüllikon-1-1 borehole.

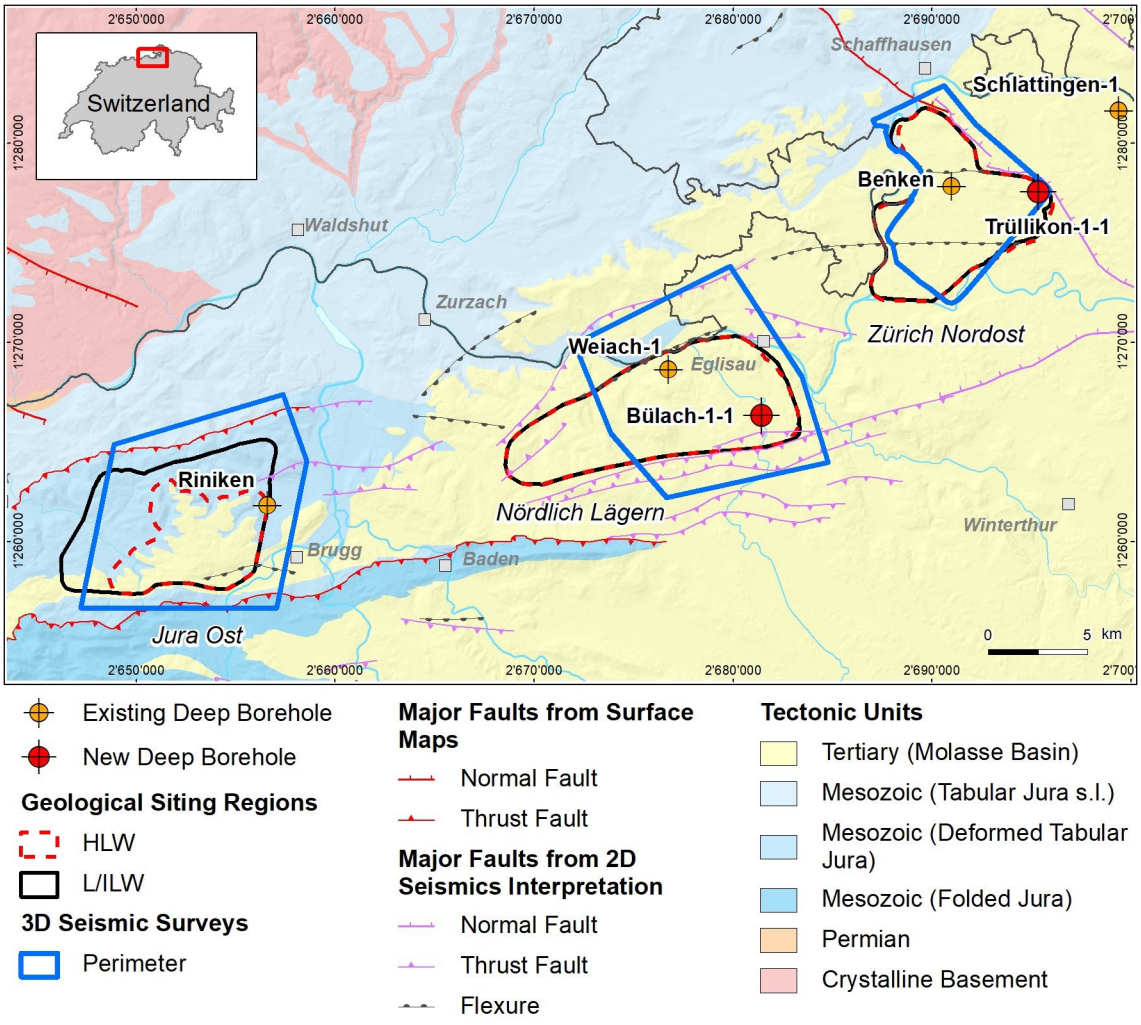

Fig. 1-1: Tectonic overview map with the three siting regions under investigation

1.2 Location and specifications of the borehole

The Trüllikon-1-1 (TRU1-1) exploratory borehole is the second borehole drilled within the framework of the TBO project. The drill site is located in the eastern part of the Zürich Nordost siting region (Fig. 1-2). The vertical borehole reached a final depth of 1'310 m (MD)[1]. The borehole specifications are provided in Tab. 1-1.

Tab. 1-1: General information about the TRU1-1 borehole

Siting region	Zürich Nordost
Municipality	Trüllikon (Canton Zürich / ZH), Switzerland
Drill site	Trüllikon-1 (TRU1)
Borehole	Trüllikon-1-1 (TRU1-1)
Coordinates	LV95: 2'695'372.648 / 1'277'548.076
Elevation	Ground level = top of rig cellar: 475.07 m above sea level (asl)
Borehole depth	1'310.0 m measured depth (MD) below ground level (bgl)
Drilling period	15. August 2019 – 5. April 2020 (spud date to end of rig release)
Drilling company	PR Marriott Drilling Ltd.
Drilling rig	Rig-16 Drillmec HH102
Drilling fluid	Water-based mud with various amounts of different components such as[2]: 46 – 712 m: Pure-Bore® 712 – 1'161 m: Potassium silicate 1'161 – 1'310 m: Sodium chloride & polymers

The lithostratigraphic profile and the casing scheme are shown in Fig. 1-3. The comparison of the core versus log depth[3] of the main lithostratigraphic boundaries in the TRU1-1 borehole is shown in Tab. 1-2.

[1] Measured depth (MD) refers to the position along the borehole trajectory, starting at ground level, which for this borehole is the top of the rig cellar. For a perfectly vertical borehole, MD below ground level (bgl) and true vertical depth (TVD) are the same. In all Dossiers depth refers to MD unless stated otherwise.

[2] For detailed information see Dossier I.

[3] Core depth refers to the depth marked on the drill cores. Log depth results from the depth observed during geophysical wireline logging. Note that the petrophysical logs have not been shifted to core depth, hence log depth differs from core depth.

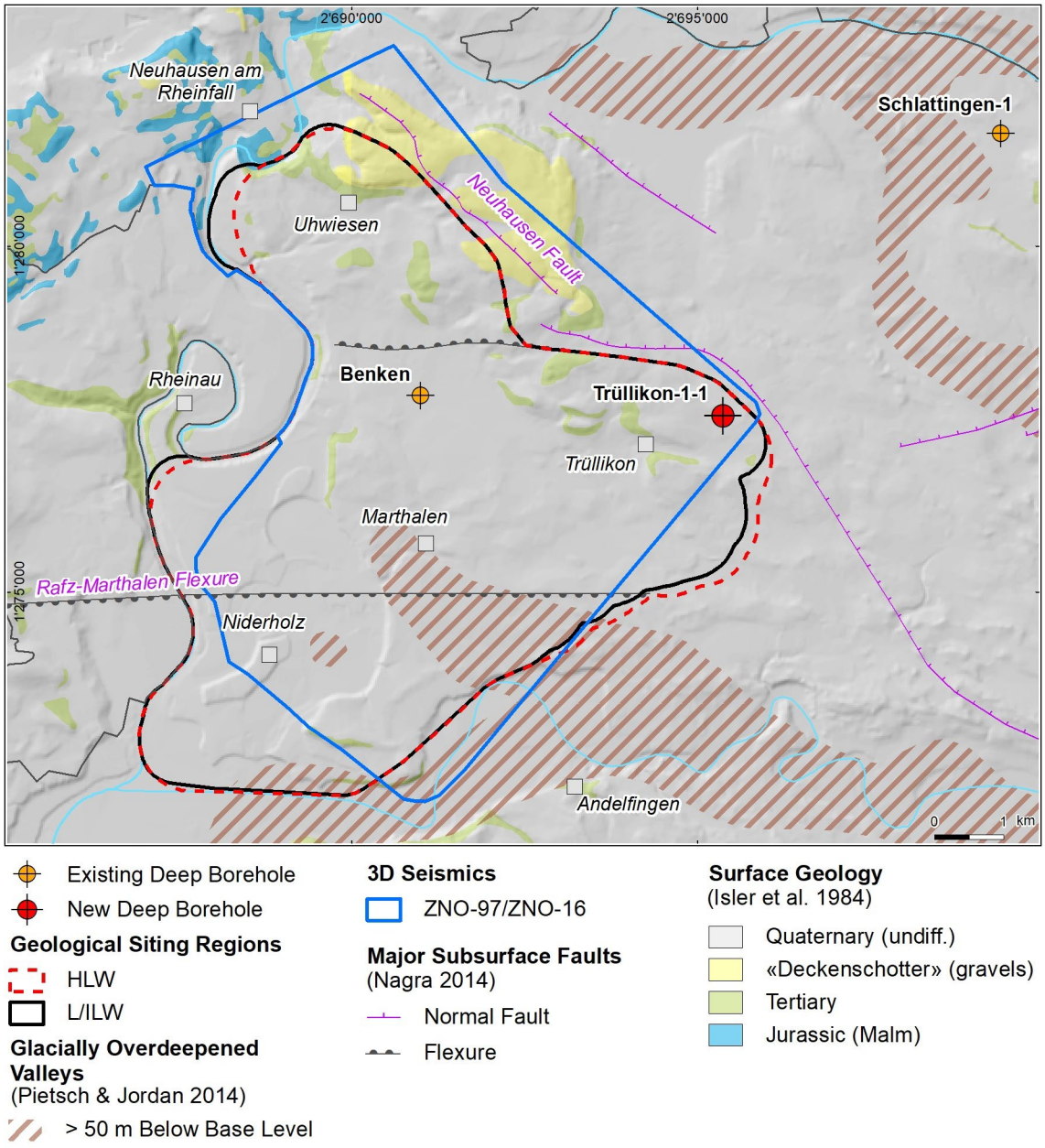

Fig. 1-2: Overview map of the investigation area in the Zürich Nordost siting region with the location of the TRU1-1 borehole in relation to the boreholes Benken and Schlattingen

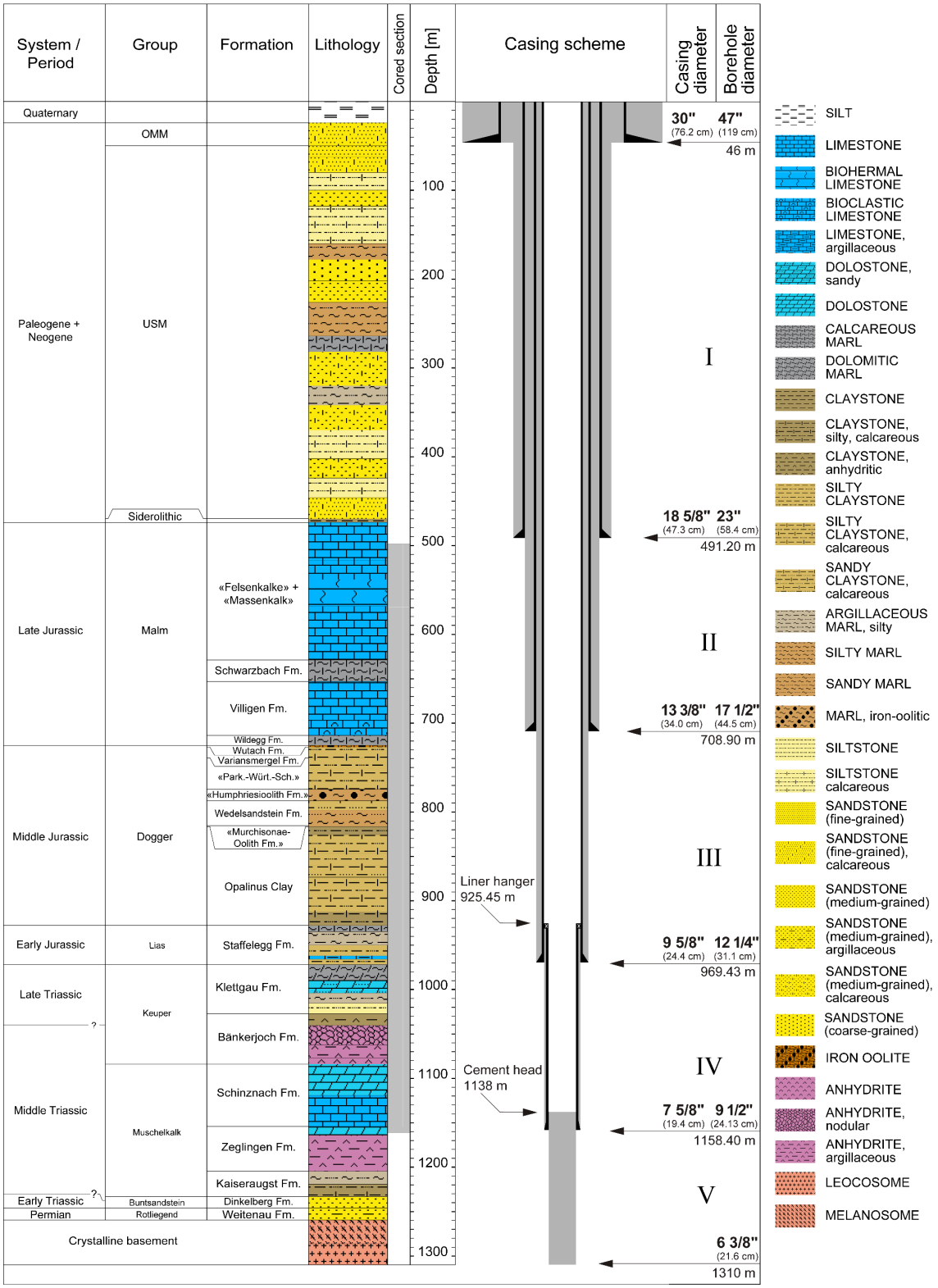

Fig. 1-3: Lithostratigraphic profile and casing scheme for the TRU1-1 borehole[4]

[4] For detailed information see Dossier I and III.

Tab. 1-2: Core and log depth for the main lithostratigraphic boundaries in the TRU1-1 borehole[5]

System / Period	Group	Formation	Core depth in m (MD)	Log depth in m (MD)	
Quaternary				**24.0**	—
Paleogene + Neogene	OMM			50.0	—
	USM			470.0	—
	Siderolithic			**474.0**	—
Jurassic	Malm	«Felsenkalke» + «Massenkalk»	628.87	628.75	—
		Schwarzbach Formation	653.29	653.15	—
		Villigen Formation	714.00	714.00	—
		Wildegg Formation	724.85	725.03	—
	Dogger	Wutach Formation	727.13	727.27	—
		Variansmergel Formation	738.97	739.06	—
		«Parkinsoni-Württembergica-Schichten»	774.55	774.66	—
		«Humphriesioolith Formation»	787.50	787.55	—
		Wedelsandstein Formation	815.51	815.50	—
		«Murchisonae-Oolith Formation»	816.42	816.43	—
		Opalinus Clay	927.91	927.87	—
	Lias	Staffelegg Formation	**971.68**	**971.55**	—
Triassic	Keuper	Klettgau Formation	1027.22	1027.44	—
		Bänkerjoch Formation	1084.01	1084.22	—
	Muschelkalk	Schinznach Formation	1154.25	1154.43	—
		Zeglingen Formation	1204.5		—
		Kaiseraugst Formation	1233.2		—
	Buntsandstein	Dinkelberg Formation	**1246.1**		—
Permian	Rotliegend	Weitenau Formation	**1259.7**		—
		Crystalline Basement	1310.0		final depth

[5] For details regarding lithostratigraphic boundaries see Dossier III; for details about depth shifts (core goniometry) see Dossier V.

1.3 Documentation structure for the TRU1-1 borehole

NAB 20-09 documents the majority of the investigations carried out in the TRU1-1 borehole, including laboratory investigations on core material. The NAB comprises a series of stand-alone dossiers addressing individual topics and a final dossier with a summary composite plot (Tab. 1-3).

This documentation aims at early publication of the data collected in the TRU1-1 borehole. It includes most of the data available approximately one year after completion of the borehole. Some analyses are still ongoing (e.g. diffusion experiments, analysis of veins, hydrochemical interpretation of water samples) and results will be published in separate reports.

The current borehole report will provide an important basis for the integration of datasets from different boreholes. The integration and interpretation of the results in the wider geological context will be documented later in separate geoscientific reports.

Tab. 1-3: List of dossiers included in NAB 20-09

Black indicates the dossier at hand.

Dossier	Title	Authors
I	TBO Trüllikon-1-1: Drilling	M. Ammen & P.-J. Palten
II	TBO Trüllikon-1-1: Core Photography	D. Kaehr & M. Gysi
III	TBO Trüllikon-1-1: Lithostratigraphy	M. Schwarz, P. Jordan, P. Schürch, H. Naef, T. Ibele, R. Felber & M. Gysi
IV	TBO Trüllikon-1-1: Microfacies, Bio- and Chemostratigraphic Analyses	S. Wohlwend, H.R. Bläsi, S. Feist-Burkhardt, B. Hostettler, U. Menkveld-Gfeller, V. Dietze & G. Deplazes
V	TBO Trüllikon-1-1: Structural Geology	A. Ebert, S. Cioldi, L. Gregorczyk, S. Rust, D. Böhni & M. Gysi
VI	TBO Trüllikon-1-1: Wireline Logging and Microhydraulic Fracturing	J. Gonus, E. Bailey, J. Desroches & R. Garrard
VII	TBO Trüllikon-1-1: Hydraulic Packer Testing	R. Schwarz, L. Schlickenrieder, H.R. Müller, S. Köhler, A. Pechstein & T. Vogt
VIII	TBO Trüllikon-1-1: Rock Properties, Porewater Characterisation and Natural Tracer Profiles	L. Aschwanden, L. Camesi, T. Gimmi, A. Jenni, M. Kiczka, U. Mäder, M. Mazurek, D. Rufer, H.N. Waber, P. Wersin, C. Zwahlen & D. Traber
IX	TBO Trüllikon-1-1: Rock-mechanical and Geomechanical Laboratory Testing	E. Crisci, L. Laloui & S. Giger
X	TBO Trüllikon-1-1: Petrophysical Log Analysis	S. Marnat & J.K. Becker
	TBO Trüllikon-1-1: Summary Plot	Nagra

1.4 Structure of Dossier IX

The report is organised as follows:

- Chapter 2 presents the aims of the laboratory testing programmes and introduces the laboratories involved.
- Chapter 3 provides an overview of core sampling, conditioning and storage methods, and also explains the non-destructive method used to evaluate core integrity prior to shipping to the laboratories.
- Chapter 4 introduces the testing methods used in the testing programmes and provides an overview of the executed tests per formation.
- Chapter 5 documents the results of the rock-mechanical testing programme.
- Chapter 6 documents the triaxial and the oedometric test results of the geomechanical testing programme. Given the greater complexity of the testing procedure and the relevance of the test results for site evaluation, these test results are more rigorously documented than the rock-mechanical test results.
- A short discussion on the representativeness of the results is provided in Chapter 7.

Furthermore, large documentation of the performed tests is reported in the appendix, and includes:

A – Photo documentation of the rock-mechanical testing programme

B – XCT (medical X-ray tomography) cross-sections, with indication of the section used for geomechanical testing

C – Diagnostic plots of the triaxial tests (geomechanical testing programme)

D – Mineralogical analysis (geomechanical testing programme)

E – Triaxial test results (geomechanical testing programme)

F – Test results in oedometric conditions (geomechanical testing programme)

2 Aims of the study and overview of the testing programme

2.1 Aims of the study and distinction of rock-mechanical and geomechanical testing programmes

For site characterisation, rock-mechanical and geomechanical properties are used for the following applications:

a) Supporting data for the detailed analysis and interpretation of in situ micro-hydraulic fracturing tests

b) Parametrise 3D geomechanical numerical models with (sub-)formation properties to assess the spatial variability of the stress tensor

c) Design of underground repository access structures

d) Hydro-mechanical properties of the host rock Opalinus Clay and its confining units

e) Volumetric behaviour (consolidation and swelling) and hydraulic properties of the host rock Opalinus Clay and its confining units

To address points a) to c) «standard» rock-mechanical tests were performed on core material in the stratigraphic interval Malm to Rotliegend, except for Opalinus Clay. «Standard» here means that the tests were performed according to national and international standards, notably the suggested methods of the International Society of Rock Mechanics (*cf.* Section 4.2). Standard tests were performed within the **"rock-mechanical testing programme"**.

In contrast, laboratory testing under points d) and e) were conducted using specialised protocols (*cf.* Section 4.3) combining rock-mechanical and soil mechanical aspects. Specifically, these protocols account for 1) the higher requirements of the low-permeability and fluid-sensitive Opalinus Clay and its argillaceous confining units to obtain robust test results, and 2) for the greater relevance of these units to evaluate the safety of a future repository. Tests performed using the specialised protocols are hereafter assigned to the **"geomechanical testing programme"**.

2.2 Overview of testing programme and contractors

2.2.1 Rock-mechanical testing programme

The rock-mechanical testing programme with core material of the TRU1-1 borehole comprised of the following testing methods:

- Indirect tensile strength (Brazilian)
- Uniaxial compressive strength (UCS)
- Triaxial compressive strength (TRX)

The following two laboratories were contracted:

- Gesteinslabor Dr. Eberhard Jahns (Germany). Main contacts were Carlo Dietl and Hansjörg Baumgartner
- NGI (Norway), main contacts were Bahman Bohloli and Kristine Halvorsen

2.2.2 Geomechanical testing programme

The geomechanical testing programme was specifically designed for Opalinus Clay and its confining units and comprised of the following testing methods with cores from the TRU1-1 borehole:

- Triaxial deformation tests with various stress paths (TRX)
- High-pressure oedometric testing (OED), including for some tests constant-head permeability phases (PERM)
- One-dimensional swelling tests (OS), carried out in oedometric conditions

Four laboratories were contracted for the geomechanical testing campaign:

- NGI (Norway), main contacts were Bahman Bohloli and Kristine Halvorsen
- RSTD (USA), main contacts were Rudy Stankovic and Russ Ewy
- Sintef (Norway), main contact was Jørn Stenebråten
- DI (Italy), main contact was Alessio Ferrari

Each laboratory is identified with a letter, used in the test results labelling (A = NGI, B = Sintef, C = RSTD, D = DI).

Specialised protocols were developed in recent years to evaluate hydro-mechanical properties of Opalinus Clay in both high-pressure oedometric tests (Favero 2017, Ferrari et al. 2016, Crisci et al. 2019) and triaxial deformation tests (Favero et al. 2018, Giger et al. 2018). In the case of triaxial testing, the testing procedures were further validated in a benchmarking study (Minardi et al. 2019, Minardi et al. 2020).

The one-dimensional swelling tests were also performed in the framework of the geomechanical testing programme but did not make use of advanced protocols.

3 Core sampling, storage and XCT scanning

3.1 Core sampling and conditioning

Cores used for geomechanical or rock-mechanical analyses (hereafter referred to as GM cores) represent one of nine major categories sampled at the borehole. Each of these categories has special requirements to minimise potential effects on laboratory analyses, and hence special conditioning methods. Target exposure time to atmosphere was set to 20 minutes for all GM cores to allow geological description and documentation (incl. core scanner for photographic description). A complete archive of core photographs, and exposure time to atmosphere prior to embedding the cores in resin is made in Nagra's internal QA/QC documentation.

(a)

(b)

(c)

(d)

Fig. 3-1: Sampling and storage workflow of GM cores

(a) Inserting core directly into PVC tube (no plastic film). (b) Rack of PVC tubes during curing with clamp bar in core at the front row (left side). (c) Labelled PVC tubes with core and top spacer (used for clamping) embedded in epoxy resin. (d) Custom made core box used for transporting and archiving. Example pictures are from borehole Bülach1-1 (Nagra 2021).

The cores were then immediately inserted in PVC tubes, and axially constrained with bar clamps (Fig. 3-1). The annulus was then filled with epoxy (Sikadur-52). The annulus between the core and the PVC tube was chosen very small (nominal 3.2 mm) to ensure no excessive temperature from curing of the epoxy develops[6]. Further details of the conditioning procedure are provided in the field manual (Rufer 2019).

A total of 88 GM cores with a cumulative length of 38 metres were conditioned in this way. An additional 10 cores were sampled later at the core storage facility. This was done to enable rock-mechanical testing to complement the in-situ testing programme (micro-hydraulic fracturing) where no conditioned core was secured, and only for hard rocks not sensitive to water exchange (drying).

3.2 Evaluation of core quality using XCT Scanning

To evaluate core integrity prior to shipping to the testing laboratories, all GM cores from Opalinus Clay and its confining units in the Upper Dogger and Lias (Staffelegg Formation) were analysed using medical X-ray computer-tomography (XCT). Details of the applied XCT method can be found in Keller & Giger (2019). The obtained image data had a voxel size of 0.25 × 0.25 × 0.4 mm. By stacking individual scans, a virtual cross-section could be obtained for each core (Fig. 3-2). It is noted that the CT-number is a proxy for material density. This enabled the detection of small cracks and a physical representation of the variability of material properties. These cross-sections were the basis for the selection of sub-coring for the geomechanical testing programme (Chapter 6, and Appendix B).

[6] Maximum measured temperature in the laboratory was < 27 °C.

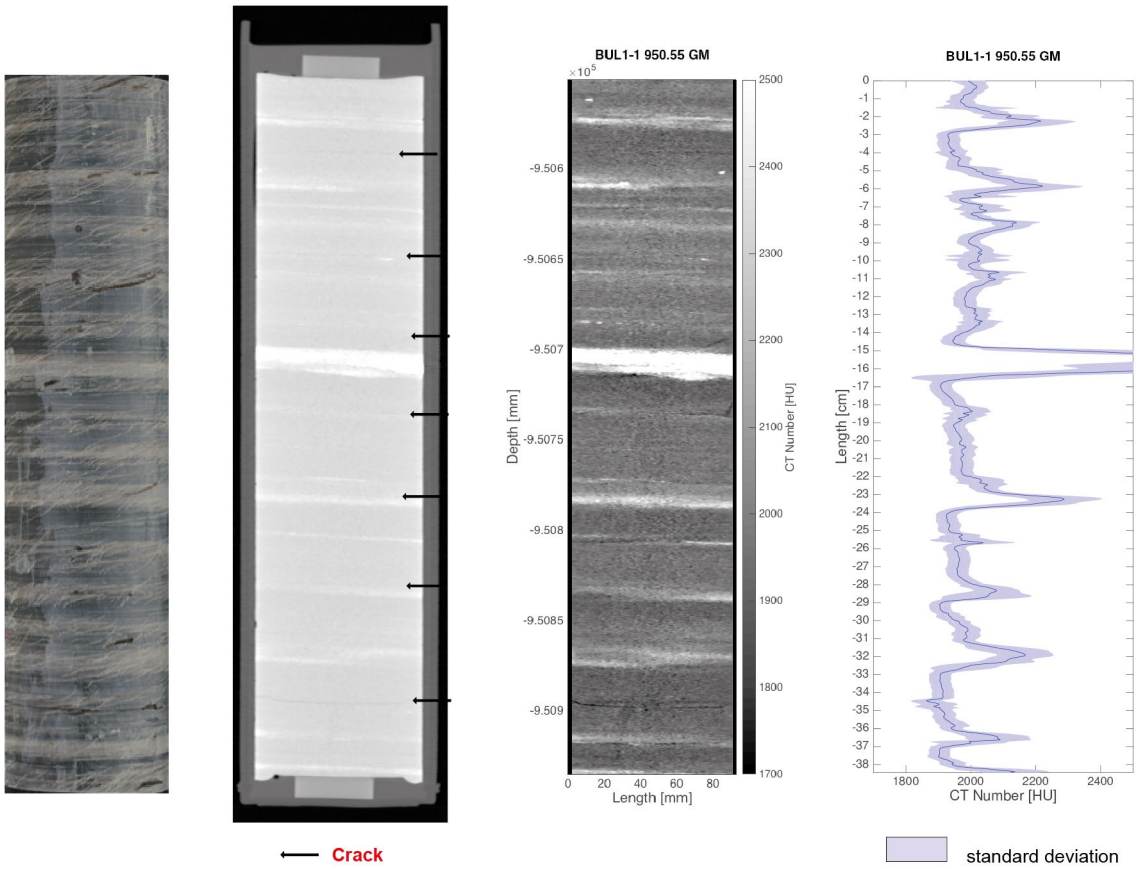

(a) (b) (c) (d)

Fig. 3-2: Cross-section of XCT stack

(a) core picture; (b) entire core in PVC tube and resin (both dark grey) and embedded spacers (light grey – subhorizontal cracks are indicated by arrows); (c) optimised image for the core only; (d) vertical profile with CT number (Hounsfield Units). Example pictures are from borehole Bülach1-1 (Nagra 2021).

4 Testing methods and overview of executed tests

4.1 Convention of sample geometry

Sedimentary geomaterials typically display transversely isotropic mechanical properties which are related to the orientation of the bedding. To study this anisotropic response, cylindrical specimens were tested in three orientations with respect to the bedding (Fig. 4-1).

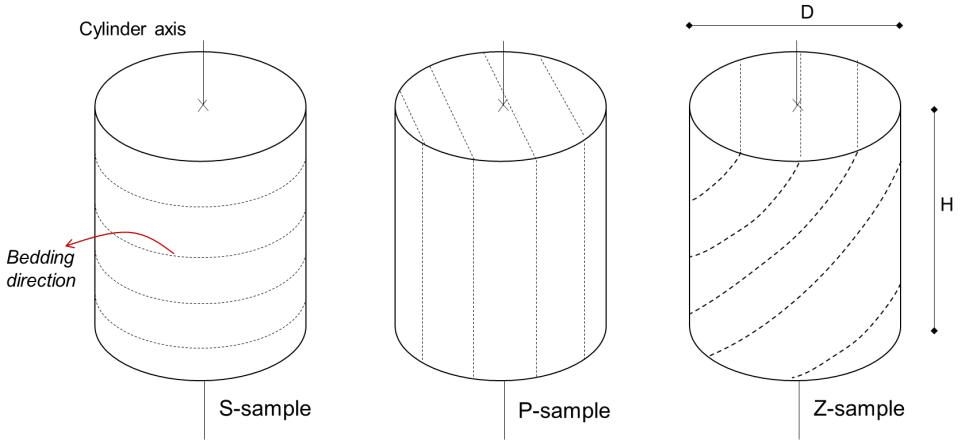

Fig. 4-1: Terminology of specimens in relation to bedding orientation

In this report, the following convention applies:

- S-samples: the cylinder axis is perpendicular to bedding direction
- P-samples: the cylinder axis is parallel to bedding direction
- Z-samples: the cylinder axis is at an angle with respect to bedding.

The convention applies to all kind of tests, however the ratio of diameter (D) to height (H) of the specimen is different. The ratio ranges from D:H ≈ 1/2 for triaxial and uniaxial tests, to D:H ≈ 1.4 in Brazilian tests and D:H ≈ 2.5 for oedometric tests.

4.2 Rock-mechanical testing programme – testing methods

4.2.1 Indirect tensile strength test (Brazilian)

The Brazilian test is a uniaxial compressive strength test aimed for the indirect determination of tensile strength, and tests were done according to ASTM standard D3967-16 (ASTM 2016).

Test specimens have a diameter between 25 and 30 mm and a width between 12.5 and 21 mm (thickness-diameter ratio of 0.50 to 0.70). Testing plugs were drilled either perpendicular to bedding (so-called "S" direction) or parallel to bedding (so-called "P" direction). The plugs were drilled with a diamond tipped hollow bit. Cooling during drilling and trimming was performed with the low viscous volatile mineral oil (Ilocut EDM 180 from Castrol, or Marcol 52). Plug trimming to the required length was carried out with a diamond chop saw with slow constant velocity feeding.

During the test, cylindrical specimens are loaded perpendicular to the cylinder axis (Fig. 4-2). For clarification, it is noted that loading was always done perpendicular to the core axis. In case of the P-samples (Fig. 4-1) loading was parallel to bedding and the tensile force perpendicular to bedding. In case of the S-samples loading and tensile force are both parallel to bedding.

The constant loading rate during testing was approximately 0.30 MPa/s. In case of the P-samples (*cf.* Section 4.1) the specimen was oriented such that loading was parallel to bedding, with the tensile force, consequently, acting perpendicular to bedding. In case of the S-samples loading and tensile force are both perpendicular to bedding. The majority of the Brazilian tests were carried out on a high precision digitally controlled electromechanical testing machine with a maximum load range of 100 kN (accuracy class 0.5) and some tests were done with a load frame of 2'000 kN load range.

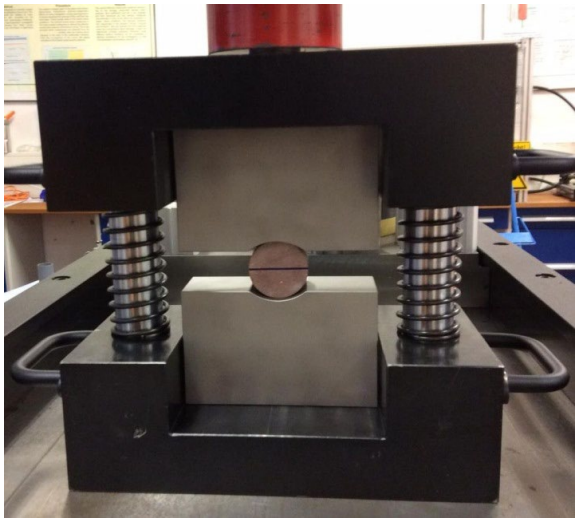

Fig. 4-2: Brazilian testing configuration with curved jaws
Plug diameter is 30 mm.

4.2.2 Unconfined compressive strength test

Unconfined compressive strength (UCS) tests were done according to ASTM standard D7012-14e1 (ASTM 2014).

Test specimens have a diameter of 25.4 mm and a length of at least 50.8 mm (length-diameter ratio of 2:1). Testing plugs were drilled either perpendicular to bedding (so-called "S" direction) or parallel to bedding (so-called "P" direction). The plugs were drilled with a diamond tipped hollow bit. Cooling during drilling and trimming was performed with the low viscous volatile mineral oil Ilocut EDM 180 from Castrol, or Marcol 52. Plug trimming to the required length was carried out with a diamond chop saw with slow constant velocity feeding. The accuracy in plane parallelism is in accordance with ASTM D4543-19 (ASTM 2019).

The majority of the UCS tests were performed on a digitally controlled, servo-hydraulic testing machine with a maximum load range of 600 kN (accuracy class 1), and some tests were performed with a load frame of 2'000 kN load range. For all tests, a constant strain rate of approximately 10^{-5} s^{-1} was applied.

Axial deformation of the specimen was measured with either one or two LVDT displacement transducers. Measurements were either done directly at the specimen or corrected for load frame deformation. Radial deformation of the specimen is measured diametric with a transverse extensometer (Fig. 4-3) or a set of radial LVDT's.

Throughout the report, the strains are calculated as the ratio of the variation in height (or diameter) to the initial height (or diameter).

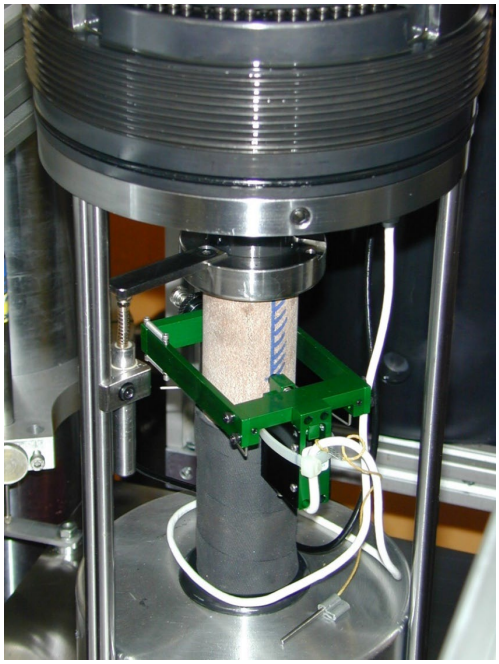

Fig. 4-3: UCS testing configuration

Note axial LVDT and transverse extensometer. Specimen diameter is 25.4 mm.

4.2.3 Triaxial deformation test

Triaxial deformation tests (TRX) tests were done according to ASTM standard D7012-14e1 (ASTM 2014) for single-stage procedure, but also included a hysteresis cycle (unload-reload) before and after peak strength (below).

Test specimens have the same dimensions as for the UCS tests (diameter 25.4 mm, length 50.8 mm) and were prepared in the same manner (*cf.* Section 4.2.2). The accuracy in plane parallelism is also in accordance with ASTM D4543-19 (ASTM 2019).

Axial (average of three LVDTs) and radial deformation of the specimen (diametric with one single strain gauge) were measured 'in-vessel' to avoid the load frame deformation being included in the results of the deformation of the individual specimen (Fig. 4-4). The measurement range of the LVDTs is ± 5 mm; their sensitivity in the range between 9 and 60 mV; non-linearity is 0.15% full scale. Three LVDTs were used to observe specimen distortions that will influence the strength measurements in a non-acceptable manner. The differential axial load (strain gauge) also was measured 'in vessel' with a load cell mounted directly below the specimen to eliminate the influence of piston friction effects to the stress measurement. The load cell used for the first specimens is a 600 kN load cell of accuracy class 0.5.

The artificial brine was composed of demineralised water and 5 g/l NaCl. An exception was the anhydrite specimen in test TRU1-1-1053TRX_S1 for which no fluid was used. The pistons are perforated to enable drained conditions. Side drains were not used. No spherical seats were used. All the important parameters were recorded automatically with different intervals, adjusted to expected speed of changes. No smoothing or filtering algorithms were applied.

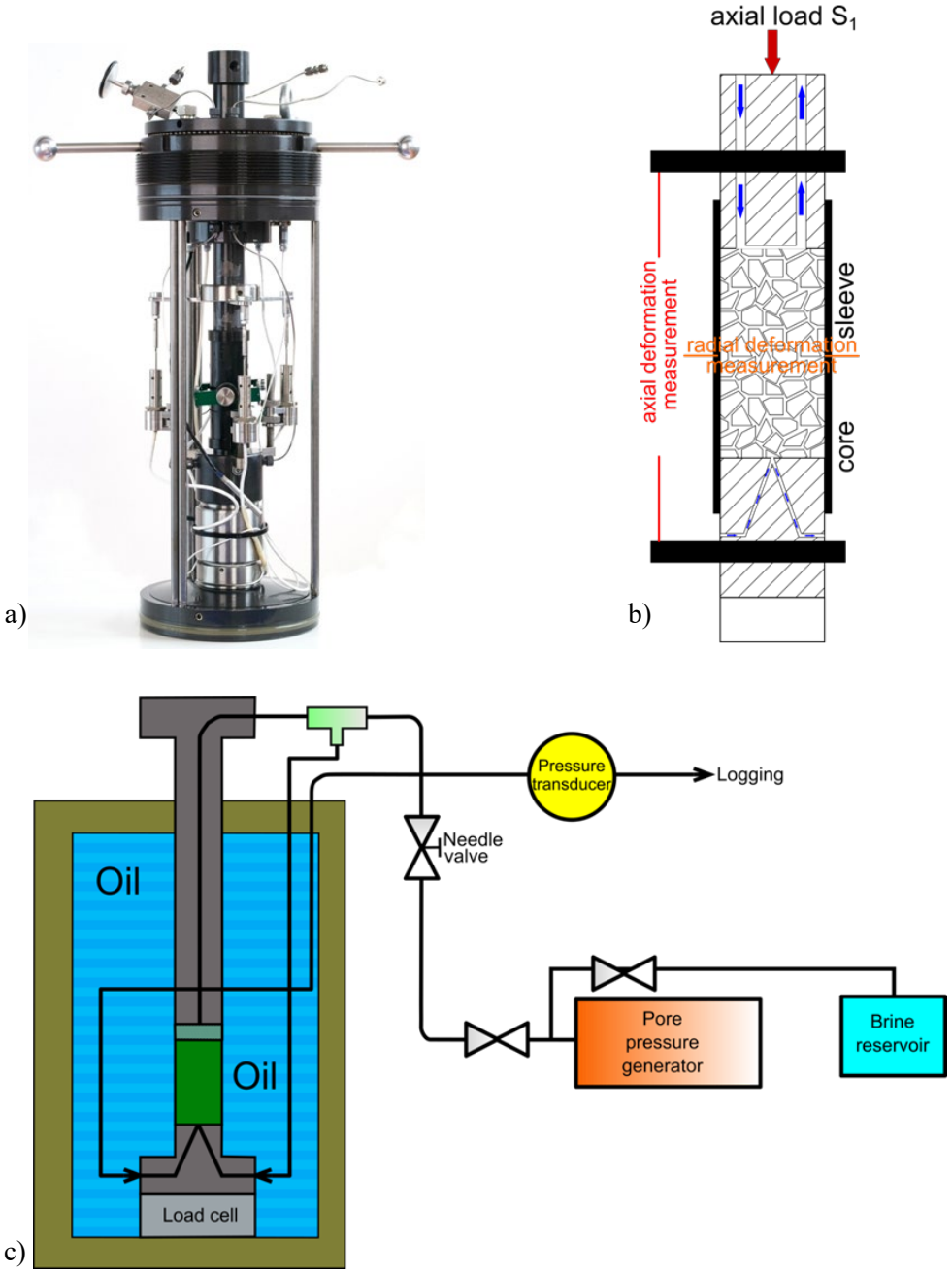

Fig. 4-4: Triaxial testing configuration used for rock-mechanical testing

Specimen in membrane with axial and radial strain sensors, pore fluid line and ultrasonics (a), schematic of the specimen (b) and the pressure cell with pore fluid system (c).

During all phases of the tests, ultrasonic velocities, both P- and S-waves, were logged and monitored according to ISRM standards (Aydin 2014). The piezometer resonance frequency was either 0.5 or 1 MHz.

The theoretically possible stress paths in a triaxial testing configuration with two independent controls (axial and radial stress) are illustrated in Fig. 4-5 in mean total stress (p) versus deviatoric stress (q) space, where:

$$p = \frac{\sigma_a + 2\sigma_r}{3} \tag{4-1}$$

$$q = \sigma_a - \sigma_r \tag{4-2}$$

where σ_a and σ_r are the total axial (direction of the cylinder axis) and radial (direction perpendicular to the cylinder axis) stress, respectively.

The upper part of the plane (compression part) summarises the stress paths that induce axial compression of the tested specimen. The shear path can be induced by either increasing the axial stress σ_a (CTC path), reducing the radial stress σ_r (RTC path) or increasing σ_a and reducing σ_r at the same time (TC path) keeping the mean total stress constant. The stress paths that induce an axial extension of the specimen are illustrated below the p-axis in Fig. 4-5. The axial extension can be induced by either decreasing the axial stress (RTE path), increasing the radial stress (CTE), or decreasing σ_a and increasing σ_r at the same time (TE path) keeping the mean total stress constant. Therefore, when the term 'reduce' is used to define the stress path, it means that one of the two stresses is decreased while the other is kept constant. On the other hand, when the term 'conventional' is used to define the stress path, it means that one of the two stresses is increased and the other is kept constant. It is noted that the illustrations in Fig. 4-5 are the stress paths for total stress only, so the tests can be conducted in either drained or undrained conditions. This means that the submitted loading conditions may differ based on the porewater pressure generation during undrained testing. For the triaxial tests of the rock-mechanical testing programme, only CTC stress paths were executed.

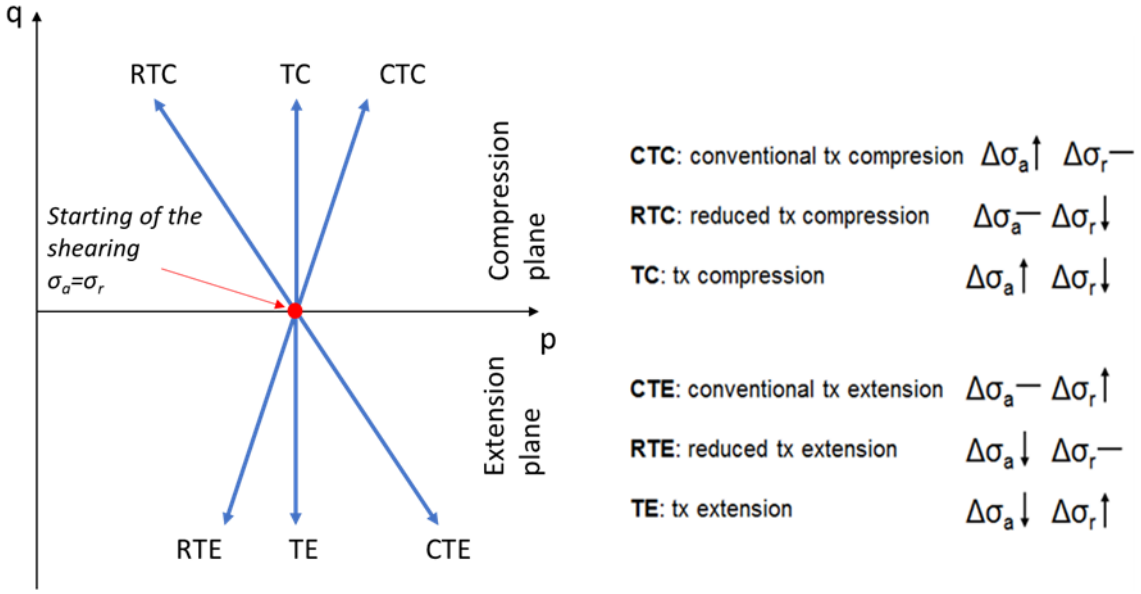

Fig. 4-5: Summary of possible stress paths that can be used to perform triaxial tests

On the right side, it is indicated which of the two stresses (axial σ_a and radial σ_r) is increased or decreased.

Test procedure

The testing procedure consisted of a maximum of four main phases:

1. Isotropic loading phase, during which the radial confining pressure and the axial load are increased simultaneously. The needle valve to the pore pressure generator is opened after the total stress has reached an equivalent value of 2 MPa. Both total mean stress (p) and fluid pressure (u_w) are then increased in concert to their respective target values: 10 to 15 MPa for p and 5 MPa for u_w.

2. *Selected tests only:* the pore-fluid-coupling parameter during isotropic loading (Skempton's B value) is evaluated in undrained conditions. During the Skempton's B test the change in pore pressure over time (Δu_w) is determined as a function of the change in isotropic pressure increase over time (Δp) (u_w is allowed to equilibrate at least for 20 minutes up to 12 – 24 hours):

$$B = \frac{\Delta u_w}{\Delta p} \tag{4-3}$$

   In the present case two to three Skempton's B tests were carried out per specimen with confining pressure increase Δp of 1 MPa.

3. *Selected tests only:* a consolidation phase is performed to determine the consolidation coefficient c_{vi}. An isotropic total stress increase (or decrease) is applied to the specimen and the deformations in time are recorded and analysed. The deformation evolves according to the dissipation of the pore water over (or under) pressure induced by the load variation. Calculation of the consolidation coefficient c_{vi} (in mm^2/h) is done according to the following equation (Head 1998):

$$c_{vi} = \frac{\pi D^2}{\lambda t_{100}} \tag{4-4}$$

   with D as the plug diameter and t_{100} as the theoretical time to 100% consolidation. The theoretical time t_{100} is found by extrapolating the linear portion of the volumetric strain versus square root of the experimental time curve (with time in h) to the final strain value. Lastly, λ is a constant depending on drainage boundary conditions.

   Depending on the lithology this test took up to several days. A consolidation phase was only requested for specimens that were estimated to be high in clay content, and therefore with potentially low permeability; for those tests, in order to allow proper drained or undrained conditions, strain rate was adjusted according to the consolidation coefficient estimation.

4. The fourth testing phase is the shearing phase or triaxial test, applying a constant deviatoric stress or strain rate. The standard strain rate was 10^{-6} s^{-1} but was adjusted based on theoretical calculations (Head 1998) using the consolidation coefficient determined in phase 3. Two tests required a lower strain rate.

The shearing phase of the triaxial tests was preceded in selected cases by a Skempton's B test for verification of specimen saturation and, subsequently, by a determination of the consolidation coefficient c_v as base for strain rate calculation. However, in the rock mechanics programme of TRU1-1 cores, consolidation coefficients was determined in one case only. Instead, strain rates were chosen based on lithological criteria (rock type, water content and mechanical properties based on UCS test results) and previous experiences (*cf.* Nagra 2021a and Nagra 2021b).

Generally, clay-rich rocks, such as clay- and siltstones or marls were tested at lower strain rates than limestones, sandstones and anhydrites. The strain rate of the single-stage triaxial tests ranges between 10^{-6} s^{-1} (9 TRX tests) and 5×10^{-7} s^{-1} (2 TRX tests). Strain rate was chosen based on lithological criteria and on the results of the determination of the consolidation coefficient c_v.

4.3 Geomechanical testing programme – testing methods

4.3.1 Synthetic pore fluid

The artificial porewater (APW) used in the geomechanical tests is based on the recipe derived from the investigations in the Schlattingen borehole (Mäder in Wersin et al. 2013), and the composition is reported in Tab. 4-1. This recipe defines a porewater saturated with respect to calcite and dolomite under atmospheric CO_2 partial pressure (lab conditions).

Towards the end of the geomechanical testing programme, the porewater chemistry was also constrained for the TRU1-1 core material (*cf.* Dossier VIII). These investigations confirm the general Na-Cl water type. The salinities in the Dogger section are somewhat higher than in the APW; e.g. chloride concentrations are in the range of 8 – 10 g/l (APW: 6.7 g/L). Towards the base of the Staffelegg Formation, the chloride contents decrease to about 4 g/L. In addition to saturation with carbonate minerals, the investigations suggest saturation with respect to the sulphate minerals celestite. But the APW was not changed for the final geomechanical tests, to be consistent with earlier tests. There was also a slight concern that higher mineralisation of the APW could lead to precipitation of saturated phases in the pore fluid lines. Finally, the slightly higher ionic strength in the pore water found in the TRU1-1 core is not anticipated to have a significant effect on hydromechanical properties (Witteveen et al. 2013, Ewy 2014, Tuttolomondo 2021).

Tab. 4-1: Recipe used for the preparation of the APW.

Compound	$mmol/kg_{H2O}$	g/kg_{H2O}
NaCl	115.26	6.7356
$NaHCO_3$	0.54	0.0456
$CaCl_2$ $2H_2O$	11.91	1.7510
KCl	2.55	0.1902
$MgCl_2$ $6H_2O$	9.17	1.8635
Na_2SO_4	24.00	3.4089

4.3.2 Triaxial deformation test (specialised protocol)

To assess the mechanical properties of Opalinus Clay and confining units, dedicated testing protocols were established (Minardi et al. 2019).

The extraction of the specimens was carefully performed in order to minimise water content loss during the operation. All involved laboratories used a drilling machine. In particular, Lab B used a special core barrel configuration where an internal piston was used to stabilise the specimen during drilling by the application of a small axial force. All labs used hydrocarbons as cooling fluids during the drilling of the specimens.

Computed tomography of the cores after drilling were used to identify the most suitable sections for extracting test specimens *(cf.* Appendix A). The target zones were selected upon EPFL and Nagra's guidance.

The conventional testing procedure indicated by Nagra to carry out triaxial tests foresaw the following steps (Fig. 4-6a):

1. An initial isotropic total stress (0.5 – 1 MPa) is applied to the specimen to ensure contact with the axial piston. The saturation of the specimen is then performed at constant volume to minimise specimen disturbance (i.e. fissure opening during resaturation); axial and radial stresses are progressively increased to keep the specimen's volume constant while it is put in contact with fluid at low back pressure. Next, the fluid back-pressure is increased to at least 2 MPa (the total stresses are also increased to keep the effective stress constant) (*ss1*), to dissolve possible air remaining in the tubing or the material. This procedure allows the determination of the axial and radial swelling pressures. The confining stress is then set equal to the axial stress (*ss2*). A pore pressure increment step is performed either at this stage (*ss3*) or before the shearing phase in order to reach the target confinment.
2. The assessment of the specimens' saturation is carried out by measuring the Skempton's B coefficient (B-check test). Two to three isotropic undrained loadings are performed. More steps are applied when unsatisfactory values are obtained.
3. Drained consolidation or swelling of the specimen is performed to reach the target consoli¬dation stress; consolidation effective stresses range between 4 and 17 MPa. The pore fluid pressure is kept constant to 8 – 10 MPa during consolidation.
4. The final stage is the shearing of the specimens at constant axial strain rate. An unloading reloading loop is performed, then the specimen is sheared until the specimen's failure and achievement of the post-peak constant deviatoric stress, in undrained or drained conditions.

This conventional testing procedure was adopted by Lab A and Lab B. A different procedure was used by Lab C and is referred to as «alternative procedure» (Fig. 4-6b). This alternative procedure foresees the equalisation of the specimen to different relative humidity values (between 92% and 98%) in desiccators before testing in order to achieve different saturation conditions. After that, the specimens were mounted in the rig, and an initial undrained loading was carried out until an increase of the pore pressure was detected. At this stage, the specimen was assumed to have achieved the fully saturated condition; B-check test was then performed in three steps. A pressure transducer was placed inside the vessel very close to the specimen to monitor the evolution of the pore fluid pressure during the application of the external mechanical stress. When this testing procedure is adopted, no artificial pore fluid is added to the specimen.

The laboratories involved in the triaxial testing programme with specialised protocols, prepared cylindrical specimens respecting the ratio D:H ≈ 0.5. In particular, the specimen nominal diameters are:

- Lab A: D = 25 mm
- Lab B: D = 25.4 mm
- Lab C: D = 19.1 mm

The labs used two drainage systems: Lab A and B used both radial drainage and drainage at the two edges, while Lab C used radial drainage and drainage at one edge of the cylinder. The strain rates to apply during shearing were defined according to the drainage conditions and the specimen dimensions (i.e., drainage length). Water content after testing is determined by oven-drying at 105 ºC for several days until constant weight.

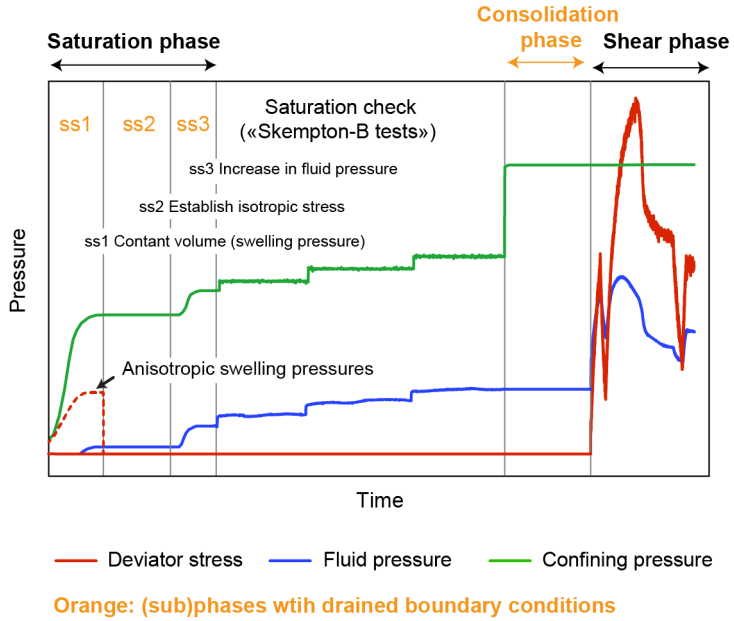

(a)

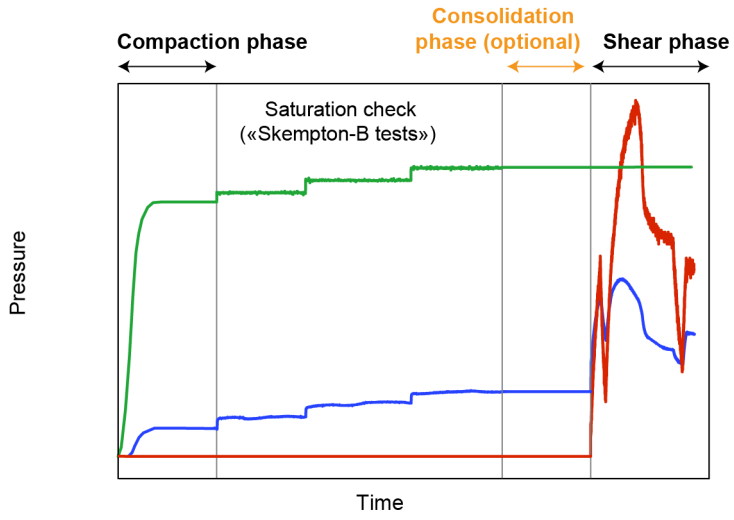

(b)

Fig. 4-6: Pressure-time sequences of triaxial deformation tests (specialised protocols)

(a) conventional and (b) alternative testing procedures for undrained boundary conditions during the shear phase.

4.3.3 Oedometric test (high-pressure, specialised protocol)

Specimens for oedometric testing are of cylindrical shape, with Diameter (D) to height (H) ratio D:H ≥ 2.5. The nominal dimensions of the specimens are:

- Lab A: D = 50.4 mm; H = 20.0 mm;
- Lab D: D = 35.0 mm; H = 12.5 mm;

The operators cut a pre-defined section of the core with a saw, through the PVC tube to minimise exposure of the geomaterial to the atmosphere. Then, the obtained slice is cut into a smaller piece to be handle within a lathe machine. No air nor water is used during the sawing process. Planarity and parallelism of the bases are verified, and the dimensions of sawn specimens are measured. In addition, Lab A covered the cut parts with a hydrocarbon oil and performed lathing at high humidity to limit the humidity gradient between the specimen and the laboratory atmosphere. After the final specimen diameter was reached, the specimen was wiped free of oil (using oil-only absorbent).

The specimen is then put into the oedometric ring, a rigid metallic ring to constrain the radial strains; silicon grease was placed on the internal surface of the ring to reduce the friction between the specimen and the metallic ring.

The specimen disks are loaded axially, and deformation is recorded with time.

Specimens are re-saturated within the apparatus in isochoric conditions. The axial deformations are kept constant by increasing the axial stress. Pore pressure is applied from the bottom side of the specimen at 50 kPa. When the swelling pressure generated by the saturation at isochoric conditions stabilises, pore pressure equal to 50 kPa is applied at the top side of the specimen. Displacements are monitored throughout this stage of the test. Once the axial stress has stabilised, the mechanical loading phase of the test can start.

The loading is performed in steps, starting from the axial swelling stress attained at the end of the resaturation phase. The incremental loading steps are performed by doubling the axial stress reached during the previous step. Each step lasted at least 24 hours. A few doubling steps (depending on the swelling stress) are performed to achieve axial stress of 10 – 15 MPa. For selected tests, a constant head permeability test (PERM) is performed at this stage, increasing the pore pressure at the bottom side and measuring the fluid flow through the specimen. The axial stress and pressure gradient are kept constant during the permeability test until steady-state conditions are achieved. Then, the bottom fluid pressure is reduced back to 50 kPa. Enough time is given for the displacement to stabilise, a minimum of 24 hours. An unloading/reloading phase follows. The specimen is then loaded in steps, up to a maximum stress of 60 MPa. Finally, an unloading phase is performed in steps to achieve axial stress of approximately 7 MPa.

After completion of the test, the oedometer cell is dismantled, and the specimen is dried in the oven to measure the water content (oven-drying at 105º C for several days until constant weight).

4.3.4 Complementary tests

In this section, complementary tests performed within the context of the geomechanical testing campaign are described: one-dimensional swelling (OS).

Specimens for one-dimensional swelling tests are placed in the oedometric cell. The top cap of the cell is mounted, but no axial stress is applied, rather than the weight itself of the cap. In case the top cap weight was not sufficient to counterbalance the pore pressure applied, an equivalent load was allowed on top of the piston. The specimen is put in contact with pore fluid at low pressure (< 50 kPa) to saturate the specimen. In the direction perpendicular to the cylinder axis, the expansion is constrained, while in the direction parallel to the cylinder axis, expansion is allowed.

The axial displacement is continuously recorded throughout the test. When the axial expansion stabilises, the top of the specimen is connected to the pore fluid reservoir, and further expansion is evaluated. When deformation stabilises, the test is considered concluded. After completion of the test, the oedometer cell is dismantled, and the specimen is dried in the oven to measure the water content.

Constant-head permeability tests were performed on 4 of the specimens tested at predefined stages during one-dimensional compression tests, at constant vertical total stress.

A pore pressure gradient between top and bottom side of the specimen was applied via two independent Pressure/Volume controllers, and the volumes of water flowing in and out of the specimen were measured. Once the flow reached a stable value (after a few days), this was used to compute the hydraulic conductivity adopting Darcy's law. After completion of the permeability phase, the oedometric test continued as described in the previous section.

4.4 Lithostratigraphy and test overview

4.4.1 Lithostratigraphy of tested core material

A brief summary is provided here on lithological characteristics of the formations of which cores were used in geomechanical testing. Further details on lithology can be found in Dossier III (TBO Trüllikon-1-1: Lithostratigraphy).

- **«Felsenkalke» + «Massenkalk»**: Well bedded limestone («Felsenkalke») to more massy sponge bioherm («Massenkalk»). Dolomitization processes cause local blurring of layering, and stylolites are common.
- **Schwarzbach Formation**: Calcareous marl to argillaceous limestone.
- **Villigen Formation**: Mostly calcareous, micritic limestone.
- **«Parkinsoni-Württembergica-Schichten»**: A uniform succession of micaceous claystone (calcareous) to argillaceous marl. The main lithology throughout the entire unit is a silty to sandy claystone (calcareous) with local transition to sandy marl as the main lithology.
- **«Humphriesioolith Formation»**: Marly interval with limestone beds which is sandwiched between two iron-oolitic beds at the top and at the base, all being very fossiliferous.
- **Wedelsandstein Formation**: silty to sandy claystone (calcareous) and sandy marl. The interbeds consist of biodetritic limestone (sandy) but a few beds at the base show a transition to calcareous sandstone and even to sandstone (calcareous). A considerable proportion of quartz sand and a rather sparse content of macrofossils are characteristic.
- **Opalinus Clay**: Argillaceous siltstones and marls to claystones. The following subdivison was specified:
  - **816.42 – 846.88 m Sub-Unit 1**: **«Subunit with silty calcareous beds» (30.46 m)**: Claystone to silty claystone (calcareous) with limestone beds and hardgrounds. In interval 833.03 to 837.04 m lenticular-bedded with mm-thick layers of siltstone to sandstone (calcareous).
  - **846.88 – 860.24 m Sub-Unit 2**: **«Upper silty subunit» (13.36 m)**: Dominated by silty claystone (calcareous), dark grey, very micaceous, lenticular-bedded by mm- to cm-thick layers of siltstone to sandstone (fine-grained) (calcareous), light grey.

  - **860.24 – 912.95 m Sub-Unit 3**: **«Mixed clay-silt-carbonate subunit» (52.71 m)**: Silty claystone (calcareous) to sandy claystone (silty, calcareous), dark grey, micaceous. Laminae and lenses of siltstone and standstone fades away at approximately 873.45 m for the remaining of this subunit, where it is rather uniform composed of silty claystone (calcareous). A conspicious feature is the cluster of siderite nodules from 875.32 m to 877.94 m.
  - **912.95 – 927.91 m Sub-Unit 4**: **«Clay-rich subunit» (14.96 m)**: Silty claystones (calcareous), laminated and with abundant siderite nodules in the upper part (to approximately 919 m), and claystone (silty, calcareous) with virtually no siderite nodules in the lower part.

- **Staffelegg Formation**: Heterogeneous succession, dominated by marl and claystone, some bituminous, and including various thin limestone horizons, some of them iron-oolitic. The tested interval at approximately 955 m belongs to the Frick Member which consists of micaceous and silty claystone.
- **Klettgau Formation**: Heterogeneous succession of carbonates, marls and sandstones. The tested interval at 989.84 m belongs to the Seebi Member and consists of dolomitic breccia in a matrix of dolomitic marl. The interval at 1'022.27 m is from the Ergolz Member and is a argillaceous marl (silty, dolomitic).
- **Bänkerjoch Formation**: Succession of sulphate sediments, interbedded by dolomitic marls, dolostones and sandstones. The tested intervals 1'050 m to 1'074 m are from anhydrites, interbedded with claystone layers.
- **Schinznach Formation**: Succession of dolomites and dolostones, partly dolomitised limestones and micritic limestones, and bituminous claystones. The tested intervals are predominantly dolostones and limestones.

4.4.2 Test overview

A total of 164[7] rock-mechanical and geomechanical tests were conducted on a total of 32 cores from borehole TRU1-1 (Tab. 4-2). The number of tests in the geomechancial testing programme is smaller than in the rock-mechanical testing programme. However, typical testing times in the geomechanical programme were 12 to 30 days for TRX+ tests and 20 to 35 days for OED+ tests. That is one order of magnitude longer than the typical TRX test in the rock-mechanical testing programme.

Cores without proper initial conditioning (PVC = 0 in Tab. 4-2) were generally only used for lithologies not sensitive to water exchange, i.e. without any macroscopic indication of damage at the time of sampling in the storage facility.

[7] The constant-head tests (PERM) are performed in some of the oedometric tests (OED+) and are therefore not counted separately in the total number of tests, but they are listed as such in Tab. 4-2 for overview.

Tab. 4-2: Overview of performed tests

The red border illustrates the clay-mineral rich interval of Opalinus Clay and confining units (focus of geomechanical testing programme). PVC indicates whether cores were conditioned in resin and core barrel on site (1) or later wrapped in aluminium foil off-site (0). TRX = triaxial test, UCS = unconfined compressive strength test, TS = indirect tensile strength test (Brazilian), TRX+ = TRX with specialised protocols, OED+ = Oedometric test with specialised protocols (high-pressure); PERM = constant-head tests in OED+ tests), OS = one-dimensional swelling test.

Core-ID	**Formation**	**Top**	**Length**	**Bottom**		**Rock-mechanical testing programme**			**Geomechanical testing programme**			
						Standard rock-mechanical tests			**Special protocols**		**Other**	
TRU1-1-		[m]	[cm]	[m]	**PVC**	**TRX**	**UCS**	**TS**	**TRX+**	**OED+**	**PERM**	**OS**
514.95/50-GM	«Felsenkalke» + «Massenkalk»	514.95	50	515.45	1		3	2				
535.82/45-GM		535.82	45	536.27	1	1	2	2				
554.58/45-GM		554.58	45	555.03	1		3	3				
605.98/31-GM		605.98	31	606.29	1	1	2	2				
613.45/54-GM		613.45	54	613.99	0		2	2				
632.56/47-GM	Schwarzbach Fm.	632.56	47	633.03	1	1	2	2				
644.45/54-GM		644.45	54	644.99	0		4	2				
653.44/54-GM	Villigen Fm	653.44	54	653.98	0		2	2				
668.22/54-GM		668.22	54	668.76	0	1	2	2				
697.48/50-GM		697.48	50	697.98	1	1	2	2				
757.32/42-GM	«Parkinsoni-W.-Sch.»	757.32	42	757.74	1			2				
775.23/40-GM	«Humphriesioolith»	775.23	40	775.63	1	2	2	2				
796.64/45-GM	Wedelsandstein Fm.	796.64	45	797.09	1					2	1	1
797.91/45-GM		797.91	45	798.36	1		4	4	1			
810.87/50-GM		810.87	50	811.37	1		4	4	1			
836.32/50-GM	Opalinus Clay	836.32	50	836.82	1				6	2	2	
851.70/50-GM		851.70	50	852.20	1				5			
875.48/39-GM		875.48	39	875.87	1				7			
878.11/43-GM		878.11	43	878.54	1					4	1	3
894.84/50-GM		894.84	50	895.34	1				5			
903.19/45-GM		903.19	45	903.64	1				6	2		2
924.96/45-GM		924.96	45	925.41	1				2	1		1
955.69/43-GM	Staffelegg Fm.	955.69	43	956.12	1					1		
989.84/46-GM	Klettgau Fm.	989.84	46	990.30	0	1	2	2				
1022.27/45-GM		1'022.27	45	1'022.72	1	1	1	2				
1050.05/35-GM	Bänkerjoch Fm.	1'050.05	35	1'050.40	1		1	2				
1053.45/50-GM		1'053.45	50	1'053.95	1	1	2	2				
1074.50/39-GM		1'074.50	39	1'074.89	1		3	2				
1093.25/50-GM	Schinznach Fm.	1'093.25	50	1'093.75	1	1	1	2				
1096.76/40-GM		1'096.76	40	1'097.16	1		2	2				
1107.82/47-GM		1'107.82	47	1'108.29	1		2	2				
1122.44/43-GM		1'122.44	43	1'122.87	1		2	2				
Total					**28**	**11**	**50**	**51**	**33**	**12**	4	**7**

5 Rock-mechanical testing

5.1 Indirect tensile strength test (Brazilian)

A total of 51 Brazilian tests were performed from two laboratories (Tab. 5-1). The splitting tensile strength (MPa) is calculated according to the following formula (curved jaws):

$$s_Z = \frac{1272 * F}{\pi * d * l} \quad (5\text{-}1)$$

with the compressive force F (in kN); the specimen diameter d (in mm) and the specimen length l (in mm). It is noted that the values of s_z are negative.

Tab. 5-1: Test results from indirect tensile strength tests

For specimen geometry see Fig. 4-1.

Test-ID	**Specimen geometry**	**Average depth**	**Bulk density**	**Water content**	**Tensile strength**
		[m]	[g/cm^3]	[wt.-%]	[MPa]
TRU1-1_514TS_S1_2	S	515.24	2.672	0.33	-7.81
TRU1-1_514TS_P1	P	515.32	2.674	0.30	-1.81
TRU1-1_535TS_P1	P	535.97	2.636	0.67	-9.26
TRU1-1_535TS_S1	S	536.02	2.636	0.71	-5.17
TRU1-1_554TS_P1	P	554.72	2.632	0.92	-3.66
TRU1-1_554TS_S1	S	554.77	2.607	1.01	-6.12
TRU1-1_554TS_S2	S	554.98	2.611	1.27	-6.57
TRU1-1_605TS_S1	S	606.01	2.638	2.01	-3.64
TRU1-1_605TS_P1	P	606.06	2.648	2.01	-3.42
TRU1-1_613TS_S1	S	613.68	2.731	0.14	-6.14
TRU1-1_613TS_P1	P	613.74	2.630	0.18	-5.26
TRU1-1_632TS_S1	S	632.62	2.593	2.23	-7.62
TRU1-1_632TS_P1	P	632.68	2.322	2.11	-3.36
TRU1-1_644TS_S1	S	644.77	2.630	0.35	-5.50
TRU1-1_644TS_P2	P	644.83	2.638	0.45	-7.23
TRU1-1_653TS_S1	S	653.67	2.641	0.34	-4.46
TRU1-1_653TS_P1	P	653.74	2.635	0.35	-6.24
TRU1-1_668TS_S1	S	668.56	2.636	0.23	-1.47
TRU1-1_668TS_P1	P	668.61	2.632	0.18	-4.63
TRU1-1_697TS_S1	S	697.66	2.670	0.36	-13.25
TRU1-1_697TS_P1	P	697.72	2.683	0.44	-5.79
TRU1-1_757TS_S1	S	757.35	2.474	5.60	-3.43
TRU1-1_757TS_P1	P	757.39	2.497	5.75	-2.19
TRU1-1_775TS_S1	S	775.25	2.603	7.79	-2.99
TRU1-1_775TS_P1	P	775.31	2.574	8.90	-1.69

Tab. 5-1: (continued)

Test-ID	**Specimen geometry**	**Average depth**	**Bulk density**	**Water content**	**Tensile strength**
		[m]	[g/cm^3]	[wt.-%]	[MPa]
TRU1-1_797TS_S1	S	797.96	2.525	3.49	-2.49
TRU1-1_797TS_S2	S	797.96	2.514	3.15	-3.66
TRU1-1_797TS_S3	P	798.00	2.538	2.77	-3.13
TRU1-1_797TS_S4	P	798.00	2.557	2.69	-3.68
TRU1-1_810TS_S5	S	810.92	2.459	4.61	-2.20
TRU1-1_810TS_S6	S	810.92	2.451	4.51	-1.70
TRU1-1_810TS_S7	P	810.95	2.456	4.57	-1.75
TRU1-1_810TS_S8	P	810.95	2.459	4.23	-2.00
TRU1-1_989TS_S1_2	S	990.14	2.667	5.04	-4.64
TRU1-1_989TS_P1	P	990.07	2.654	0.41	-3.89
TRU1-1_1022TS_S1	S	1'022.33	2.494	6.05	-5.07
TRU1-1_1022TS_P1	P	1'022.35	2.514	5.44	-1.61
TRU1-1_1050TS_S1	S	1'050.07	2.596	4.72	-3.44
TRU1-1_1050TS_P1	P	1'050.12	2.528	5.52	-2.12
TRU1-1_1053TS_P1	P	1'053.73	2.733	1.40	-6.73
TRU1-1_1053TS_S1	S	1'053.77	2.667	2.96	-5.10
TRU1-1_1074TS_S1	S	1'074.70	2.839	1.32	-6.74
TRU1-1_1074TS_P1	P	1'074.75	2.820	1.38	-5.30
TRU1-1_1093TS_S1	S	1'093.27	2.542	5.38	-4.86
TRU1-1_1093TS_P1	P	1'093.31	2.535	5.77	-5.26
TRU1-1_1096TS_S1	S	1'096.99	2.559	5.36	-6.51
TRU1-1_1096TS_P1	P	1'097.04	2.564	5.24	-5.07
TRU1-1_1107TS_S1	S	1'107.87	2.403	5.73	-5.48
TRU1-1_1107TS_P1	P	1'107.92	2.521	6.10	-6.03
TRU1-1_1122TS_S1	S	1'122.58	2.728	0.58	-10.88
TRU1-1_1122TS_P1	P	1'122.63	2.712	0.23	-7.40

The test results yielded values from -13.25 MPa to -1.47 MPa for S-samples and -9.26 MPa to -1.61 MPa for P-samples. Photographs of the specimens before and after testing can be found in Appendix A.

5.2 Unconfined compressive strength tests

A total of 51 UCS tests were performed (Tab. 5-2). Photographs of the specimens before and after testing can be found in Appendix A.

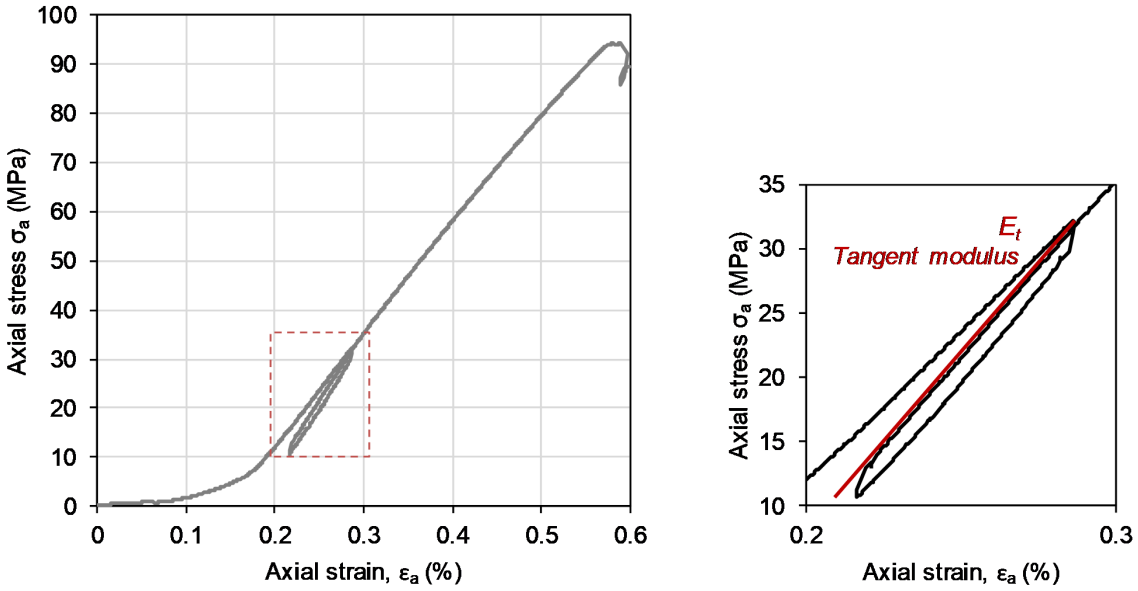

Fig. 5-1: Stress strain diagram for UCS test

On the right zoom into the unload reload loop, and definition of tangent and secant Young's moduli. Example from test BUL1-1_661UCS_S1 (Nagra 2021).

At the linear portion of the axial load cycle, an unload-reload cycle was performed by reducing the axial stress to 1/3 of the actual load, and hysteresis was observed. The cycle was performed for determining the elastic properties of the rock. The Young's modulus E (in GPa) was determined as an average reload modulus using the slope of the rising portion of the hysteresis as the ratio between the axial load change $\Delta\sigma_a$ (in MPa) and the induced axial strain $\Delta\varepsilon_a$ (dimensionless) according to the equation:

$$E = \frac{\Delta\sigma_a}{\Delta\varepsilon_a} \tag{5-2}$$

The Poisson's ratio (ν) is calculated as the negative ratio between the delta in radial $\Delta\varepsilon_r$ and axial strain $\Delta\varepsilon_a$:

$$\nu = -\frac{\Delta\varepsilon_r}{\Delta\varepsilon_a} \tag{5-3}$$

An example of calculation of tangent E modulus is reported in Fig. 5-1.

Following the hysteresis, the axial load was again increased until peak strength was reached, and the specimen was allowed to fail. The compressive peak strength was derived from the peak value of the axial load.

Some tests did not include and unloading-reloading cycle (marked in Tab. 5-2). For those tests, the elastic properties are computed at 50% of the maximum shear strength. Based on the available information from the other tests (where unloading-reloading cycles were performed), it is estimated that the Young Moduli E_{50} correspond to 50 – 80% of the moduli computed over a reloading path as shown in Fig. 5-3.

Tab. 5-2: Test results from UCS test

[a] No unloading and reloading was perfomred. Young's modulus refers to E_{50}. For specimen geometry see Fig. 4-1.

Test-ID	**Specimen geometry**	**Average depth**	**Bulk density**	**Water content**	**Young's modulus**	**Poisson's ratio**	**Peak strength**	**Strain at peak strength**
		[m]	[g/cm^3]	[wt.-%]	[GPa]	[-]	[MPa]	[%]
TRU1-1_514UCS_S1	S	515.14	2.695	0.23	34.2	0.16	124.1	0.49
TRU1-1_514UCS_P1	P	515.13	2.699	0.22	29.2	0.23	62.8	0.45
TRU1-1_514UCS_S2	S	515.21	2.708	0.31	30.5	0.68	76.9	0.58
TRU1-1_535UCS_P1_2	P	535.84	2.663	0.50	32.4	0.18	242.7	0.80
TRU1-1_535UCS_S1	S	535.89	2.682	0.64	33.3	0.23	147.0	0.47
TRU1-1_554UCS_S1	S	554.87	2.617	1.28	24.5	0.11	62.1	0.34
TRU1-1_554UCS_S2	S	554.93	2.611	1.24	29.4	0.15	154.8	0.56
TRU1-1_554UCS_P1	P	554.92	2.601	1.43	20.5	0.14	39.7	0.50
TRU1-1_605UCS_S1	S	606.14	2.662	2.20	15.1	0.21	64.8	0.75
TRU1-1_605UCS_P1	P	606.14	2.681	2.17	19.6	0.31	74.8	0.66
TRU1-1_613UCS_S1	S	613.52	2.653	0.19	28.3	0.12	142.5	0.58
TRU1-1_613UCS_P1	P	613.51	2.647	0.20	31.4	0.16	144.4	0.50
TRU1-1_632UCS_S1	S	632.77	2.631	2.29	15.3	0.23	78.9	0.91
TRU1-1_632UCS_P1	P	632.77	2.636	2.27	20.6	0.2	86.7	0.64
TRU1-1_644UCS_S1	S	644.66	2.626	0.64	21.4	0.15	107.3	0.76
TRU1-1_644UCS_P1	P	644.64	2.641	0.66	28.5	0.2	101.2	0.45
TRU1-1_644UCS_S2	S	644.73	2.658	0.39	29.05	0.16	168.02	0.69
TRU1-1_644UCS_P2	P	644.71	2.654	0.42	24.57	0.14	91.77	0.49
TRU1-1_653UCS_S1	S	653.87	2.632	0.40	25.53	n.a.	169.68	0.79
TRU1-1_653UCS_P1	P	653.86	2.632	0.37	29.61	0.17	160.22	0.65
TRU1-1_668UCS_S1	S	668.69	2.657	0.21	29.38	0.18	182.76	0.67
TRU1-1_668UCS_P1	P	668.68	2.652	0.20	31.91	0.23	179.03	0.63
TRU1-1_697UCS_S1	S	697.59	2.695	0.74	20.23	0.14	106.75	0.59
TRU1-1_697UCS_P1	P	697.59	2.696	0.77	24.34	0.16	96.72	0.46
TRU1-1_775UCS_S1	S	775.38	2.619	5.23	13.55	0.25	53.46	0.56
TRU1-1_775UCS_P1	P	775.38	2.632	4.90	14.72	0.19	52.76	0.50
TRU1-1_797UCS_S1	S	798.22	2.540	2.20	15.39[a]	0.30	63.08	0.60
TRU1-1_797UCS_S2	S	798.22	2.567	2.20	14.15[a]	0.28	60.82	0.68
TRU1-1_797UCS_S3	P	798.08	2.551	2.50	21.54[a]	0.36	63.91	0.41
TRU1-1_797UCS_S4	P	798.08	2.553	2.40	19.97[a]	0.26	60.92	0.50
TRU1-1_810UCS_S5	S	811.06	2.473	3.80	8.25[a]	0.34	42.19	0.84
TRU1-1_810UCS_S6	S	811.06	2.473	3.80	7.28[a]	0.29	35.09	0.80
TRU1-1_810UCS_S7	P	811.01	2.472	3.90	11.27[a]	0.34	38.99	0.46
TRU1-1_810UCS_S8	P	811.01	2.476	3.90	11.07[a]	0.41	43.95	0.52
TRU1-1_989UCS_S1	S	989.99	2.693	0.42	23.75	0.19	52.04	0.47
TRU1-1_989UCS_P1	P	989.99	2.703	0.50	24.96	0.31	56.36	0.34
TRU1-1_1022UCS_P1	P	1022.42	2.519	5.49	13.41	0.56	50.88	0.50

Tab. 5-2: (continued)

Test-ID	Specimen geometry	Average depth	Bulk density	Water content	Young's modulus	Poisson's ratio	Peak strength	Strain at peak strength
		[m]	[g/cm^3]	[wt.-%]	[GPa]	[-]	[MPa]	[%]
TRU1-1_1050UCS_P1	P	1050.20	2.565	4.64	17.28	0.46	29.62	0.21
TRU1-1_1053UCS_P1	P	1053.50	2.837	0.65	28.42	0.15	103.23	0.58
TRU1-1_1053UCS_S2	S	1053.68	2.81	1.08	20.91	0.15	54.11	0.39
TRU1-1_1074UCS_S1	S	1074.65	2.922	0.40	32.86	0.13	83.95	0.36
TRU1-1_1074UCS_P1	P	1074.65	2.952	0.21	31.36	0.11	83.95	0.45
TRU1-1_1074UCS_S2	S	1074.84	2.781	2.14	14.6	0.11	29.81	0.34
TRU1-1_1093UCS_S1	S	1093.37	2.501	5.59	21.91	0.3	50.03	0.35
TRU1-1_1096UCS_S1	S	1097.11	2.584	4.61	25.81	0.15	123.95	0.62
TRU1-1_1096UCS_P1	P	1097.11	2.581	5.12	25.68	0.18	94.57	0.53
TRU1-1_1107UCS_S1	S	1108.24	2.467	7.16	18.1	0.25	57.38	0.49
TRU1-1_1107UCS_P1	P	1108.24	2.51	6.49	17.37	0.22	74.25	0.71
TRU1-1_1122UCS_S1	S	1122.82	2.759	0.42	31.81	0.14	247.21	0.89
TRU1-1_1122UCS_P1	P	1122.82	2.771	0.33	35.26	0.16	246.99	0.87

The relatively large lithologic variability of tested specimens is reflected by the test results, ranging just over one order of magnitude both for Youngs moduli and strength. Most UCS plugs failed by longitudinal splitting or due to spalling.

During test TRU1-1_653UCS_S1 an error occurred in lateral extension measurement, therefore Poisson's ratio could not be computed, and the specimen of tests TRU1-1_1022UCS_P1 was pre-damaged (microfissures, cf. Appendix A)

A number of tests especially in limestones of the Malm were controlled by planes of relative weakness, e.g. healed fractures (TRU1-1_514UCS_P1, TRU1-1_514UCS_S2 and TRU1-1 _554UCS_P1) or stylolites (TRU1-1_554UCS_S1, TRU1-1_613UCS_P1). Specimens TRU1-1 _1053UCS_P1 and TRU1-1_1053UCS_S1 failed along a pronounced material change parallel to their bedding.

5.3 Triaxial deformation tests

A total of 11 triaxial tests were performed. Photographs of the specimens before and after testing can be found in Appendix A.

Basic properties and test conditions are provided in Tab. 5-3. The water content reported refers to the final, post-test measurement. With some exceptions, tests were conducted undrained with an initial fluid pressure of 5 MPa. The exceptions were one test (1053TRX_S1, anhydrite) where no pore fluid pressure was applied, and several tests with slightly larger pore pressure (approximately 6 – 7 MPa) to allow monitoring of fluid pressure in undrained conditions where larger dilation occurs (see below).

A consolidation phase was performed for test 775TRX_S1 to constrain the consolidation coefficient, which was used to examine the appropriate strain rate. In the same test and in tests 775TRX_S2 Skempton's B values were also constrained[8]. Confining pressure in all tests ranged from 10 to 18 MPa. Ultrasonic velocities were recorded throughout the tests, and the tabulated values in Tab. 5-3 were constrained at the start of the shear phase. Signals were either too weak or unclear for the S-wave velocity in some tests. The range of values of confining stress and pore pressure were chosen to reflect approximately expected in situ state conditions, but at the same time it was decided not to change the values proportionally to depth of extraction to enable comparisons of test results between lithologies.

Tab. 5-3: Basic properties and triaxial test results from consolidation and saturation stage

For specimen geometry see Fig. 4-1.

Test-ID **TRU1-1**	**Specimen geometry**	**Average depth**	**Bulk density**	**Water content**	**Pore pressure**	**Confining pressure**	**Consolidation coefficient c_v**	**Skempton's B**	**P-wave velocity**	**S-wave velocity**
		[m]	[g/cm^3]	[wt.-%]	[MPa]	[MPa]	[mm^2/h]	[-]	[m/s]	[m/s]
535TRX_S2	S	536.11	2.661	1.85	5.0	10.0			6'169	3'144
605TRX_S1	S	606.23	2.640	4.75	7.0	14.0		0.70	4'243	2'100
632TRX_S1	S	632.87	2.621	3.23	7.0	12.0		0.65	4'290	2'335
668TRX_S1	S	668.25	2.618	1.25	5.0	10.0			5'749	2'979
697TRX_S1	S	697.79	2.686	1.15	5.0	10.0			6'121	3'150
775TRX_S1	S	775.49	2.654	4.94	7.0	12.0	64	0.59	4'084	
775TRX_S2	S	775.49	2.632	7.17	6.7	15.0		0.52	3'924	
989TRX_S1	S	990.16	2.691	1.18	5.0	10.0			5'950	3'195
1022TRX_P1	P	1'022.60	2.500	7.16	5.0	10.0			3'971	
1053TRX_S1	S	1'053.67	2.818	0.86	dry	10.0			5'364	
1093TRX_S1	S	1'093.58	2.530	7.19	5.0	10.0			4'984	2'780

Undrained testing in several tests proved challenging. In some tests the positive pore pressure build-up during the loading phase was significant. To avoid pore pressure exceeding the confining pressure, drained testing conditions were enabled when the pore pressure reached a level of 0.5 MPa below the confining pressure (Fig. 5-2, left side). This was implemented in 8 tests (Tab. 5-4; stress path noted as CTC).

In some cases, post-peak stress equilibration was not achieved. Rapid stress decreases occurred in a few cases (Fig. 5-2, right side) and no post-peak strength was assigned in Tab. 5-4.

[8] The tabulated values in Tab. 5-3 are not corrected for potential equipment compliance.

In test 668TRX_S1 (Fig. 5-2, right side), the sudden stress decrease was followed by a leakage through the specimen sleeve, that caused a connection between imposed cell pressure and measured pore pressure and pore pressure measurement recorded an unrealistic increase at the end of the shearing.

In test 632TRX_S1 (Fig. 5-2, left side) the post peak strength was approaching a stable value when a sudden drop in deviatoric stress occurred. A slide along the fracture is envisaged. For this test the post-peak strength value was selected before the rapid stress decrease.

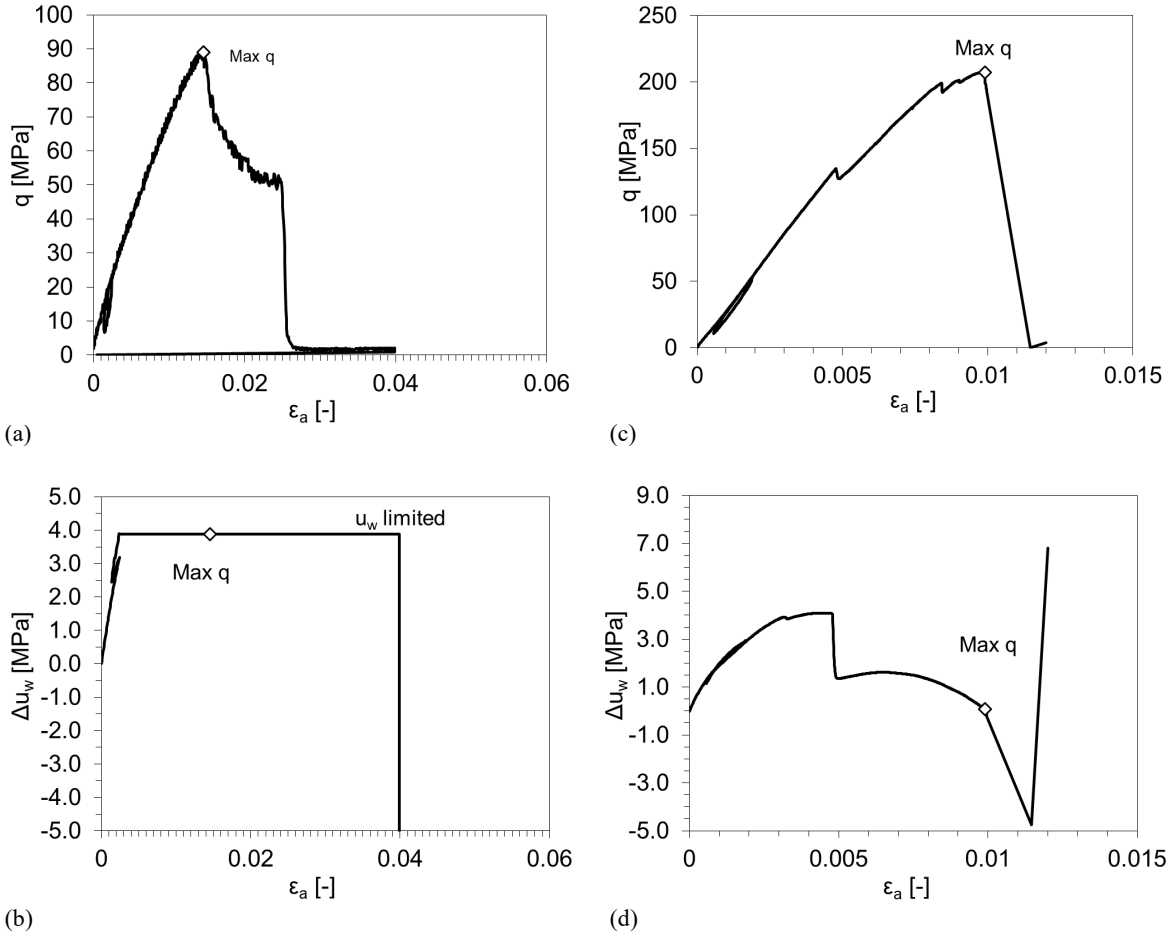

Fig. 5-2: Examples of problematic pore pressure evolution during undrained testing

(a), (b) Example test 632TRX_S1, with deviatoric stress (q, (a)) and generated pore fluid pressure (Δu_w, (b)). Pore fluid pressure was held constant to avoid fluid pressure exceeding the confining pressure. After peak, a sudden axial stress drop occurred. A slide along the fracture is envisaged.

(c), (d) Example test 668TRX_S1, (q, (a), Δu_w, (b)) sudden post-peak drop, followed by sleeve rupture and oil pressure leak (pore pressure increases).

Tab. 5-4: Triaxial test results from the shear phase

[a] Pore fluid pressure was kept 0.5 MPa below confining pressure. [b] Specimen broke early during shearing.

Test-ID **TRU1-1**	**Stress path**	**Strain Rate**	**Young's modulus**	**Poisson's ratio**	**Deviatoric stress at peak (q = σ1 – σ3)**	**Radial total stress at peak (σ3)**	**Pore pressure at peak**	**Axial strain at peak**	**post-peak q**	**Post-peak p'**
		[1/s]	[GPa]	[-]	[MPa]	[MPa]	MPa]	[%]	[MPa]	[MPa]
535TRX_S2	CTC	1E-06	36.3	0.22	166.4[a]	10.0	5.0	0.66	86.0	33.7
605TRX_S1	CTC	1E-06	5.2	0.57	43.4[a,b]	14.0	13.0	1.10		
632TRX_S1	CTC	1E-06	11.7	0.31	89.0[a]	12.0	11.0	1.41	49.5	17.3
668TRX_S1	CTC	1E-06	30.0	0.24	207.2[a]	10.0	4.8	1.00		
697TRX_S1	CTC	1E-06	35.8	0.22	285.3[a]	10.0	9.0	0.95	11.3	4.7
775TRX_S1	CTC	5E-07	13.0	0.46	47.3[a]	12.0	11.0	0.58	29.5	10.8
775TRX_S2	CTCU	5E-07	10.6	0.37	41.4	15.0	10.7	0.72	27.6	18.8
989TRX_S1	CTC	1E-06	24.4	0.19	65.0[a]	10.0	6.7	0.42		
1022TRX_P1	CTCU	1E-06	13.7	0.47	50.3	10.0	8.1	0.55	26.0	13.0
1053TRX_S1	CTC	1E-06	24.7	0.13	87.5[a]	10.0	dry	0.59	42.4	24.1
1093TRX_S1	CTCU	1E-06	27.3	0.38	112.8	10.0	3.2	0.65	57.3	29.3

6 Geomechanical testing programme

In the TRU1-1 geomechanical testing campaign, 33 triaxial tests were performed. Three geometries (Section 5.1) were selected: S, P and Z samples. Z samples were prepared in order to obtain specimen shearing along the bedding direction, i.e. to investigate the direction with potentially the minimum strength. The angle to bedding was decided based on the results from the previous BUL1-1 testing campaign and first results with P- and S-samples of TRU1-1.

Z-samples were prepared with two orientations with respect to the bedding: 4 Z-samples were prepared with an angle of 55°-60° between the bedding direction and the horizontal plane (i.e., 30°-35° between bedding direction and the cylinder axis) and 2 specimens were prepared with an angle of 70° (i.e., 20° between bedding direction and the cylinder axis).

In addition, 12 one-dimensional compression (including 4 constant-head permeability tests) and 7 one-dimensional swelling tests were also performed in oedometric conditions.

In the following sections, the test results of the experimental campaign are presented. First, the main geotechnical and intrinsic properties are reported (Section 6.1). Then, in Sections 6.2 and 6.3, the results of tests in triaxial and oedometric conditions are reported.

6.1 Geotechnical and intrinsic properties of tested cores

6.1.1 Water content and native activity

The laboratories involved in the testing campaign also determined basic properties of the tested specimens. The water content of the specimens before and after testing was determined, and the results are reported in Fig. 6-1.

For the triaxial tests, the first phase of each test consisted in imposing saturated conditions to the specimen, either (i) by injecting water in isochoric conditions, measuring the generated swelling pressure (conventional testing procedure), or (ii) by isotropically compressing the specimen until positive pore pressure is developed (alternative testing procedure) (*cf.* Fig. 4-6).

When the conventional testing procedure is used, the water content before and after the tests generally differs, and in the case of undrained boundary conditions, the difference may primarily be attributed to re-saturation in the rig. This is the case for results from Lab A and Lab B. Using the alternative testing procedure (Lab C), no fluid is added to the specimen whilst in the rig. Therefore, the water content before and after the test is expected to be the same. For drained boundary conditions, volumetric deformation during testing may also alter the water content of the specimen (data points marked with *d* for drained, in Fig. 6-1). Additional sources of discrepancy between the water content before and after tests can be attributed to the handling of the specimen when dismantling the test (e.g., loss of solid mass while removing the specimen from the sleeve, drained unloading phases which allow further swelling and water content increase).

The water content and the Native Activity of the material were also measured on trimming pieces from a part of the section from which testing specimens were extracted. The Native Activity of a specimen corresponds to the value of relative humidity in equilibrium with the specimen native state, with no variation of the initial water content[9].

The measurements were done by placing a piece of freshly cut material within a closed container and measuring the resulting (relative) humidity generated within the container (Ewy 2015) by the use of psychrometer. No measurements were done by Lab B.

Results are reported in Fig. 6-2. All cores exhibit high Native Activity, above 70%, with peaks at approximately 85%, indicating excellent preservation conditions.

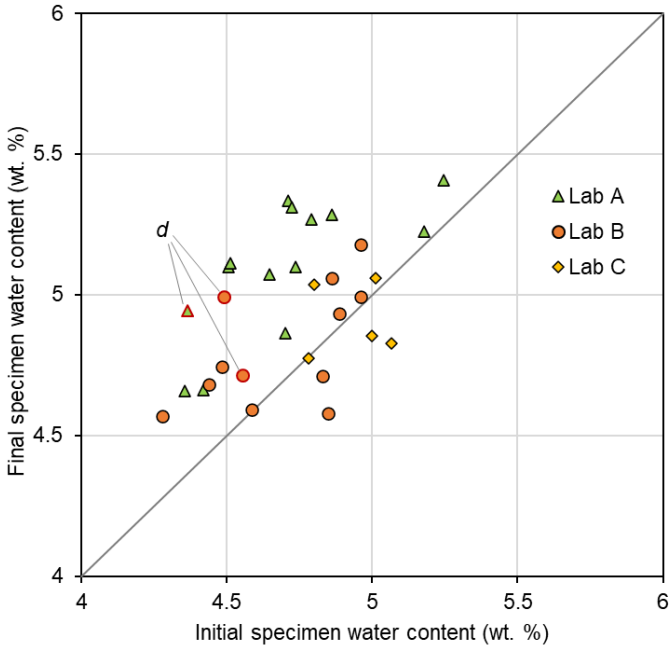

Fig. 6-1: Initial versus final water content of triaxial specimens

d indicates specimens from drained tests.

[9] In a specimen in contact with controlled relative humidity, if water content increases, then that relative humidity value is greater than the Native Activity value of the shale. Conversely, if there is a water content decrease, then that relative humidity value is less than the Native Activity.

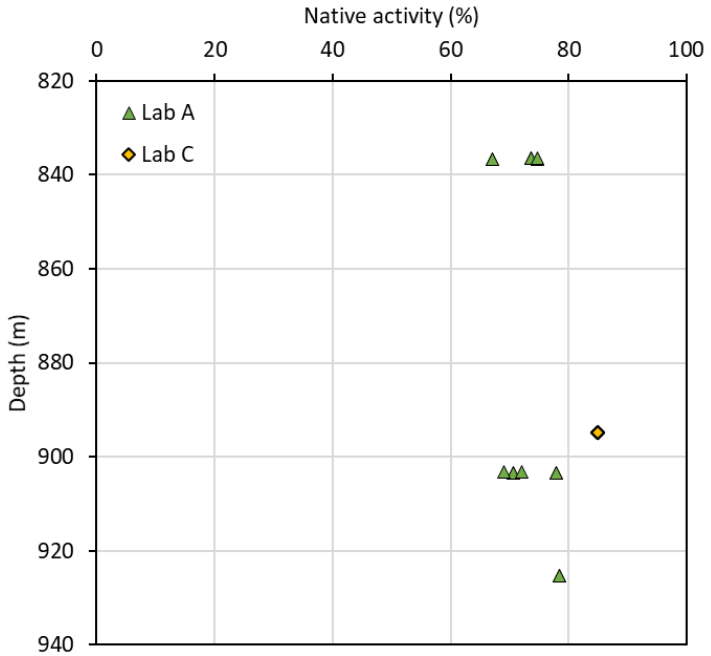

Fig. 6-2: Native activity of trimming versus depth of collection

Results grouped by laboratory.

6.1.2 Atterberg limits, plasticity index, grain size distribution

In the context of the oedometric testing campaign Lab A and D performed geotechnical characterisation of the tested cores. They determined Atterberg limits and plasticity index, and Lab D additionally determined also the grain size distribution.

Atterberg limits were determined according to ASTM D4318-17 (ASTM 2017a); the material was manually crushed with a rubber-tipped pestle. Only the portion with grain dimension lower than 0.425 mm was used. Lab A used the ASTM One-Point method to determine the liquid limit. The one-point uses only one measurement (with the Casagrande cup), and a correcting factor defined by the standard.

Grain size distributions were determined according to ad-hoc procedures developed by the laboratories, according to Nagra's indications. The main aspects of the procedure of Lab D are here summarised. Lab D adopted a procedure implemented during previous projects involving Opalinus Clay and which is based on the ASTM D6913-17 (ASTM 2017b) and D7928-17 (ASTM 2017c); a gentle pre-crushing was performed manually with a rubber-tipped pestle, to separate the aggregates avoiding the breakage of individual particles. Before the test, the material was submerged in distilled water for 24 hours and sieved using water. Grain size distribution was determined by wet sieving for particles larger than 0.075 mm, and by sedimentation (by the use of a hydrometer) for the smaller particles.

Atterberg limits and granulometric fractions are summarised in Tab. 6-1. The results on the Atterberg limits show consistency between the laboratories. Concerning the granulometric fractions, the results show a slightly lower clay fraction (29 – 33 wt.-%) with respect to the clay mineralogical content determined by XRD (41 – 52 wt.-%; Appendix D).

Granulometric fraction (sand, silt and clay) are distinguished (as by standard) on the dimension of the particles. It has to be pointed out that there could be particles in the silt granulometric fraction which are clay-mineral particles or aggregates with a larger size than the clay – silt threshold; on the other hand, there may be particles in the clay granulometric fraction which are minerals other than clays having fine particles dimension. All the previous considerations contribute to the difference between granulometric and mineralogical clay fractions.

Tab. 6-1: Atterberg limits and grain size fractions for the tested cores

Core ID	**Lab**	**Core interval**	**w_L**	**w_P**	**PI**	**Gravel**	**Sand**	**Silt**	**Clay**
		[cm]	[-]	[-]	[-]	[%]	[%]	[%]	[%]
TRU1-1-796.64/45-GM	D	0 – 6	0.40	0.23	0.17	0	8.7	61.3	30.0
TRU1-1-878.11/43-GM	D	11 – 14	0.34	0.22	0.12	0	2.1	68.7	29.2
TRU1-1-878.11/43-GM	D	29 – 31	0.34	0.21	0.13	0	3.8	62.8	33.4
TRU1-1 836.32/50-GM	A	3 – 8	0.25	0.17	0.07	-	-	-	-
TRU1-1 836.32/50-GM	A	8 – 13	0.27	0.19	0.08	-	-	-	-
TRU1-1 903.19/45-GM	A	33 – 36	0.24	0.18	0.06	-	-	-	-
TRU1-1 903.19/45-GM	A	10 – 11	0.24	0.17	0.07	-	-	-	-
TRU1-1 924.96/45-GM	A	12 – 17	0.24	0.17	0.07	-	-	-	-
TRU1-1 955.69/42-GM	A	29 – 34	0.21	0.16	0.05	-	-	-	-

6.2 Triaxial tests with specialised protocols

An overview of the performed tests is presented in Tab. 6-2. Each test is labelled with an ID indicating the main features of the test.

For example, the triaxial test ID A1_TRU1_1_836_5P5CTCU indicates the laboratory that performed the test (A), a testing sequential number (1), the borehole name (TRU1-1), the specimen depth (836.5 m), the specimen geometry (P), effective confinement before shearing (5 MPa), the stress path (CTCU).

It is reported in Tab. 6-2 for each tested specimen:

- Specimen ID, as above described
- Core depth [m]
- Geological formation, as presented in Section 4.4.1
- Specimen geometry
- Total confining stress, p_0 [MPa] at the beginning of the shearing phase
- Pore pressure [MPa] at the beginning of the shearing phase
- Effective confining stress p'_0 [MPa] at the beginning of the shearing phase
- Stress path, as presented in Fig. 4-5
- Indication of shearing in drained conditions (d)
- Initial void ratio, computed using a reference solid density of 2.70 g/cm^3

- Initial porosity, computed using a reference solid density of 2.70 g/cm^3
- Initial and final water content.

The initial part of the ID (hereafter Specimen ID), including the laboratory and the sequential number is afterwards used as short code to quickly identify specific test point in the entire set of results.

Tab. 6-2: Conducted triaxial tests

Specimen ID, shearing phase characteristics, specimen initial (and final) conditions

Specimen ID	**Specimen location and geometry**			**Shearing phase characteristics**					**Specimen initial conditions**			
	Core depth [m]	**Formation**	**Specimen Geometry**	**Total confining Stress,** p_0 [MPa]	**Pore pressure,** u_{w0} (MPa]	**Effective confining stress** p'_0 [MPa]	**Stress Path**	**Drained shearing** (d)	**Initial void ratio,** e_0* [-]	**Initial porosity,** n_0 [-]	**Initial water content,** w_0 [%]	**Final water content,** wf [%]
A15_TRU1_1_798_21S10CTCU	797.21	Wedel-sdst. Fm.	S	15	5	10	CTCU		0.087	0.008	2.33	3.14
A16_TRU1_1_811_05S10CTCU	811.05		S	18	8	10	CTCU		0.126	0.112	4.18	5.29
A1_TRU1_1_836_5P5CTCU	836.5	Opalinus Clay	P	14	9	5	CTCU		0.126	0.112	4.65	5.07
A2_TRU1_1_836_5P11CTCU	836.5		P	20	9	11	CTCU		0.140	0.123	4.71	5.33
A4_TRU1_1_836_55S8CTCU	836.54		S	17	9	8	CTCU		0.136	0.119	4.72	5.31
A3_TRU1_1_836_55S13CTCU	836.55		S	22	9	13	CTCU		0.132	0.116	4.70	4.86
A13_TRU1_1_836_64Z13CTCU	836.64		Z	22	9	13	CTCU		0.127	0.112	4.42	4.66
A14_TRU1_1_836_64Z7CTCU	836.64		Z	16	9	7	CTCU		0.131	0.115	4.51	5.11
B4_TRU1_1_851_86P13CTCU	851.86		P	22	9	13	CTCU		0.113	0.102	3.88	-
B5_TRU1_1_851_88P7CTCU	851.88		P	16	9	7	CTCU		0.113	0.101	4.28	4.57
B1_TRU1_1_851_94S13CTCU	851.94		S	22	9	13	CTCU		0.120	0.107	4.44	4.68
B2_TRU1_1_851_94S10CTCU	851.94		S	19	9	10	CTCU		0.138	0.122	4.96	5.18
B3_TRU1_1_851_94S7CTCU	851.94		S	16	9	7	CTCU		0.130	0.115	4.86	5.06
B8_TRU1_1_875_56_P13CTCU	875.56		P	22	9	13	CTCU		0.116	0.104	4.59	4.59
B9_TRU1_1_875_56P8CTC	875.56		P	17	9	8	CTC	d	0.117	0.104	4.56	4.71
B13_TRU1_1_875_65P9TC	875.65		P	18	9	9	TC	d	0.117	0.105	4.49	4.99
B12_TRU1_1_875_69Z13CTCU	875.69		Z	22	9	13	CTCU		0.122	0.109	4.48	4.75
B7_TRU1_1_875_76_S7CTCU	875.76		S	16	9	7	CTCU		0.127	0.113	4.89	4.93
B6_TRU1_1_875_77S13CTCU	875.77		S	22	9	13	CTCU		0.123	0.109	4.83	4.71
B10_TRU1_1_875_84Z13CTCU	875.84		Z (70°)	22	9	13	CTCU		0.130	0.115	4.96	4.99
B11_TRU1_1_875_84Z7CTCU	875.84		Z (70°)	16	9	7	CTCU		0.125	0.111	4.85	4.58
C1_TRU1_1_895_08P13CTCU	895.08		P	22	9	13	CTCU		0.133	0.117	5.00	4.85
C2_TRU1_1_895_08P5CTCU	895.08		P	14	9	5	CTCU		0.139	0.122	4.80	5.04
C4_TRU1_1_895_08S4CTCU	895.08		S	14	10	4	CTCU		0.144	0.126	5.06	4.83
C5_TRU1_1_895_08S13CTCU	895.08		S	22	9	13	CTCU		0.143	0.125	4.78	4.77
C3_TRU1_1_895_15Z5CTCU	895.155		Z	14	9.3	4.7	CTCU		0.142	0.124	5.01	5.06
A12_TRU1_1_903_32P5CTC	903.19		P	14	9	5	CTC	d	0.124	0.111	4.86	5.28
A11_TRU1_1_903_4S5CTC	903.19		S	14	9	5	CTC	d	0.112	0.101	4.37	4.94
A7_TRU1_1_903_43S13CTCU	903.43		S	22	9	13	CTCU		0.114	0.102	4.36	4.66
A8_TRU1_1_903_43S8CTCU	903.43		S	17	9	8	CTCU		0.115	0.103	4.51	5.10
A5_TRU1_1_903_49P4CTCU	903.49		P	13	9	4	CTCU		0.122	0.108	4.74	5.10
A6_TRU1_1_903_49P8CTCU	903.49		P	17	9	8	CTCU		0.125	0.111	4.79	5.27
A9_TRU1_1_925_21_S13CTCU	925.21		S	22	9	13	CTCU		0.122	0.109	5.18	5.23
A10_TRU1_1_925_21S8CTCU	925.21		S	17	9	8	CTCU		0.123	0.110	5.25	5.41

6.2.1 Saturation and consolidation phase

6.2.1.1 Swelling pressure

In the conventional triaxial procedure (adopted by Lab A and B), the specimen saturation was conducted imposing isochoric condition and monitoring the evolution of the axial and radial stress. The effective stress reached at the end of the saturation phase is called swelling pressure, and the results (grouped by S- and P-geometries, respectively) are reported in Fig. 6-3 versus the specimen initial water content (before saturation). For specimens with S geometry, the radial direction corresponds the one of the bedding, while the axial is perpendicular to it. Swelling pressure was found to be higher in the axial direction. No clear trend between swelling pressure and water content is found for this set of tests. It has to be noted that the specimens water content varied within a limited range (about 1%), which may be not sufficient to infer a trend.

On the other hand, in P-sample, the axial direction corresponds to the bedding direction, while the radial stress is obtained by maintaining close to zero the average of the deformation in the two radial directions, perpendicular and parallel to bedding.

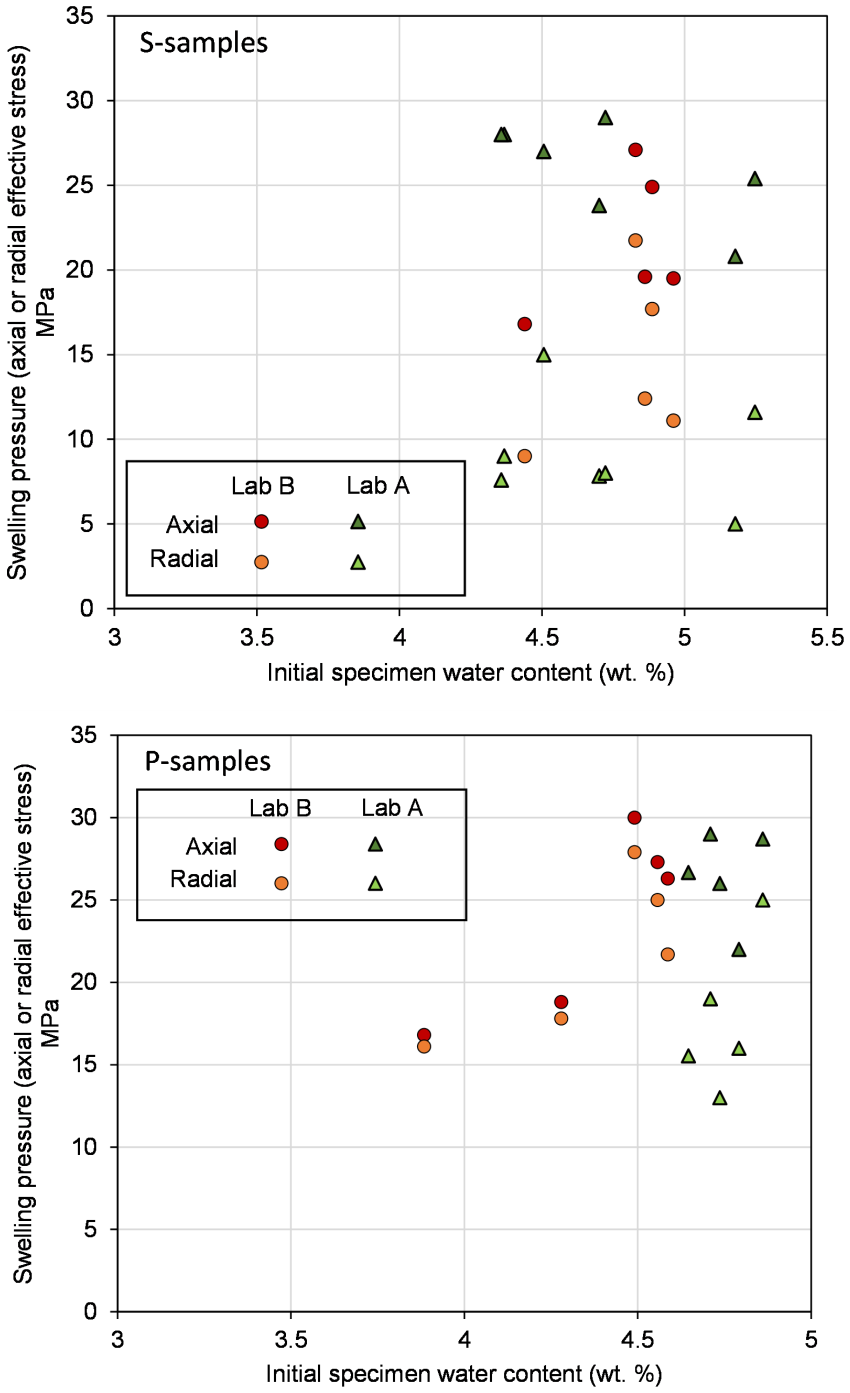

Fig. 6-3: Radial and axial swelling pressure versus initial specimen water content
S-samples (above) and P-samples (below).

6.2.1.2 B check tests

In each test, the specimen saturation was verified, performing Skempton's B checks. B values were computed over multiple steps. If the difference in B values among the steps was less than 10%, the average of the measurements was considered as the B coefficient and associated with the average effective confinement level at which B segments were performed. The values are reported in Fig. 6-4 for all results.

The compressibility of the apparatus can affect the accuracy of the measured B values. Wissa (1969) proposed a correction to the B value to consider the compressibility of the dead volume of water (i.e., the water in the drainage system) and the compressibility of the system (tubes and transducers). However, several researchers (e.g., Ghabezloo & Sulem 2010) show that the compressibility of modern types of steel tubes and transducers has a negligible impact on the B measurements compared to the dead water volume impact. Therefore, the results of the testing campaign have been analysed considering the dead water volume in each apparatus, and B values results ($B_{correct}$) were computed as (Wissa 1969, Favero et al. 2018):

$$B_{correct} = \frac{1}{\frac{1}{B_{obs}} - \frac{V_L}{V}\frac{K}{K_f(1-K/K_s)}} \tag{6-1}$$

where B_{obs} is the measured B value, V_L is the volume of fluid in the pore-water lines, V is the volume of the specimen, K is the bulk modulus of the specimen, K_f bulk modulus of the pore fluid, and K_s is the bulk modulus of the solid phase. Bulk and solid moduli K = 6 MPa and Ks = 50 MPa were considered for the corrections. The correction was applied for results of laboratories A and B, while lab C apparatus considers a close to zero dead volume; therefore, no correction was applied. It has to be noted that the dead volume in apparatus from lab A (2'200 mm^3) is about three times larger than that of lab B (700 mm^3). The results for the measured and corrected B values are reported in Fig. 6-4. A slight B value decrease with stress increase was detected. An average value of 0.83 was calculated and marked as a dotted line in the graph.

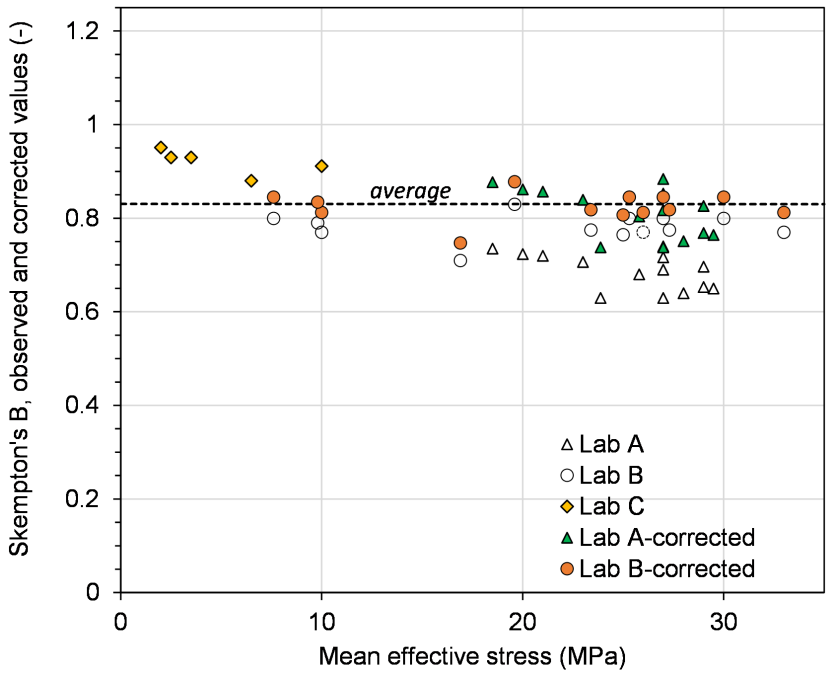

Fig. 6-4: Average Skempton's B values

B values versus the corresponding effective mean stress; data from TRU1-1 (Opalinus Clay): Observed and corrected values accounting for dead water volume.

6.2.1.3 Consolidation phase

Drained consolidation phases were performed to achieve the target effective confining stress for shearing, and allow for determining the consolidation coefficient, according to Head (1998). The time to consolidate was obtained applying the square root of time method in the evaluation of the evolution of the volumetric strain. It is noted that the method refers to an instantaneous loading of the sample. However, in most test adopting a conventional method, the stress level at the end of saturation is higher than the target value for shearing, hence an unloading (with consequent swelling of the sample) was performed. Performing quasi-instantaneous unloading is challenging, given the stress levels involved, and often a ramp of several hours needs to be used. Therefore, the consolidation coefficient obtained from these results may be underestimated. It is further noted that the values were obtained by considering the time to consolidate excluding the time required to load. The obtained values for all tested specimens of Opalinus Clay are reported in Fig. 6 5 versus the mean effective stress at the end of the consolidation phase.

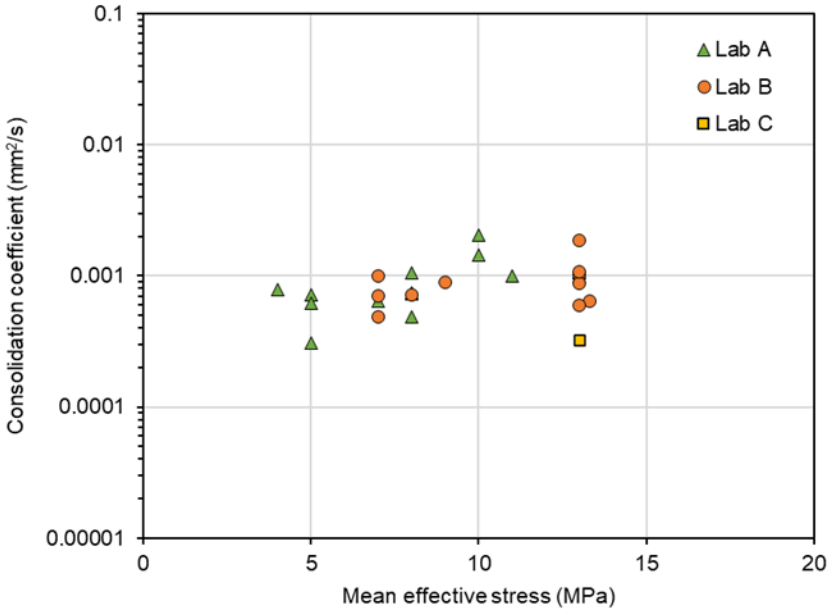

Fig. 6-5: Consolidation coefficient for Opalinus Clay specimens (all geometries)

6.2.2 Shearing phase

This section provides the results of the shearing phase of tests. The stress paths are reported in the q – p′ plane, where q is the deviatoric stress (Eq. 4-1) and p′ is the mean effective stress, obtained subtracting to the total effective stress (Eq. 4-2) the pore water pressure u_w.

6.2.2.1 Stress paths of Opalinus Clay subunits

This section focuses on the stress paths obtained on Opalinus Clay specimens during the shearing phase of the tests. The behaviour of the tested specimens is characterised by a pronounced non-linearity before the peak stress and softening response after the peak. A similar evolution of the deviatoric stress (q) and pore water pressure (u_w) with axial effective strain is observed among tests (see Appendix B).

The effective stress paths obtained on Opalinus Clay specimens are here grouped by the lithological sub-units (Fig. 6-6), as presented in Section 4.4.1. The results of subunit 3 are further subdivided by specimen geometry: P-samples, S- and Z-samples.

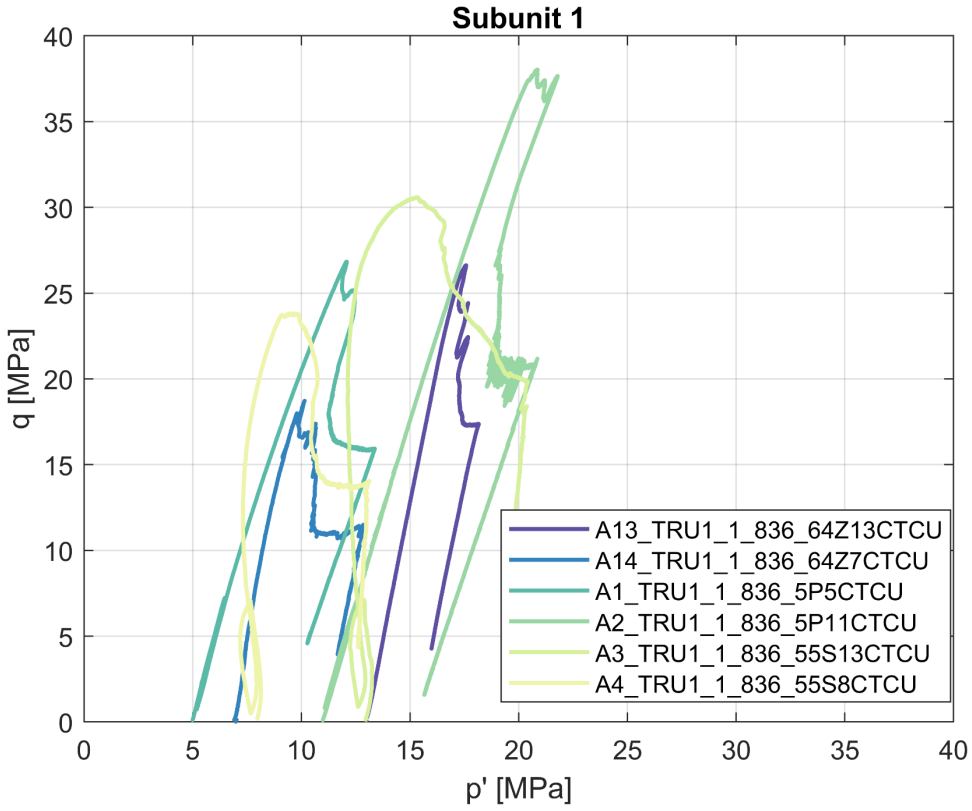

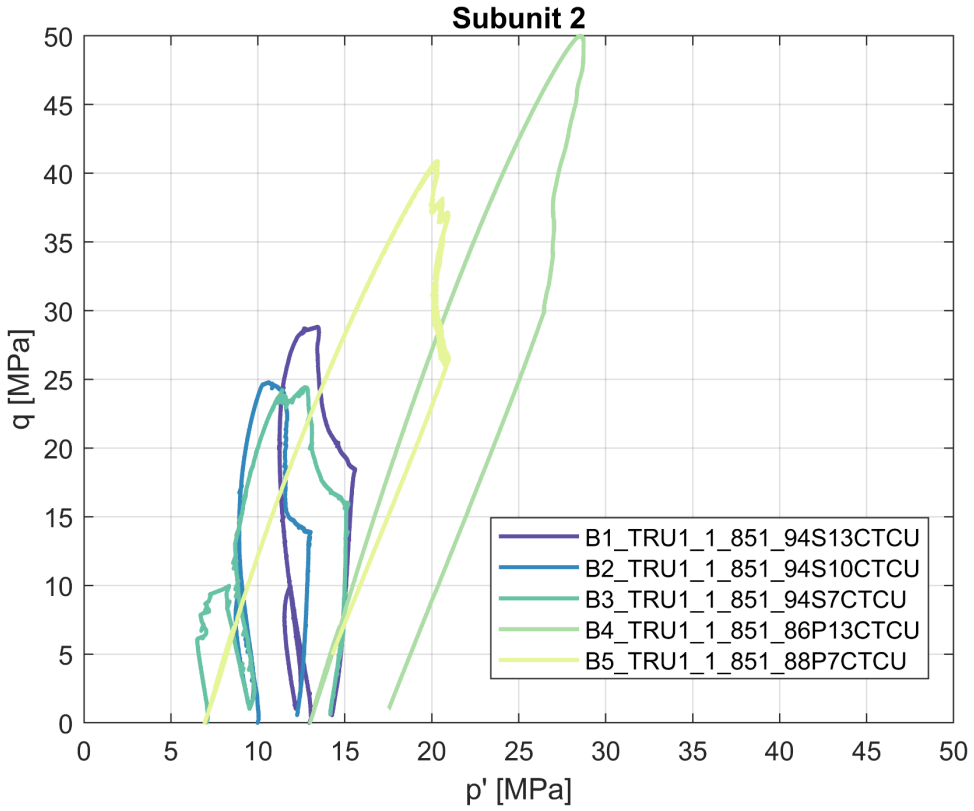

Fig. 6-6: Effective stress paths of tested specimens grouped by lithological (sub) unit

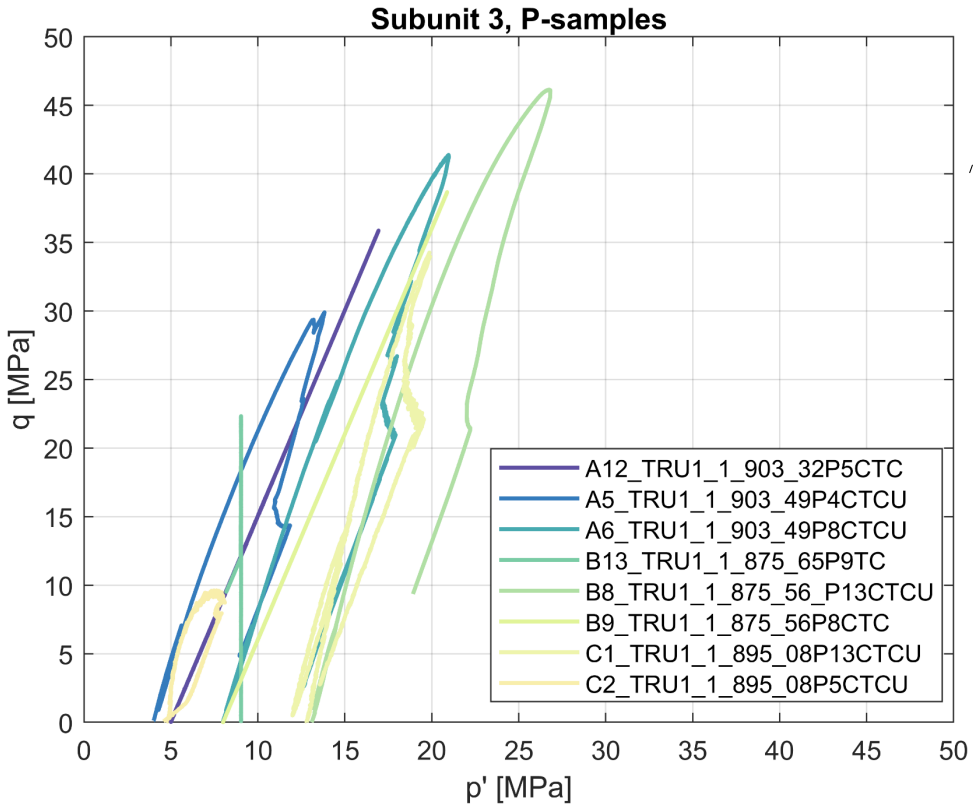

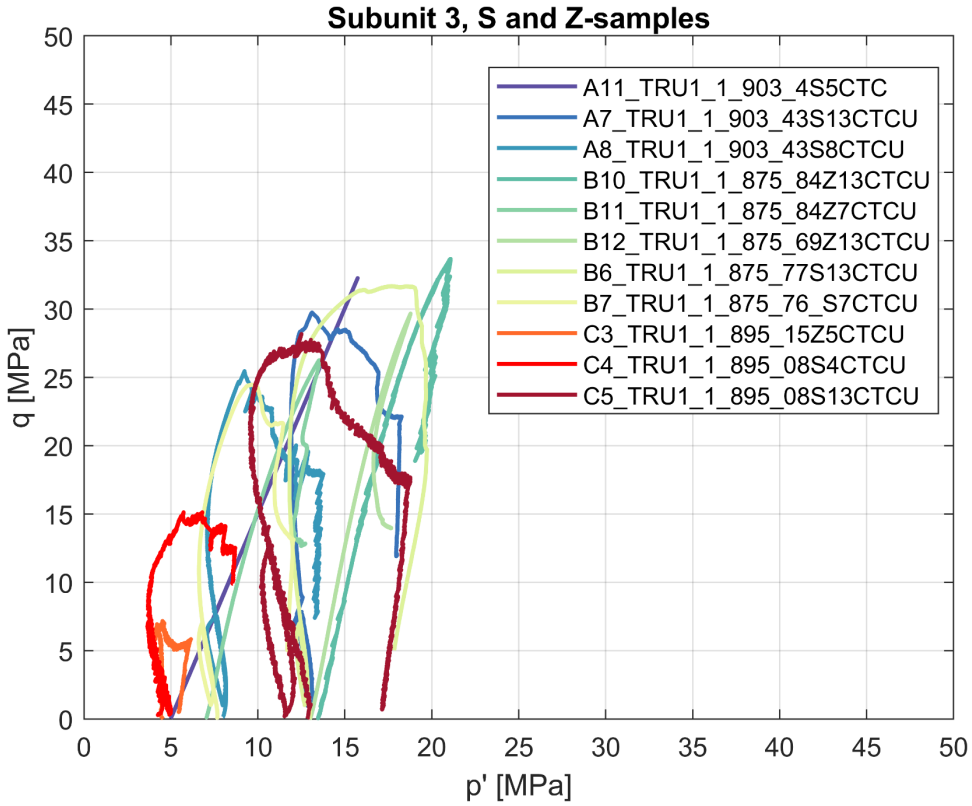

Fig. 6-6: Effective stress paths of tested specimens grouped by lithological (sub) unit (continued)

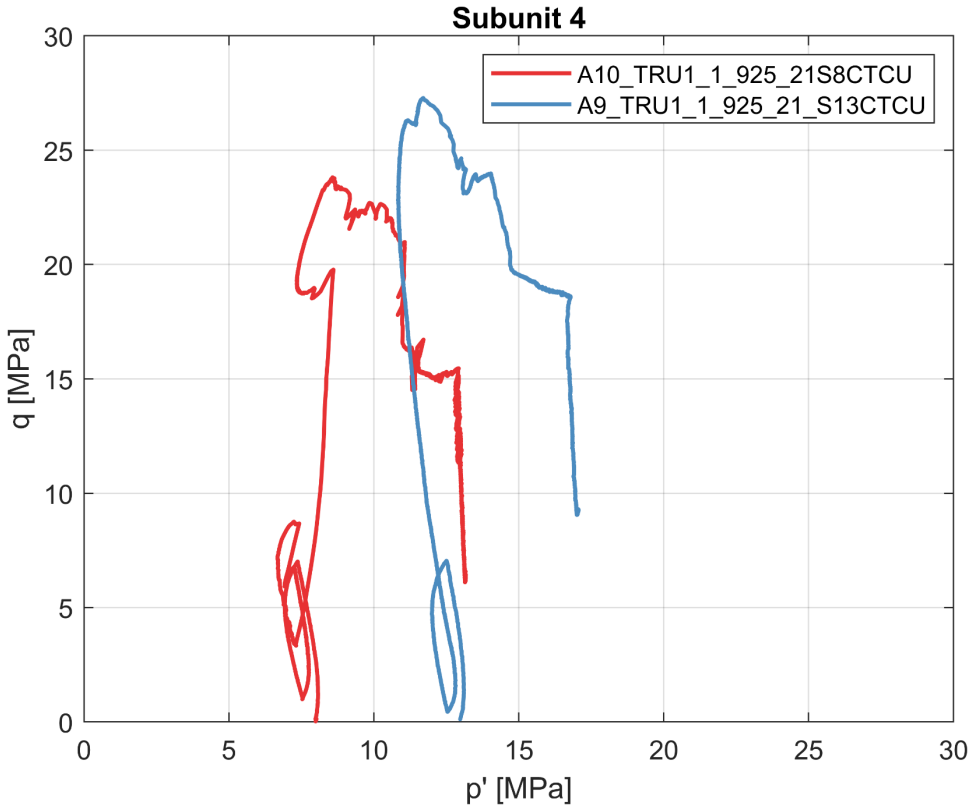

Fig. 6-6: Effective stress paths of tested specimens grouped by lithological (sub) unit (continued)

Some tests exhibited an unusual stress path evolution, or a peak shear strength lower compared to the majority of the results. These tests are analysed in more detail in the last section of Chapter 6.

6.2.2.2 Elastic phase

The analysis of the elastic parameters is presented in this section. Unloading/reloading cycles were performed to estimate the elastic response of the material during an unloading phase. As requested in the testing procedure, the cycles were carried out during the shearing of the specimens before the achievement of the peak stress.

During unloading and reloading, shales present a hysteretic and non-linear behaviour. Depending on the strain amplitude of the unloading-reloading loop, the secant moduli may vary considerably. The strains are calculated as the ratio of the variation in height (or diameter) to the initial height (or diameter). To eliminate the dependency of the moduli on the amplitude of the unloading loop, the elastic modulus for all analysed tests was computed as the secant modulus during unloading for a pre-fixed strain range, 0.02 – 0.04% from the beginning of the unloading phase (Fig. 6-7). The strain calculation refers to the initial specimen height. The strain amplitude was selected as common to all the analysed test results.

Small-strain moduli were also evaluated from the stress cycles (Fig. 6-7) according to the procedure presented in Giger et al. (2018).

An example of elastic moduli evaluation is reported in Fig. 6-7, with reference to test BUL1_1_950_62S9CTCU_B (BUL1-1 testing campaign, Nagra 2021). The top graph in Fig. 6-7 shows the evolution of the secant moduli with the axial strain range used for their computation, for the unloading phase. A clear non-linear decrease of the modulus is observed with the axial strain, which reflects the non-linearity of the material's response. This feature highlights the importance of the axial strain range adopted to perform unloading-reloading cycles. Different ranges lead to different moduli, making a comparison among the tests difficult and misleading. Generally, larger strain ranges lead to lower moduli (Minardi et al. 2019).

A summary plot comparing small strain moduli and secant moduli is provided in Fig. 6-8. It is highlighted that small strain moduli are always higher than the secant moduli computed over the common strain range. Secant moduli from P and S samples are provided in Fig. 6-9, sorted by specimen final water content. In the case of P-tests, higher values of the undrained elastic moduli with respect to S-tests are observed.

Results are reported in Fig. 6-10 (also, Appendix E). In terms of radial response, the relationship between axial and radial deformations during the unloading phase of the cycles performed before the achievement of the peak stress was used ($-\Delta\varepsilon_r/\Delta\varepsilon_a$) for the assessment of the drained Poisson's ratio (ν) and the undrained equivalent. In the undrained conditions, deviations from the theoretical value of 0.5 typically obtained from the linear isotropic elasticity are due to the anisotropic features of the material and possible poroelastic effects. The computed parameters for both drained and undrained unloading loops are also reported in Fig. 6-10, divided by specimen geometry (S and P) and along with the corresponding elastic moduli.

For P-samples, the radial sensors detected the expected anisotropic response, with higher deformation in the direction perpendicular, compared to the direction parallel to the bedding plane. As

a consequence, the Poisson's ratio computed using the strain perpendicular to bedding are higher than those parallel to bedding (values in Appendix E). This agrees with previous findings. It is worth to mention that the difference appears to drop for increasing confining effective stress.

Ultrasonic velocities of P (Vp) and S (Vs) waves were also measured by Lab A, B, and C. In particular, the Lab A and Lab C measured the velocity of both P and S waves in the axial direction (Vp and Vs). Lab B measured the velocity of P waves in the axial (Vp) and radial (Vph) directions. These configurations allowed the estimation of the wave velocities considering the anisotropic structure of the tested specimens (bedding orientation).

Results are shown in Fig. 6-11. It is worth noting that the reported wave velocities by Lab C were obtained at a deviatoric stress level of a few MPa (data in Appendix E), while Lab A and B measured wave velocity at the end of the consolidation phase. However, the effect of the difference in deviatoric load among laboratories seems negligible.

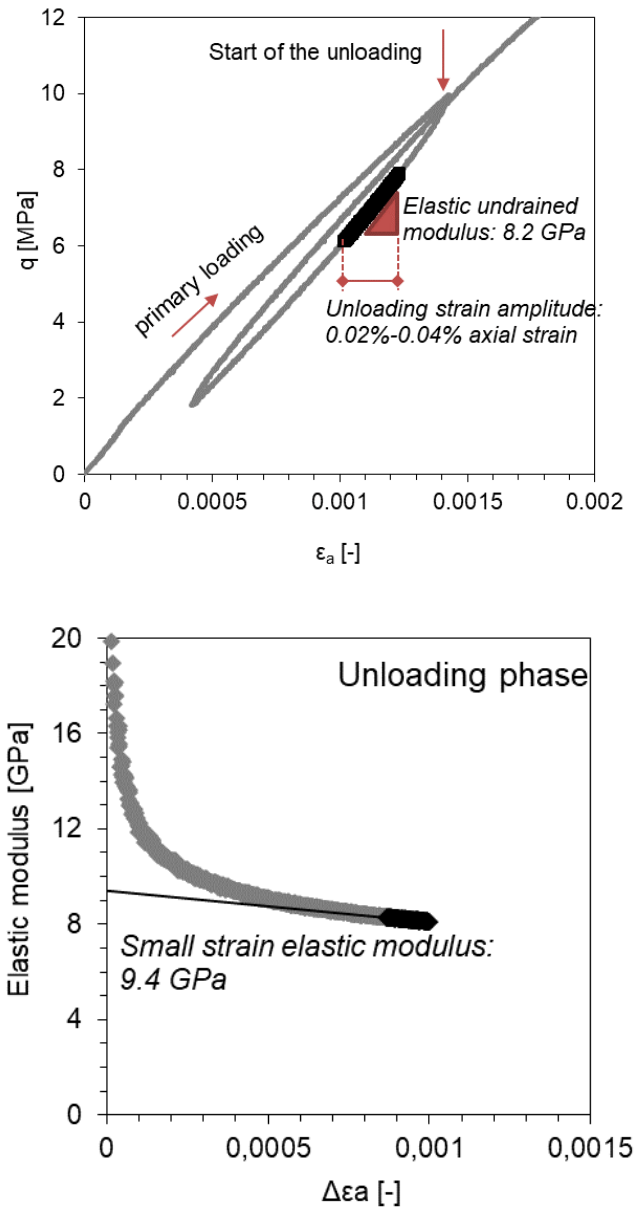

Fig. 6-7: Unloading-reloading cycle and small strain elastic modulus in triaxial tests

Determination of the elastic undrained moduli (E_u) during the unloading phase, for a pre-determined strain amplitude (top); small strain elastic modulus obtained on the unloading phase (bottom) (test BUL1_1_950_62S9CTCU_B, Nagra, 2021).

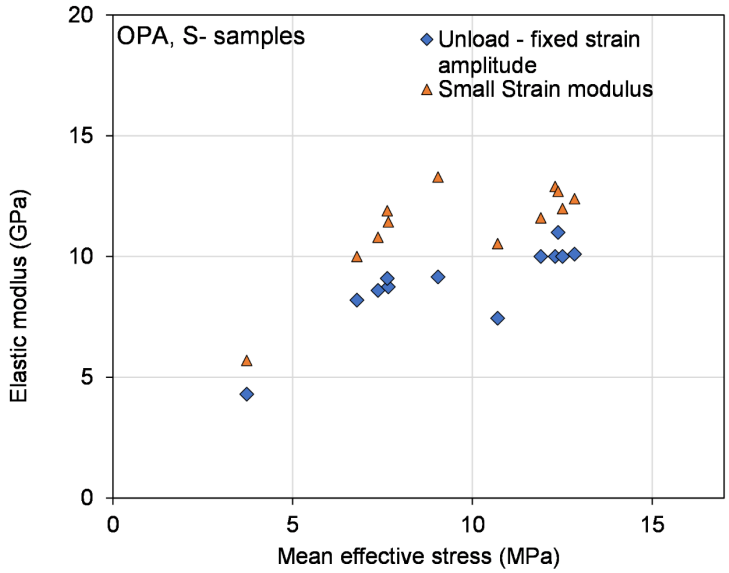

Fig. 6-8: Elastic undrained moduli calculated over an unloading (UL) path: modulus of a fixed strain interval and small strain extrapolation

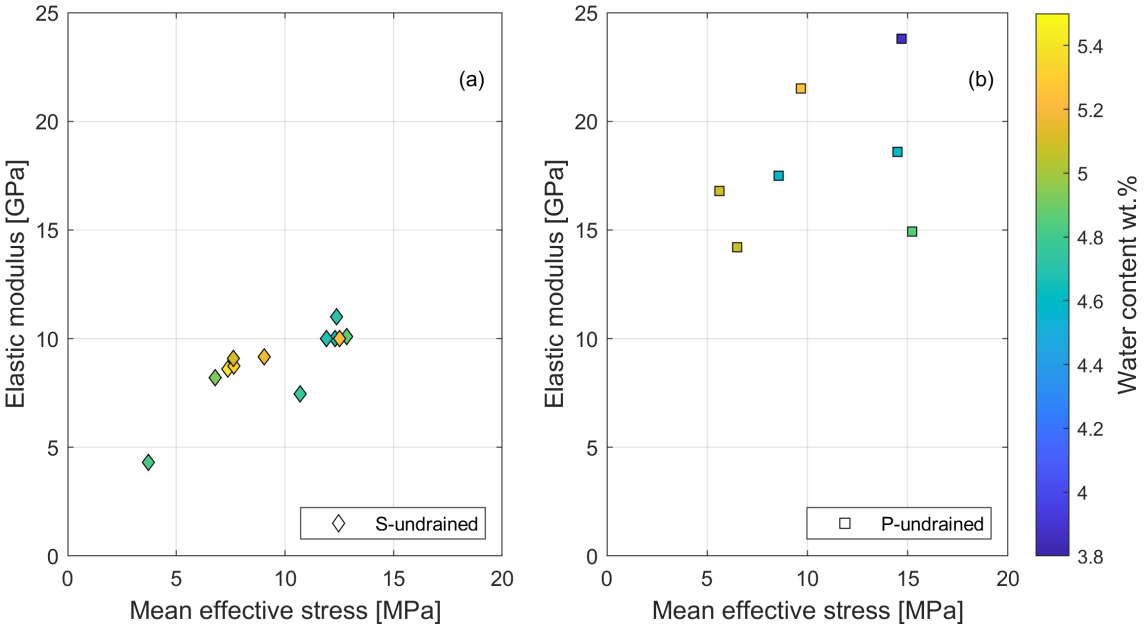

Fig. 6-9: Elastic undrained moduli, sorted by specimen final water content

Moduli are calculated over a fixed strain interval during unloading (UL) path: P and S geometries, sorted by water content.

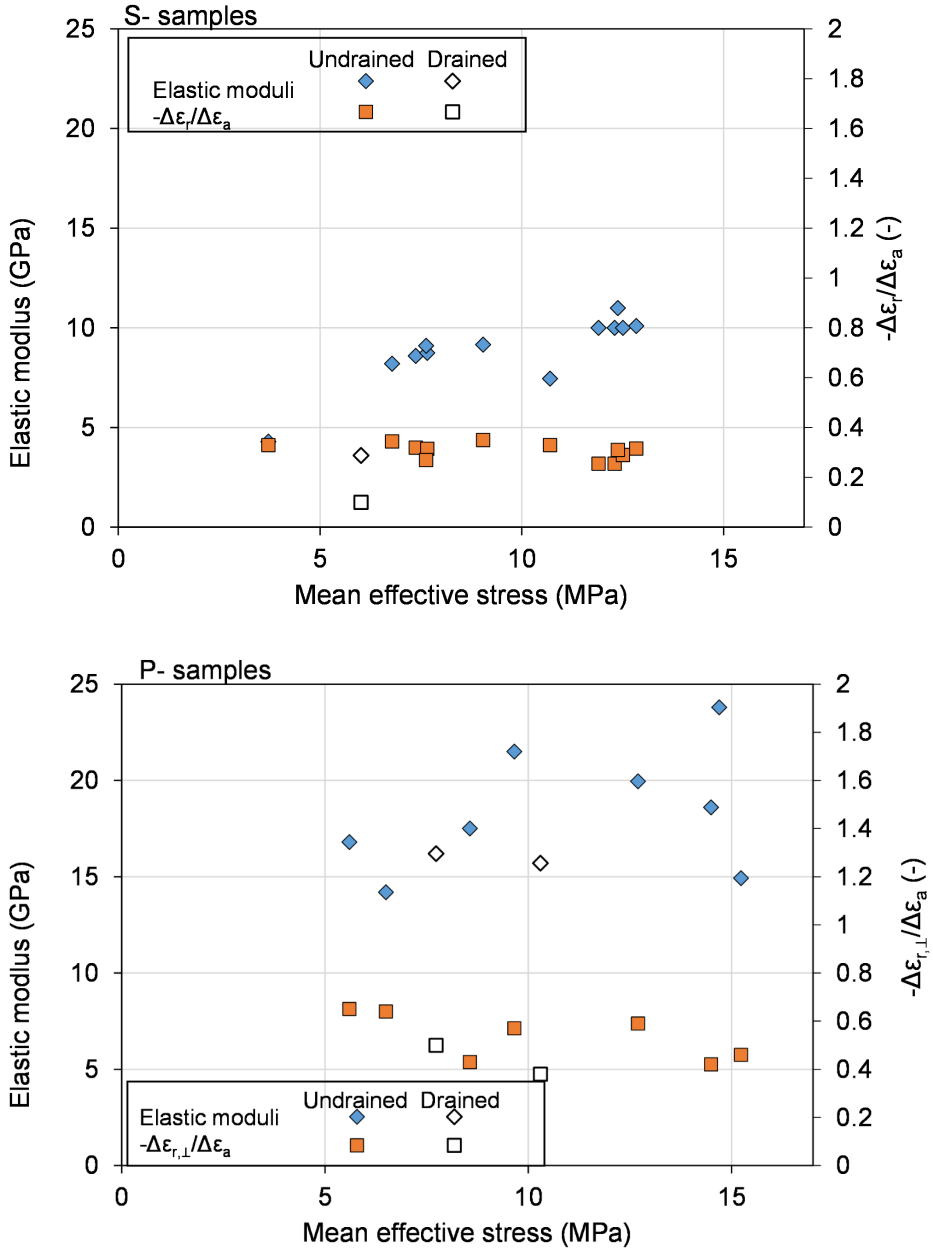

Fig. 6-10: Elastic drained and undrained properties

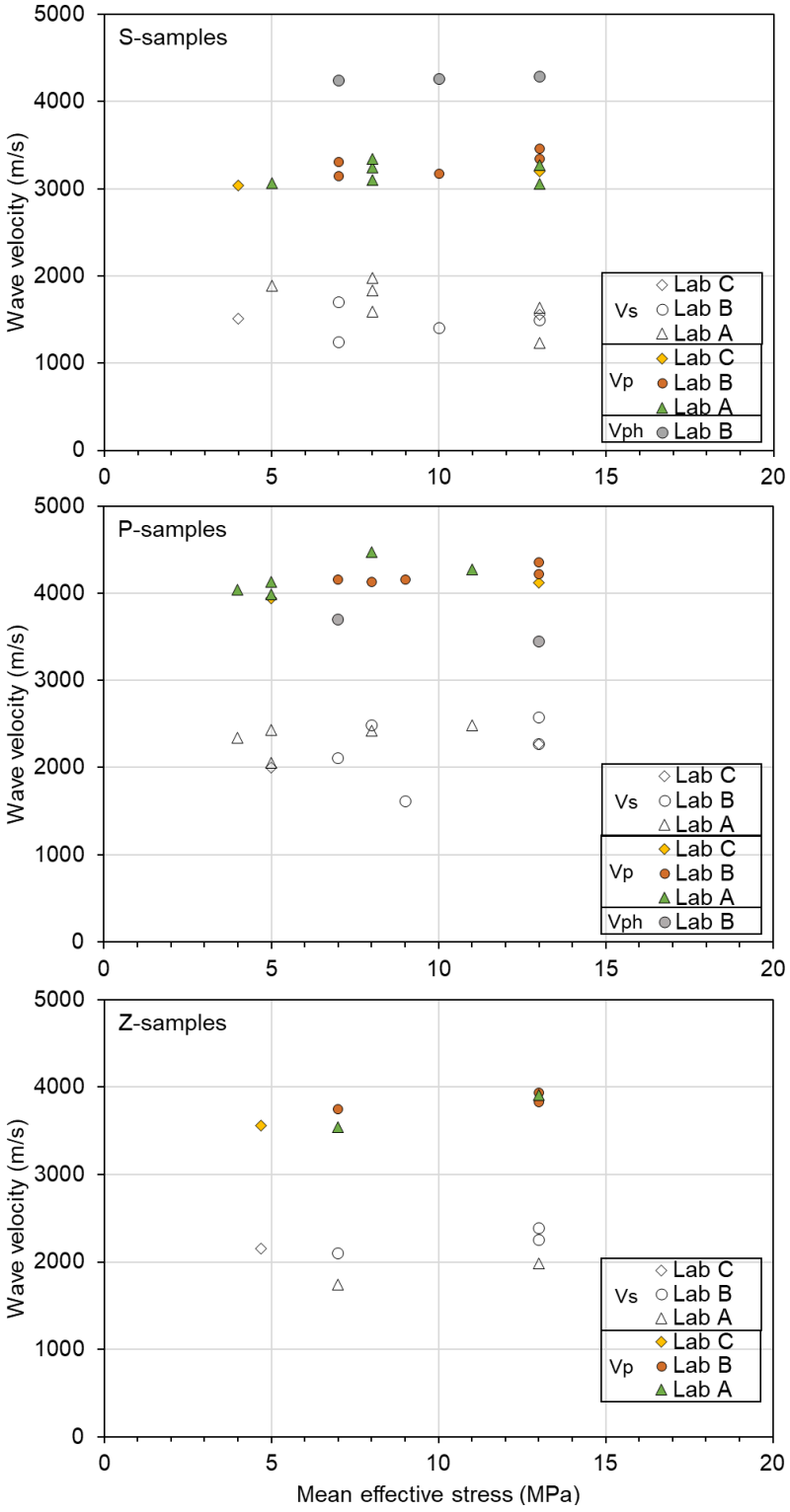

Fig. 6-11: Wave velocities at the beginning of the shearing phase

Results are divided by specimen geometry. Lab C measured wave velocities after starting shearing, at a few MPa of deviatoric stress (data in Appendix E).

6.2.2.3 Pore pressure evolution

In Fig. 6-12, the stress levels ($p' - q$), at which the maximum value of the *AB* parameter and the maximum pore pressure u_w is reached, are plotted, along with the peak shear strength for all test results (data in Appendix B). q is the deviatoric stress, p' is the mean effective stress, Δu_w is the variation of pore fluid pressure from the beginning of the shearing, AB is the ratio between the Δu_w and q. The results are divided by specimen geometry. On each graph, the tests that showed an unexpected response (i.e. peak strength considerably lower than the majority of the tests or inconsistent stress path evolution) are highlighted. Those tests are indicated with a short code, being the initial part of the Specimen ID (Section 6.2). Those tests are analysed in detail in a following dedicated section (Section 6.2.2.6).

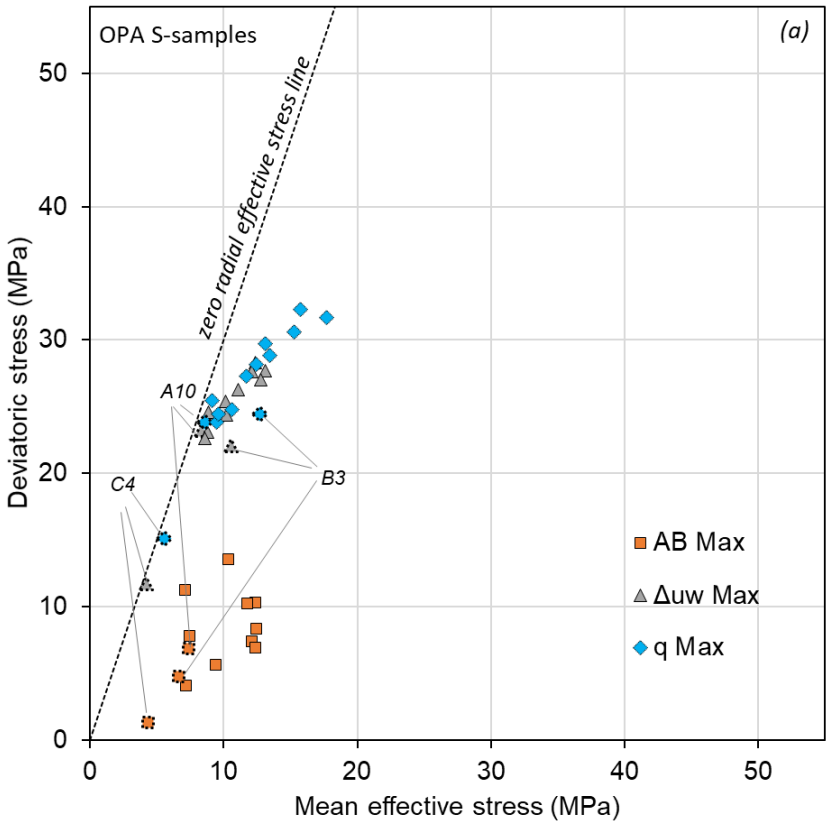

Fig. 6-12: Stress level at which the maximum deviatoric stress, the maximum value of pore pressure and the maximum value of the AB parameter are achieved

OPA results, all geometries (a) S-samples, (b) P-samples and (c) Z-samples. Tests that showed an unexpected response are highlighted.

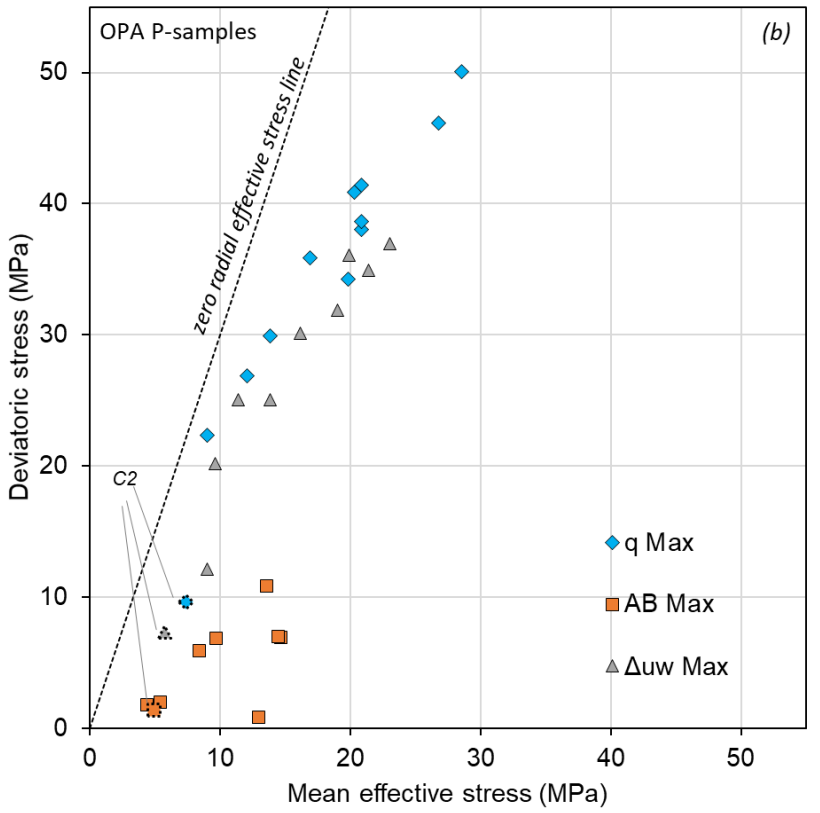

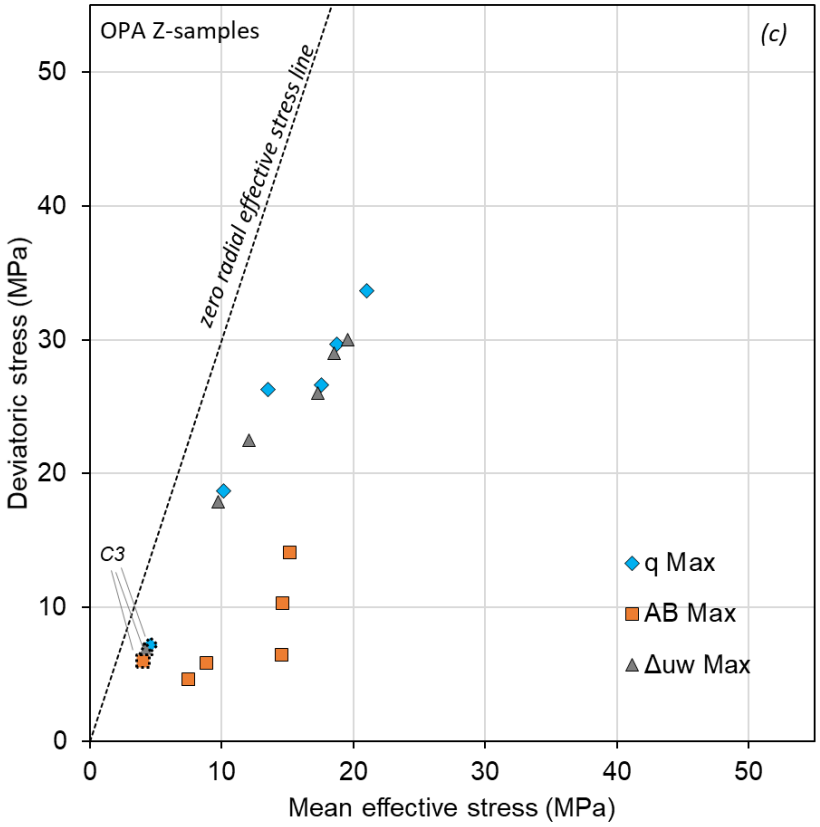

Fig. 6-12: (continued)

6.2.2.4 Shear strength

For all tested specimens, during shearing, a peak in deviatoric stress was achieved, before softening occurred, followed by near-constant deviatoric stress. The peak value is below reported, as the *peak shear strength*, while the constant deviatoric stress achieved while continuing shearing (axial strain up to 2 – 3%) is hereafter referred to as *post-peak shear strength*.

In Fig. 6-13, peak (a) and post-peak shear strength (b) are reported in the $p' - q$ plane. Only Opalinus Clay results are reported and grouped by specimen geometry. The dotted lines highlight the pair of $p' - q$ values, at which radial effective stress equals zero. This line would correspond to the same boundary conditions as a UCS test if pore fluid pressure was zero. The stress states on the left side of this line cannot be achieved (negative radial effective stress) in a triaxial apparatus.

In Fig. 6-14 the peak shear strength results are analysed, sorted by the water content (Fig. 6-14a) of the specimens (obtained at the end of the test) and by clay mineral content (Fig. 6-14b), where available. The plot includes the results of S-samples of Opalinus Clay. The results are reported also in Fig. 6-15 in terms of radial versus axial effective stress.

In a few cases, the pore pressure building up during shearing in undrained conditions reached nearly the level of the total confining stress, bringing the radial effective stress close to zero, and a few tests showed peak shear strength lower that the majority of the tests. Those results already highlighted in Fig. 6-12 (previous section) are analysed in more detail in Section 6.2.2.6 (Analysis of the outliers).

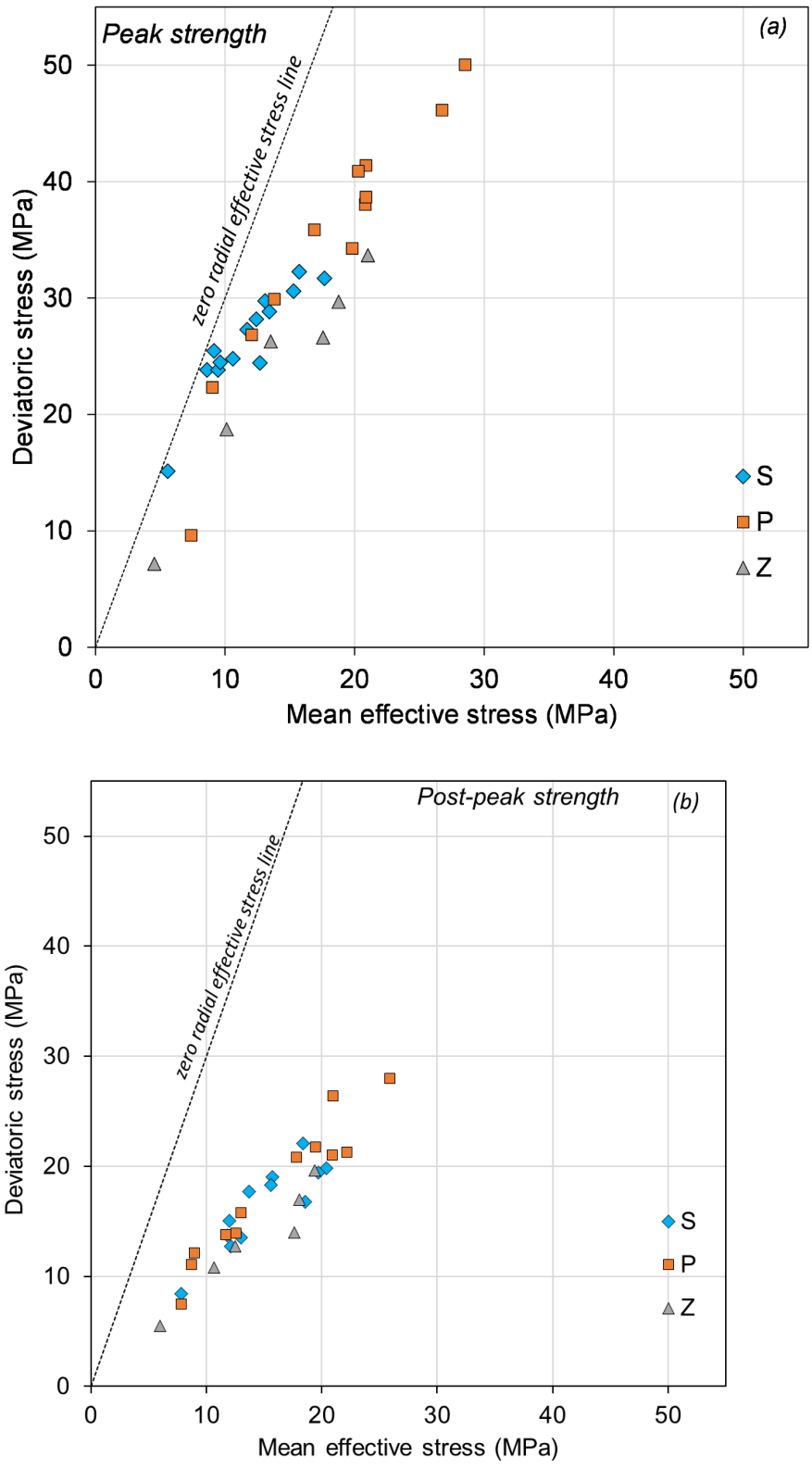

Fig. 6-13: Peak (a) and post-peak (b) shear strength of Opalinus Clay TRU1-1 specimens
Results divided by geometry.

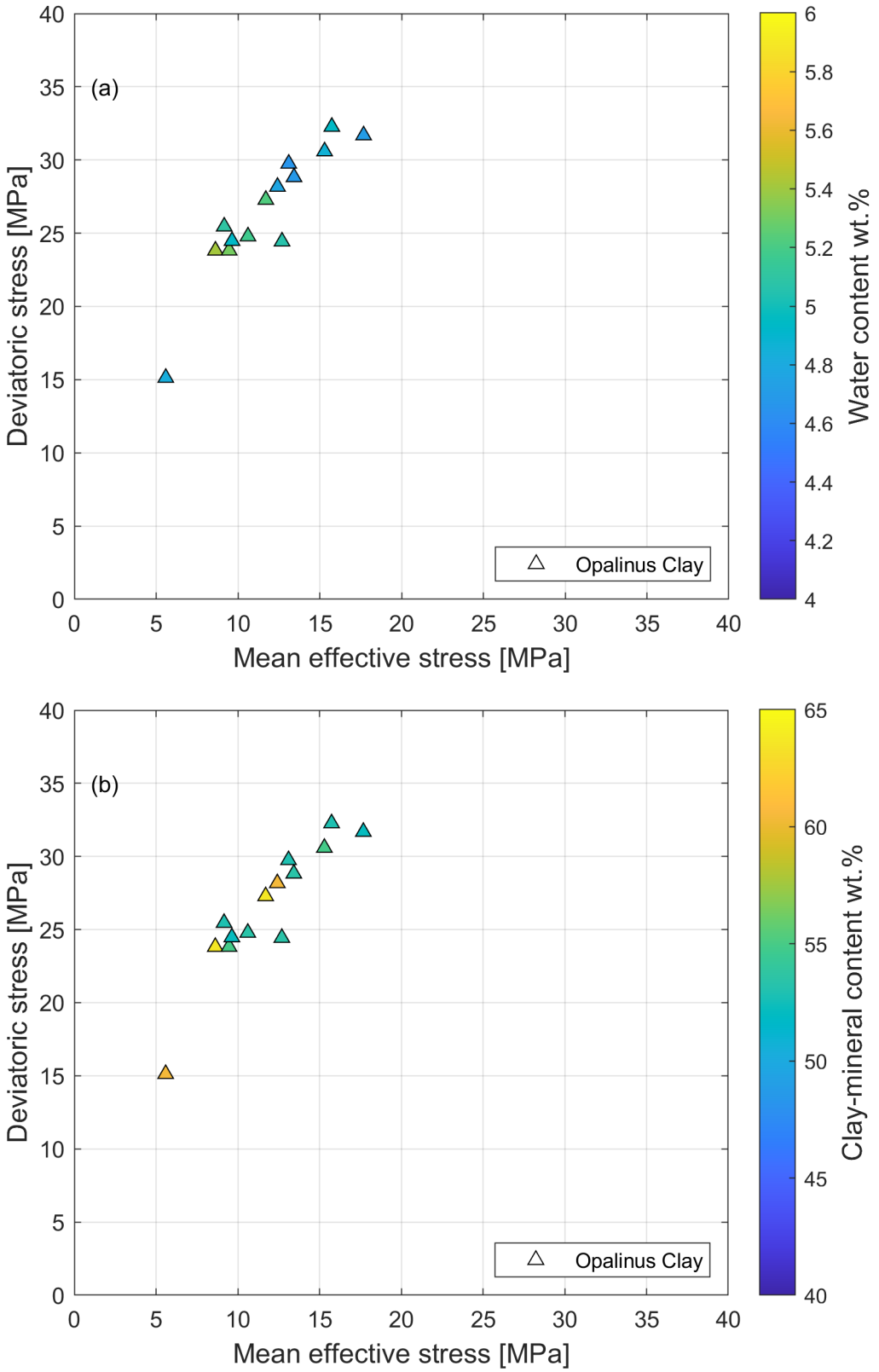

Fig. 6-14: Peak shear strength of specimens of Opalinus Clay and confining units

Results in mean effective versus deviatoric stress, sorted by (a) water content and (b) clay mineral content, when available. Only S-samples are reported.

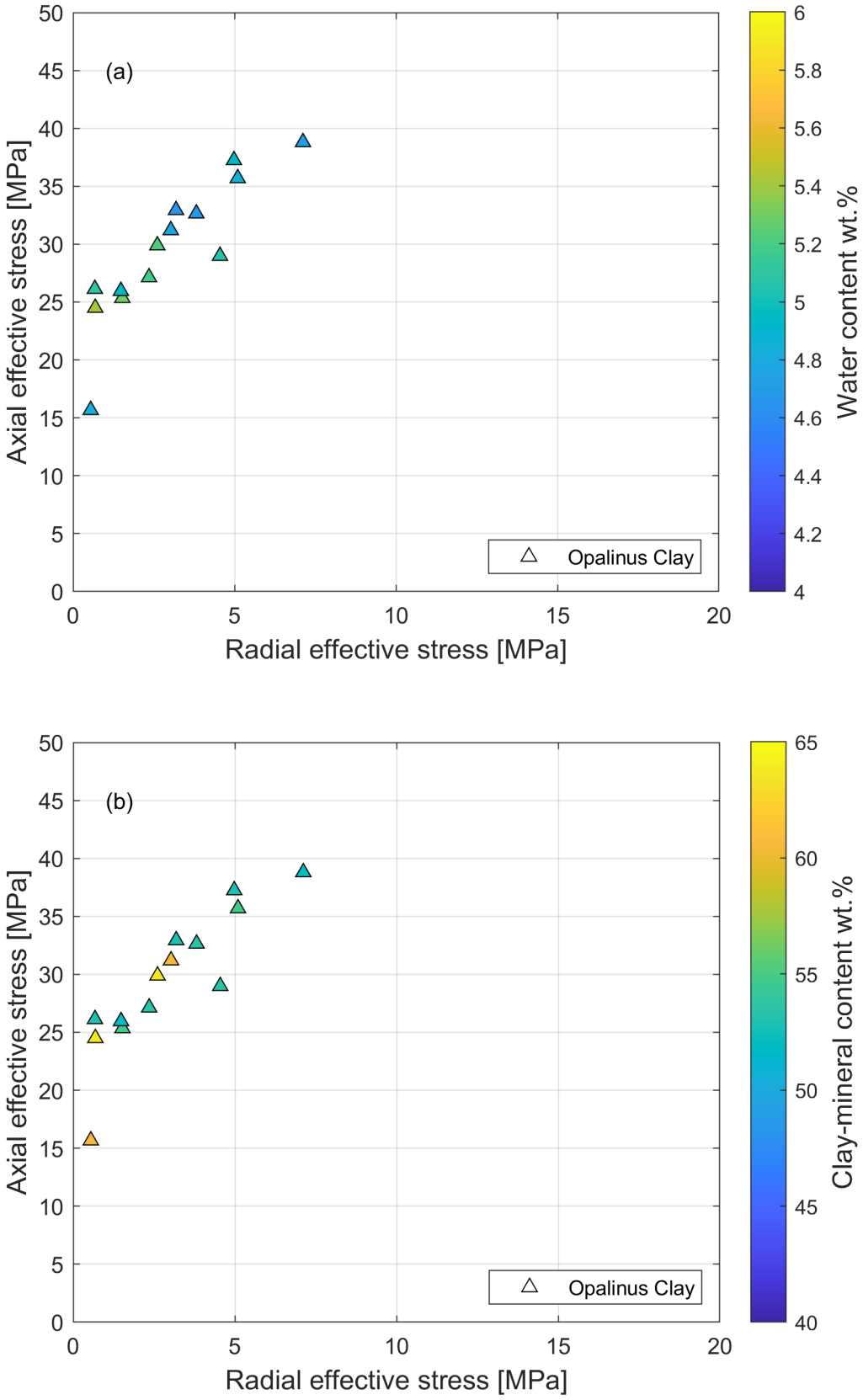

Fig. 6-15: Peak shear strength of specimens of Opalinus Clay and confining units

Results in radial versus axial effective stress, sorted by (a) water content and (b) clay mineral content, when available. Only S-samples are reported.

6.2.2.5 Analysis of the Z-samples results

Two orientations were tested for specimens cored with an angle with respect to the bedding direction. The results on specimens with Z geometry are reported in Fig. 6-16. Four specimens were obtained with an angle of 55 – 60° between the bedding direction and the horizontal plane. Two specimens were obtained with an angle of 70° from the horizontal (marked in Fig. 6-18 with the angle direction). Consistently with initial calculations for the orientation of bedding with minimum strength, the two specimens oriented to 70° showed higher peak strength compared to the same results on specimens oriented at 60°. Peak strength in test C3_TRU1_1_895_ 15Z5CTCU is much lower than what can be expected by drawing a virtual regression line to all other tests with a 55 – 60° angle between bedding and the horizontal plane (Fig. 6-16a). In the stress – strain diagram, that test exhibits hardly any post-peak softening compared to the other Z-test results. Finally, the maximum of AB coincides with the maximum values of uw and peak strength (qMax). All these observations suggest that the specimen was pre-damaged. It is noted that bedding-parallel microfissures can amplify the effect on peak strength in Z-samples compared to S- or P-samples, in which the failure plane is evolving across the bedding planes.

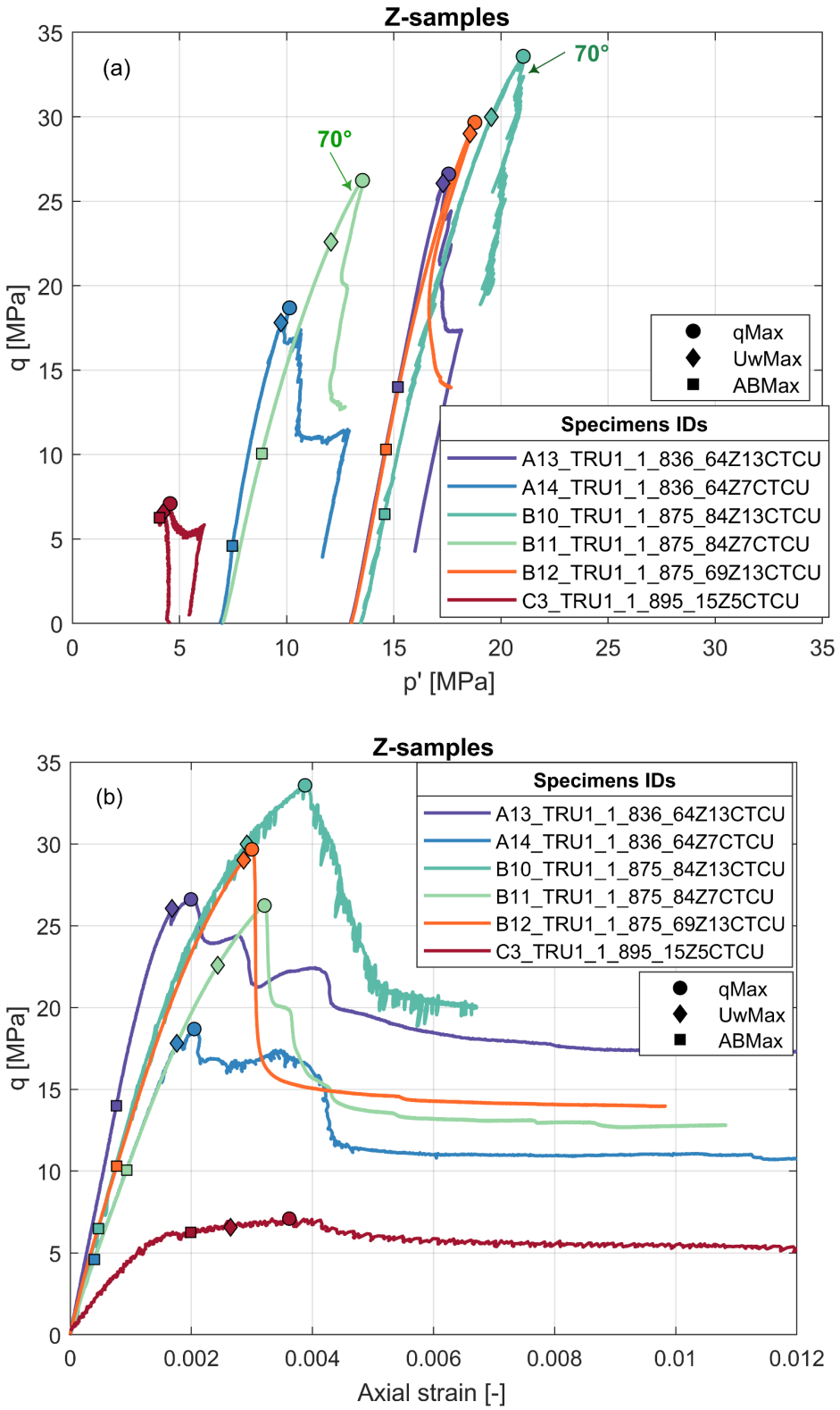

Fig. 6-16: Deviatoric stress (a) and axial strain (b) during shearing phase of Z-geometry specimens

6.2.2.6 Analysis of the outlier results

In this section, tests that showed a response significantly different from the majority of the results (outliers) are analysed in more detail. Diagnostic plots are available in Appendix C.

Test A10_TRU1_1_925_21S8CTCU

For this test, the laboratory reported that after the first unloading, an uncontrolled and unplanned second unloading occurred (Fig. 6-17). The prescribed strain rate was not maintained, and a rather fast loading (more than one order of magnitude faster) occurred, followed by a minor bounce back of the stress. The unexpected response yielded a sudden pore pressure increase. After that, the correct strain rate (10^{-7} s^{-1}) was established. The resulting stress path is reported in Fig. 6-18, however, during the phase in which the strain rate control was lost, the pore pressure cannot be considered in equilibrium throughout the sample, and the measured value is not representative of the entire specimen response. The stress path corresponding to this phase is reported with a dotted line, since this is affected by an uncertainty. In the following, the correct strain rate was recovered, and it may be assumed that at peak the pore pressure was in equilibrium throughout the specimen.

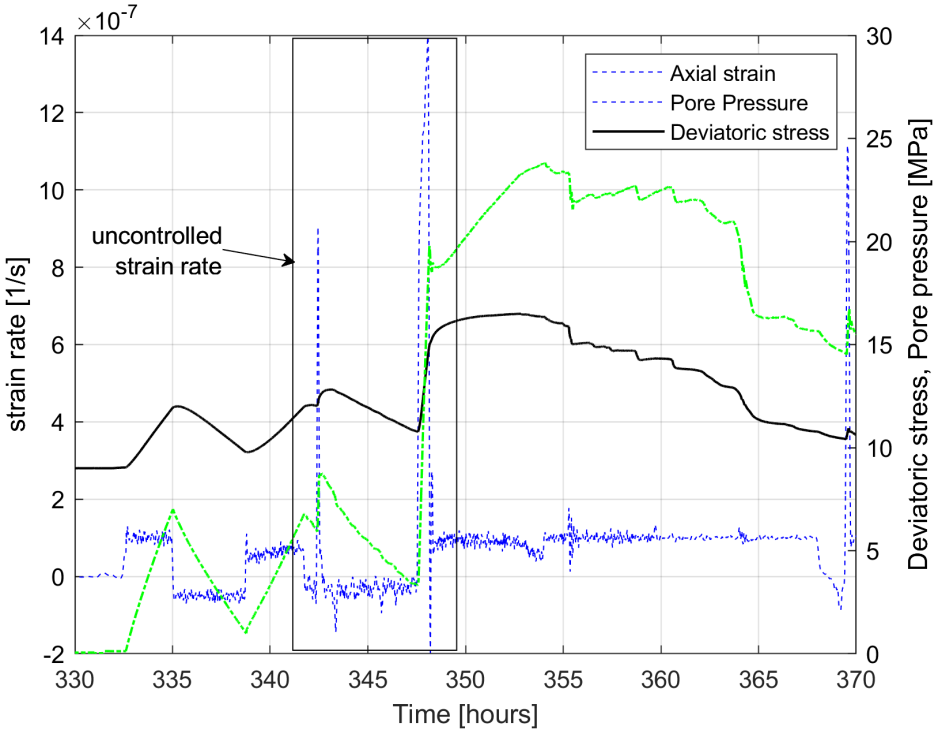

Fig. 6-17: Deviatoric stress, axial strain and pore pressure evolution during shearing phase

Test A10_TRU1_1_925_21S8CTCU. The uncontrolled second unload and the fast reload are highlighted. The pore pressure evolution, for q between 5 and 20 MPa cannot be considered representative of the whole specimen.

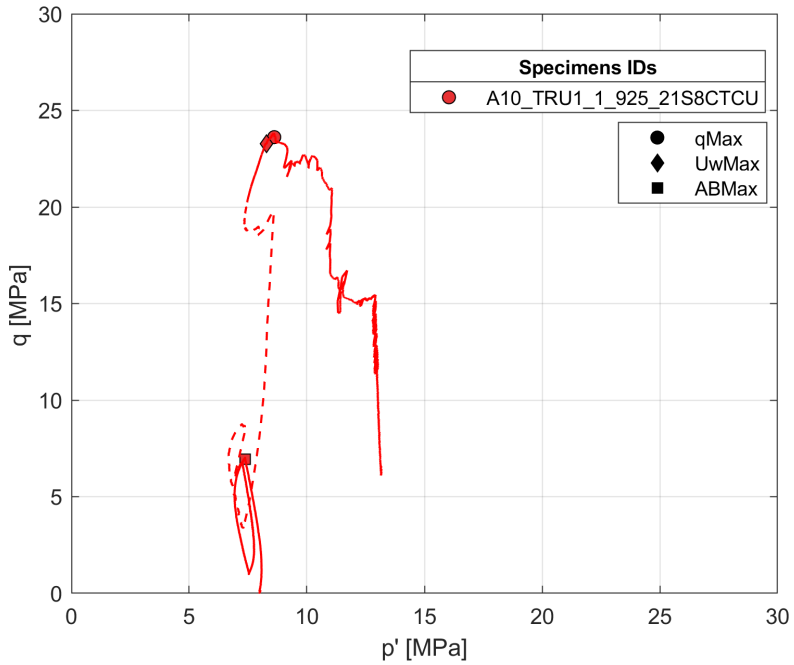

Fig. 6-18: Stress path of test A10_TRU1_1_925_21S8CTCU

Uncontrolled second unloading and following reloading yielded a pore pressure evolution, for q between ~ 5 – 20 MPa (dotted line) that cannot be considered representative of the whole specimen.

Test B3_TRU1_1_851_94S7CTCU

For this test, the laboratory reported a pore pressure leakage during shearing. This is compatible with the anomalous pore pressure decrease during unload-reload (initial part of the shearing phase in Fig. 6-19): during unloading the pore pressure decrease is greater than the corresponding deviatoric stress decrease. The computed effective stress path results unrealistically shifted towards the right of the plane (Fig. 6-21) The pore pressure measurement cannot be considered representative of the pore pressure within the specimen.

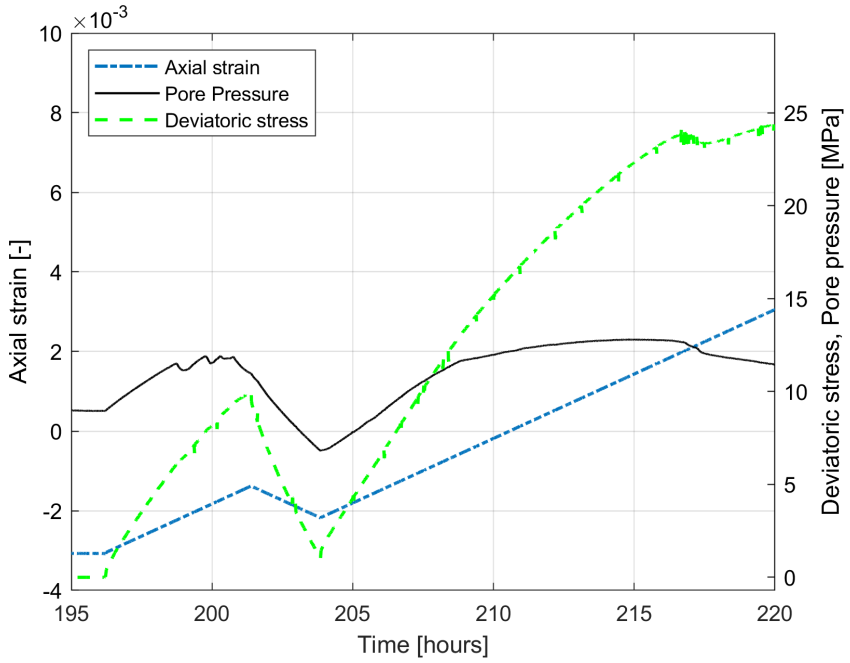

Fig. 6-19: Deviatoric stress, axial strain and pore pressure evolution during shearing phase

Test B3_TRU1_1_851_94S7CTCU. Zoom onto the initial unload, where pore pressure drop occurred.

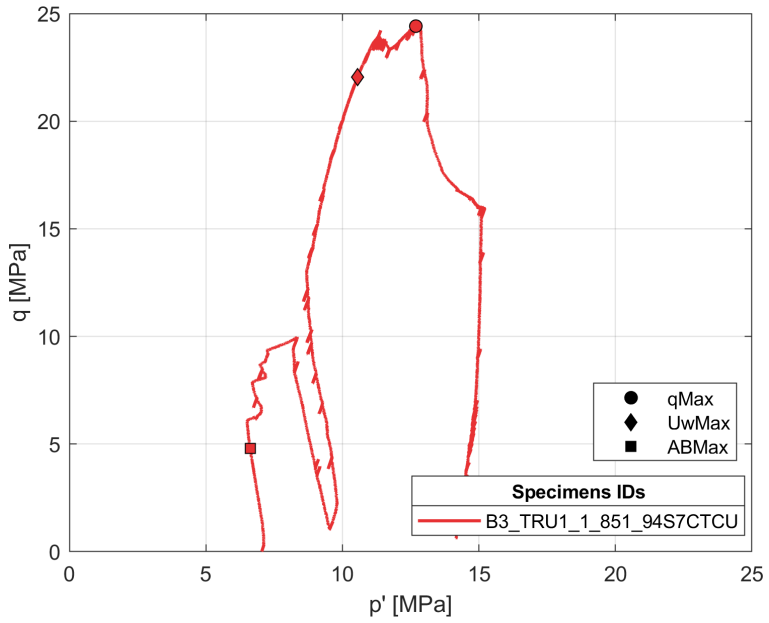

Fig. 6-20: Stress path of test B3_TRU1_1_851_94S7CTCU

Pore pressure measurment was affected by a leakage in the drainage system, and the consequent value is not representative of the specimen pore pressure. Effective stress path is affected by an error.

Test C2_TRU1_1_895_08P5CTCU

In this test, a peak strength lower than the expected value, based on the other experimental results, was observed. In Fig. 6-21 the stress path and strain evolution are reported. It is noted that a limited post-peak softening was recorded, which is unusual for Opalinus Clay at low effective confining stress. This response is attributed to a pre-damage of the specimen, possibly induced during specimen preparation, that altered the peak (i.e. intact) shear strength of the material.

The results are compared to a specimen for which no damage signs are shown: in Fig. 6-21, the results are plotted together with those of test A5_TRU1_1_903_49P4CTCU, performed on a specimen from the same lithological subunit, tested on the same stress path and similar initial confinement. The two specimens have similar water content and mineralogical composition and were expected to have similar mechanical response. Test C2_TRU1_1_895_08P5CTCU achieved similar stress at the maximum AB value, then maximum pore pressure was reached at low stress value compared to the analogous test. Stiffness is also lower in the specimen suspected to be damaged.

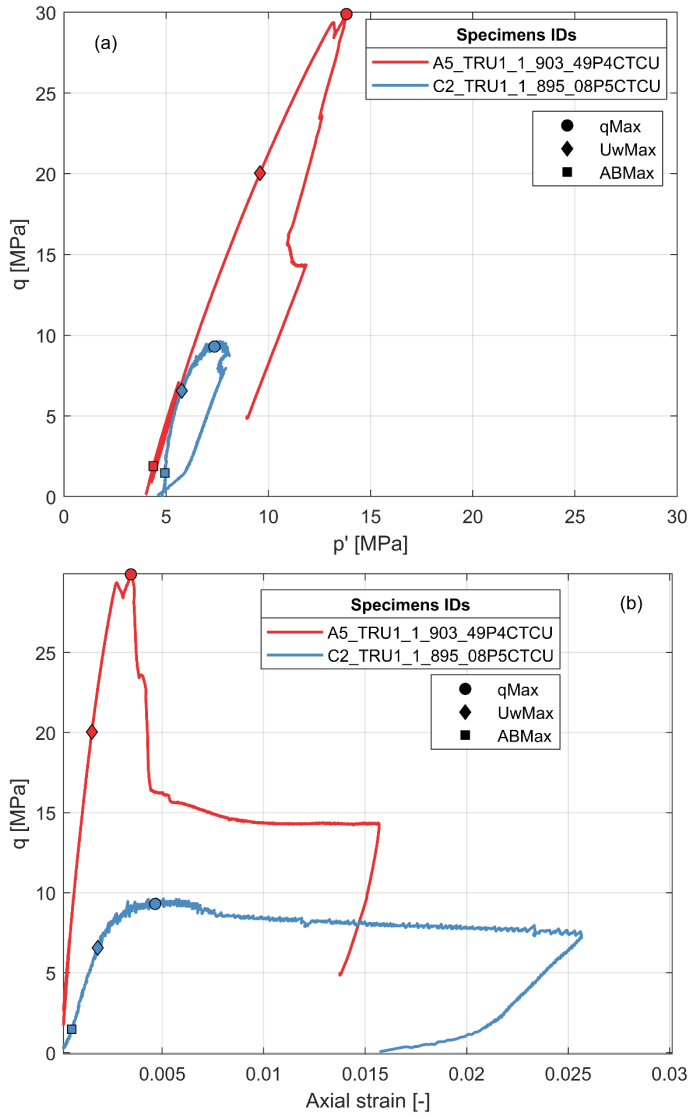

Fig. 6-21: Test C2_TRU1_1_895_08P5CTCU and A5_TRU1_1_903_49P4CTCU results compared

Deviatoric stress evolution with (a) mean effective stress and (b) axial strain.

A similar response was pointed out in the previous section for the Z test C3_TRU1_1_895_ 15Z5CTCU.

Test C4_TRU1_1_895_08S4CTCU

In this test, the evolution of the deviatoric stress approaching and following the maximum value showed an unusual response (Figs. 6-22a and b). A series of rather short drops in deviatoric stress occurred at axial strains between 0.007 and 0.01, followed by two marked drops (at axial strain 0.011 and 0.017), and relatively small increases. Peak strength occurs at a distinctly low deviatoric stress of approximately 15 MPa despite comparable values in water content and clay mineral content with respect to other tests (*cf.* Figs. 6-14 and 6-15). A stable post peak strength was then achieved. In this case as well, as in the previous, peak and post peak shear strength difference is limited. It is also noted that, in this test the effective radial stress reached an extremely small value (below 0.5 MPa) close to peak shear strength (Fig. 6-23). The almost null effective confinement is suspected to have facilitated the opening of fissures within the specimen, which could have contributed to a premature failure of the specimen. Full diagnostic plots are available in the Appendix C.

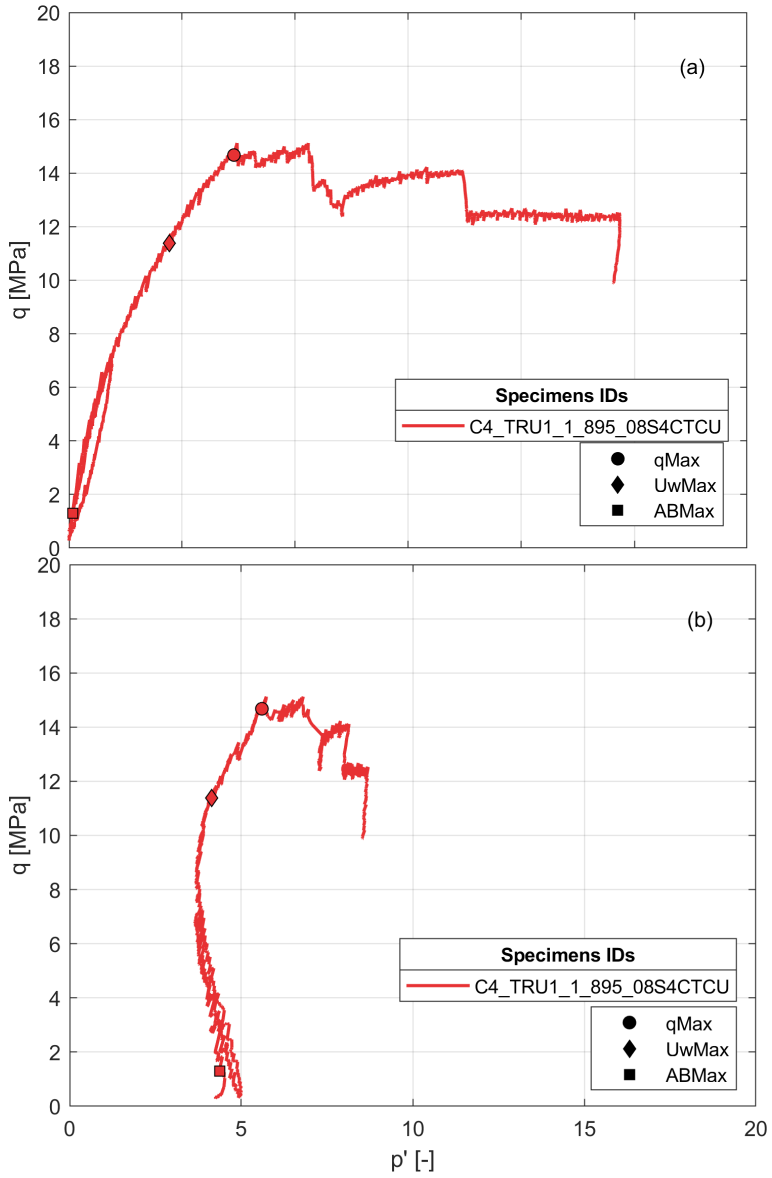

Fig. 6-22: Test C4_TRU1_1_895_08S4CTCU results

Deviatoric stress evolution with (a) axial strain and (b) mean effective stress.

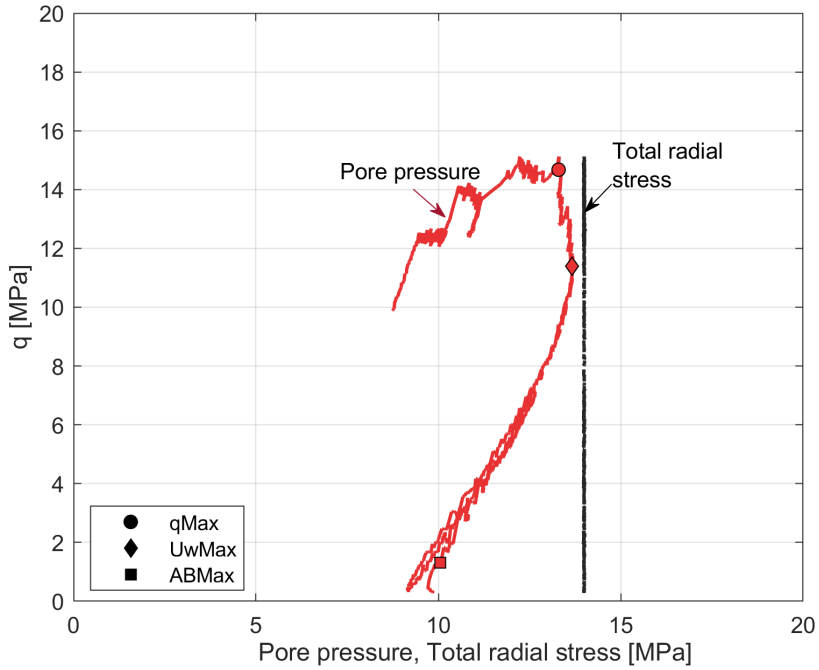

Fig. 6-23: C4_TRU1_1_895_08S4CTCU results

Pore pressure and total radila stress versus deviatoric stress.

6.3 Oedometric tests, one-dimensional swelling and complementary permeability tests

This section includes the results obtained on:

- High pressure oedometric tests (OED), including constant-head permeability tests (PERM)
- One-dimensional swelling test (OS)

The OED, OS tests were obtained in oedometric (lateral strain prevented) conditions. For 4 specimens, during oedometric test, a constant head permeability phase was performed.

6.3.1 Overview of the performed tests and initial specimen conditions

The tests in oedometric conditions were labelled by indicating the letter of the laboratory that performed the test (e.g. Lab A), a sequential number (01) and the type of test (OED = oedometric, OS = one-dimensional swelling). An overview of the performed tests is provided in Tab. 6-3.

Tab. 6-3: Tests performed in oedometric conditions and complementary permeability tests
For specimen geometry see Fig. 4-1.

ID	**Depth** [m]	**Laboratory**	**Specimen geometry**	**Formation**
D01OED_TRU1_1	796.67	D	P	Wedelsandstein Fm.
D02OED_TRU1_1	878.37	D	S	Opalinus Clay
D03OED_TRU1_1	878.21	D	S	Opalinus Clay
D04OED_TRU1_1	878.48	D	S	Opalinus Clay
D05OED_TRU1_1	796.775	D	S	Wedelsandstein Fm.
D06OED_TRU1_1	878.48	D	P	Opalinus Clay
D01_OS_TRU1_1	796.73	D	S	Wedelsandstein Fm.
D02_OS_TRU1_1	878.21	D	S	Opalinus Clay
D03_OS_TRU1_1	878.38	D	P	Opalinus Clay
D04_OS_TRU1_1	878.45	D	S	Opalinus Clay
A01OED_TRU1_1	836.38	A	P	Opalinus Clay
A02OED_TRU1_1	836.43	A	S	Opalinus Clay
A03OED_TRU1_1	903.54	A	S	Opalinus Clay
A04OED_TRU1_1	903.25	A	P	Opalinus Clay
A05OED_TRU1_1	925.1	A	P	Opalinus Clay
A06OED_TRU1_1	956.01	A	P	Staffelegg Fm.
A01_OS_TRU1_1	925.22	A	S	Opalinus Clay
A02_OS_TRU1_1	903.58	A	S	Opalinus Clay
A03_OS_TRU1_1	903.61	A	S	Opalinus Clay

6.3.2 Oedometric test results

The settlement over time curve for each loading increment is analysed adopting an extension to consolidation theory tailored on shales response (Ferrari et al. 2016). The solution combines a modified form of the classical Biot theory (Biot 1941), to account for the behaviour of shales under oedometric conditions, and an extended one-dimensional consolidation theory, to consider the poroelastic behaviour of shales and time-dependent loading conditions. For each loading step, the method allows for the identification of the primary consolidation settlement, related to the water overpressure dissipation, the secondary compression coefficient, the hydraulic conductivity.

As an example, the results of one oedometric test is reported in Fig. 6-24, in terms of oedometric curves. The graph presents the void ratio (e) obtained at the end of the primary consolidation, versus the vertical effective stress (σ'_v). The initial void ratio (e_0), the swelling pressure attained at the end of the resaturation phase (S_p), the yield stress ($\sigma'_{v,y}$) obtained through the Casagrande's construction, the compressibility (C_c) and the unloading (C_s) indexes are marked in the figure. The results from the performed tests are summarised in Tab. 6-4. Corresponding plots are reported in Appendix F. Tab. 6-4 also includes the effective stress level at which the constant head permeability test was performed, where applicable.

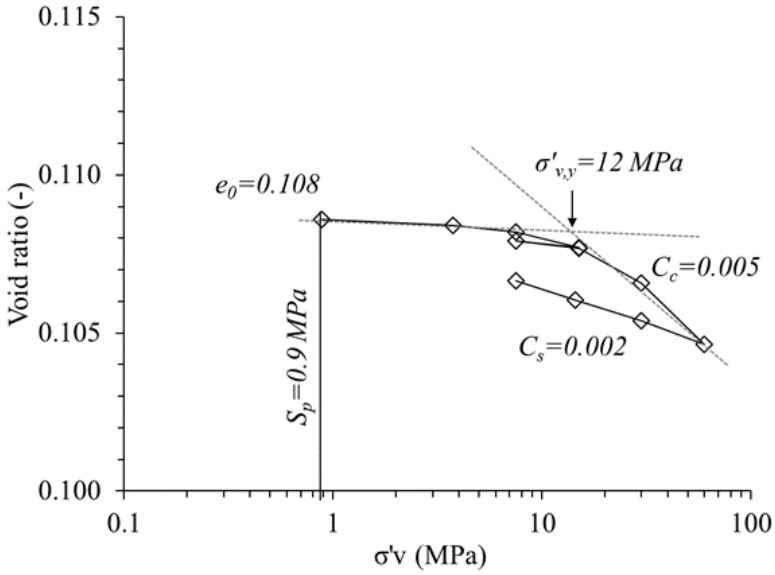

Fig. 6-24: Oedometric curve in void ratio versus vertical effective stress plane
Results from A04OED_TRU1_1.

Tab. 6-4: Oedometric test results
For specimen geometry see Fig. 4-1.

Specimen ID	**Specimen geometry**	**Specimen depth**	e_0	Cc	S_P	$\sigma'_{v,y}$	Cs	**PERM test** at σ'_v
		[m]	[-]	[-]	[MPa]	[MPa]	[-]	[MPa]
D01OED_TRU1_1	P	796.67	0.135	0.012	7	10.4	0.002	14.0
D02OED_TRU1_1	S	878.37	0.146	0.021	6.6	13.0	0.012	
D03OED_TRU1_1	S	878.21	0.145	0.018	3	10.0	0.011	
D04OED_TRU1_1	S	878.48	0.135	0.019	3.5	8	0.008	20.0
D05OED_TRU1_1	S	796.775	0.144	0.021	14.8	19.0	0.007	
D06OED_TRU1_1	P	878.48	0.129	0.013	6.1	6.9	0.005	
A01OED_TRU1_1	P	836.38	0.129	0.018	4.0	13	0.011	15.0
A02OED_TRU1_1	S	836.43	0.118	0.004	0.5	11.5	0.002	15.0
A03OED_TRU1_1	S	903.54	0.106	0.0132	3.8	11	0.0085	
A04OED_TRU1_1	P	903.25	0.108	0.005	0.9	12	0.0023	
A05OED_TRU1_1	P	925.1	0.130	0.006	0.25	10.1	0.0022	
A06OED_TRU1_1	P	956.01	0.131	0.007	0.05	12	0.0031	

A wide range of swelling pressures was measured in oedometric conditions, ranging from fractions of MPa (typically for P geometries) up to about 14.9 MPa. It is noted that those values are generally lower than those obtained in triaxial conditions. This is attributed to a more precise strain control available in the triaxial setups.

6.3.3 Hydraulic conductivity: direct and indirect measurements

From the consolidation theory application, hydraulic conductivity at each loading step can be derived. In the following Fig. 6-25, the hydraulic conductivity of P and S samples obtained from consolidation theory are reported. The ranges of values obtained upon primary loading are represented as the average plus bars: the plot considers the values obtained for a range of vertical effective stress comparable to what is expected in situ (5 – 20 MPa). The results are combined with constant head permeability measurements and labelled with the values of vertical effective stress (for oedometric conditions) or mean effective stress (for triaxial conditions) at which the test was performed. Data of hydraulic conductivity computed form the consolidation and those from constant head tests are reported in Tab. 6-5.

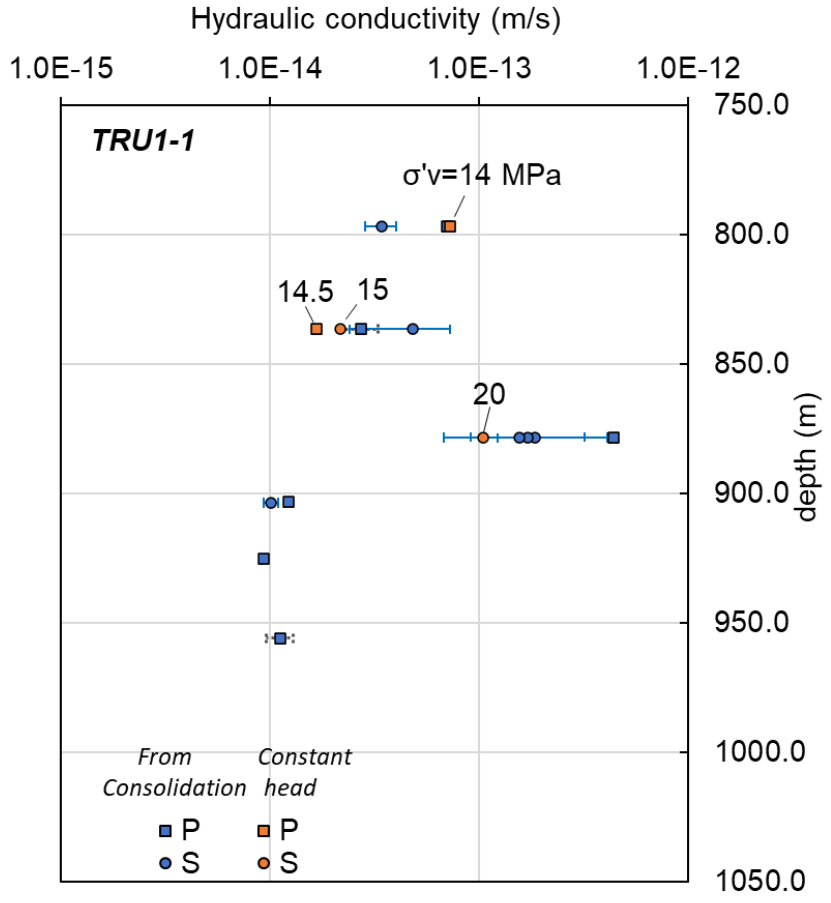

Fig. 6-25: Hydraulic conductivity versus depth

Results obtained from the analysis consolidation test and constant-head tests in oedometric and triaxial conditions.

Tab. 6-5: Hydraulic conductivity test results: from consolidaiton and constant head tests

Specimen ID	**Specimen geometry**	**Depth**	**Consolidation stages**			**Constant head tests**	
			Average k (5 – 20 MPa)	**Minimum k**	**Maximum k**	**k**	σ'_v
		[m]	[m/s]	[m/s]	[m/s]	[m/s]	[MPa]
D01OED_TRU1_1	P	796.67	7.0E-14	7.0E-14	7.0E-14	7.2E-14	14
D02OED_TRU1_1	S	878.37	1.8E-13	6.8E-14	4.1E-13		
D03OED_TRU1_1	S	878.21	1.7E-13	9.1E-14	3.2E-13		
D04OED_TRU1_1	S	878.48	1.6E-13	1.2E-13	1.9E-13	1.0E-13	14
D05OED_TRU1_1	S	796.78	3.4E-14	2.8E-14	4.0E-14		
D06OED_TRU1_1	P	878.48	4.4E-13	4.4E-13	4.4E-13		
A01OED_TRU1_1	P	836.38	2.7E-14	2.2E-14	3.3E-14	1.7E-14	15
A02OED_TRU1_1	S	836.43	4.8E-14	2.4E-14	7.3E-14	2.2E-14	15
A03OED_TRU1_1	S	903.54	1.0E-14	9.3E-15	1.1E-14		
A04OED_TRU1_1	P	903.26	1.2E-14	1.2E-14	1.2E-14		
A05OED_TRU1_1	P	925.10	1.6E-14	1.5E-14	1.6E-14		
A06OED_TRU1_1	P	956.01	1.1E-14	9.5E-15	1.3E-14		

6.3.4 One-dimensional swelling tests

The results of the one-dimensional swelling tests are reported in this section. An example of the evolution of the axial strain in time, while providing pore fluid allowing for one-dimensional swelling is reported in Fig. 6-26. The results are summarised in Tab. 6-6 (plots in Appendix F). The table reports the swelling pressure ε_{swell} attained once the deformation stabilised in absolute value (the minus sign is dropped for the sake of simplicity). Pore pressure u_w adopted during the test is also reported.

Lab D performed four tests, injecting pressure at 50 kPa and applying constant stress to counterbalance the fluid pressure. Lab A injected water at ~ 7 kPa., counterbalanced by the weight of the top piston.

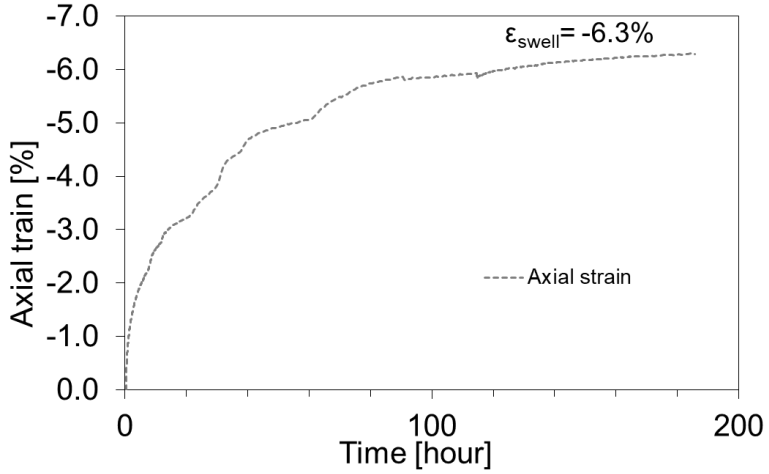

Fig. 6-26: One-dimensional swelling test, evolution of the axial strain in time
Results obtained on specimen D01OS_TRU11.

Tab. 6-6: One-dimensional swelling test results
For specimen geometry see Fig. 4-1.

Specimen ID	**Core depth**	**Specimen geometry**	**Formation**	ε_{swell} (absolute value)	u_w
	[m]			[%]	[kPa]
D01OS_TRU1_1	796.73	S	Wedelsandstein Fm.	6.27	50
D02OS_TRU1_1	878.21	S	Opalinus Clay	0.83	50
D03OS_TRU1_1	878.38	P	Opalinus Clay	5.94	50
D04OS_TRU1_1	878.45	S	Opalinus Clay	2.2	50
A01OS_TRU1_1	925.22	S	Opalinus Clay	0.549	~ 7
A02OS_TRU1_1	903.58	S	Opalinus Clay	1.253	~ 7
A03OS_TRU1_1	903.61	S	Opalinus Clay	1.255	~ 7

7 Representativeness of test results

A critical question revolving around any rock-mechanical or geomechanical laboratory programme is how representative the chosen specimens are for a given formation. This depends on several factors, notably material heterogeneity.

One possible way to address this is to compare wave velocities derived from the sonic scanner in situ (Fig. 7-1 blue line) and ultrasonic velocities constrained in triaxial tests on core in the laboratory (*cf.* Tabs. 5-4 and 6-2, orange points in Fig. 7-1). Such correlations can be used for both i) checking the plausibility of test results and ii) estimating the variability of material properties in (sub-)formations. Therefore, the tests conducted in the rock-mechanical testing programme with formations other than Opalinus Clay (and confining units) are used as guidance to estimate rock-mechanical formation properties.

In contrast, the ambition of the geomechanical testing programme (of Opalinus Clay in particular) is to cover the relevant spectrum of material properties by actual laboratory testing. Whether this was achieved is primarily assessed by comparing the basic properties and mineralogy of tested specimens with the larger database (*cf.* Dossier VIII). In this larger database, water content and mineralogy were constrained every 2 to 3 m along the 112 m thick interval of Opalinus Clay, and each measurement reflects a mean value over a 25 cm core interval.

The water content of geomechanically tested specimens was measured on trimming material from the specimen preparation and on the specimens themselves (before and after testing). For a same specimen, these values were averaged, and the error bar constructed to include the variability in the measurements. Those results are reported versus the specimens sourcing depth in Fig. 7-2. Based on water content, the comparison with the larger database reveals that the spectrum of water content is covered by the geomechanical tests.

The bulk mineralogy was also assessed for the tested specimens. However, it is noted that for a given depth interval multiple «twin specimens» were sourced to constrain stress-dependent properties of the same material. As the material variability in the horizontal direction in the Opalinus Clay is considered very small compared to the variability in the vertical direction, only one specimen was generally used for a given depth interval as a reference mineralogy for other specimens. This assumption verified with repeated analyses of two plugs from an identical depth interval. The clay mineral content in the two analyses varied by only 2 wt.-%, consistent with a value of 3 wt.-% in a previous comparison (Minardi et al. 2019). Therefore, the bulk mineralogy obtained on one specimen was attributed to the other specimens from the same vertical interval of the core. The clay-mineral content (%) is reported in Fig. 7-3 against the depth, together with the large database obtained from University of Bern (*cf.* Dossier VIII).

The comparisons of Figs. 7-2 and 7-3 demonstrate that tested specimens in the geomechanical testing programme capture nicely the material variability and can thus be considered representative of the entire formation.

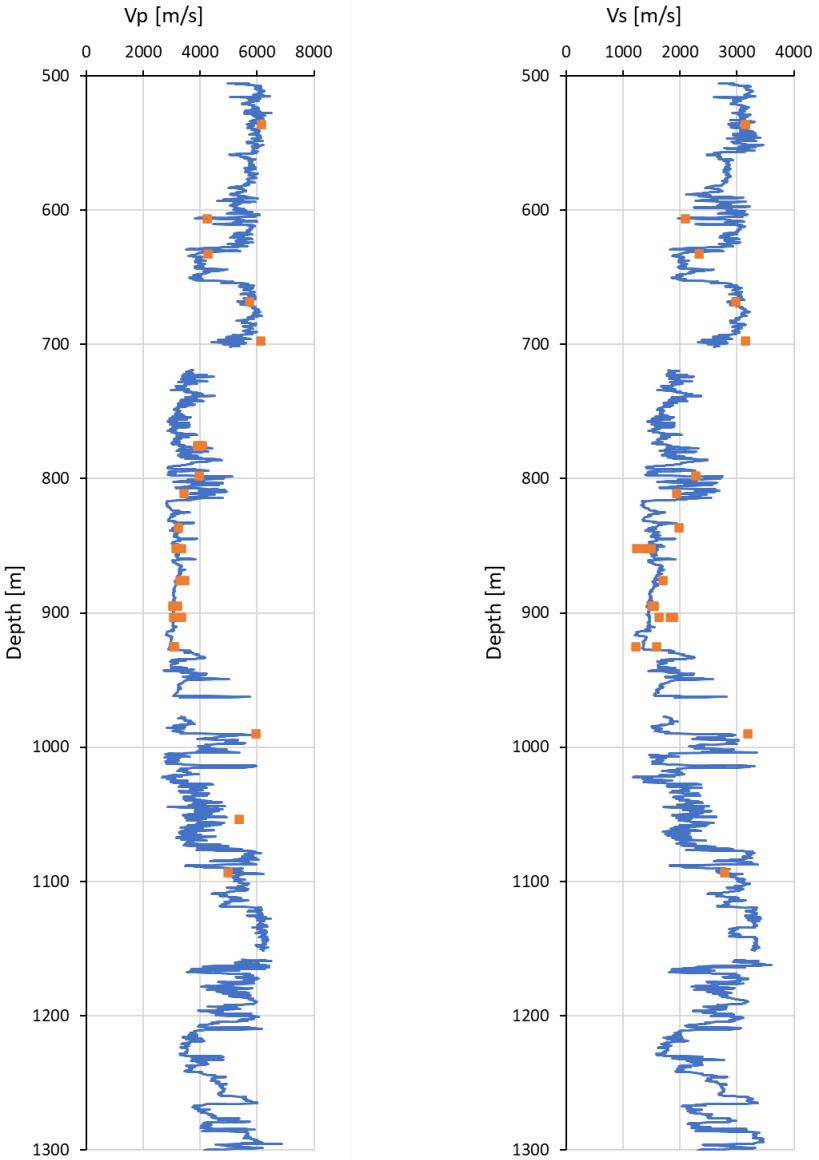

Fig. 7-1: Compressional (a) and shear-wave velocities (b) from borehole and lab testing

Blue line: continuous measurements from borehole sonic scanner (kHz frequency). The gaps in the continuous velocity measurements at 708 m, 969 m and 1'158 m were due to constraints of the logging tool string in the selected casing scheme. Orange squares: lab-measurements (MHz frequency).

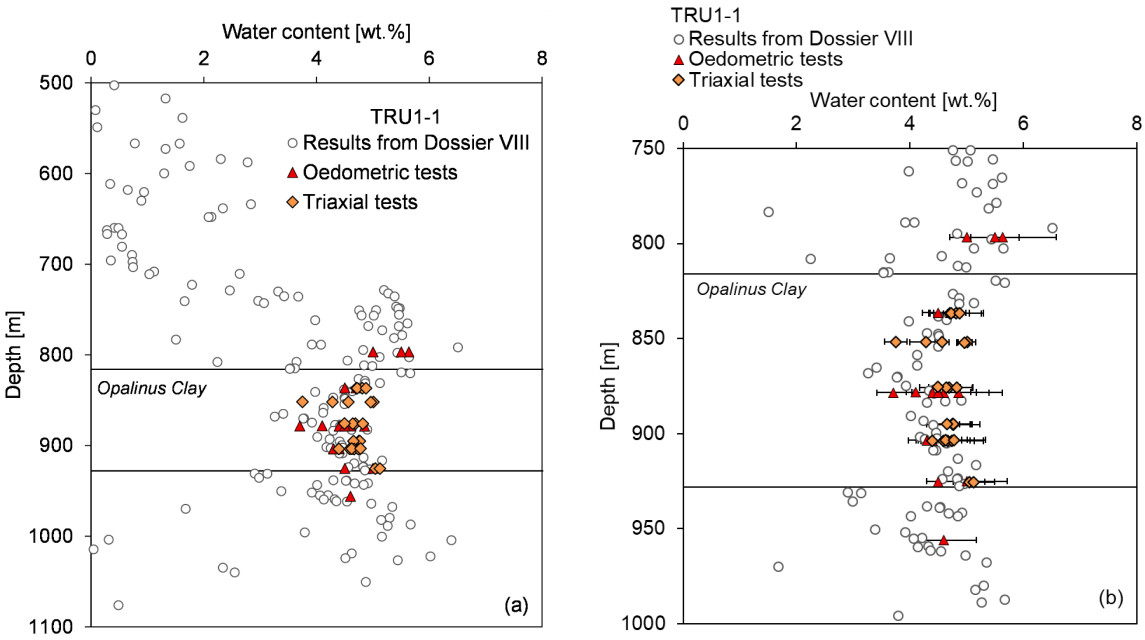

Fig. 7-2: Comparison of the water content vs. depth from the large data base and from those tested in this report

Results include those from Dossier VIII for the TRU1-1 borehole (a) and zoom into the Opalinus Clay and confining units' section (b).

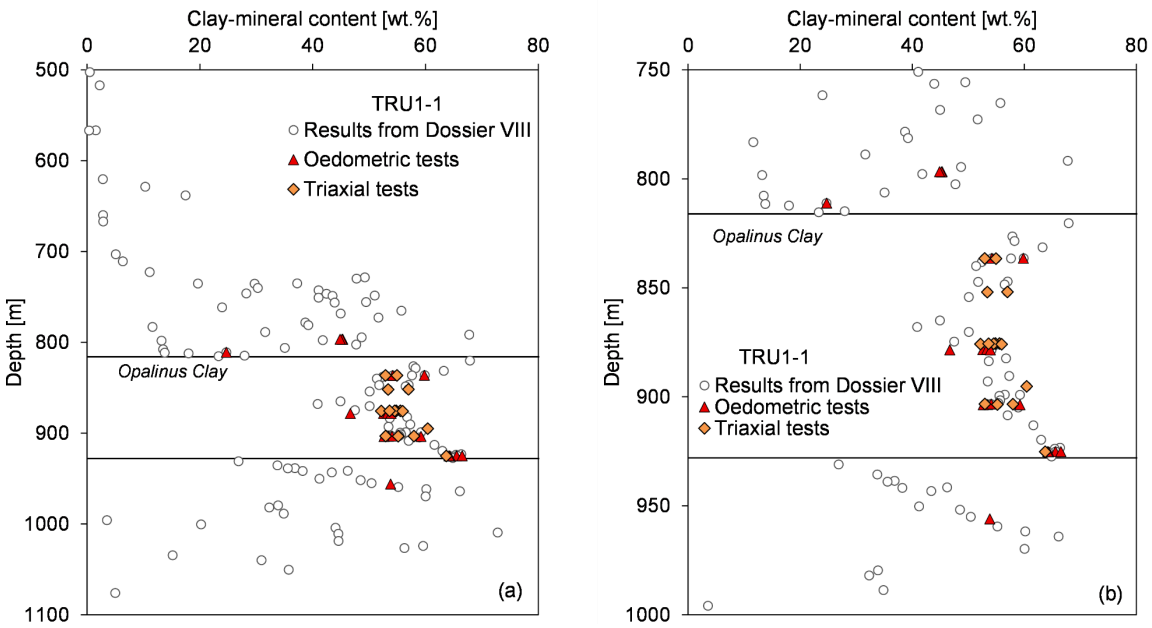

Fig. 7-3: Clay-mineral content vs. depth vs. depth from the large data base and from those tested in this report

Results include those from Dossier VIII for the TRU1-1 borehole (a) and zoom into the Opalinus Clay and confining units' section (b).

8 References

ASTM (2014): D7012-14e1: Standard test method for compressive strength and elastic moduli of intact rock core specimens under varying states of stress and temperatures. ASTM International, West Conshohocken, PA.

ASTM (2016): D3967-16: Standard test method for splitting tensile strength of intact rock core specimens. ASTM International, West Conshohocken, PA.

ASTM (2017a): D4318-17e1: Standard test methods for liquid limit, plastic limit, and plasticity index of soils. ASTM International, West Conshohocken, PA.

ASTM (2017b): D6913/D6913M-17: Standard test methods for particle-size distribution (gradation) of soils using sieve analysis. ASTM International, West Conshohocken, PA.

ASTM (2017c): D7928-17: Standard test method for particle-size distribution (gradation) of fine-grained soils using the sedimentation (hydrometer) analysis. ASTM International, West Conshohocken, PA.

ASTM (2019): D4543-19: Preparing rock core as cylindrical specimens and verifying conformance to dimensional and shape tolerances. ASTM International, West Conshohocken, PA.

Aydin, A. (2014): Upgraded ISRM suggested method for determining sound velocity by Ultrasonic Pulse Transmission Technique. Rock Mechanics and Rock Engingeering 47, 255-259.

Biot, M.A. (1941): General theory of three-dimensional consolidation. Journal of Applied Physics 12/2, 155-164.

Crisci, E., Ferrari, A., Giger, S.B. & Laloui, L. (2019): Hydro-mechanical behaviour of shallow Opalinus Clay shale. Eng. Geol. 251, 214-227. https://doi.org/10.1016/j.enggeo.2019.01.016

Ewy, R.T. (2014): Shale swelling/shrinkage and water content change due to imposed suction and due to direct brine contact. Acta Geotech. 9, 869-886. https://doi.org/10.1007/s11440-013-0297-5

Ewy, R.T. (2015): Shale/claystone response to air and liquid exposure, and implications for handling, sampling and testing. International Journal of Rock Mechanics and Mining Sciences 80, 388-401. https://doi.org/10.1016/j.ijrmms.2015.10.009

Favero, V. (2017): Multiphysical behaviour of shales from Northern Switzerland. https://doi.org/10.5075/epfl-thesis-7539, urn:nbn:ch:bel-epfl-thesis7539-7

Favero, V., Ferrari, A. & Laloui, L. (2018): Anisotropic behaviour of Opalinus Clay through consolidated and drained triaxial testing in saturated conditions. Rock Mechanics and Rock Engineering 51, 1305-1319.

Ferrari, A., Favero, V. & Laloui, L. (2016): One-dimensional compression and consolidation of shales. Int. J. Rock Mech. Min. Sci. 88, 286-300. https://doi.org/10.1016/j.ijrmms.2016.07.030

Ghabezloo, S. & Sulem, J. (2010): Effect of the volume of the drainage system on the measurement of undrained thermo-poro-elastic parameters. International Journal of Rock Mechanics and Mining Sciences 47, 60-68. https://doi.org/10.1016/j.ijrmms.2009.03.001

Giger, S.B., Ewy, R.T., Favero, V., Stankovic, R. & Keller, L.M. (2018): Consolidated-undrained triaxial testing of Opalinus Clay: Results and method validation. Geomechanics for Energy and the Environment 14, 16-28.

Head, K.H. (1998): Manual of soil laboratory testing. Volume 3: Effective stress tests. Second Edition John Wiley and Sons.

Isler, A., Pasquier, F. & Huber, M. (1984): Geologische Karte der zentralen Nordschweiz 1:100'000. Herausgegeben von der Nagra und der Schweiz. Geol. Komm.

Keller, L.M. & Giger, S.B. (2019): Petrophysical properties of Opalinus Clay drill cores determined from Med-XCT images. Geotech. Geol. Eng. 37/4, 3507-3522. https://doi.org/10.1007/s10706-019-00815-2

Minardi, A., Ferrari, A. & Laloui, L. (2019): Benchmark study on triaxial testing of Opalinus Clay: Analysis and comparative evaluation of tests results. Nagra Arbeitsbericht NAB 19-18.

Minardi, A., Giger, S.B., Ewy, R.T., Stankovic, R., Stenebråten, J., Soldal, M., Rosone, M.. Ferrari, A. & Laloui, L. (2020): Benchmark study of undrained triaxial testing of Opalinus Clay shale: Results and implications for robust testing. Geomechanics for Energy and the Environment 25, 100210.

Nagra (2014): SGT Etappe 2: Vorschlag weiter zu untersuchender geologischer Standortgebiete mit zugehörigen Standortarealen für die Oberflächenanlage. Geologische Grundlagen. Dossier II: Sedimentologische und tektonische Verhältnisse. Nagra Technischer Bericht NTB 14-02.

Nagra (2021): TBO Bülach-1-1: Data Report. Dossier IX Rock-mechanical and Geomechanical Laboratory Testing. Nagra Arbeitsbericht NAB 20-08.

Pietsch, J. & Jordan, P. (2014). Digitales Höhenmodell Basis Quartär der Nordschweiz – Version 2013 (SGT E2) und ausgewählte Auswertungen. Nagra Arbeitsbericht NAB 14-02.

Rufer, D. (2019): Field manual: Drill core sampling for analytical purposes. Nagra Arbeitsbericht NAB 19-13.

Tuttolomondo, A. (2020): Effective stress for unsaturated active clays and in-situ effective stress estimation methodology. EPFL PhD Thesis n° 8291.

Wissa, A.E.Z. (1969): Pore pressure measurement in saturated stiff soils. Journal of the Soil Mechanics and Foundations Division 95, 1063-1074.

Wersin, P., Mazurek, M., Waber, H.N., Mäder, U.K., Gimmi, T., Rufer, D. & de Haller, A. (2013): Rock and porewater characterisation on drillcores from the Schlattingen borehole Nagra Arbeitsbericht NAB 12-54.

Witteveen, P., Ferrari, A. & Laloui, L. (2013): An experimental and constitutive investigation on the chemo-mechanical behaviour of a clay. Geotechnique 63/3, 244-255.

Appendix A Photo documentation of the rock-mechanical testing programme

TS (average depth of sample) **TRU1-1**

before testing **after testing**

515.24 m These samples are substitutes. For details, see Chapter 4 in the report.

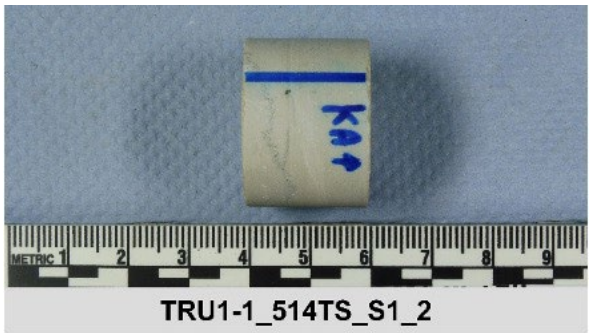

515.32 m

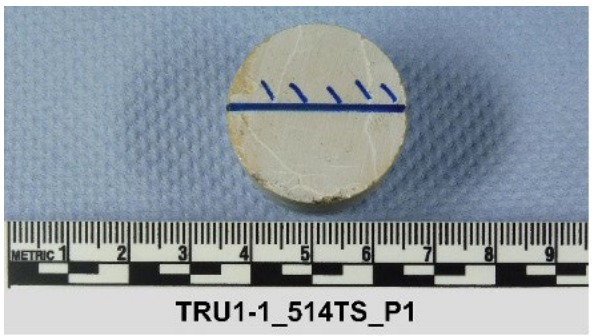

before testing **after testing**

535.97 m

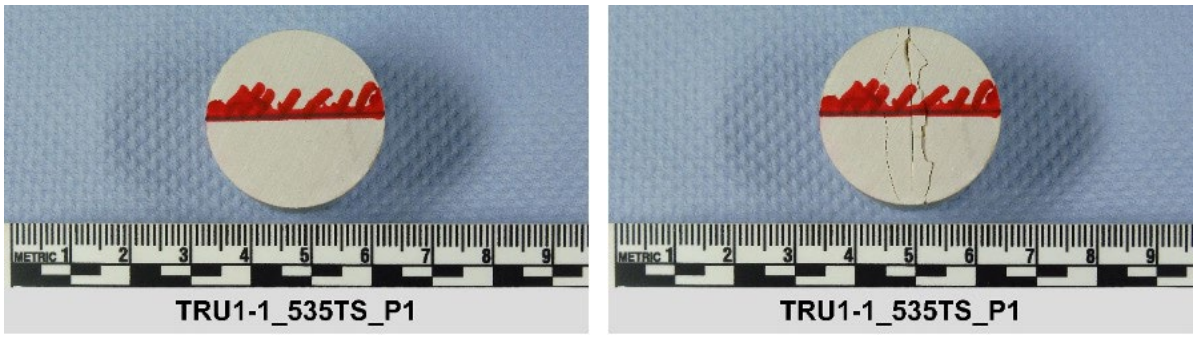

536.02 m

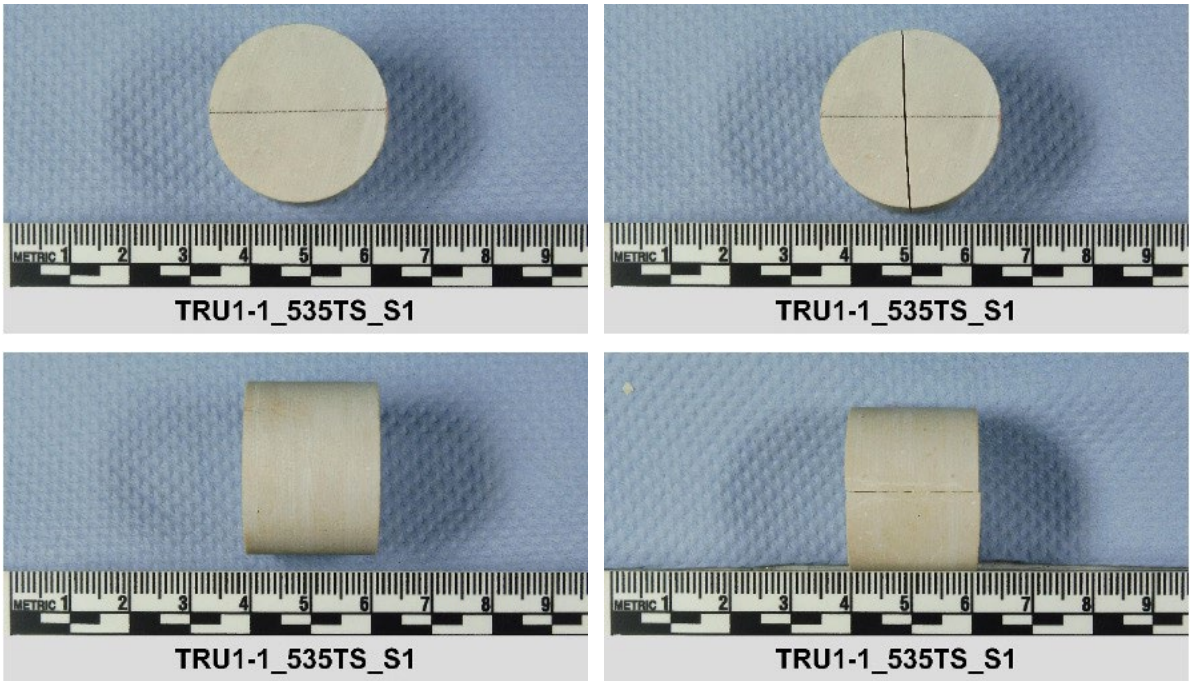

before testing **after testing**

554.72 m

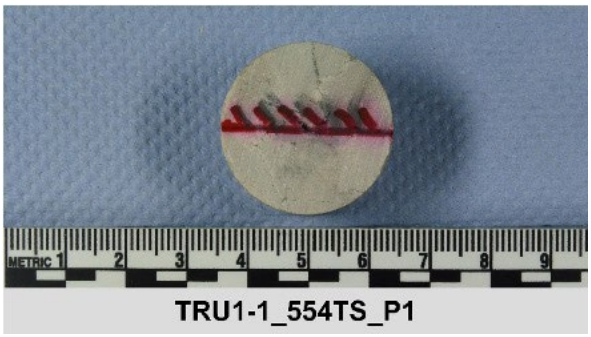

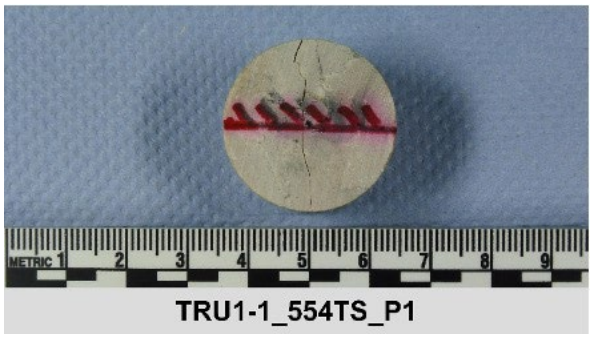

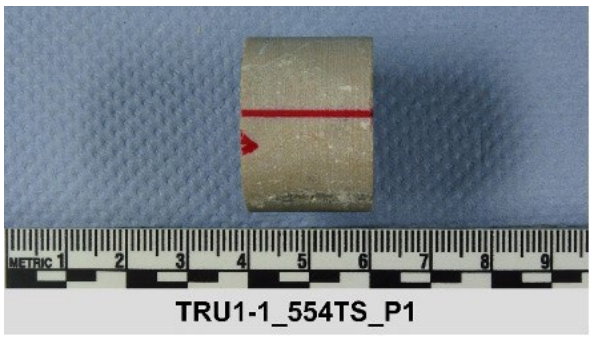

554.77 m

before testing **after testing**

554.98 m

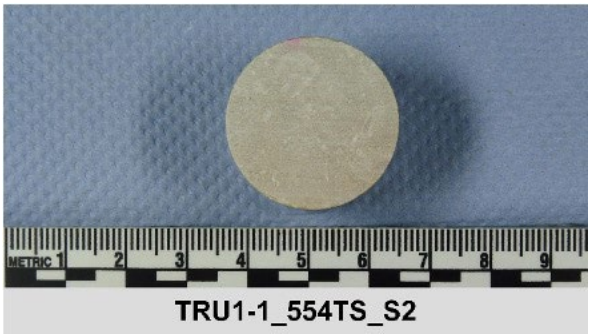

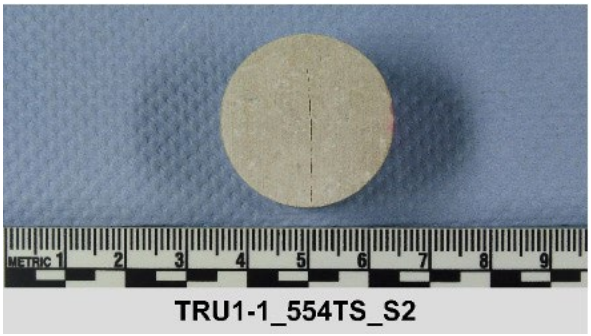

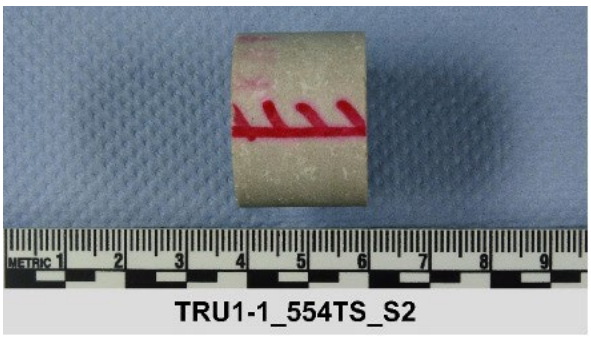

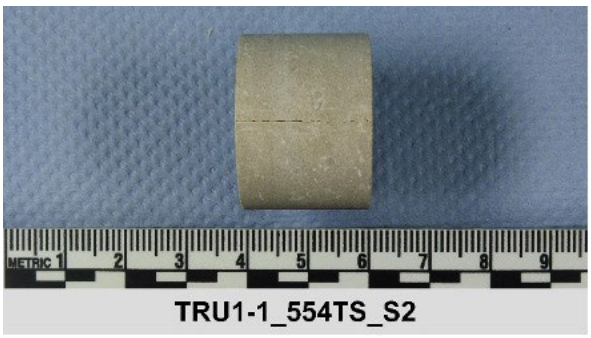

606.01 m

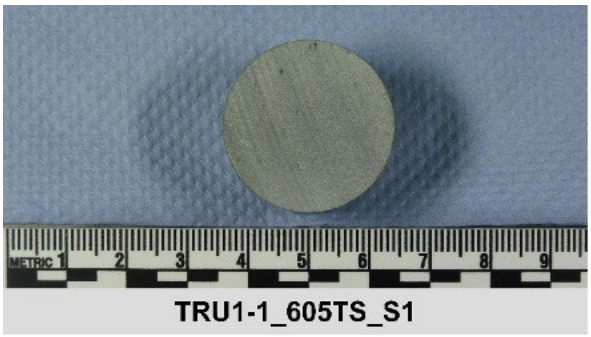

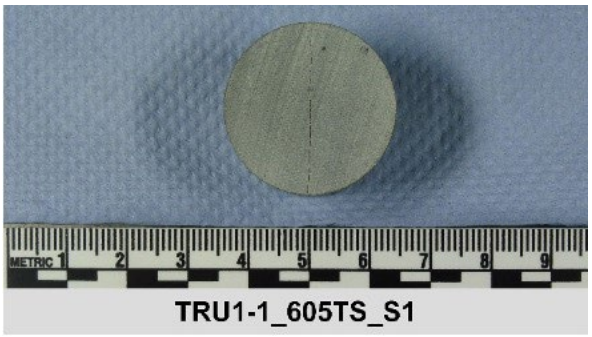

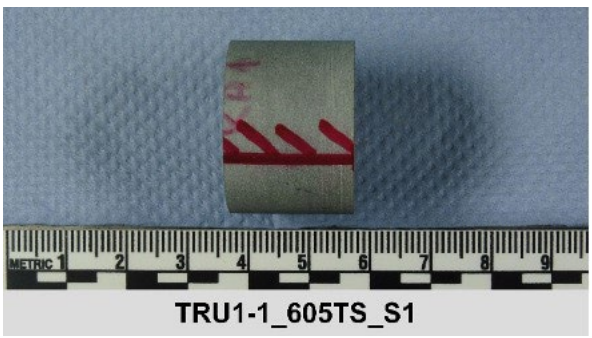

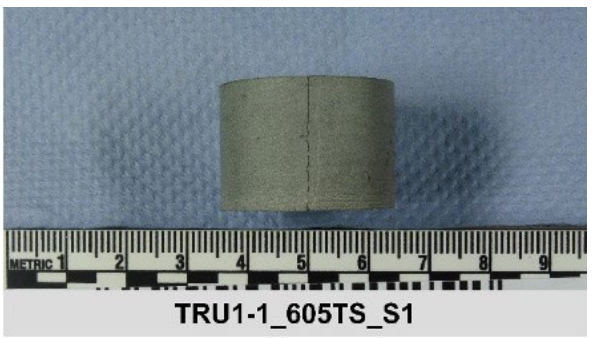

before testing	**after testing**
606.06 m	
Picture of TRU1-1_605TS_P1 from before the test is missing	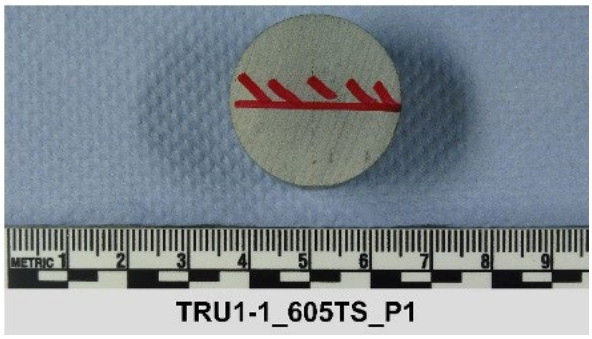
Picture of TRU1-1_605TS_P1 from before the test is missing	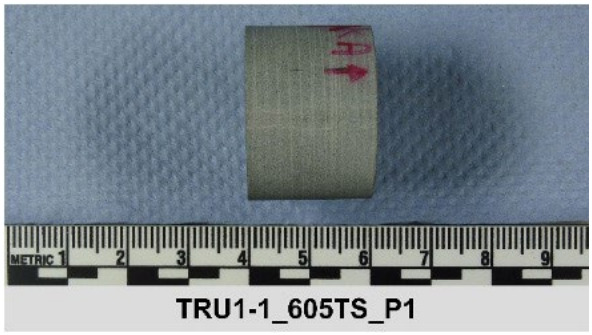
613.68 m	
	
	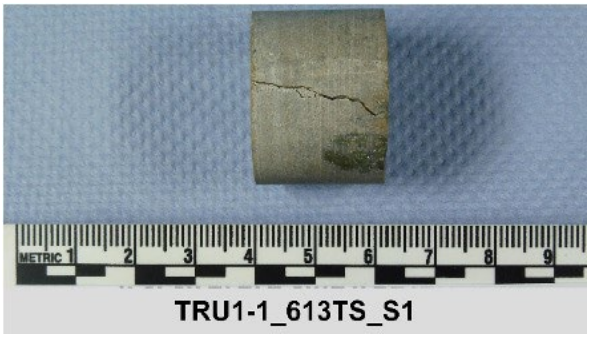

before testing **after testing**

613.74 m

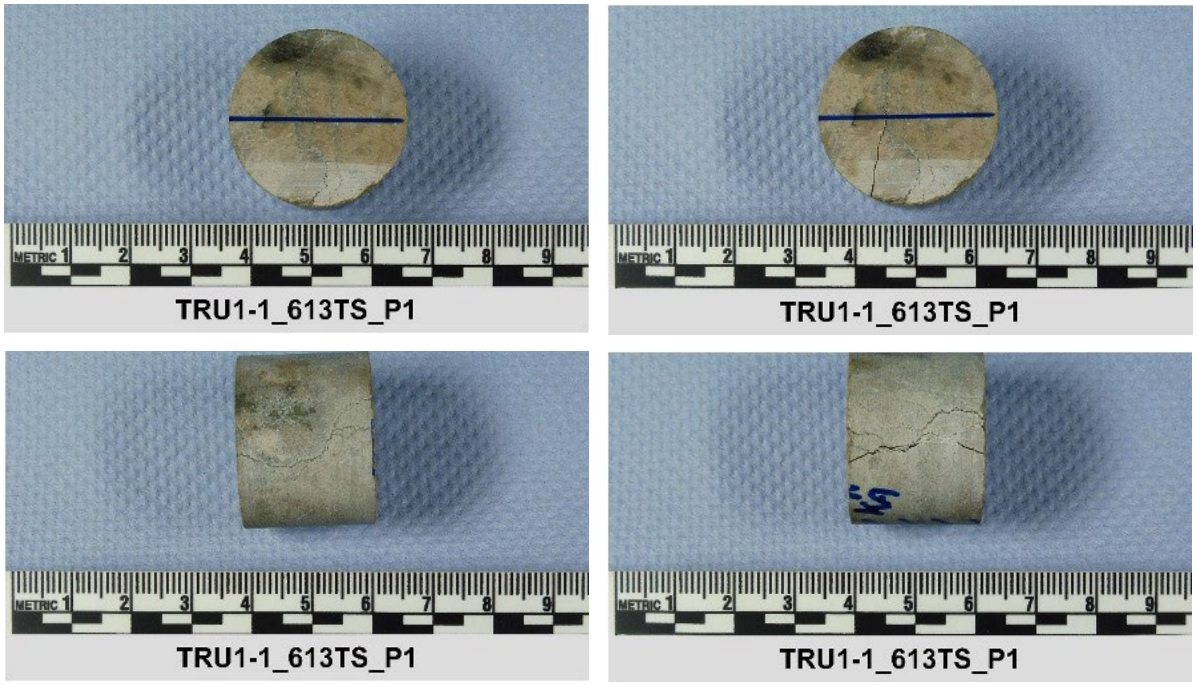

632.62 m

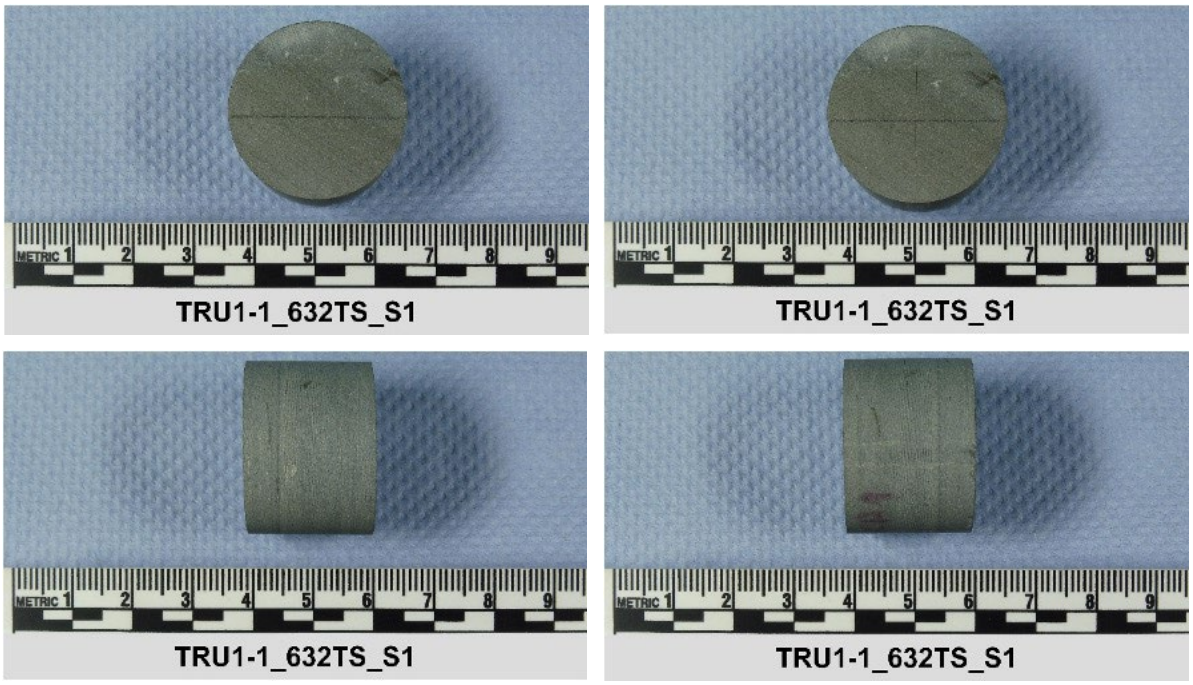

before testing **after testing**

632.68 m

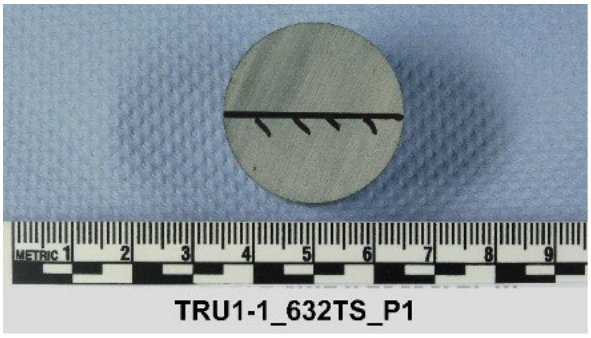

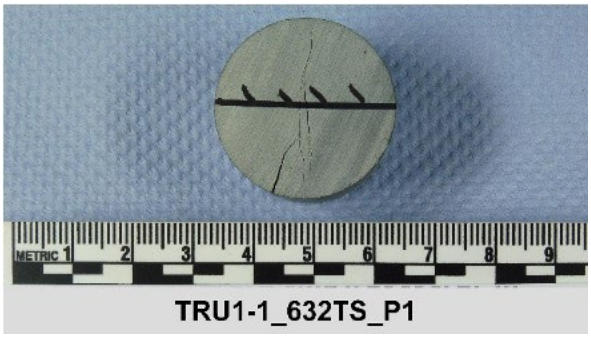

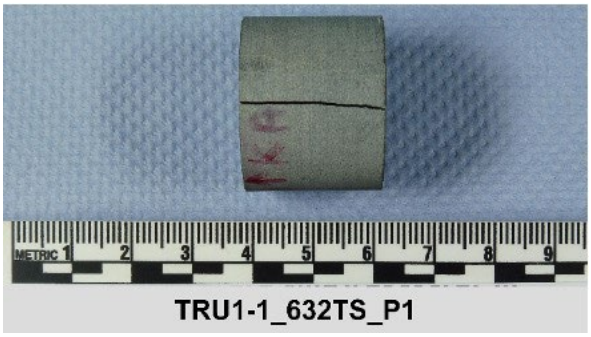

644.77 m

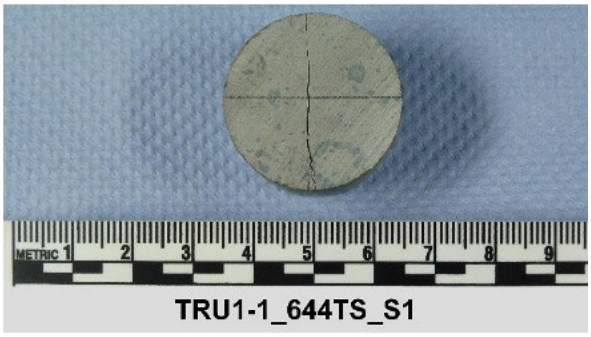

before testing **after testing**

644.83 m

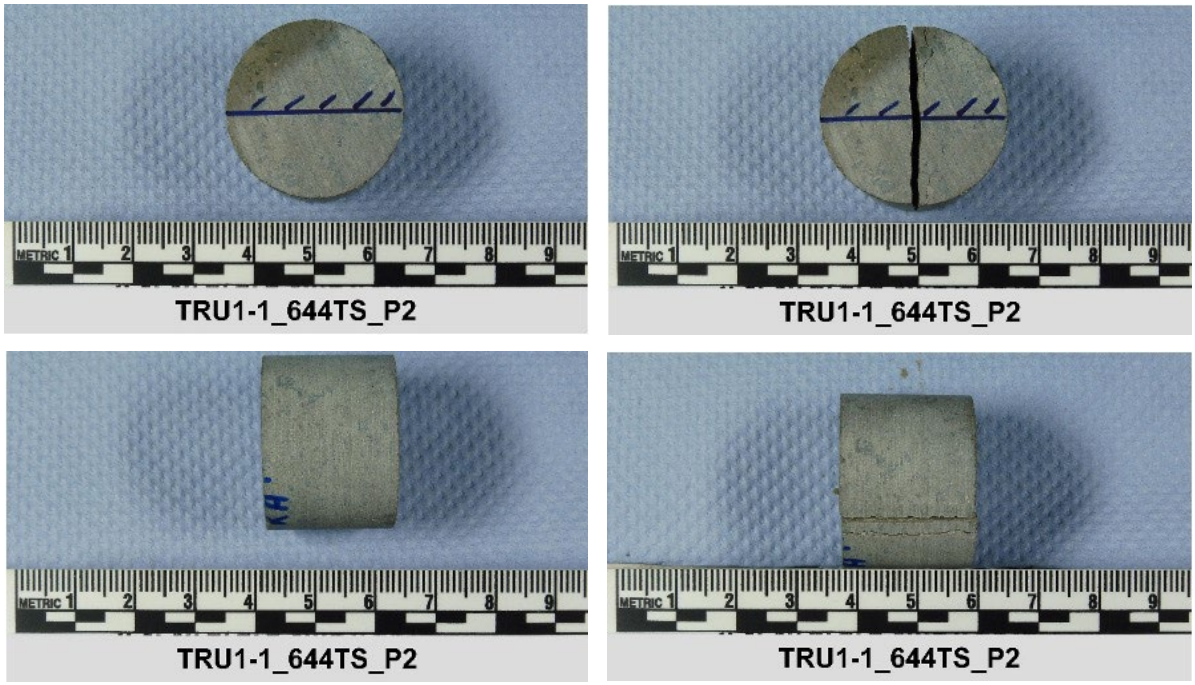

653.67 m

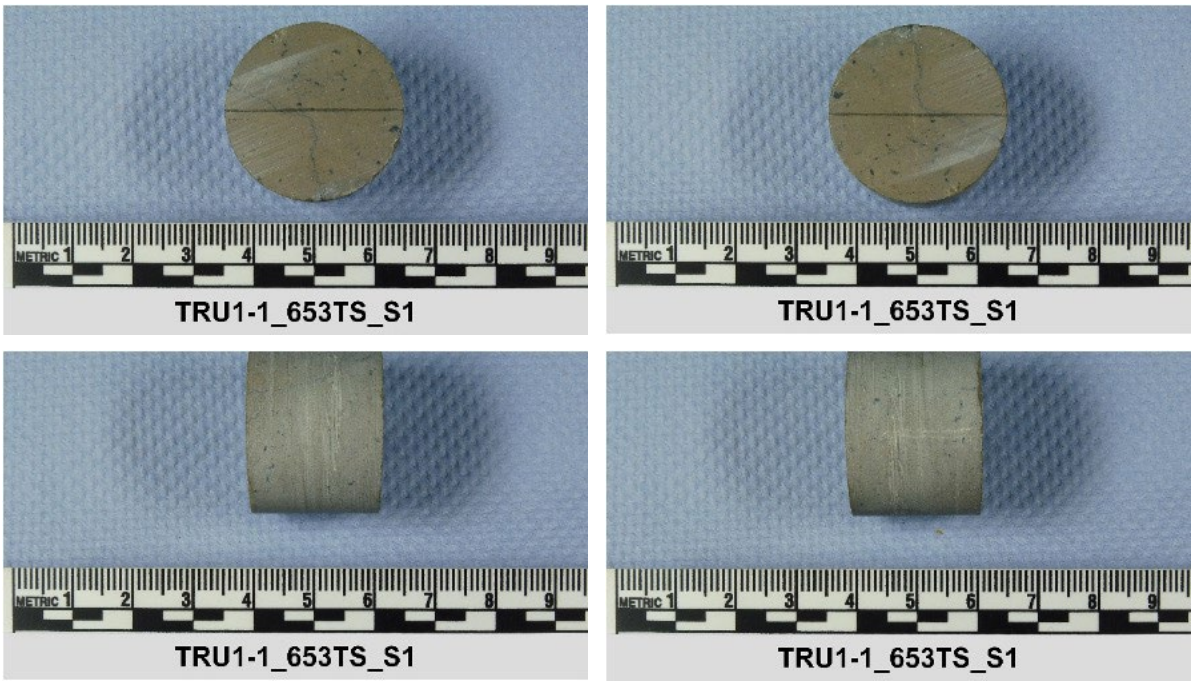

before testing **after testing**

653.74 m

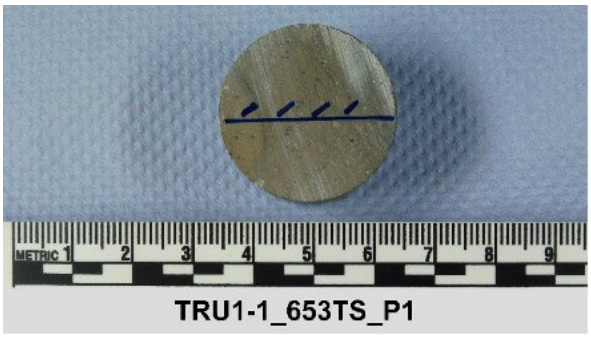

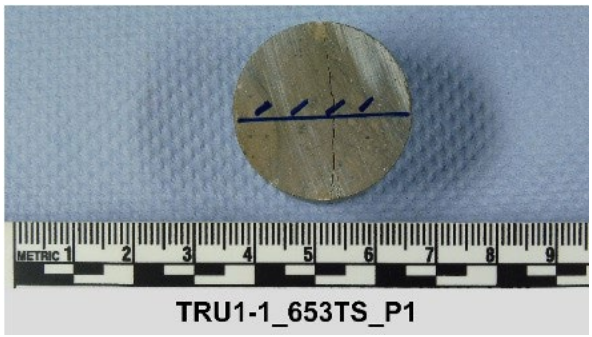

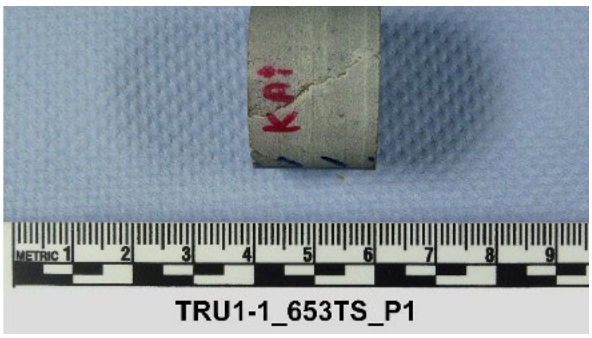

668.56 m

before testing **after testing**

668.61 m

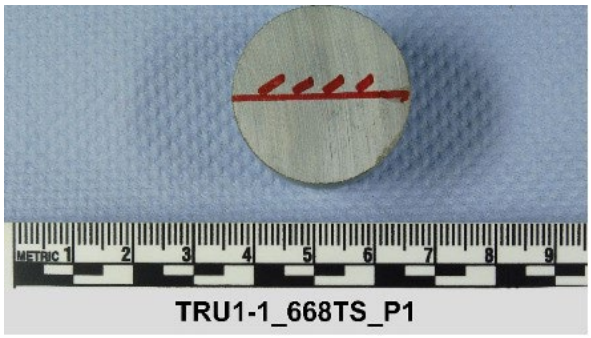

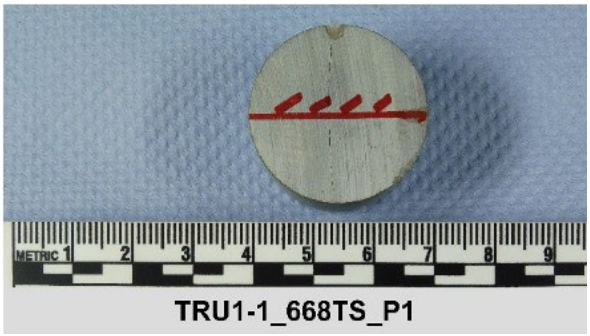

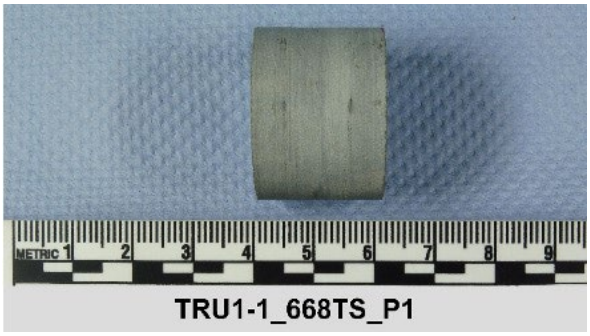

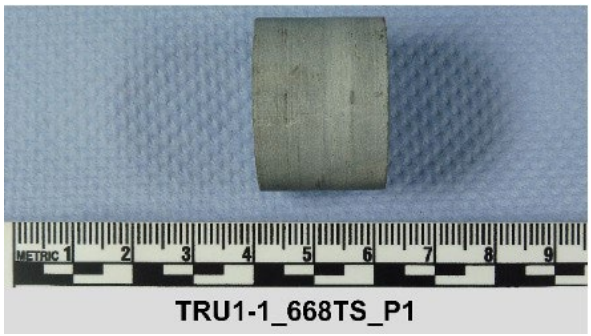

697.66 m

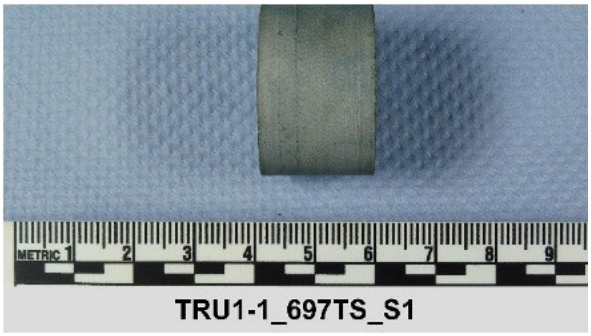

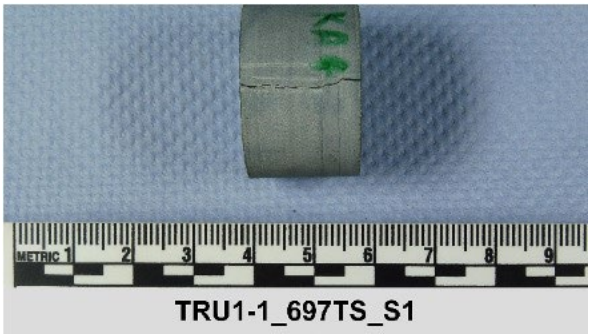

before testing **after testing**

697.72 m

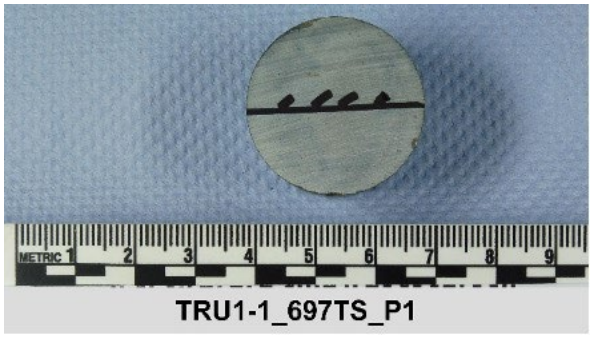

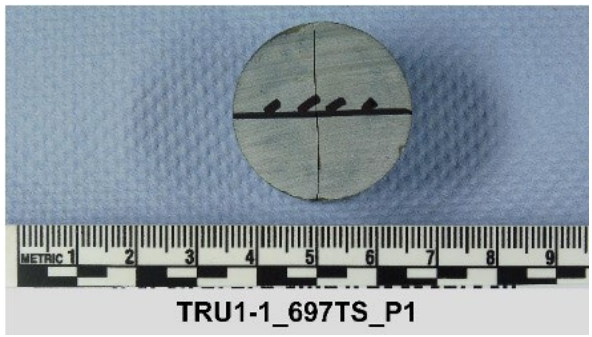

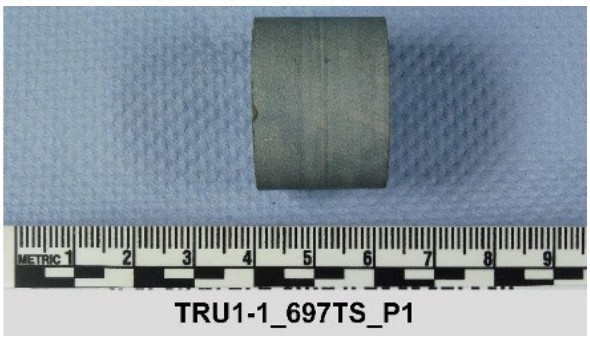

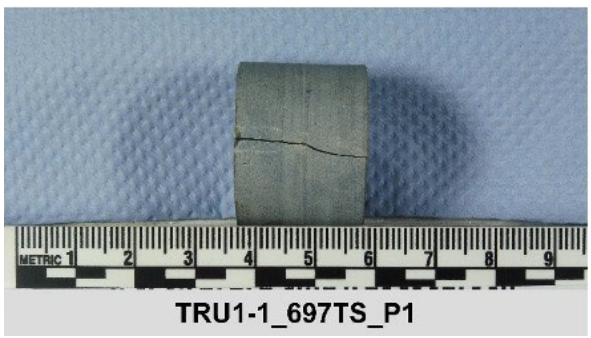

757.35 m

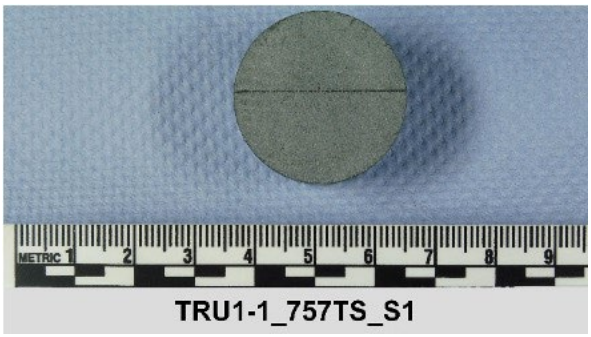

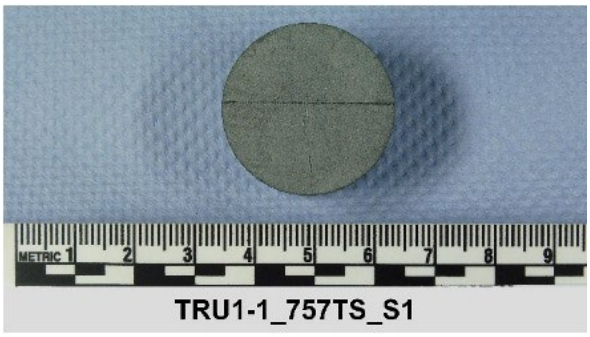

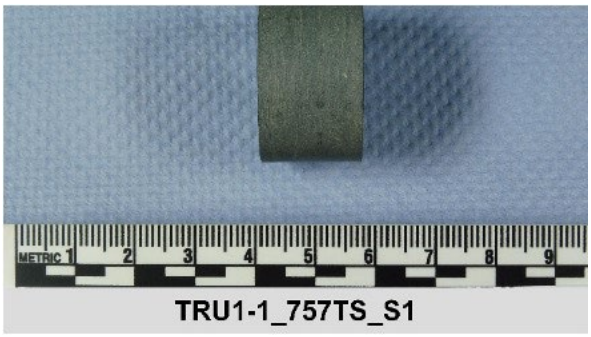

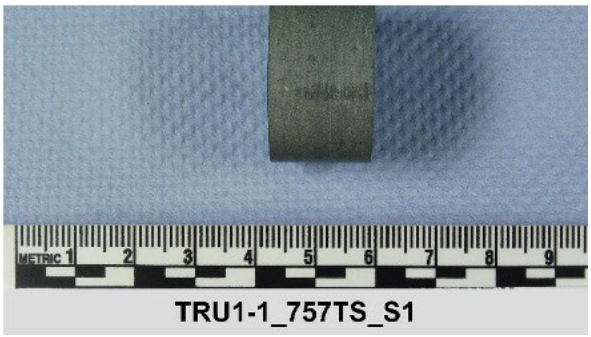

before testing **after testing**

757.39 m

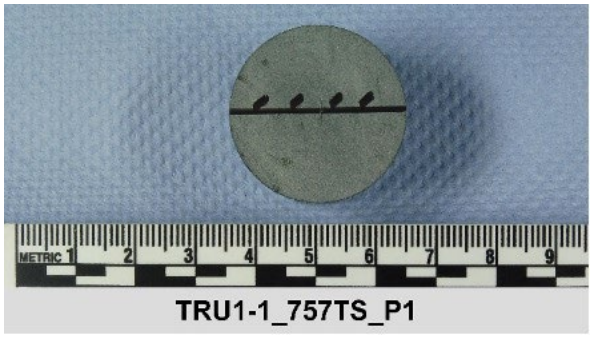

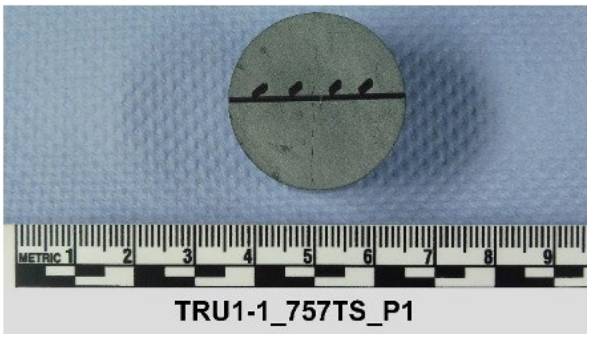

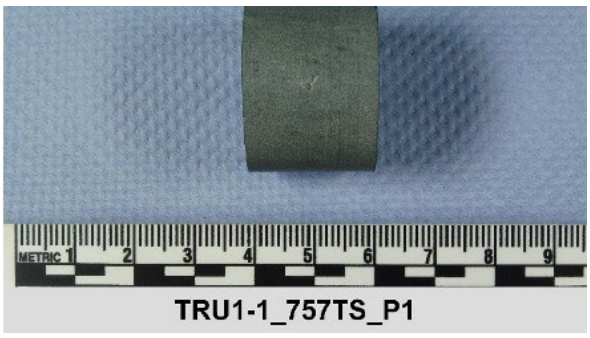

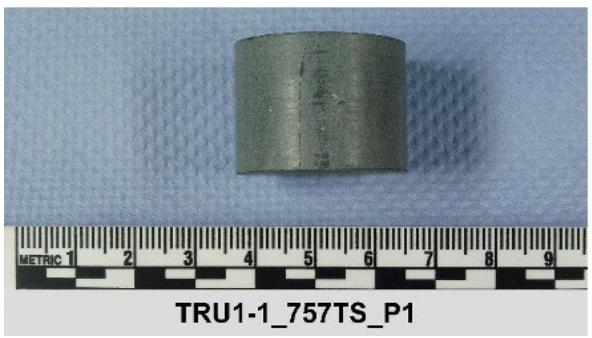

775.25 m

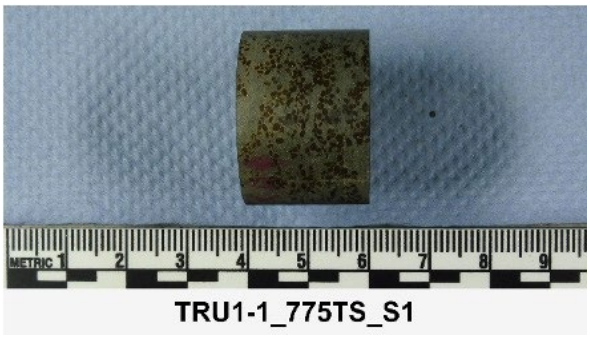

before testing **after testing**

775.31 m

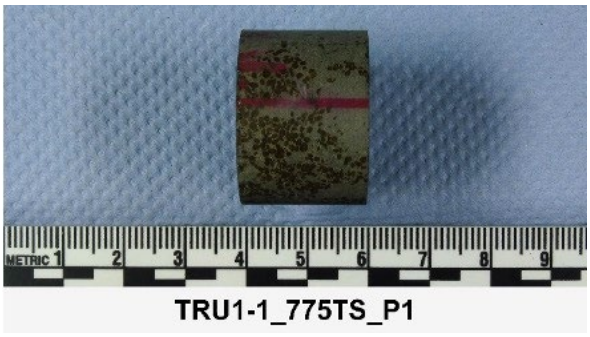

797.96 m

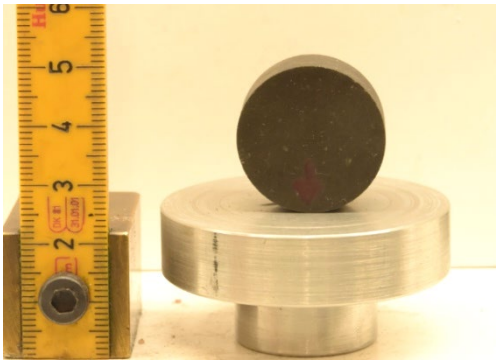

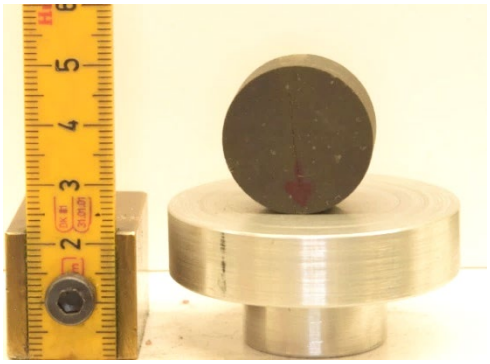

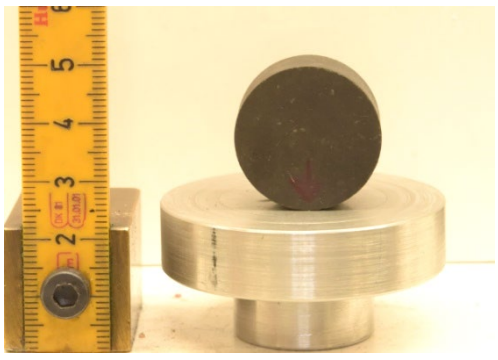

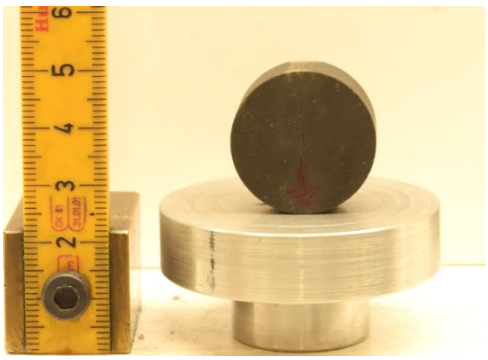

before testing

after testing

798.00 m

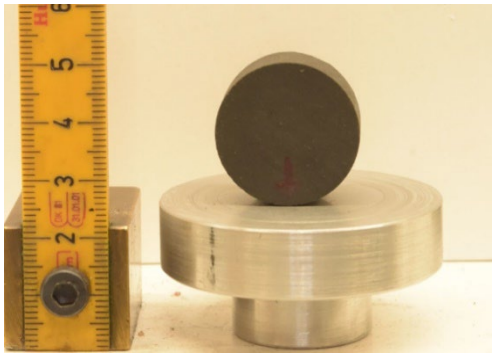

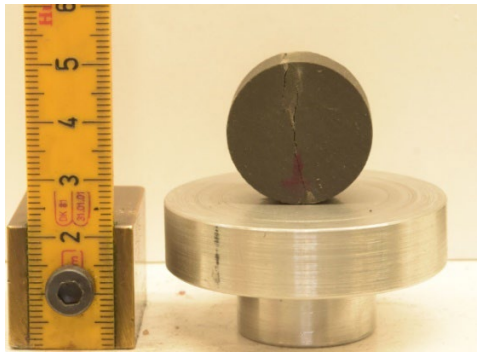

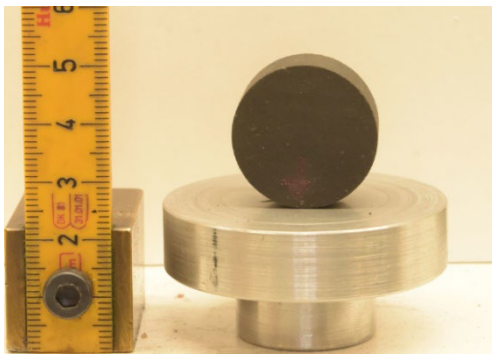

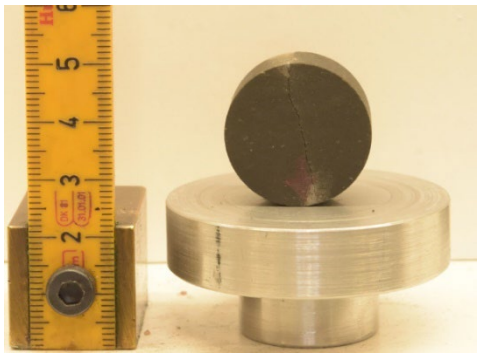

810.92 m

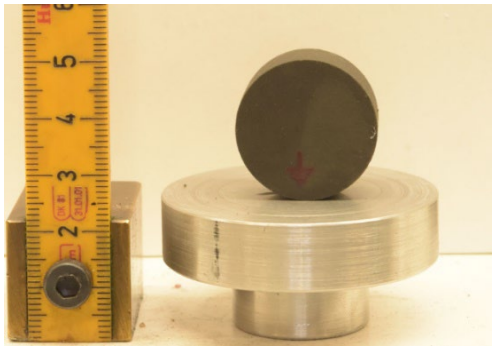

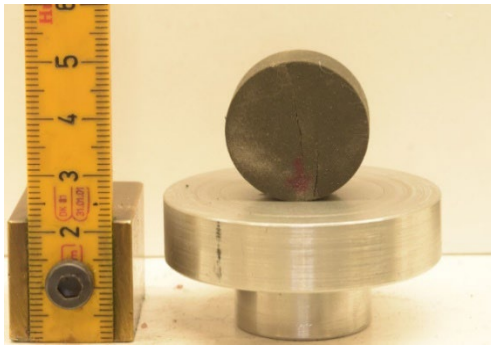

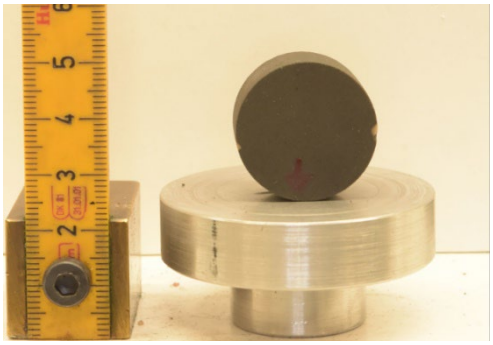

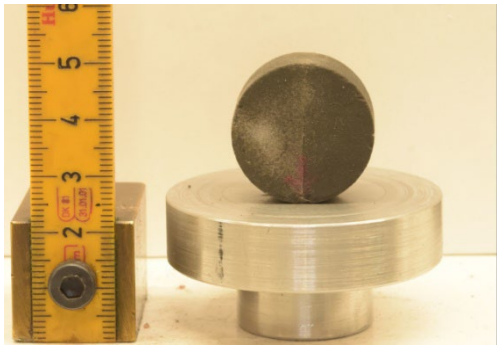

before testing **after testing**

810.95 m

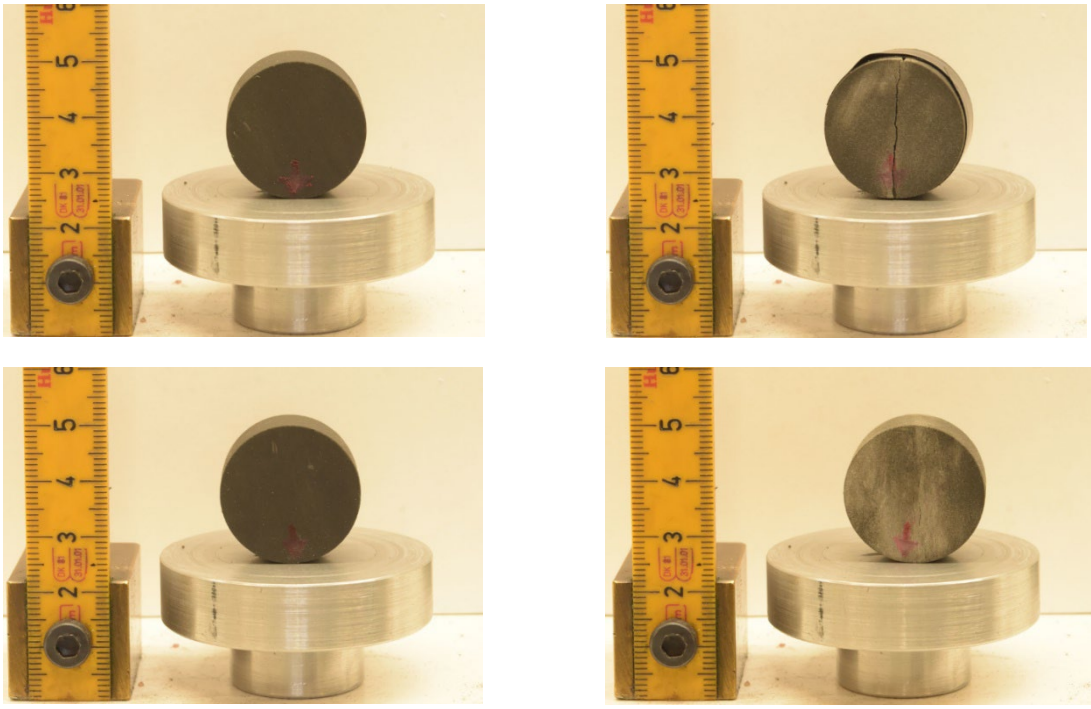

990.14 m

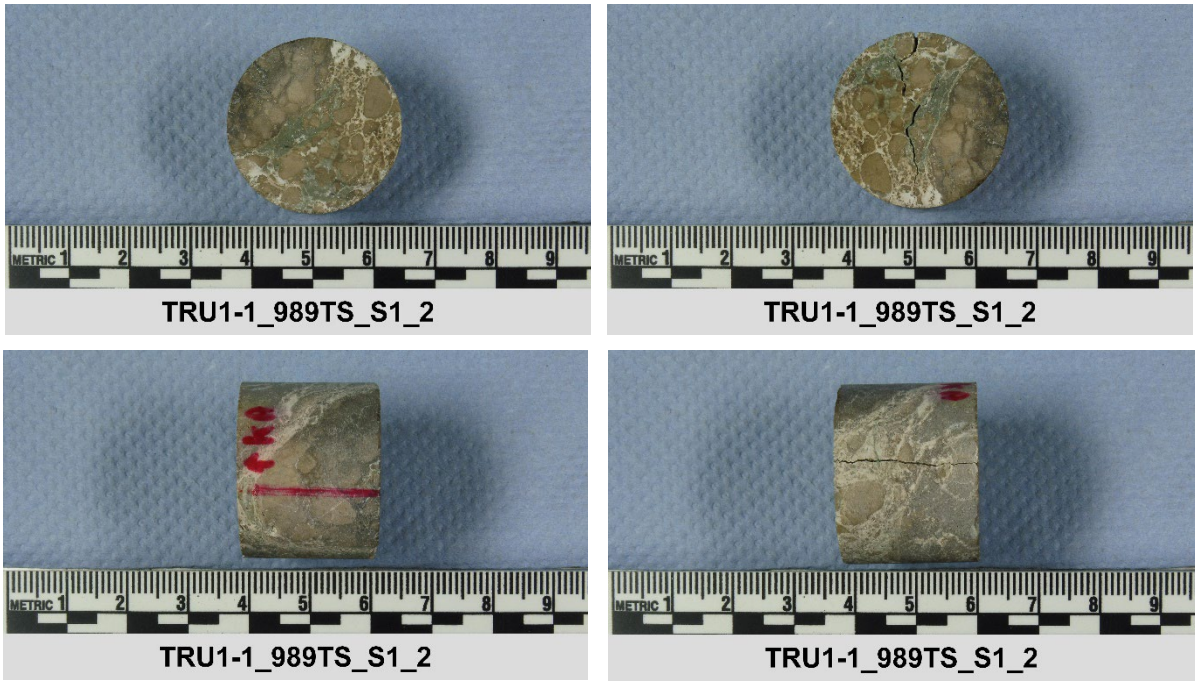

before testing **after testing**

990.07 m

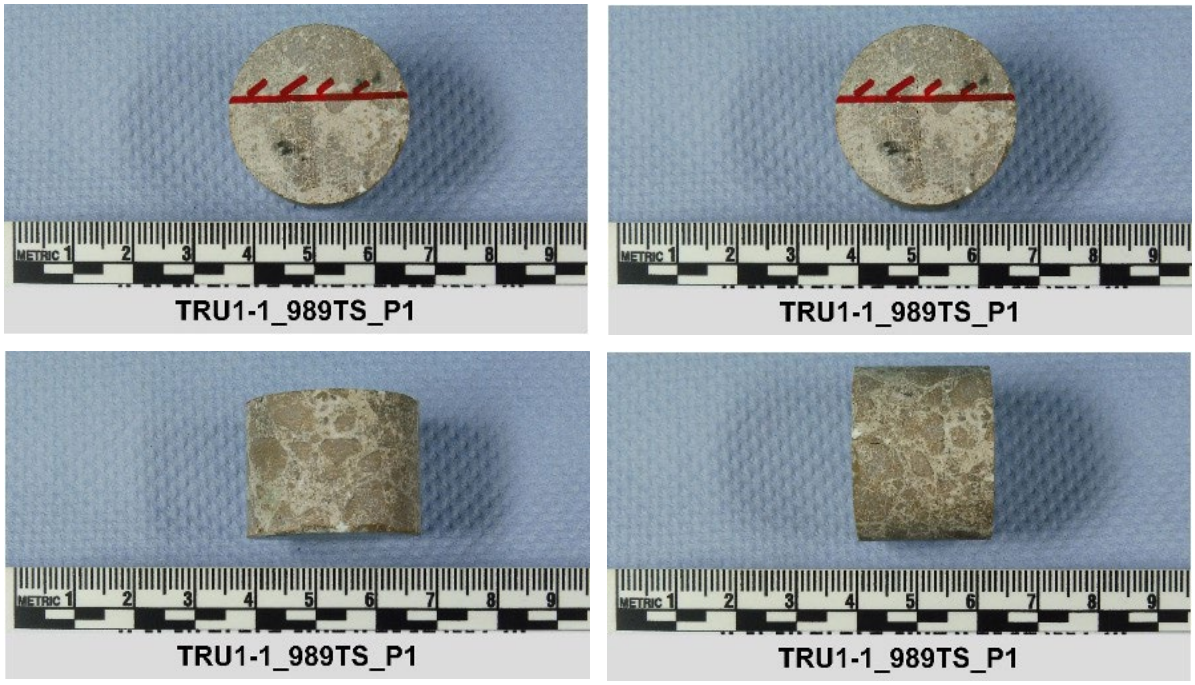

1022.33 m

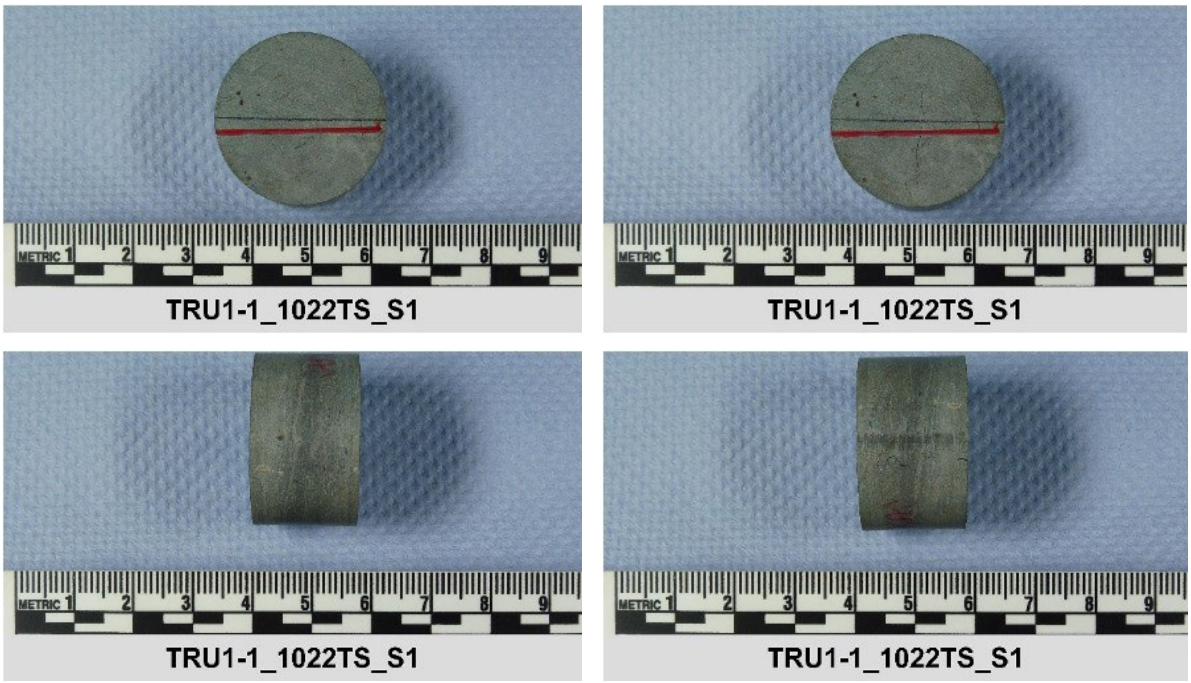

before testing **after testing**

1022.35 m

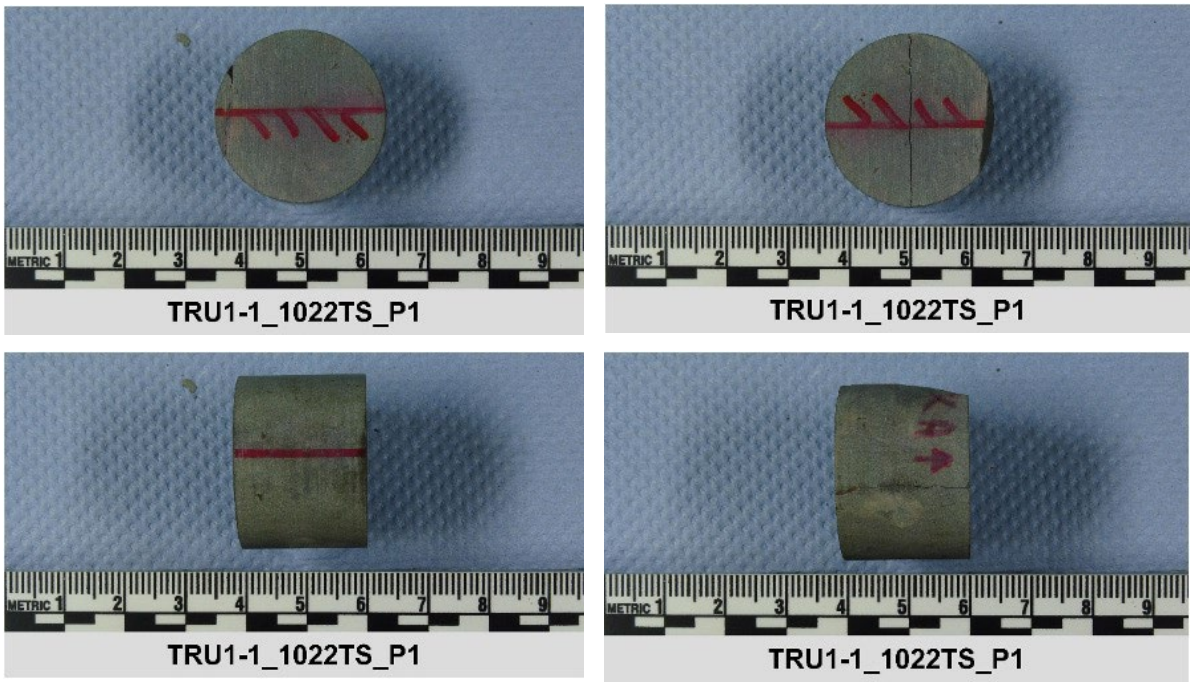

1050.07 m

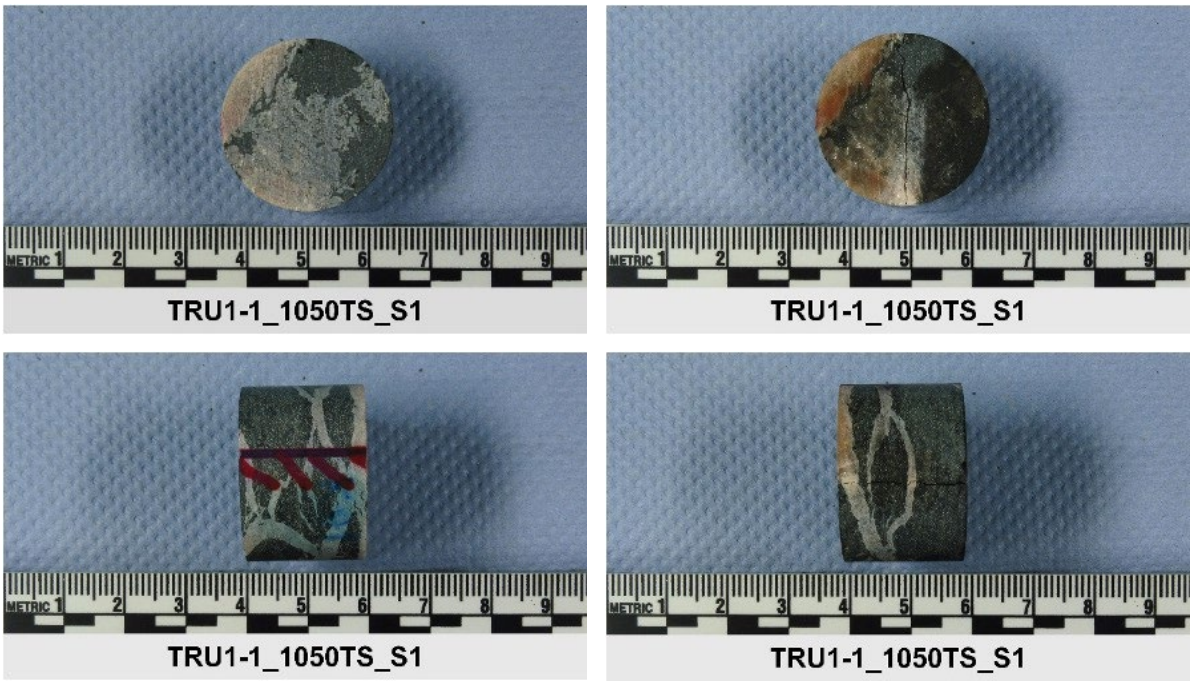

before testing **after testing**

1050.12 m

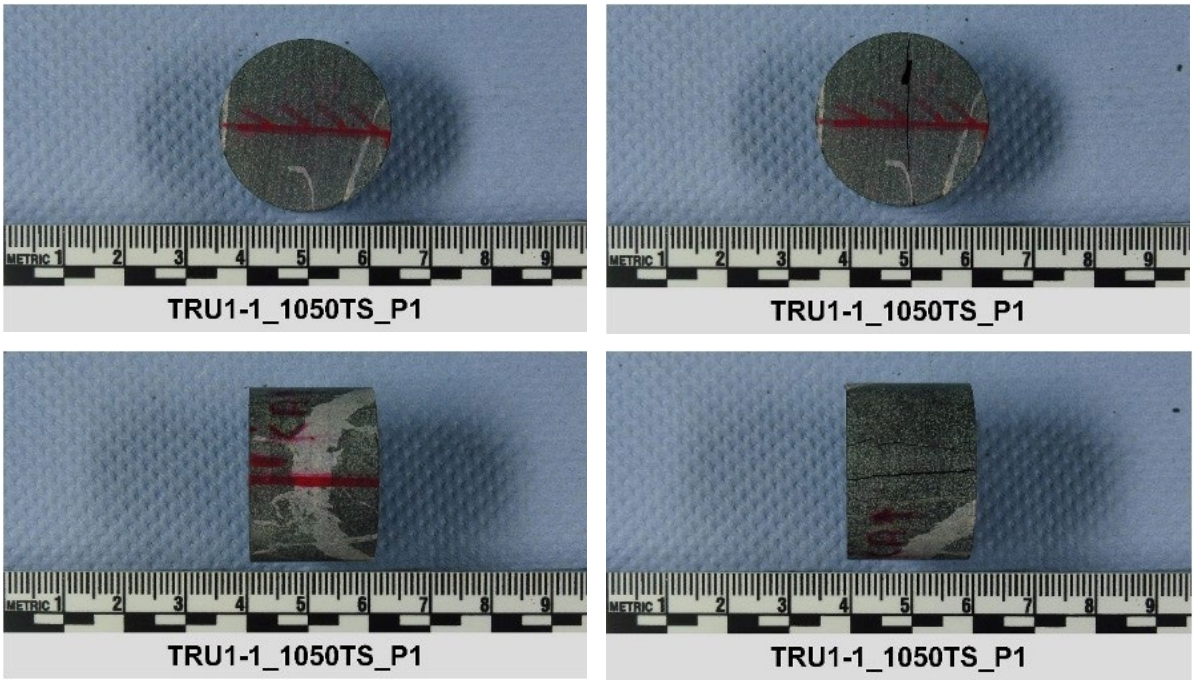

1053.73 m

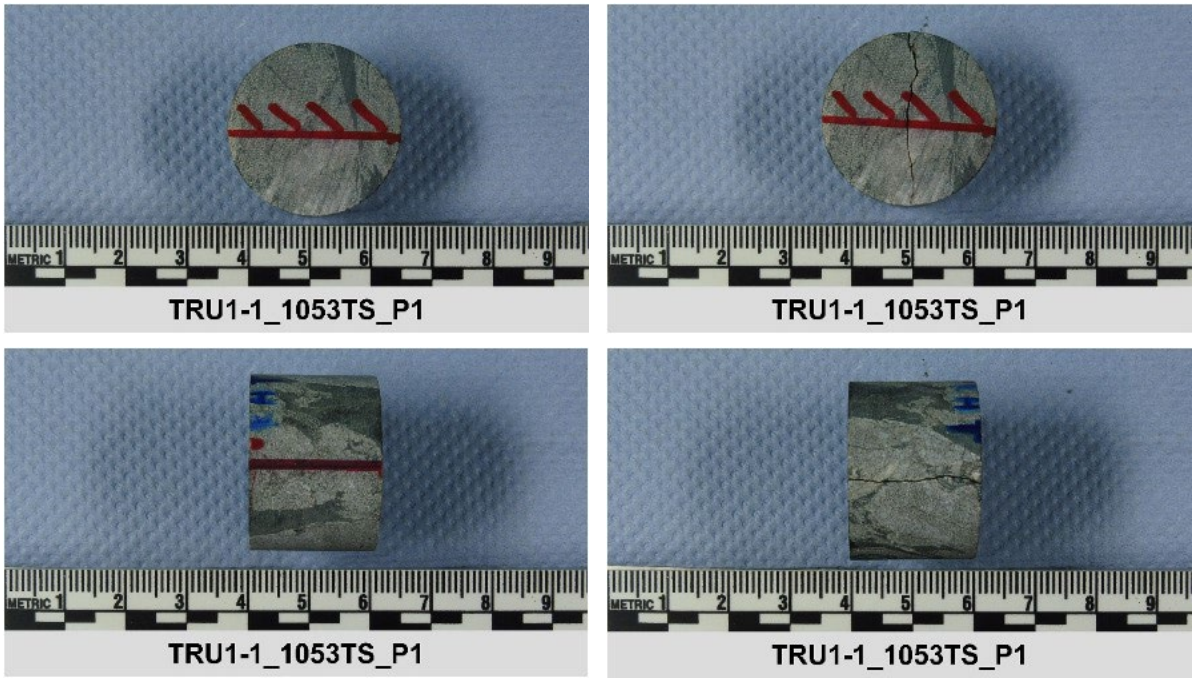

before testing **after testing**

1053.77 m

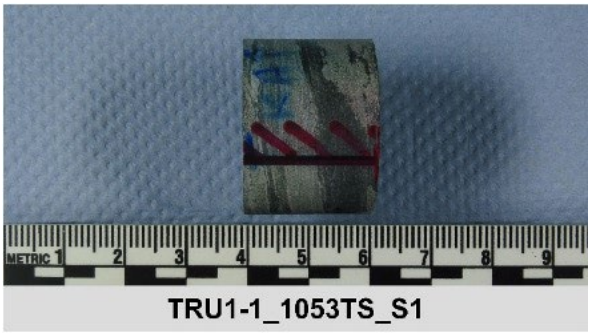

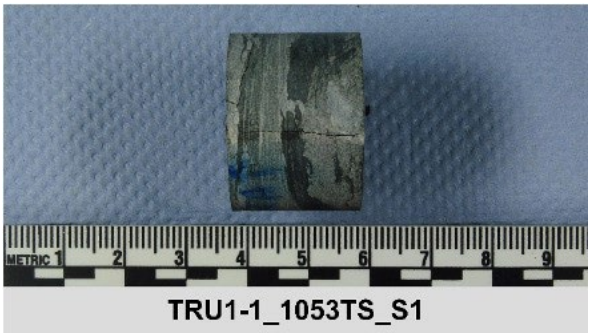

1074.70 m

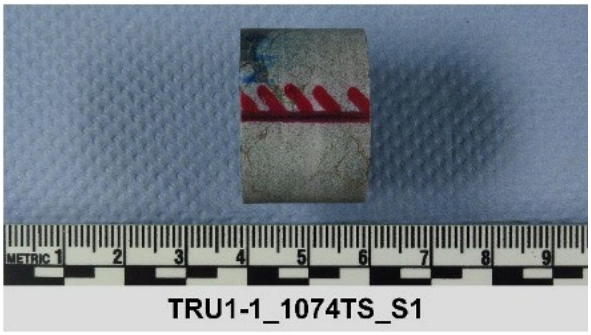

before testing **after testing**

1074.75 m

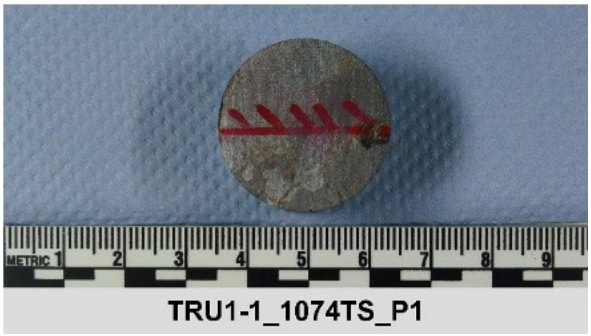

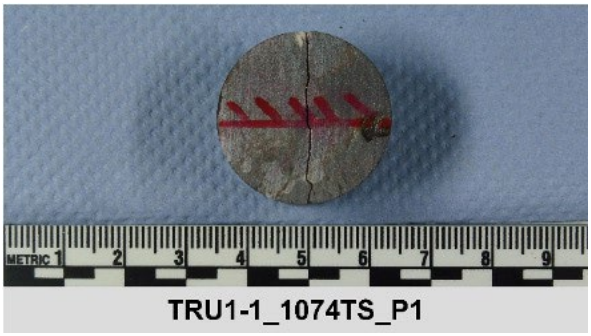

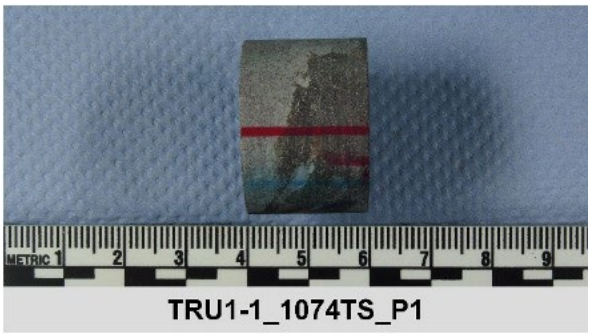

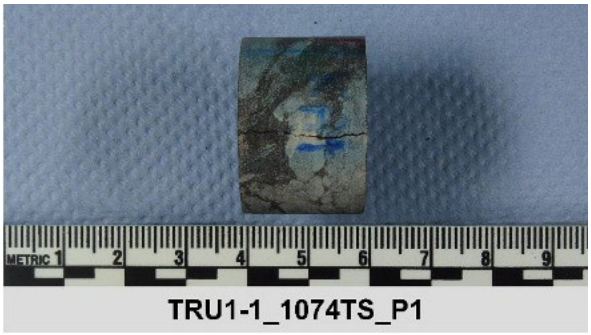

1093.27

before testing **after testing**

1093.31 m

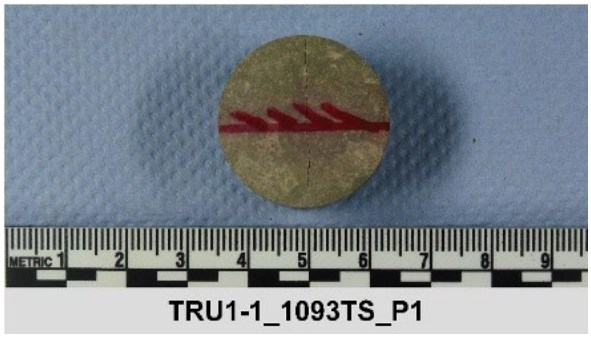

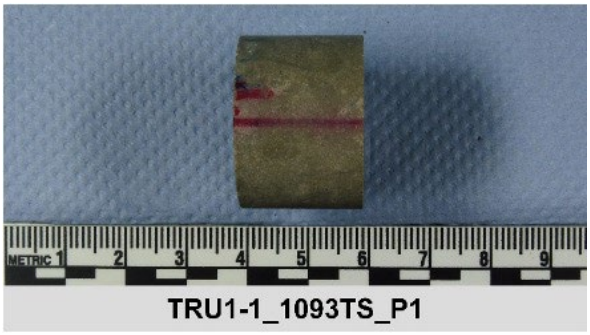

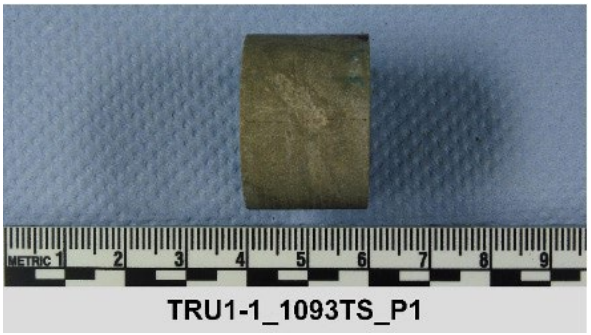

1096.99 m

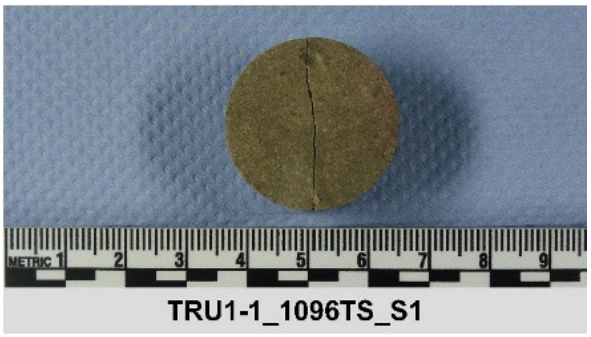

before testing **after testing**

1097.04 m

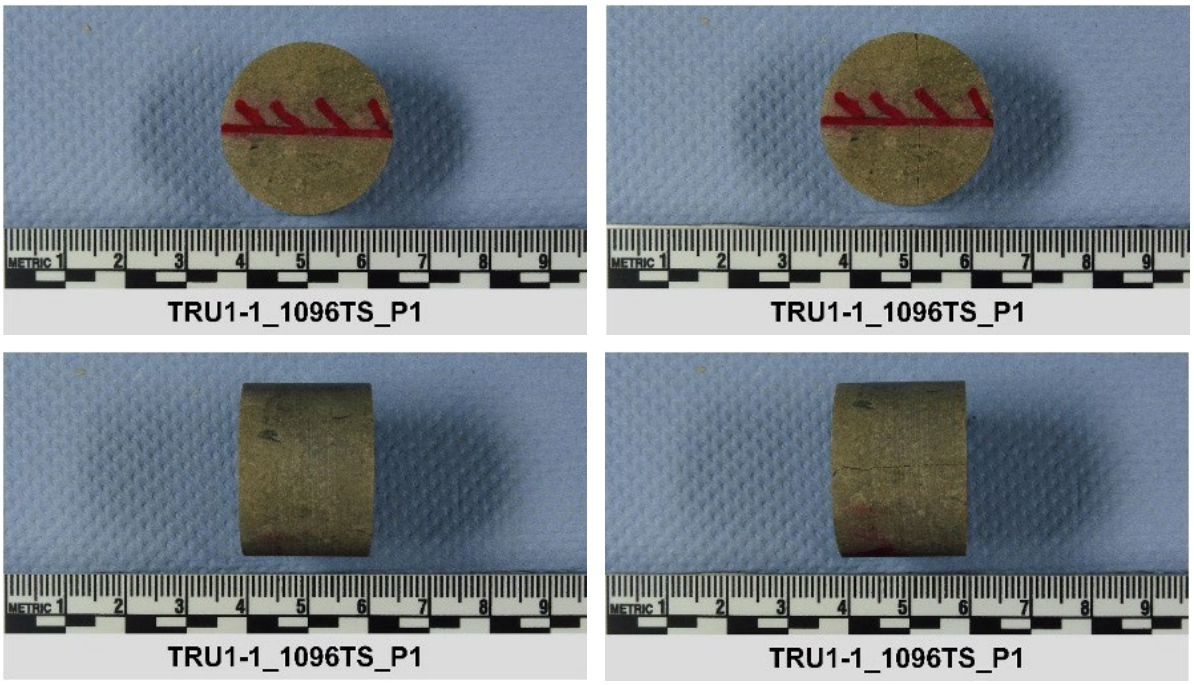

1107.87 m

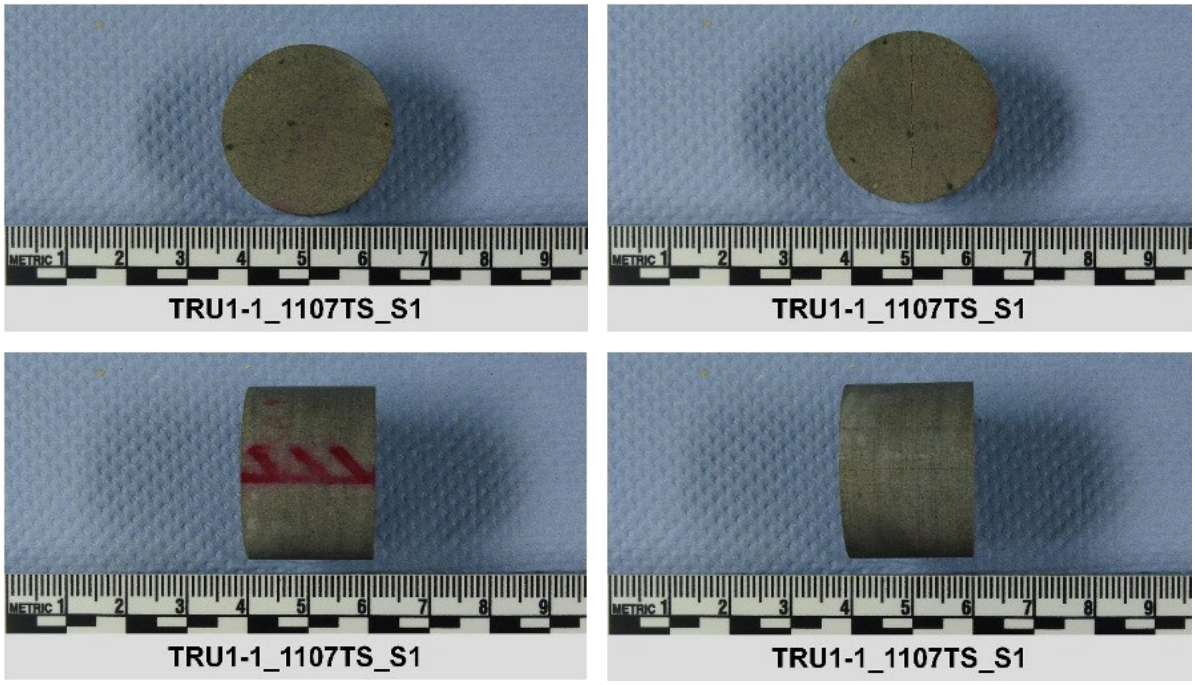

before testing **after testing**

1107.92 m

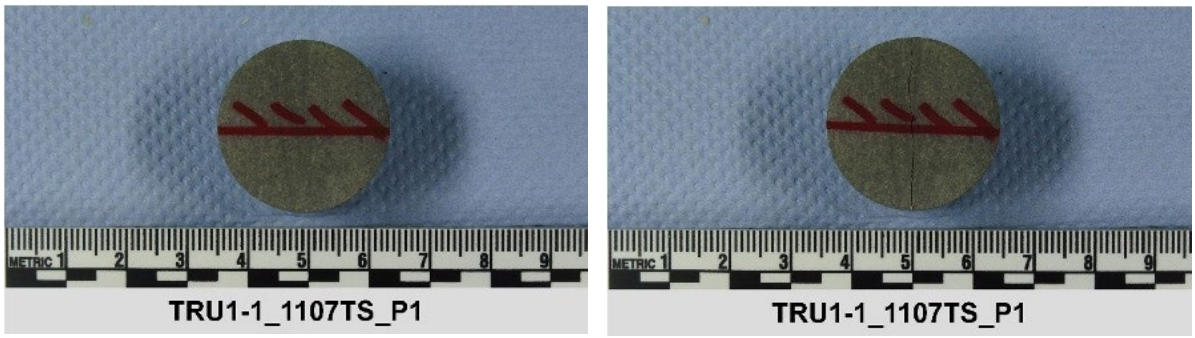

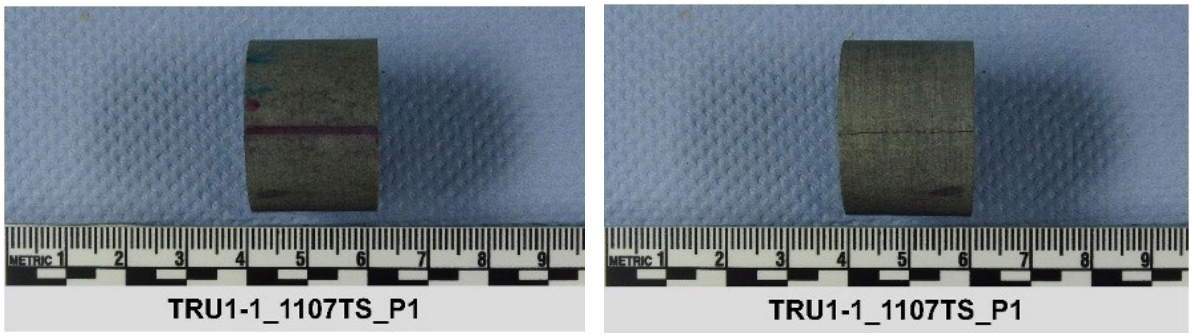

1122.58 m

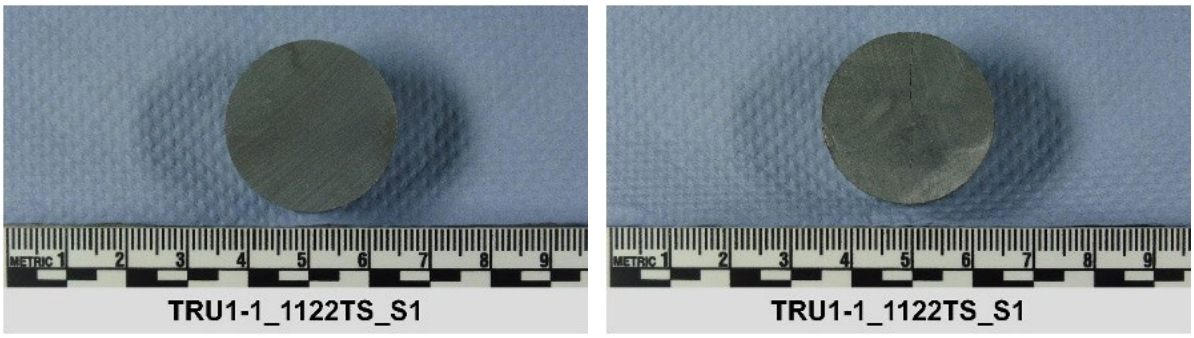

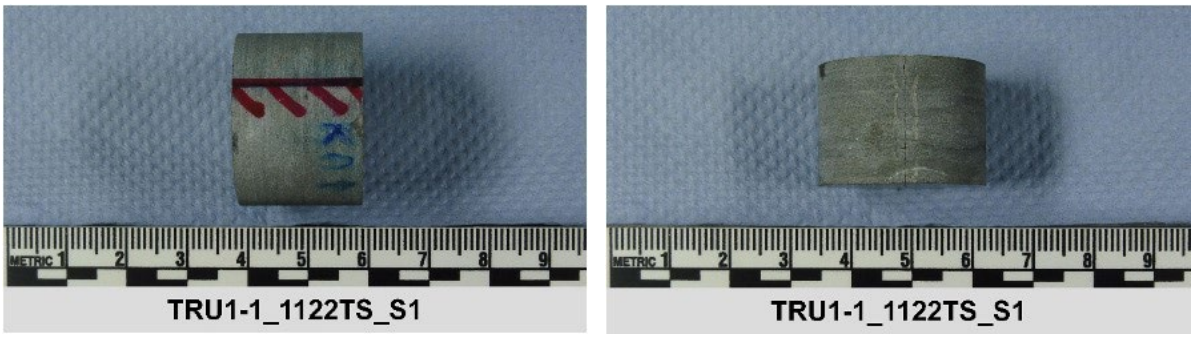

before testing **after testing**

1122.63 m

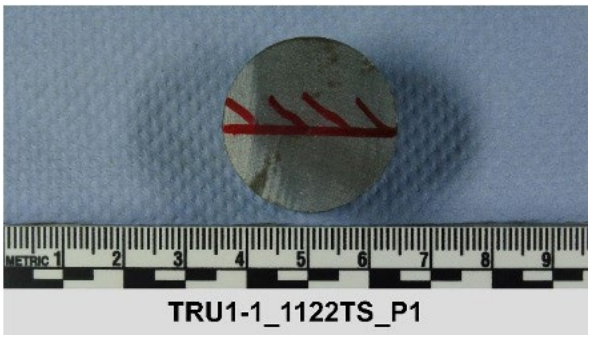

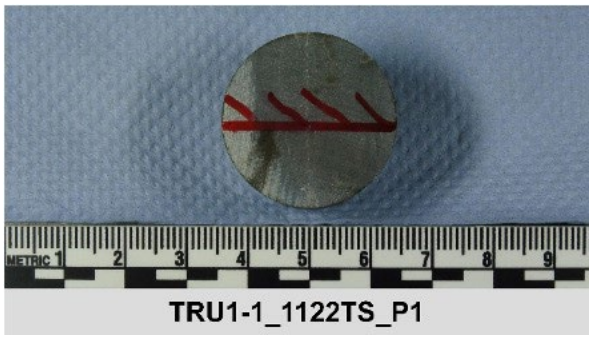

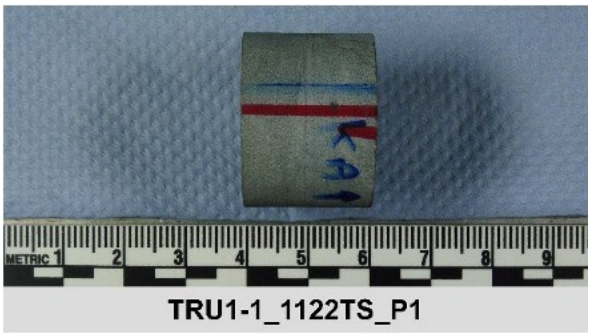

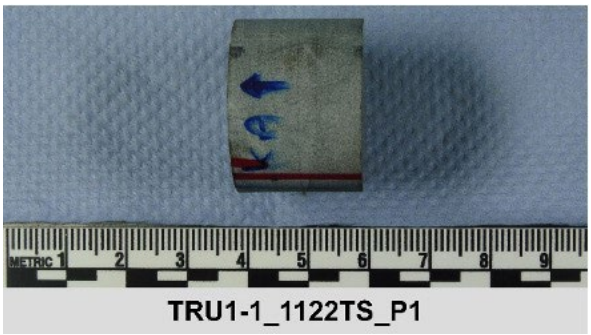

990.13 m

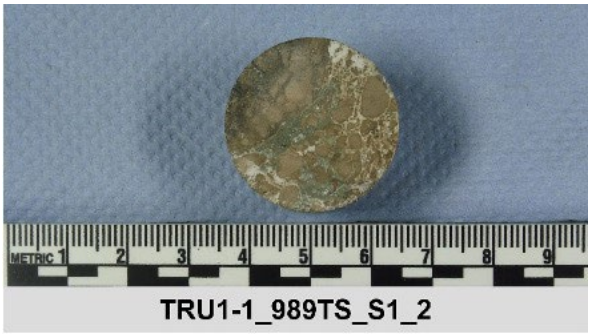

UCS (average depth of sample) **TRU1-1**

before testing **after testing**

515.14 m

515.13 m

515.21 m

535.84 m

before testing **after testing**

535.89 m

535.87 m (broke before testing)

554.87 m

554.93 m

before testing **after testing**

554.92 m

606.14 m

606.14 m

613.52 m

before testing **after testing**

613.51 m

632.77 m

632.77 m

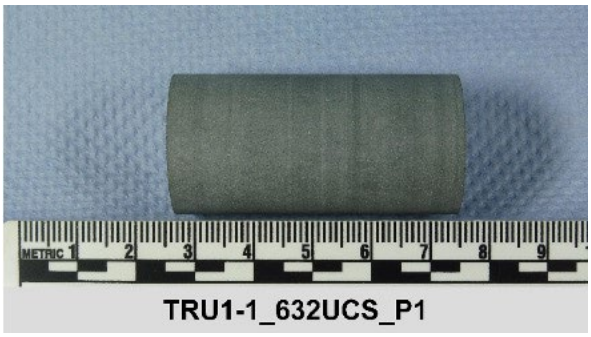

644.66 m

before testing **after testing**

644.64 m

644.73 m

644.71 m

653.87 m

before testing **after testing**

653.86 m

668.69 m

668.68 m

697.59 m

before testing **after testing**

697.59 m

775.38 m

775.38 m

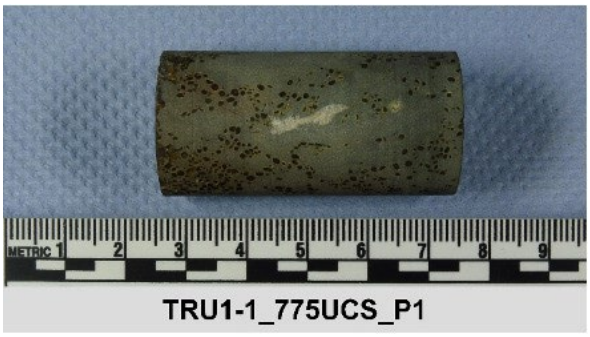

before testing **after testing**

798.08 m

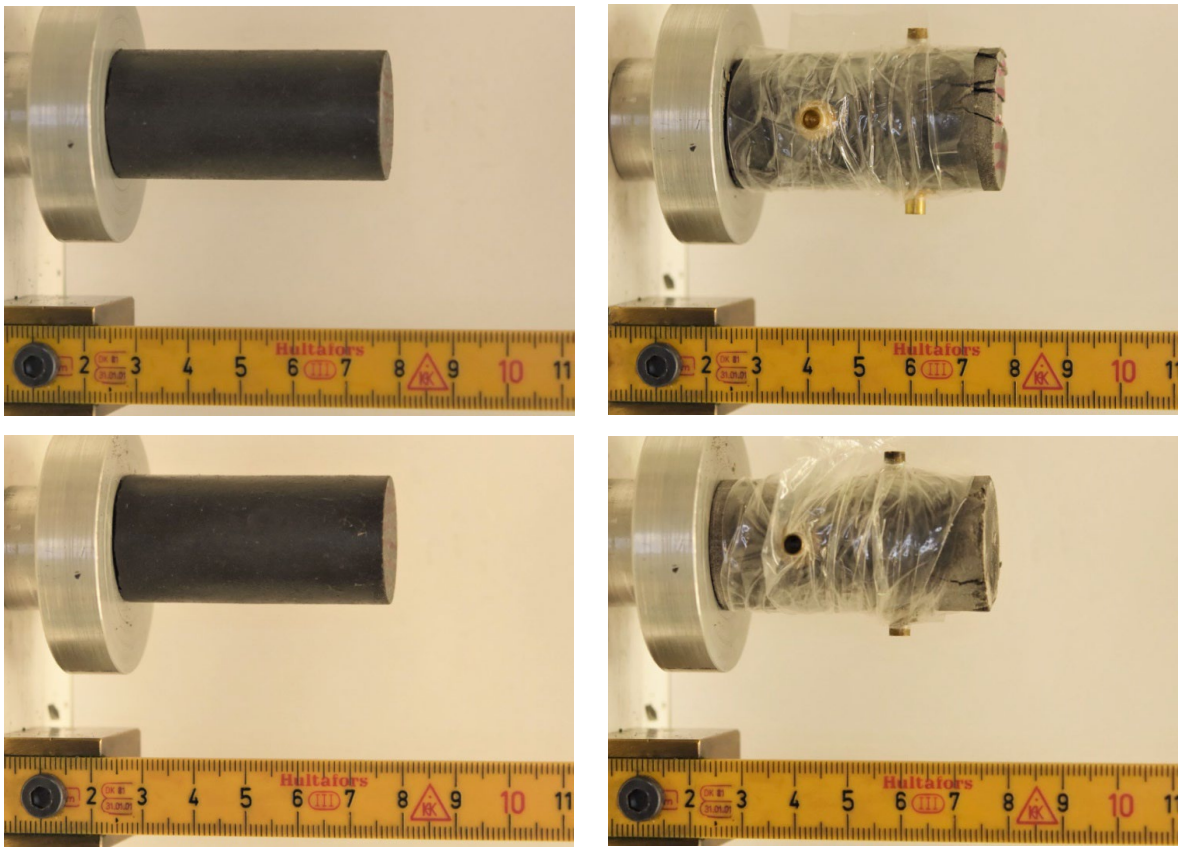

798.22 m

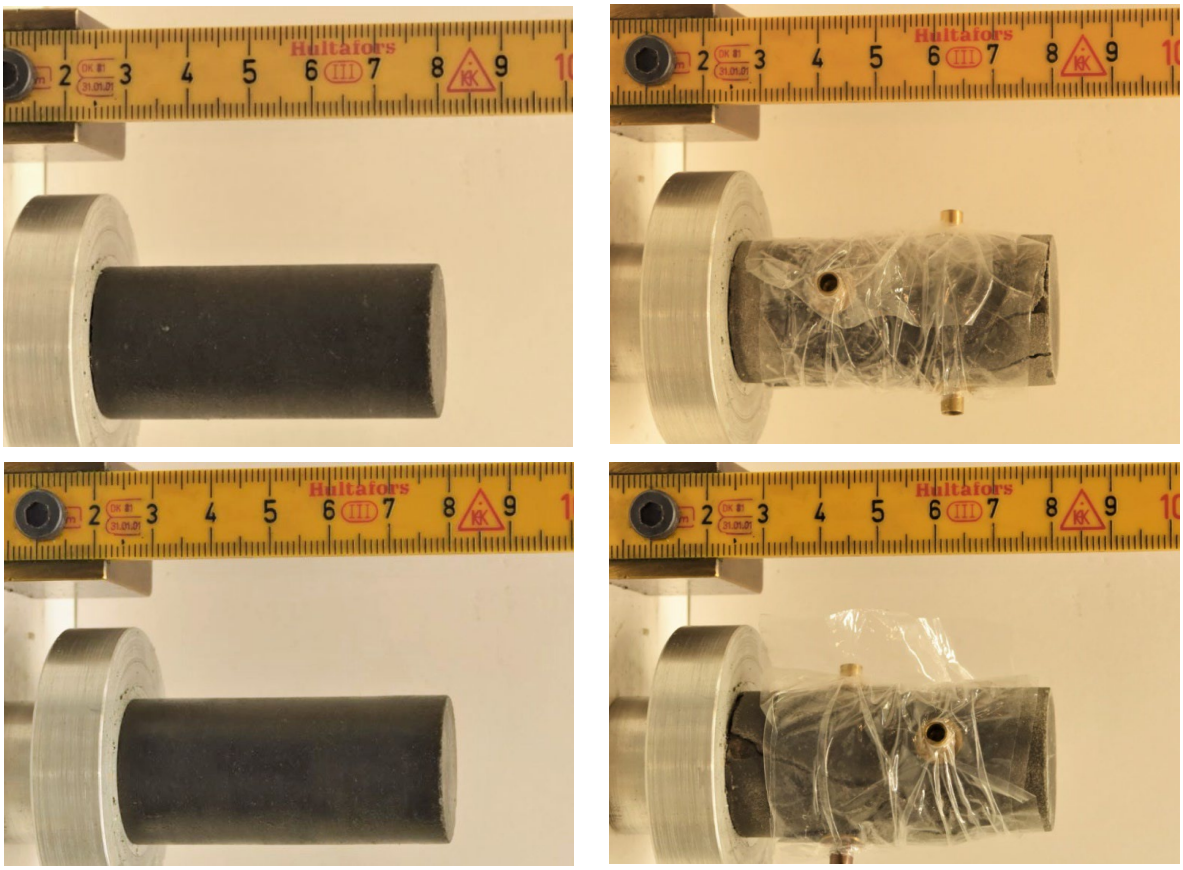

before testing **after testing**

811.01 m

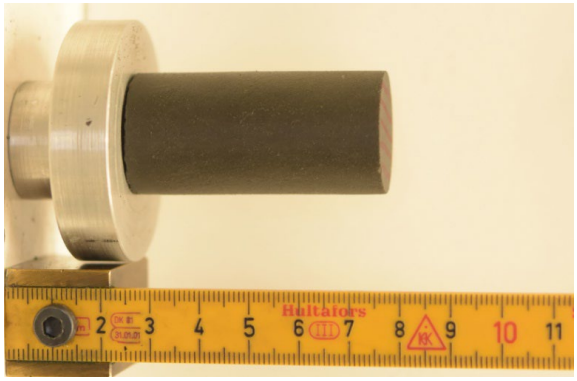

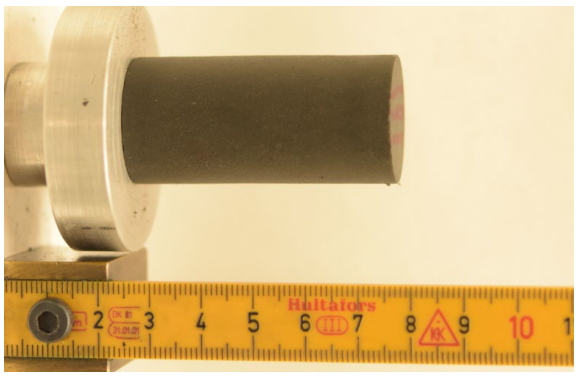
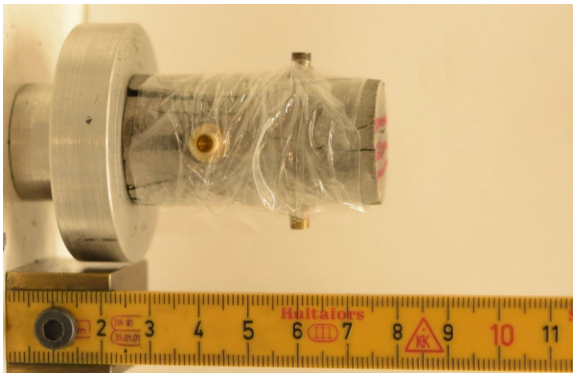

811.06 m

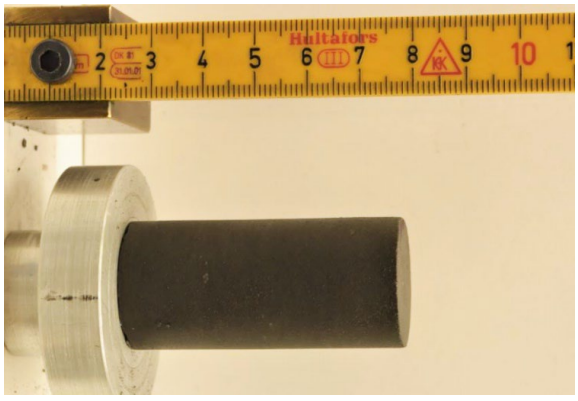
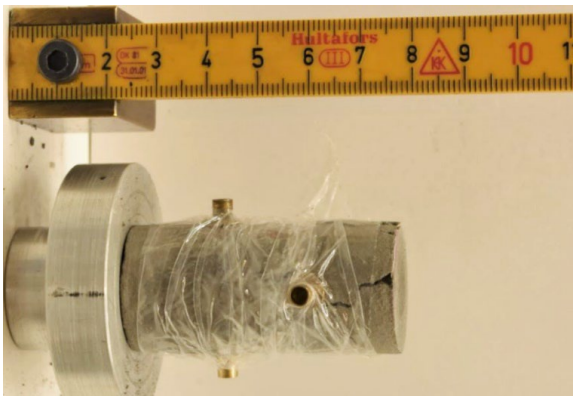
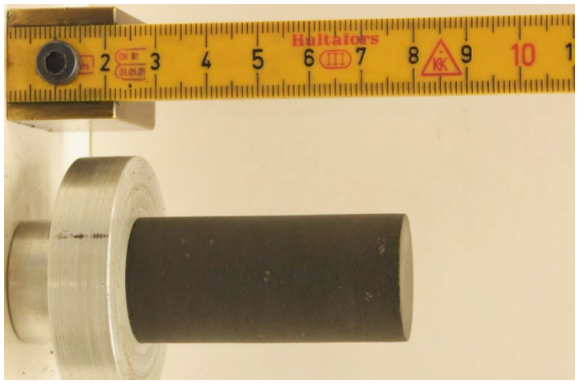
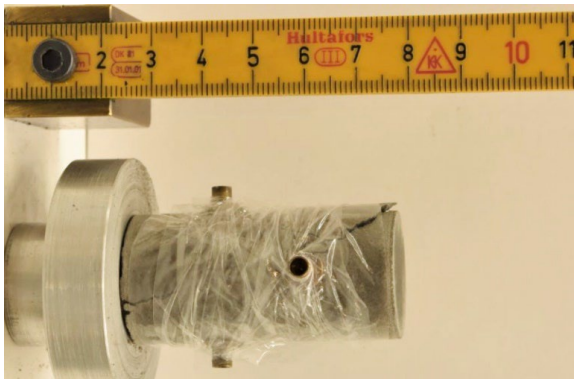

before testing **after testing**

986.99 m

989.99 m

1022.42 m

1050.20 m

before testing **after testing**

1053.50 m

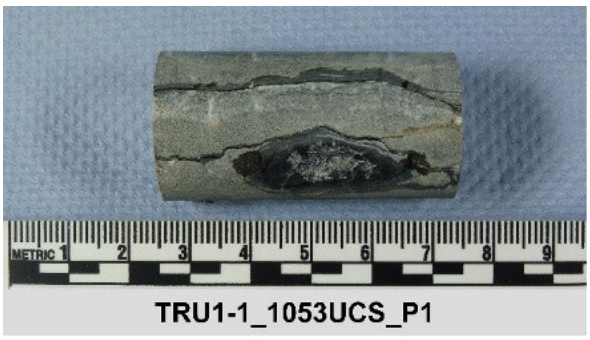

1053.68 m

1074.65 m

1074.65 m

before testing **after testing**

1074.84 m

1093.37 m

1097.11 m

1097.11 m

before testing **after testing**

1108.24 m

1108.24 m

1122.82 m

1122.82 m

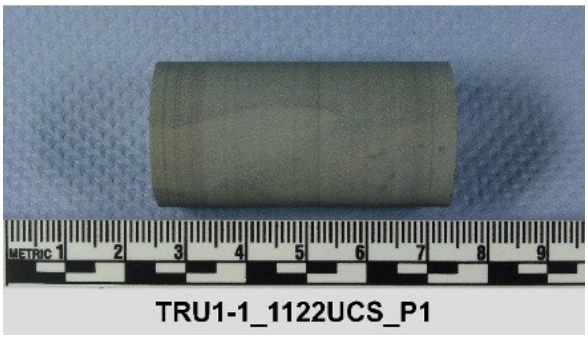

TRX (depth of sample top)

before testing

536.11 m

606.23 m

632.87 m

668.25 m

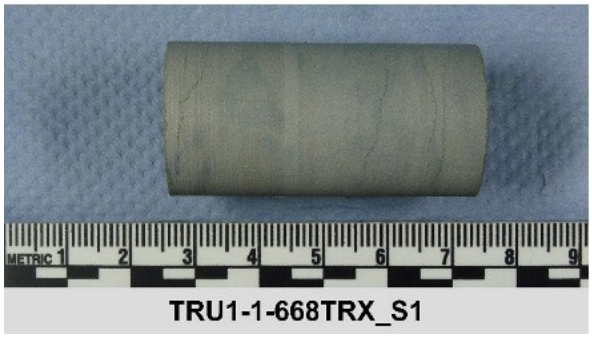

TRU1-1

after testing

before testing **after testing**

697.79 m

775.49 m

775.49 m

990.16 m

before testing **after testing**

1022.60 m

1053.67 m

1093.58 m

Appendix B XCT cross-sections with selection of test specimens

The computed tomography scans of the tested cores are here reported, and the sections used in the testing programme are indicated.

TRU1-1 796.64/45 GM

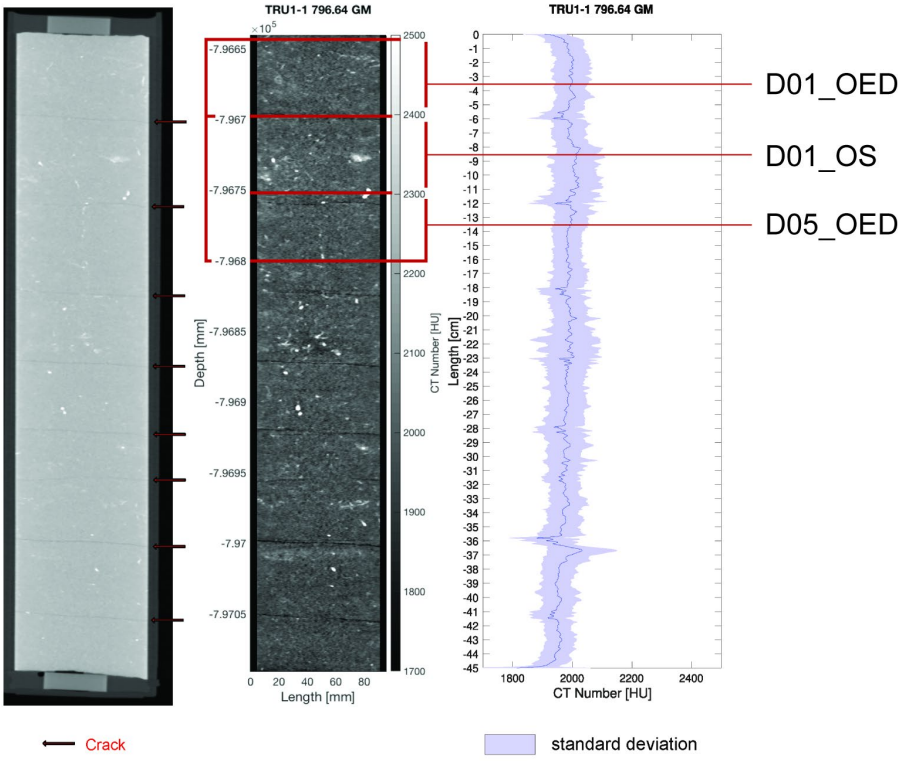

TRU1-1 797.91/45 GM

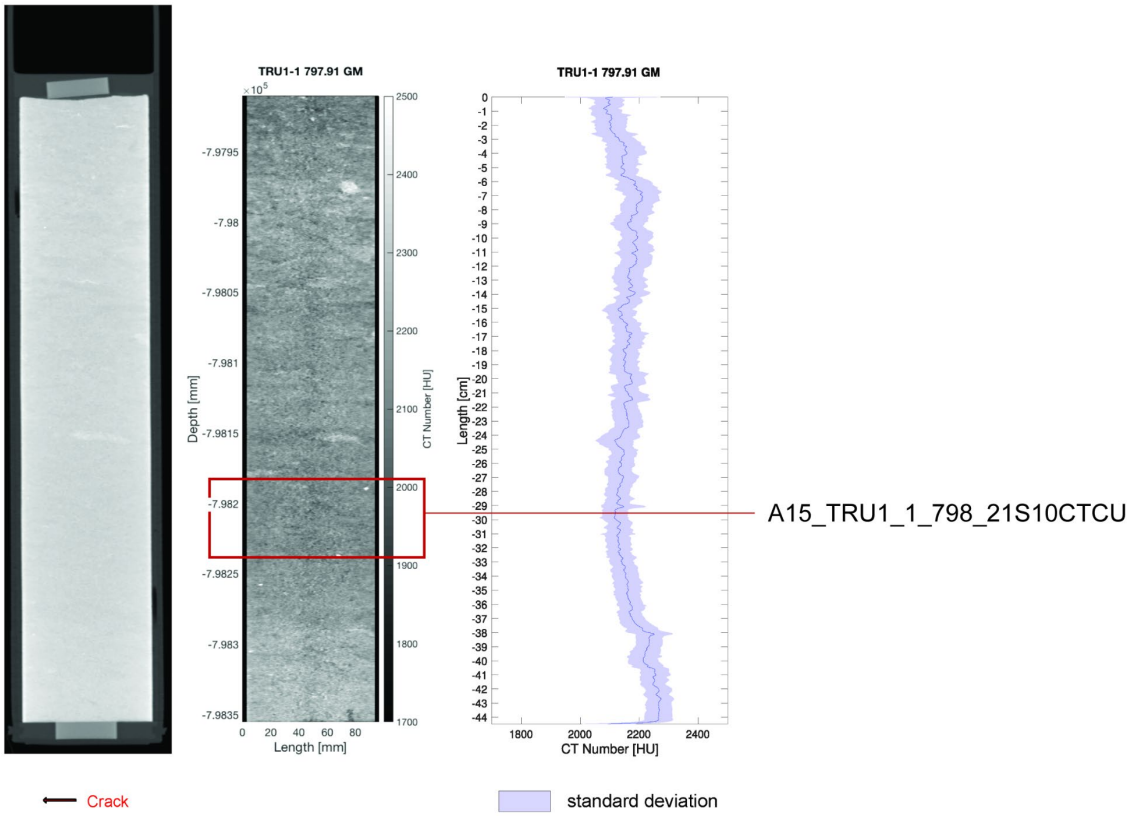

TRU1-1 810.87/50 GM

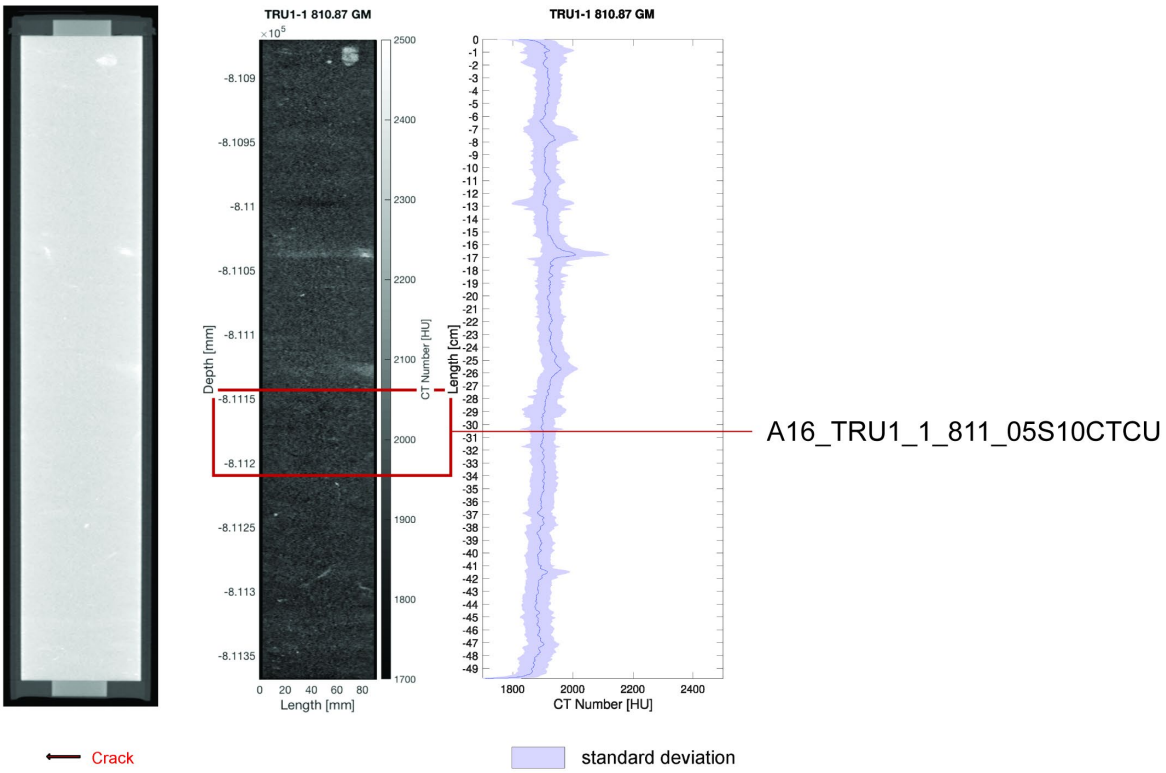

TRU1-1 836.32/50 GM

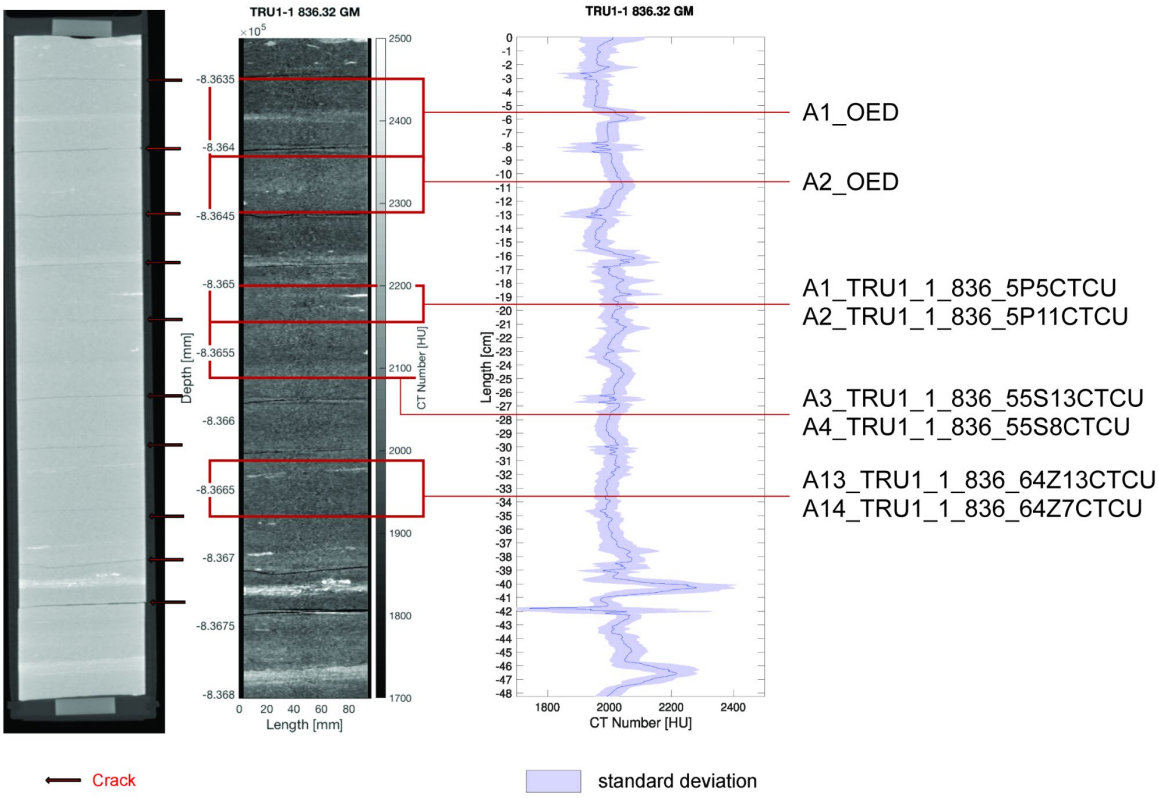

TRU1-1 851.70/50 GM

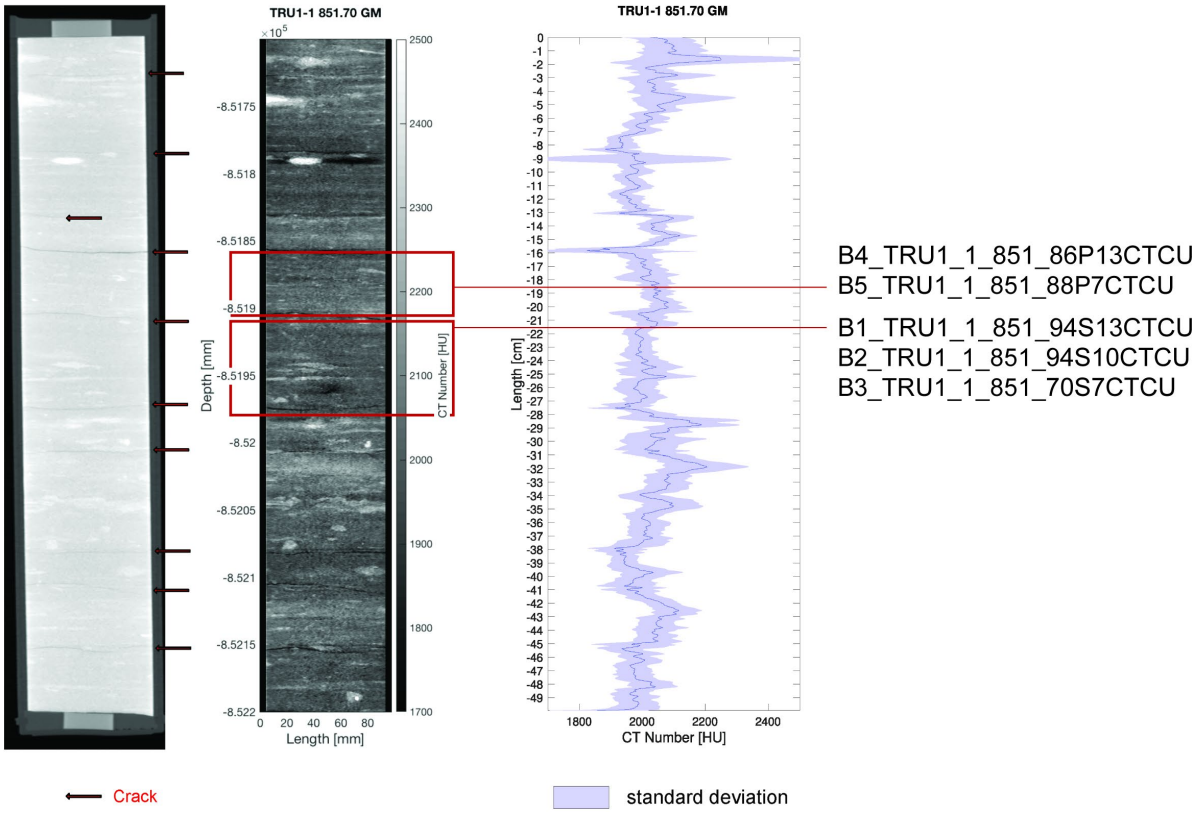

TRU1-1 875.48/39 GM

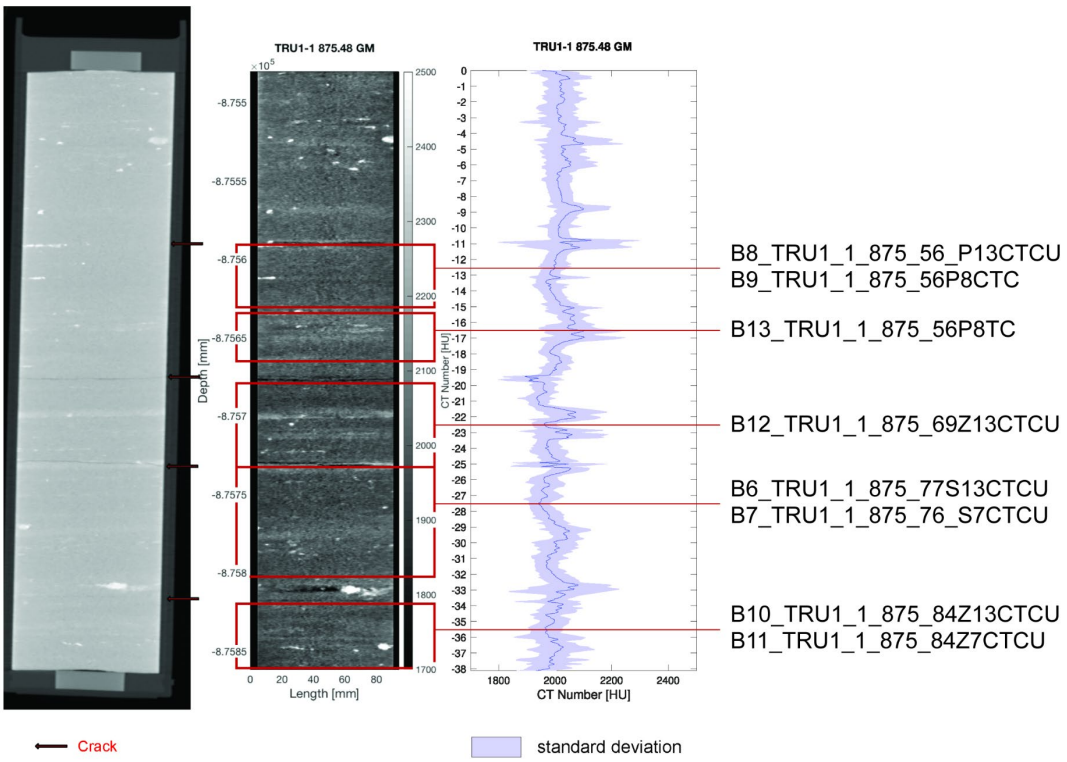

TRU1-1 878.11/43 GM

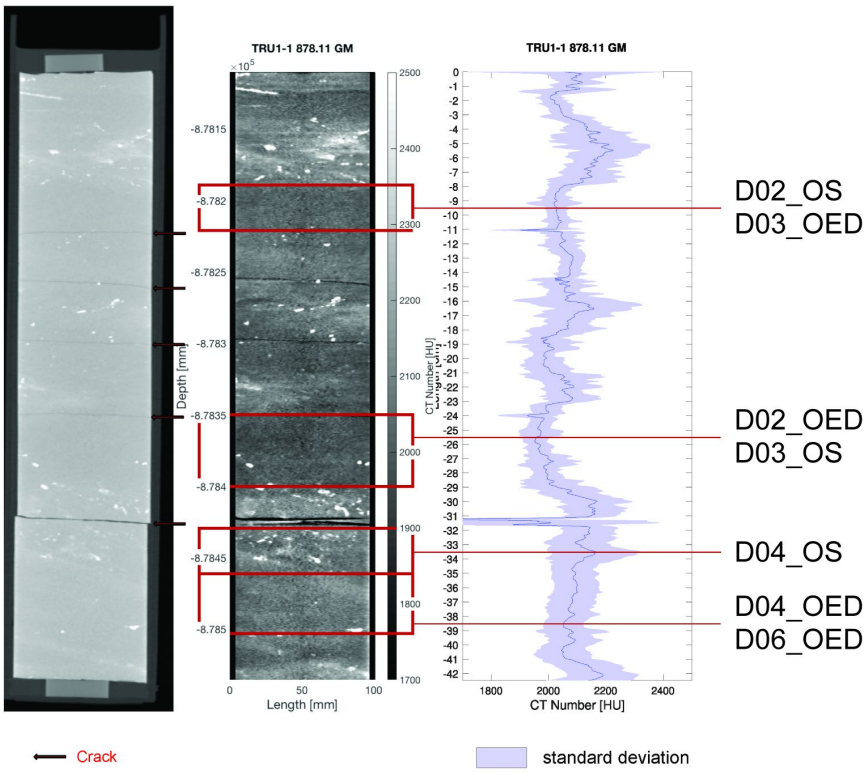

TRU1-1 903.19/45 GM

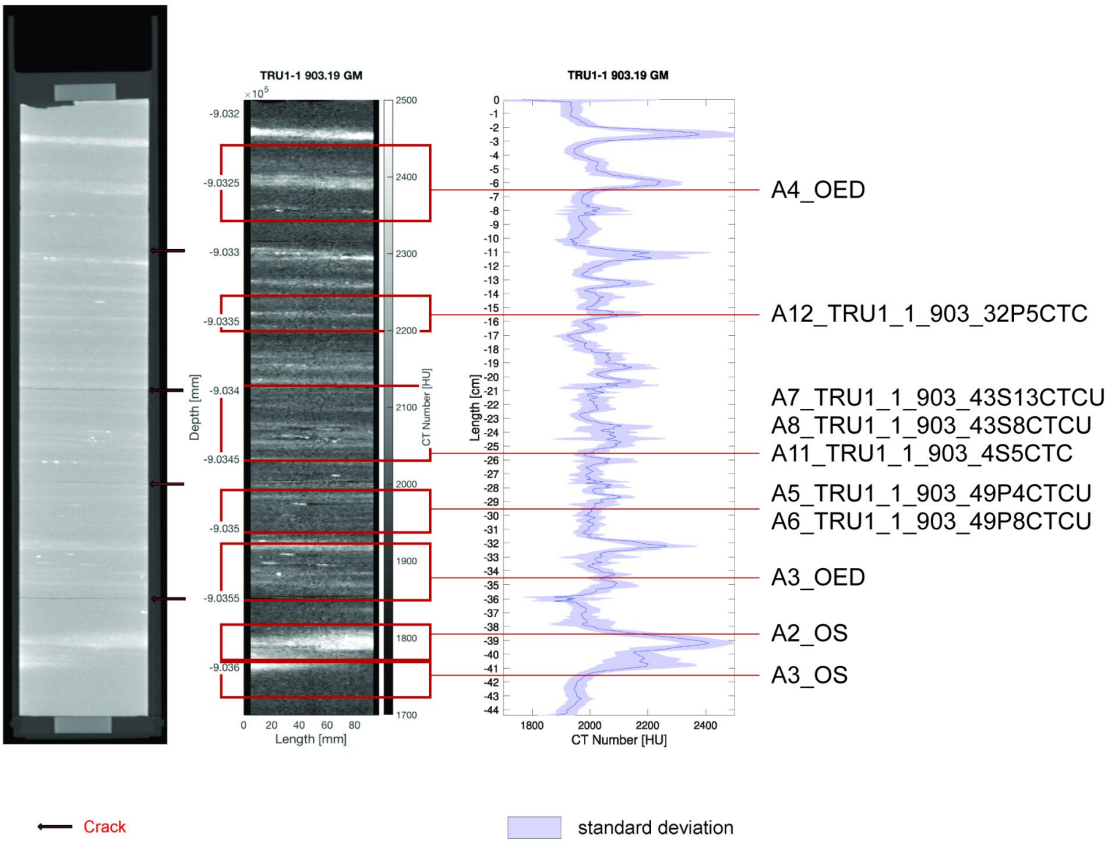

TRU1-1 924.96/45 GM

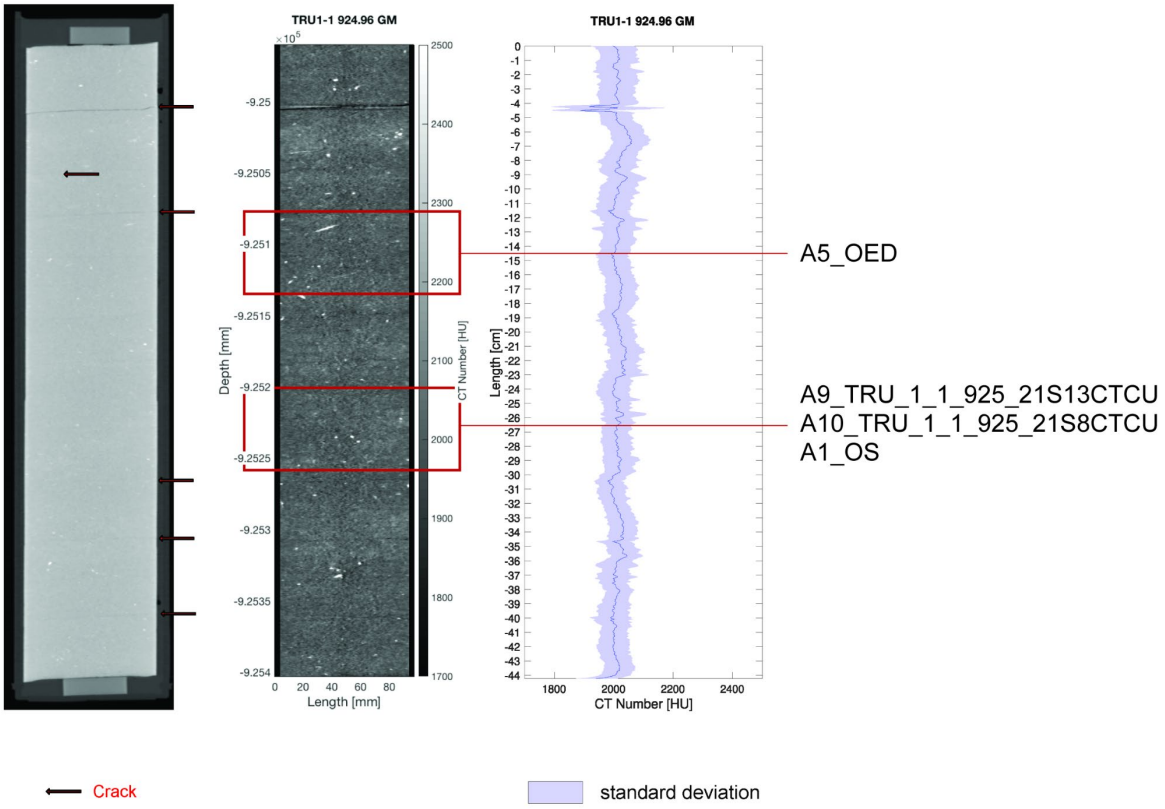

TRU1-1 955.69/43 GM

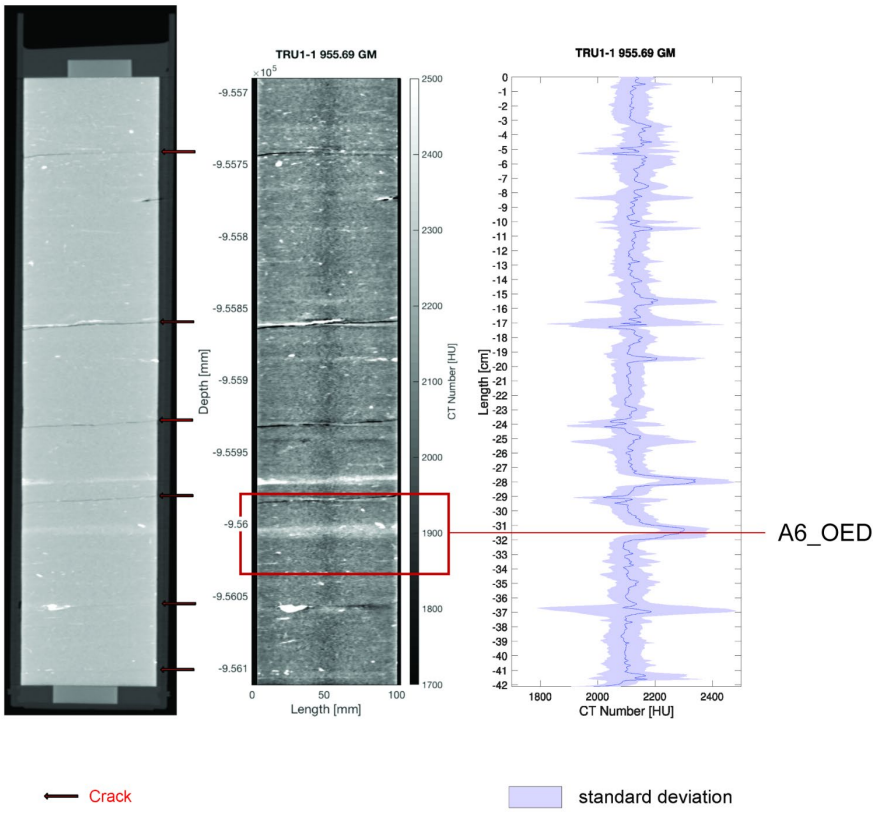

Appendix C Diagnostic plots of triaxial tests (geomechanical testing programme)

For each triaxial test, the diagnostic plots are here reported (order of tests according to Tab. E-2). The plots include: the evolution of axial and radial strains with deviatoric stress q, the pore pressure change Δu_w during shearing versus the axial strain ε_a, the stress path in the p'-q plane, the pore pressure variation Δu_w and the AB parameter evolution with q. In all the plots, the conditions at which the maximum deviatoric stress (Max q), the maximum pore pressure change (Max Δu_w) and the maximum AB (Max AB) (excluding evolution during unload/reload loops) are marked, as mentioned in Section 6.2.2.4 Testing conditions are reported in Tab. 6-2.

A15_TRU1-1_798_21S10CTCU

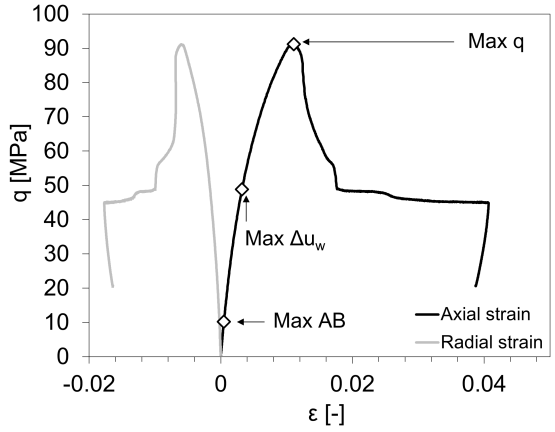

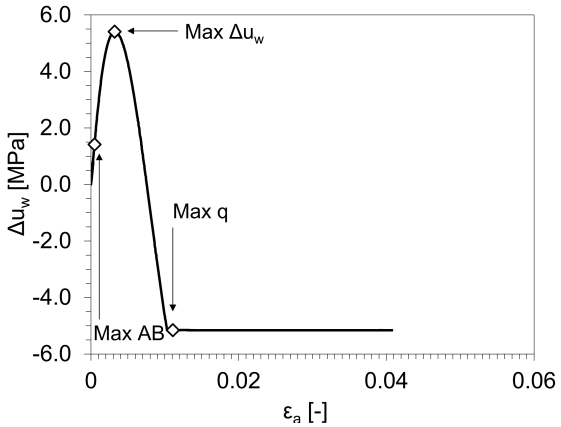

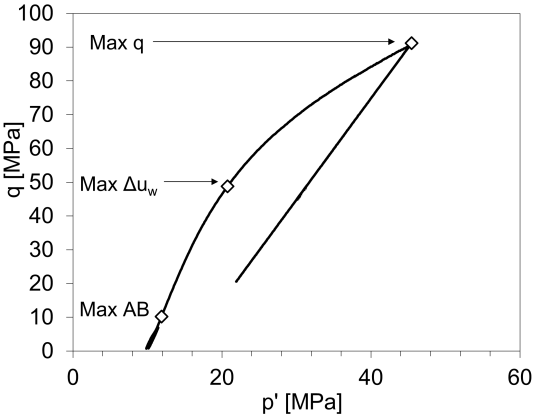

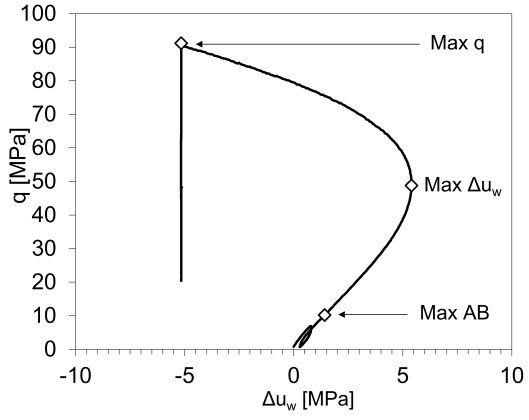

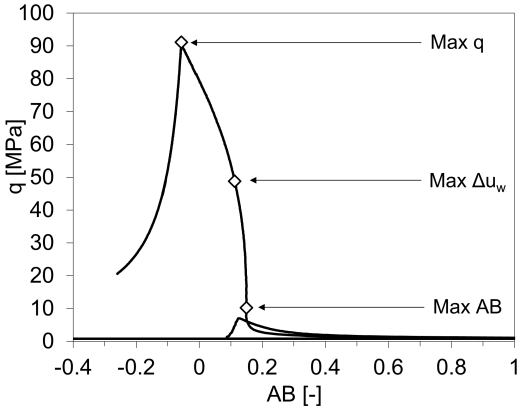

A16_TRU1-1_811_05S10CTCU

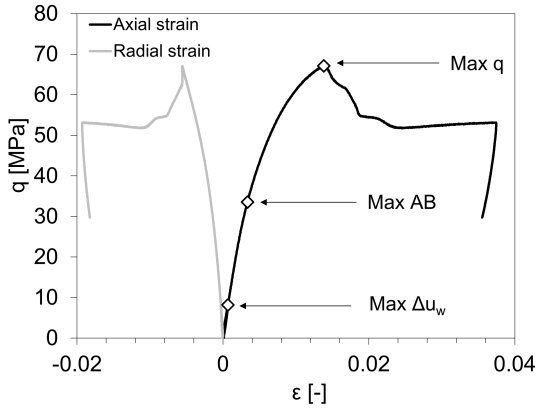

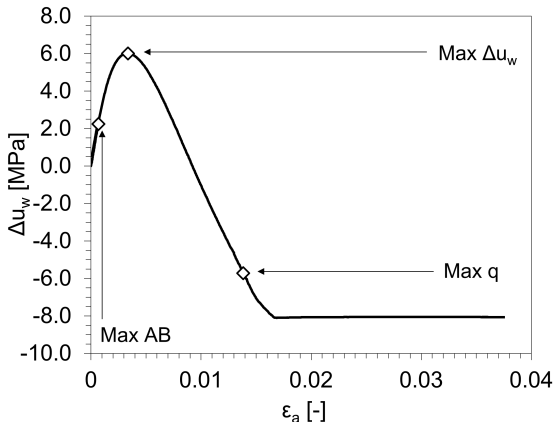

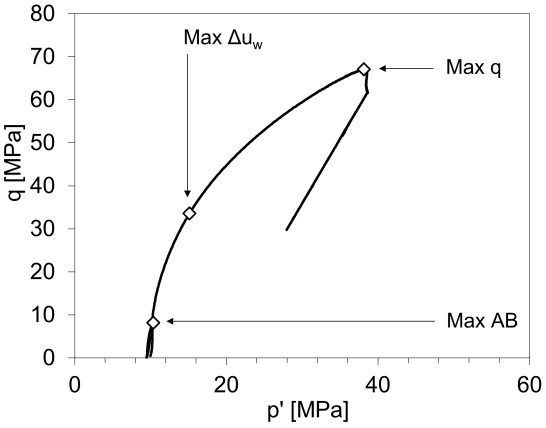

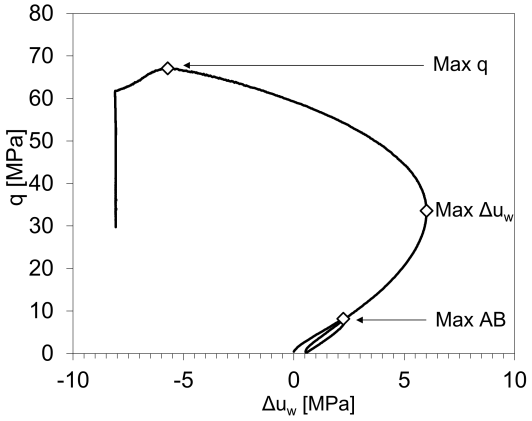

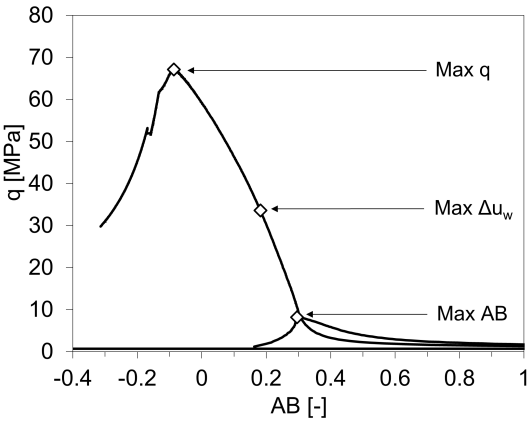

A1_TRU1-1_863_5P5CTCU

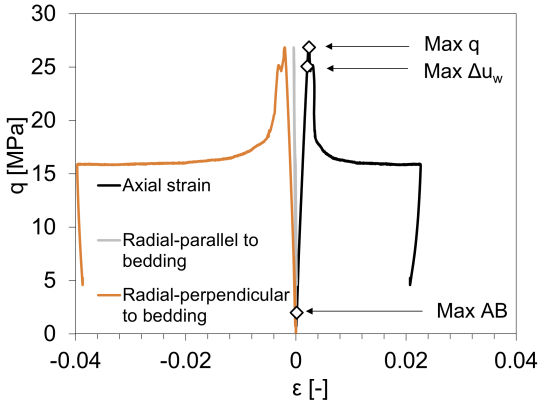

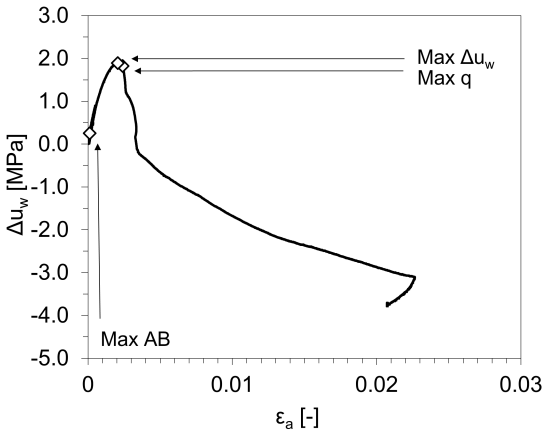

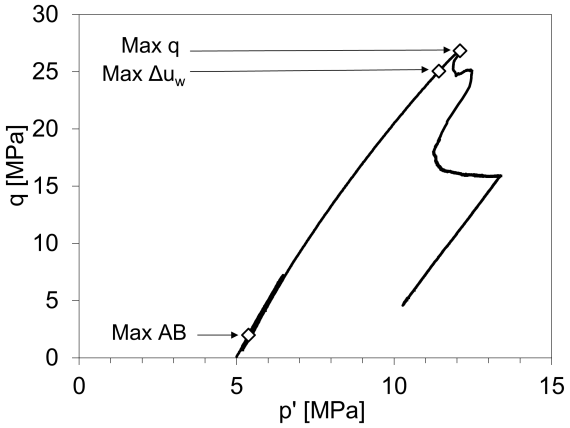

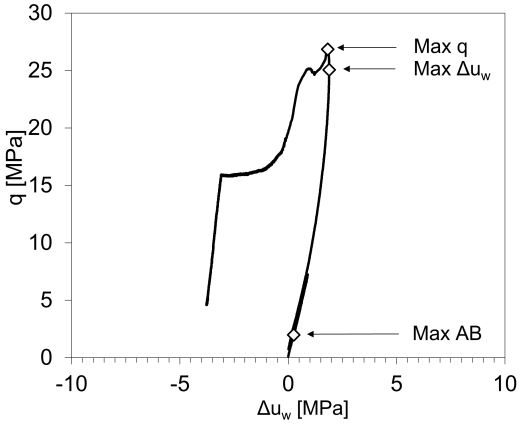

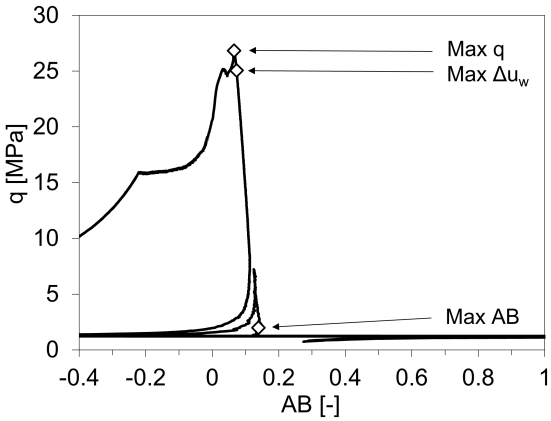

A2_TRU1-1_863_5P11CTCU

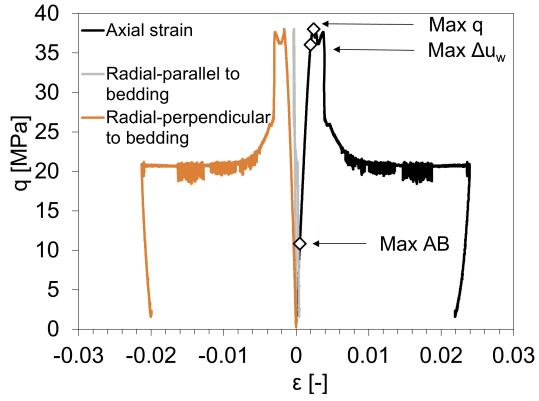

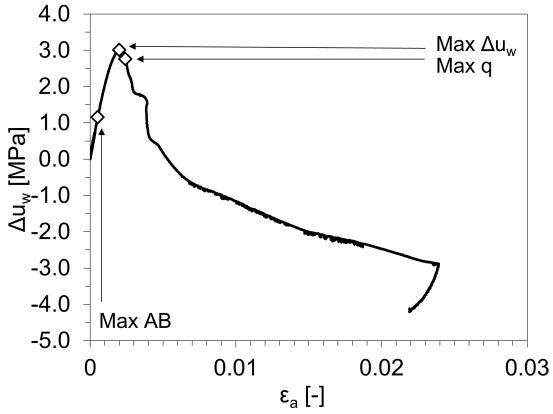

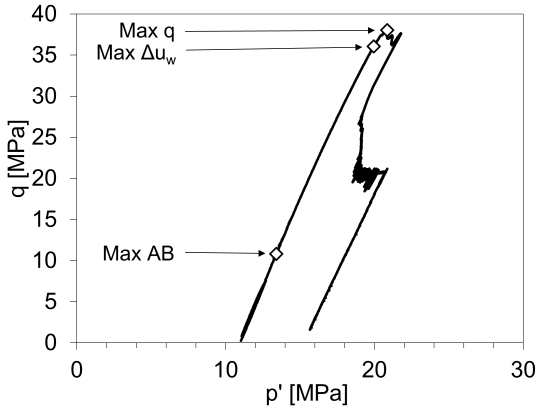

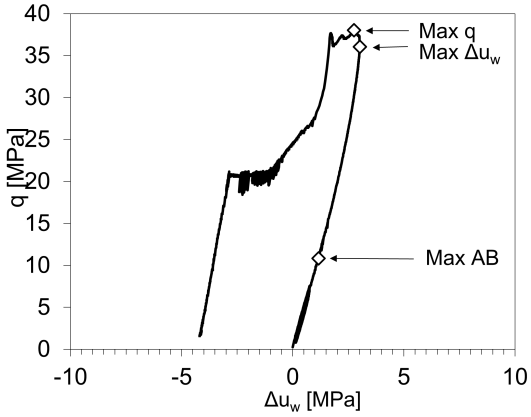

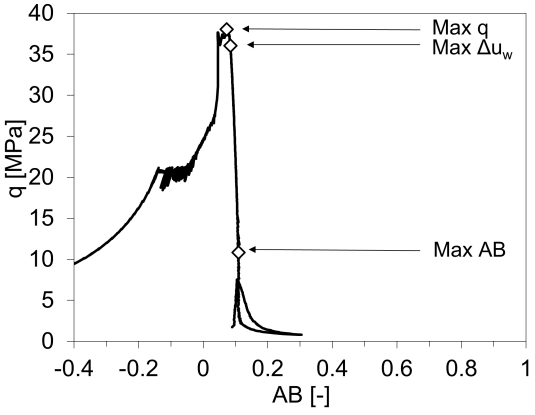

A4_TRU1-1_836_55S8CTCU

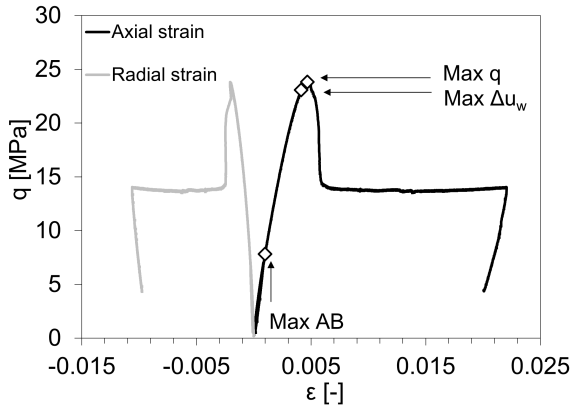

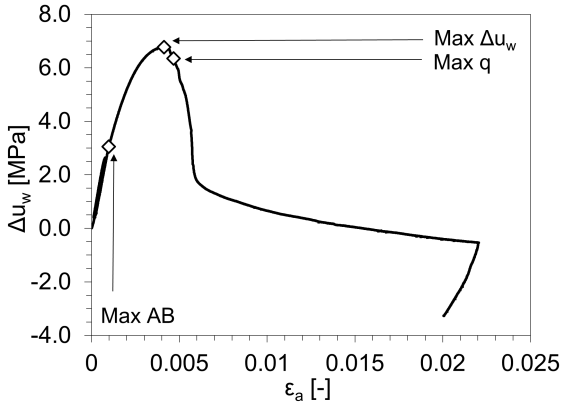

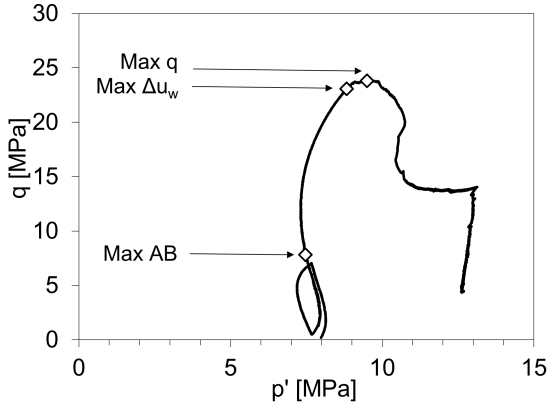

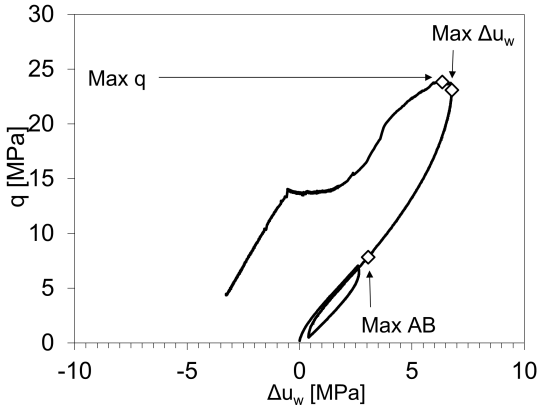

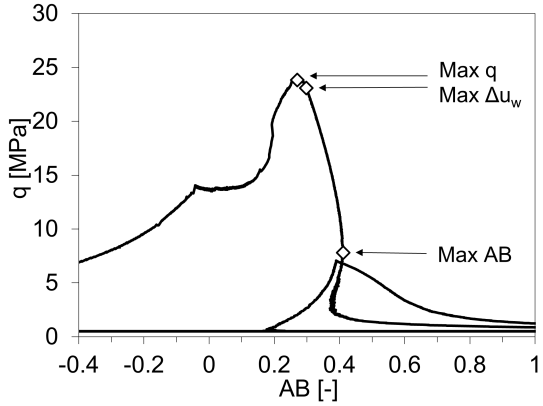

A3_TRU1-1_836_55S13CTCU

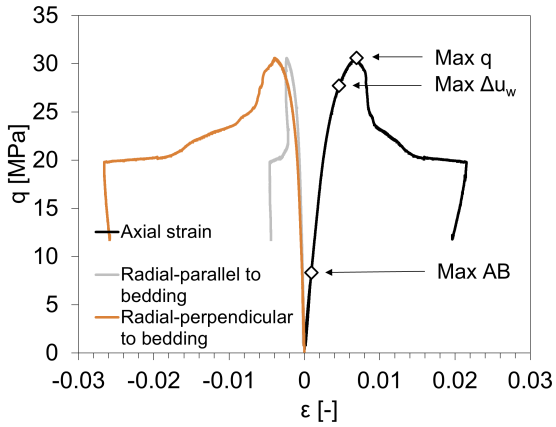

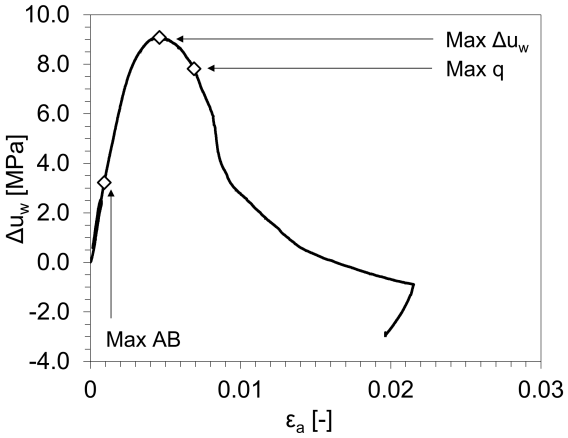

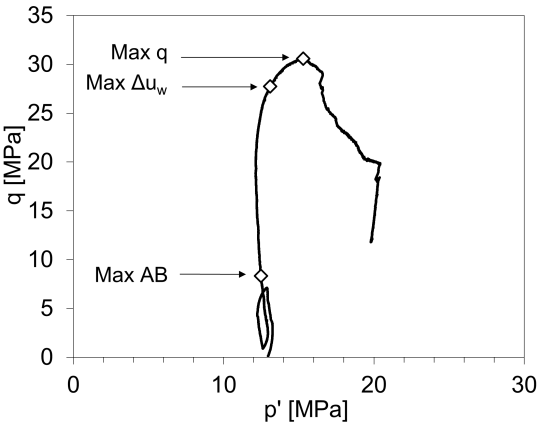

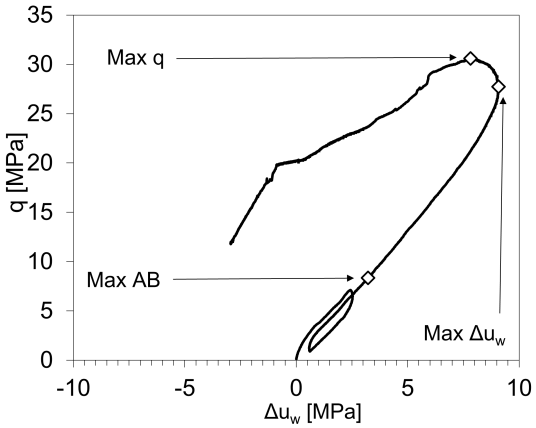

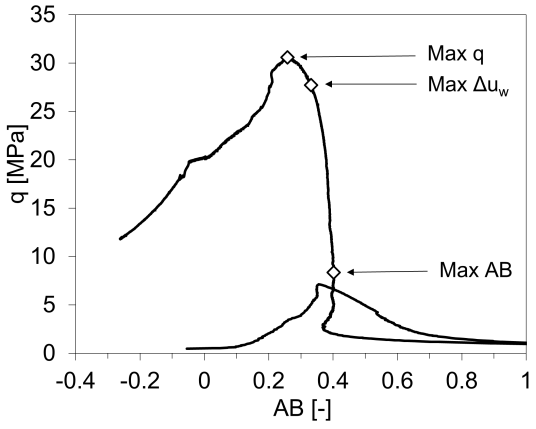

A13_TRU1-1_836_64Z13CTCU

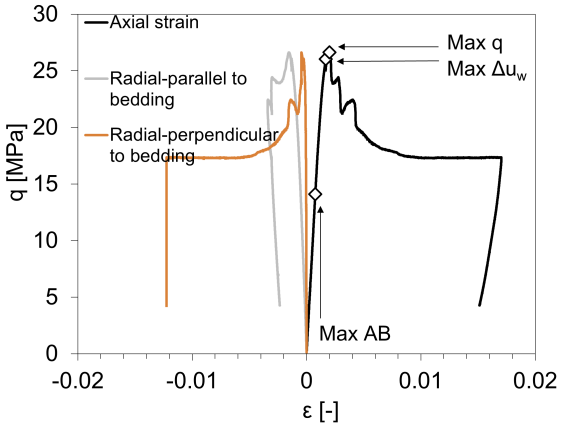

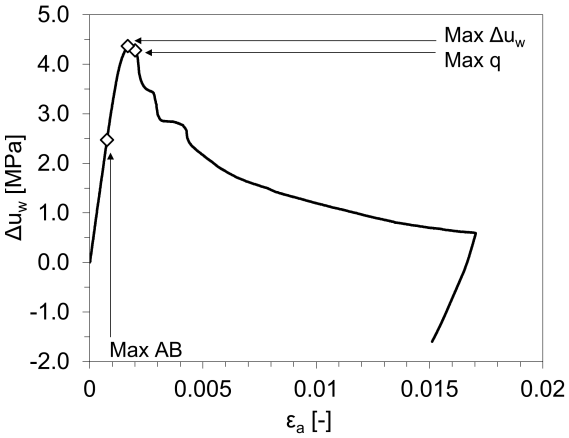

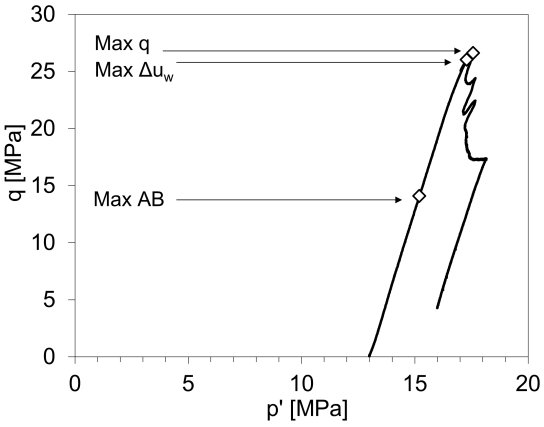

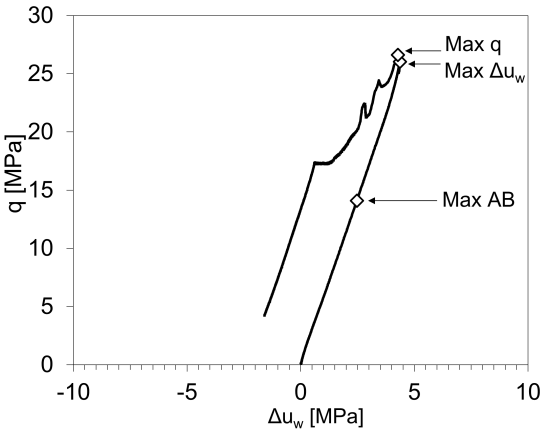

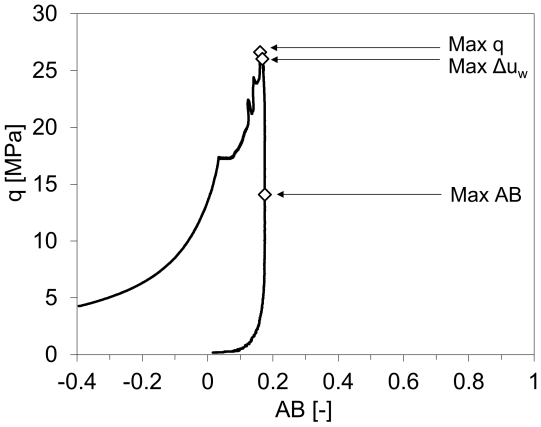

A14_TRU1-1_836_64Z7CTCU

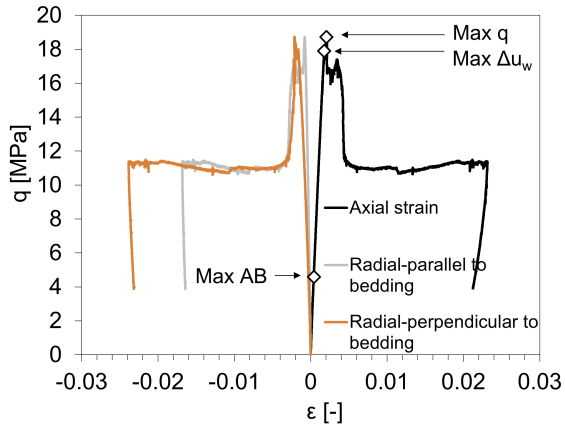

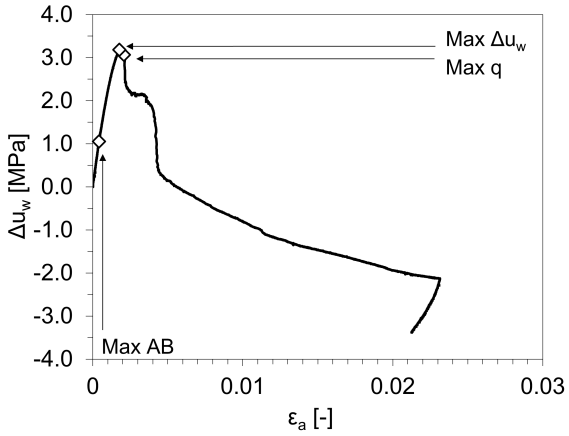

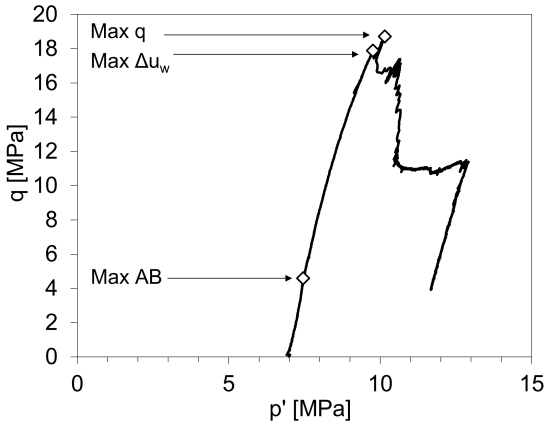

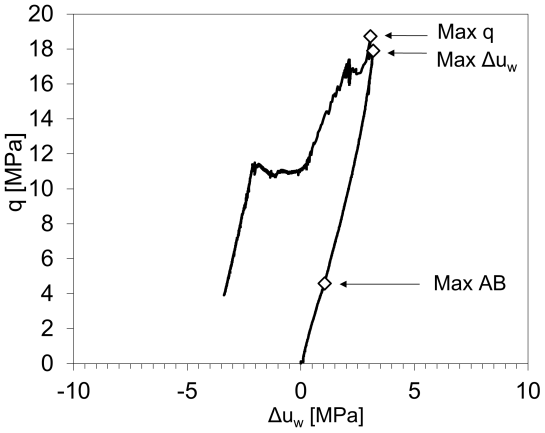

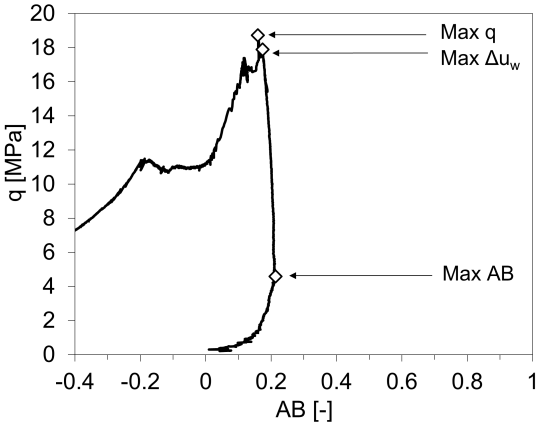

B4_TRU1_1_851_86P13CTCU

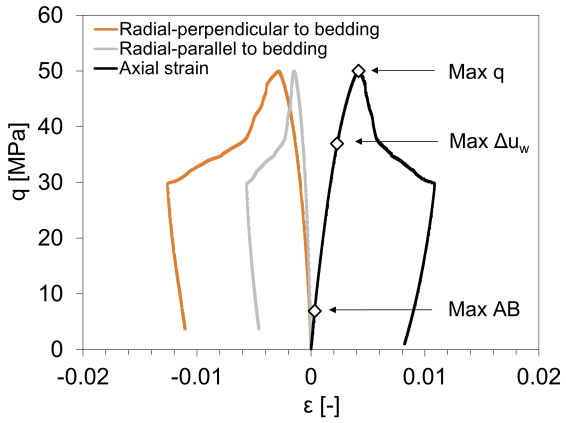

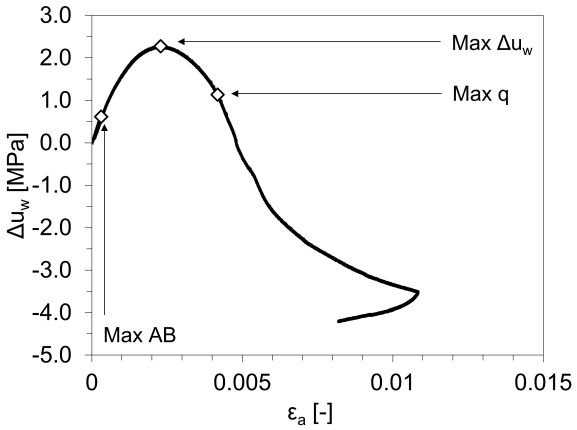

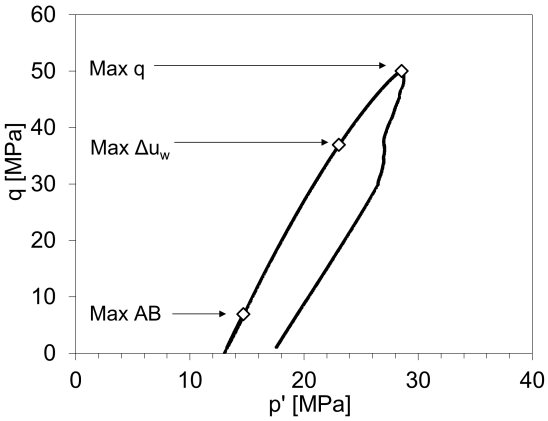

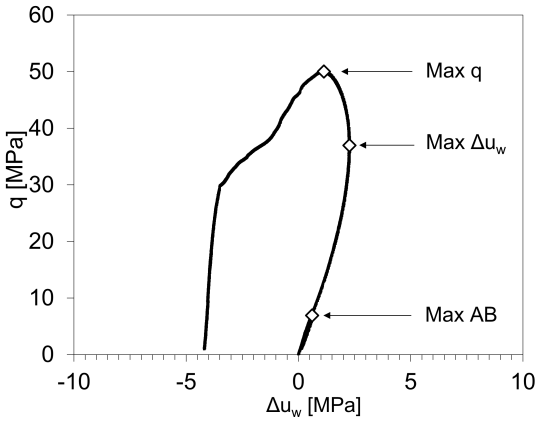

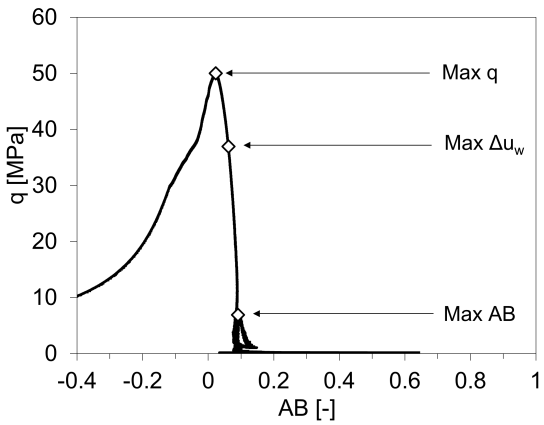

B5_TRU1_1_851_88P7CTCU

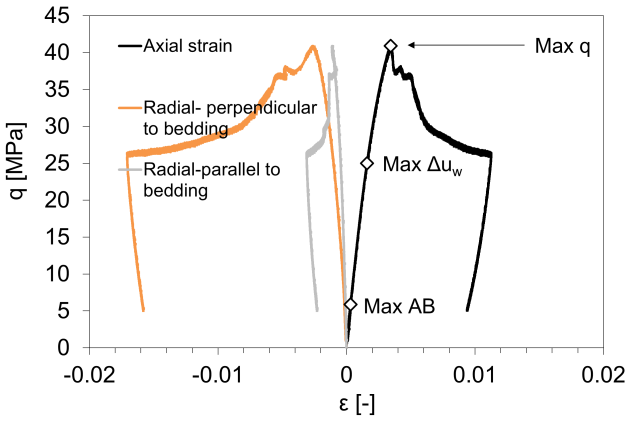

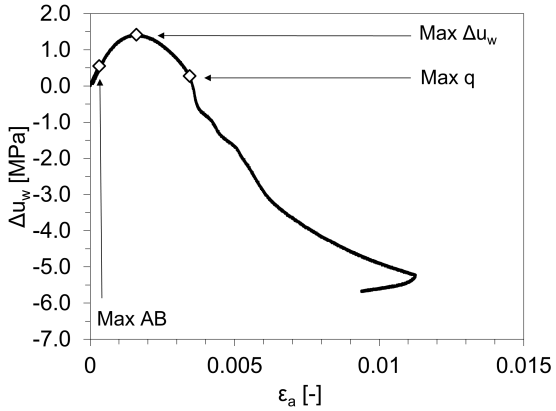

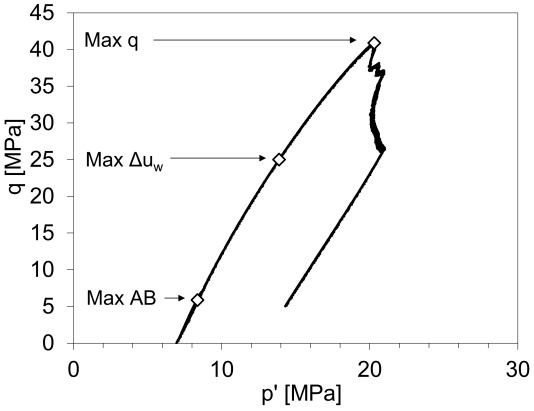

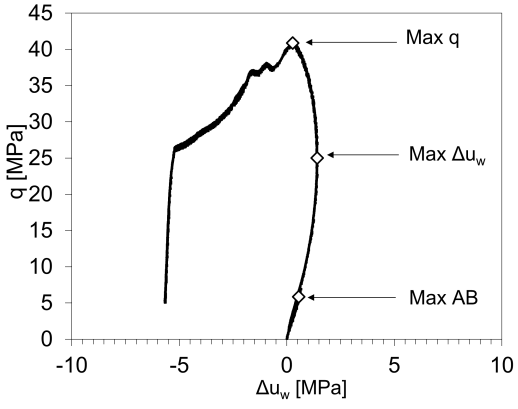

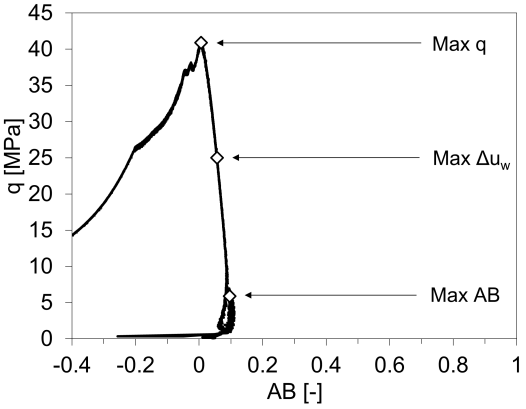

B1_TRU1_1_851_94S13CTCU

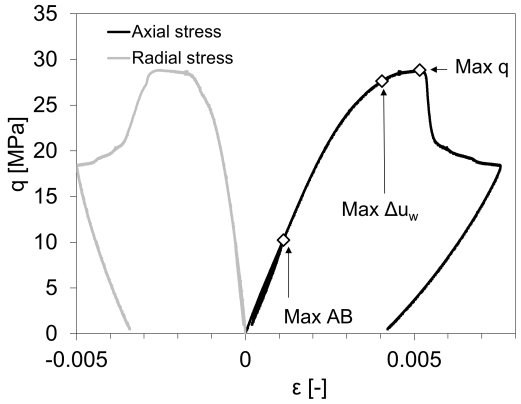

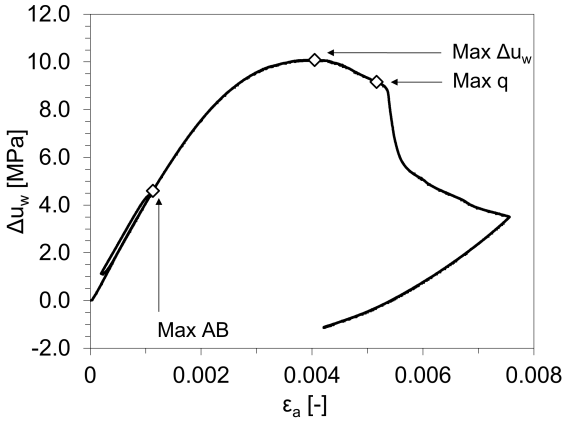

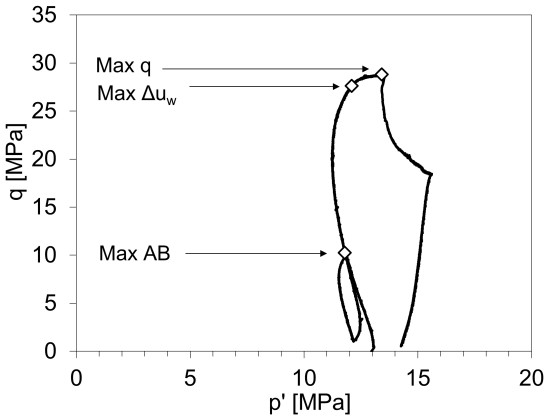

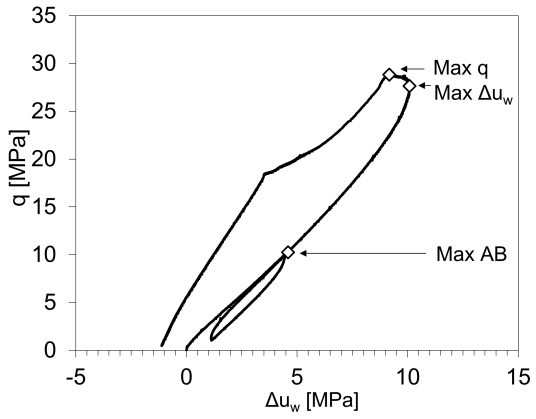

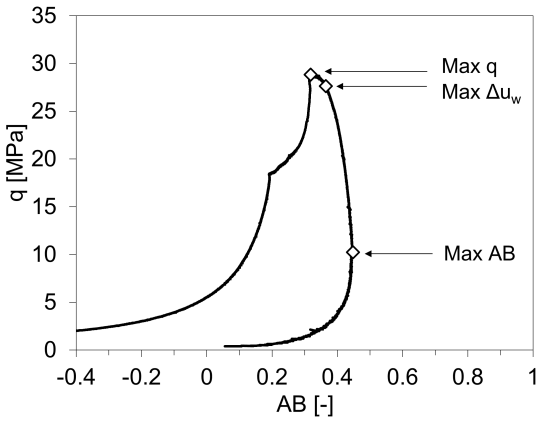

B2_TRU1_1_851_94S10CTCU

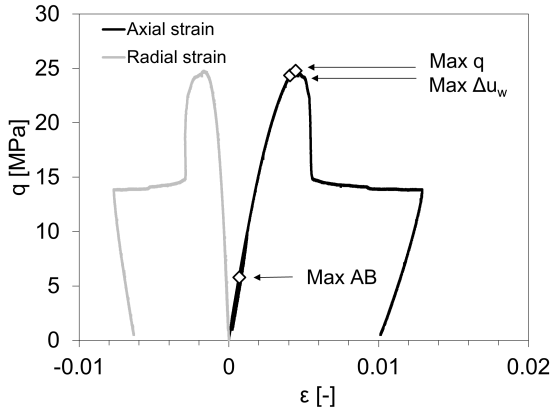

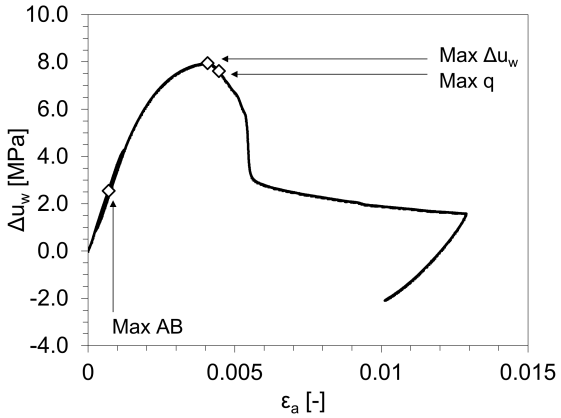

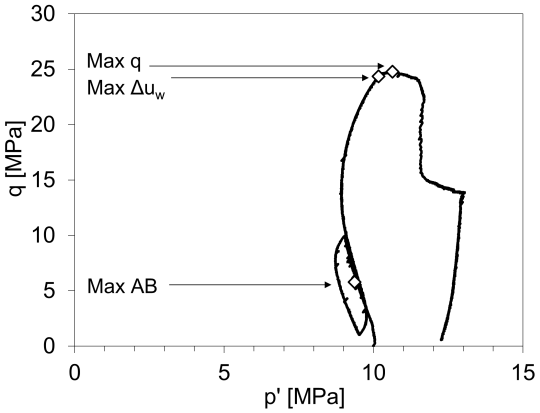

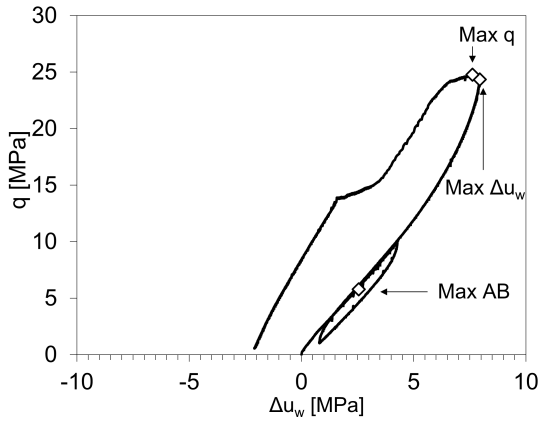

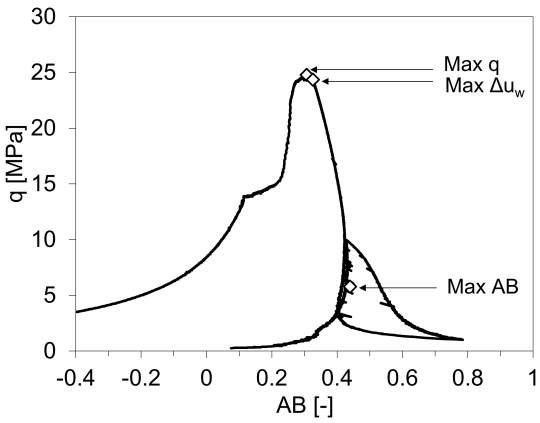

B3_TRU1_1_851_94S7CTCU

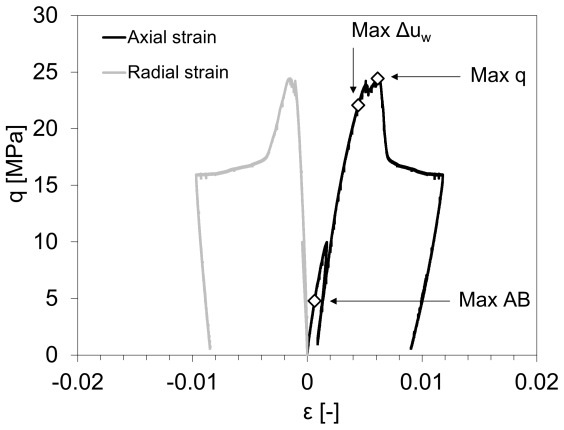

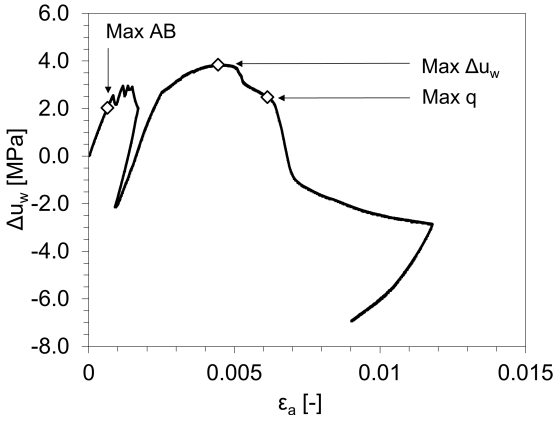

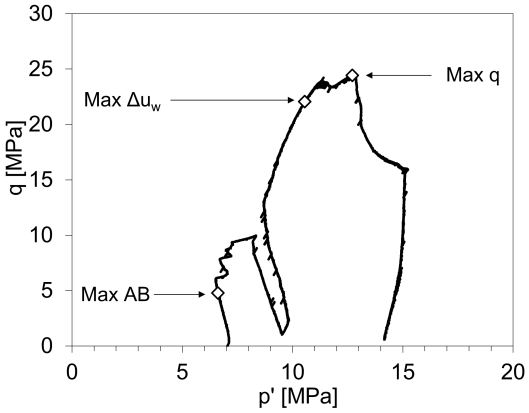

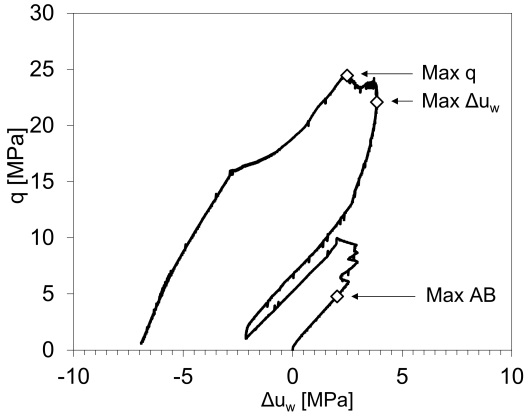

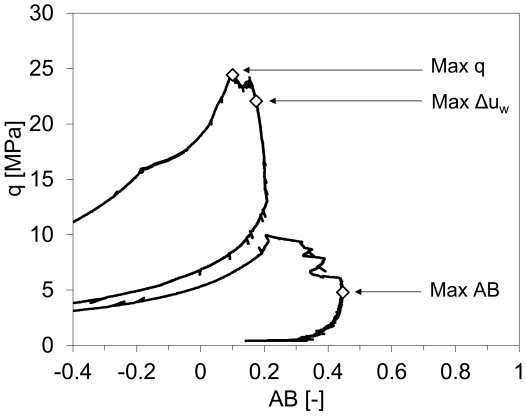

B8_TRU1_1_875_56_P13CTCU

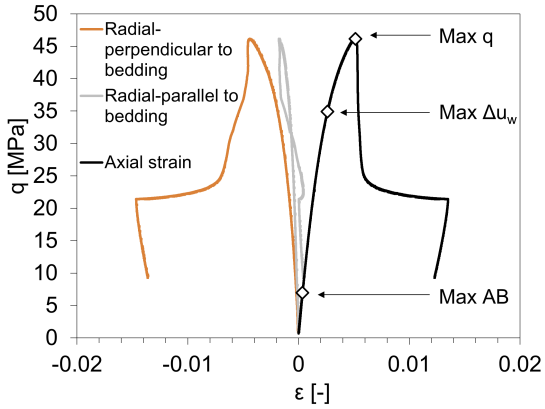

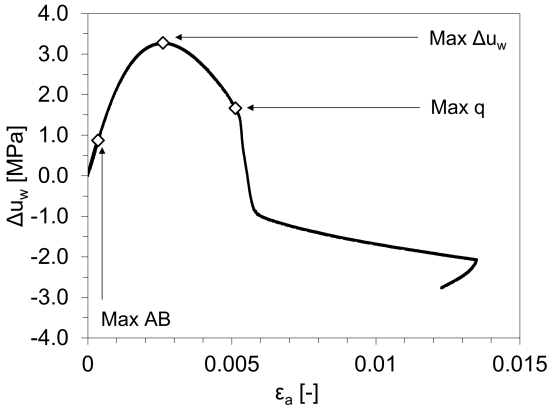

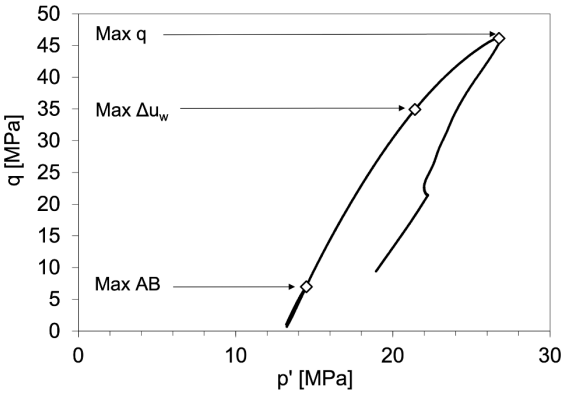

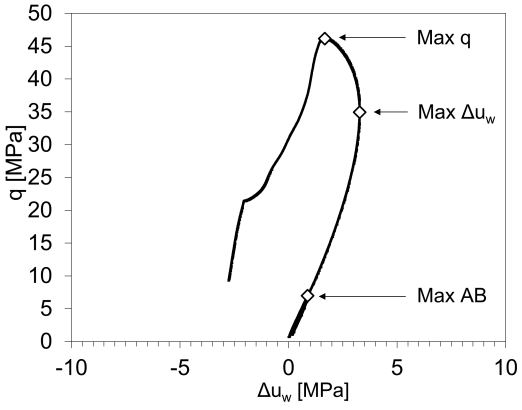

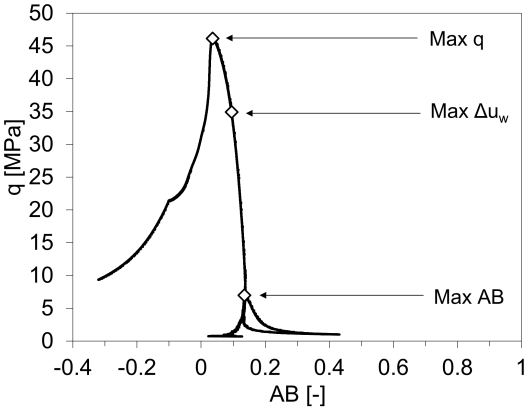

B9_TRU1_1_875_56P8CTC

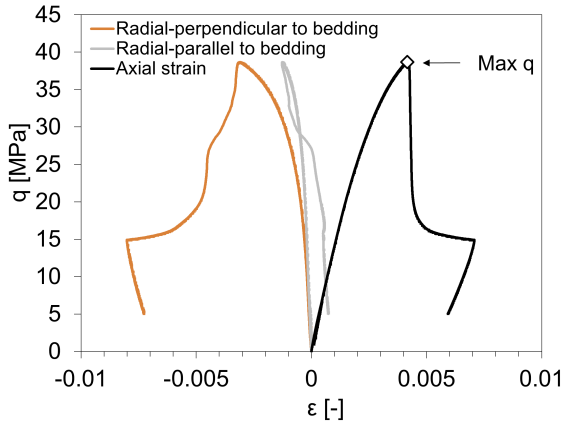

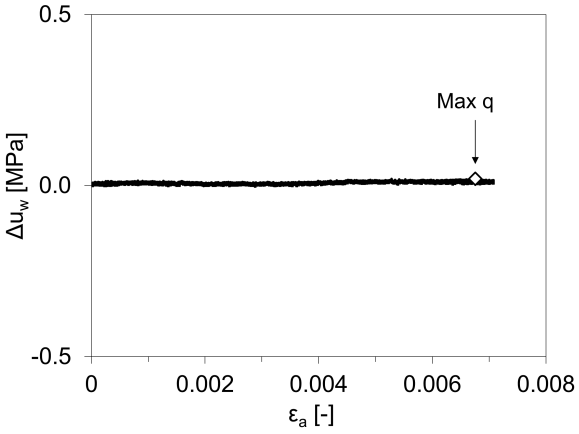

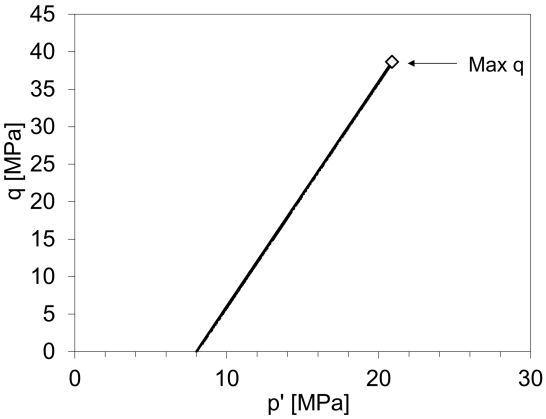

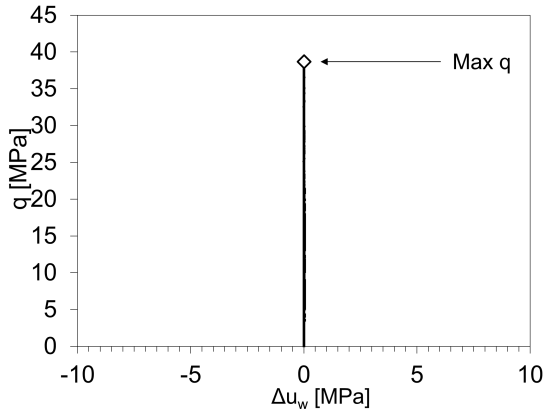

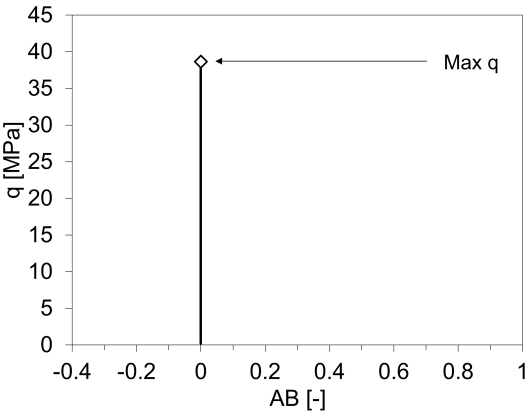

B13_TRU1_1_875_65P9TC

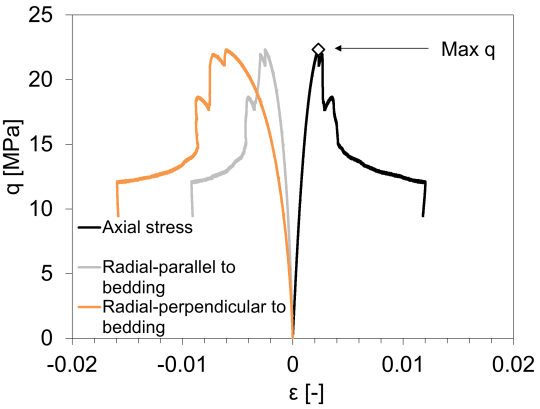

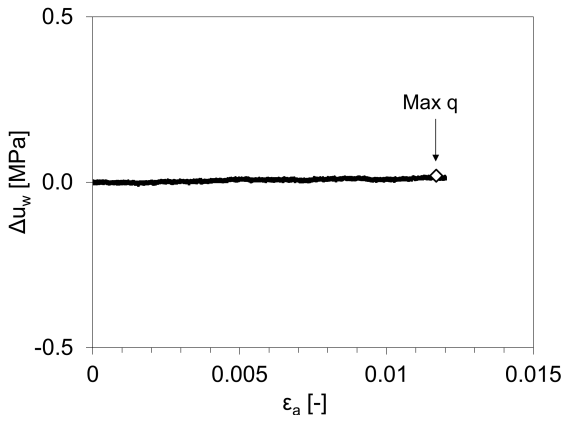

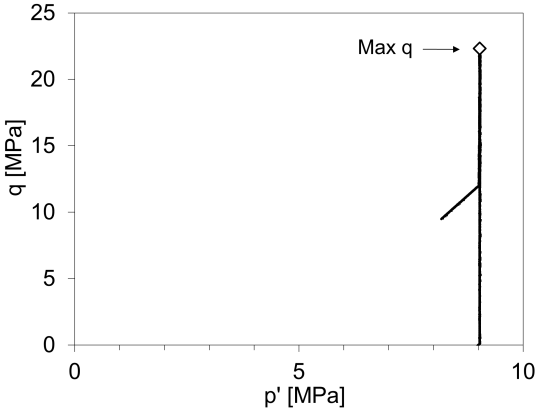

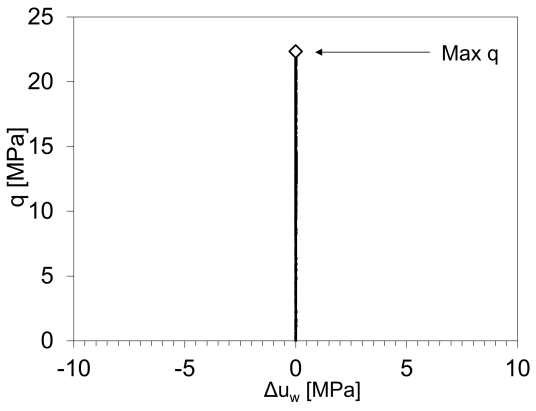

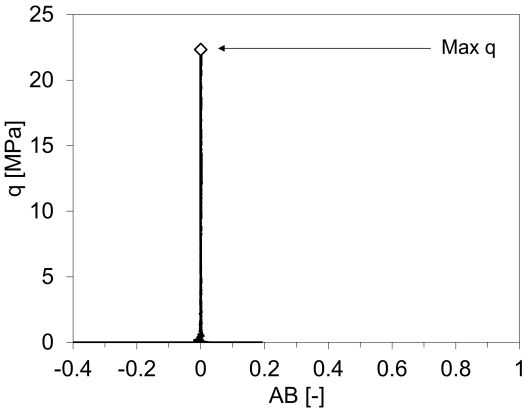

B12_TRU1_1_875_69Z13CTCU

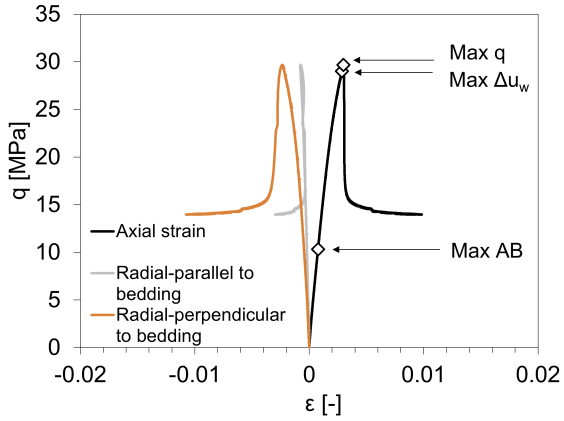

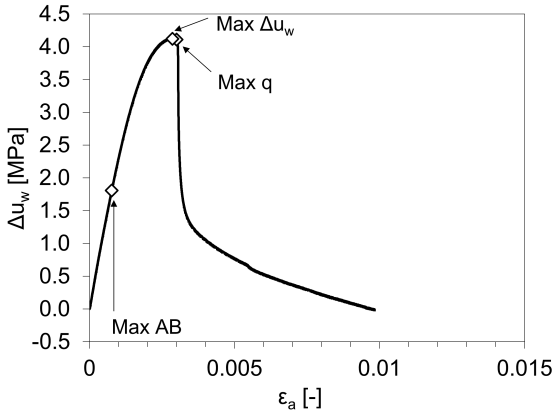

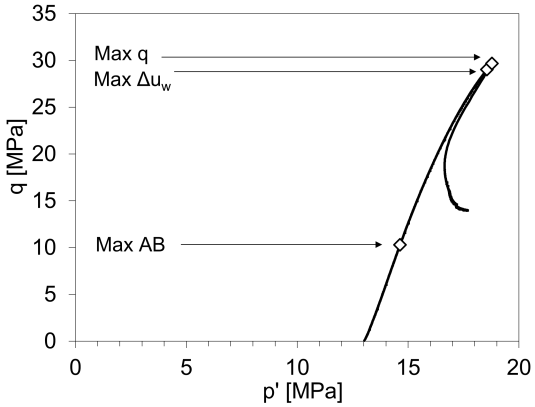

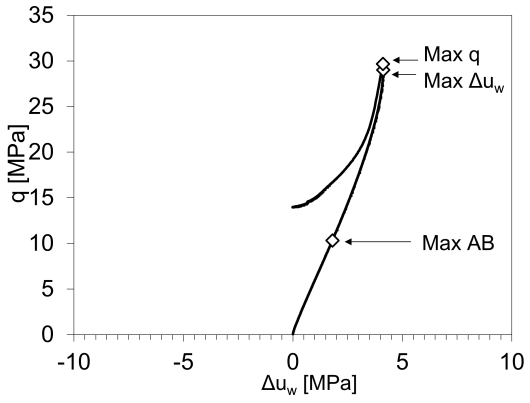

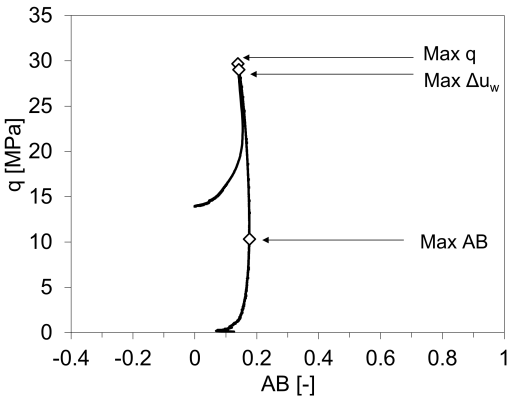

B7_TRU1_1_875_76S7CTCU

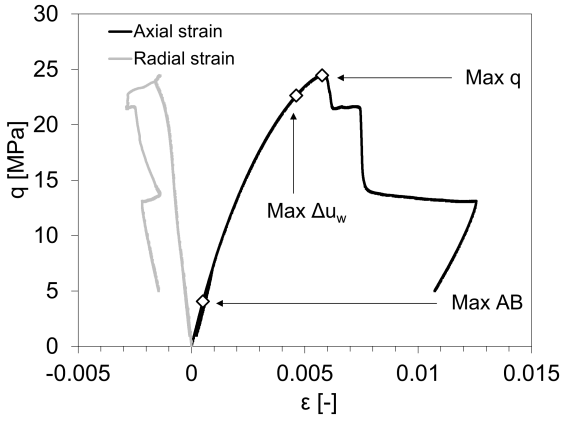

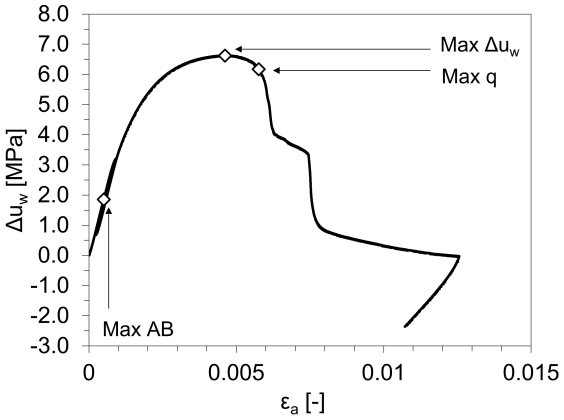

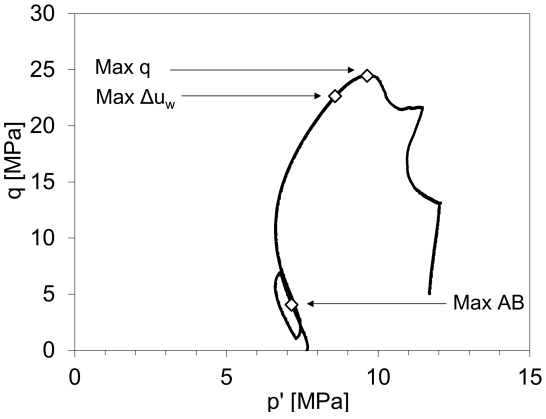

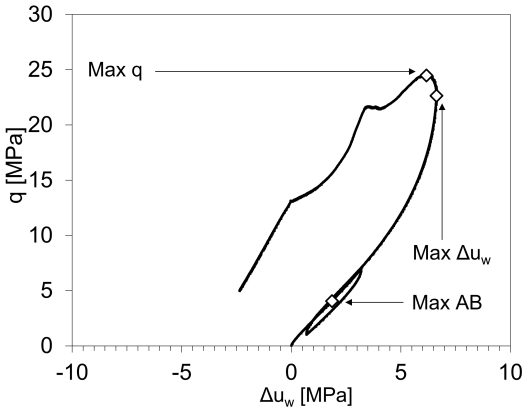

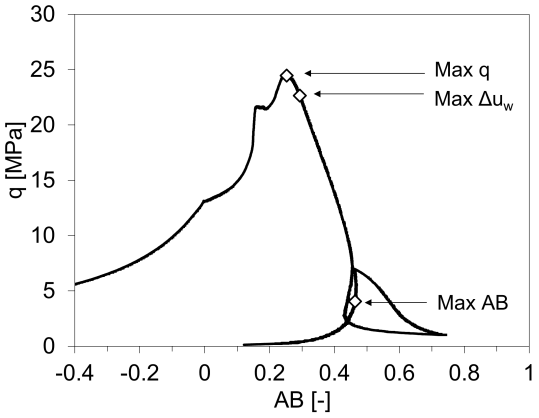

B6_TRU1_1_875_77S13CTCU

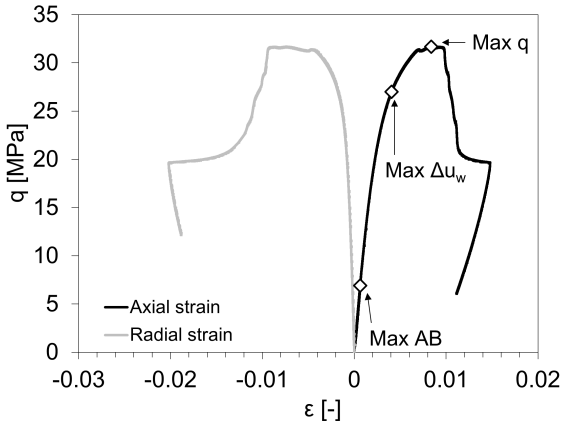

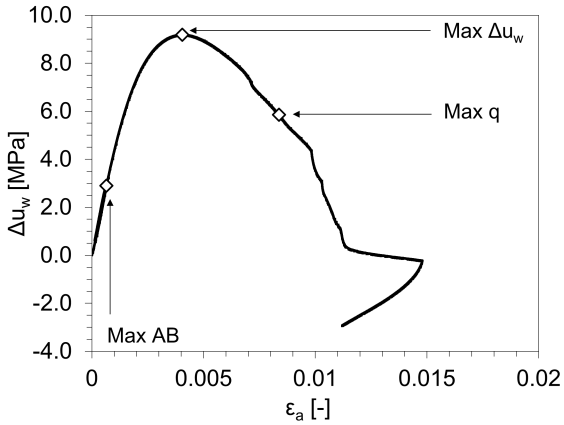

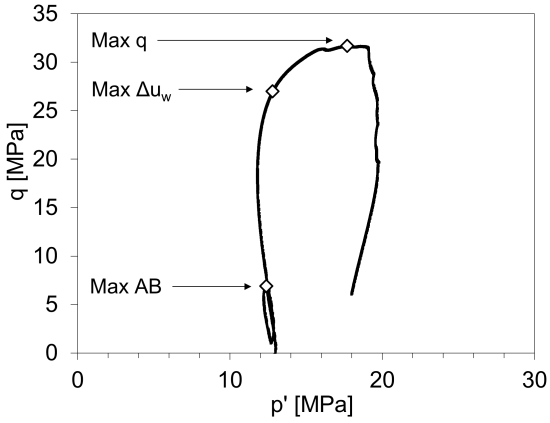

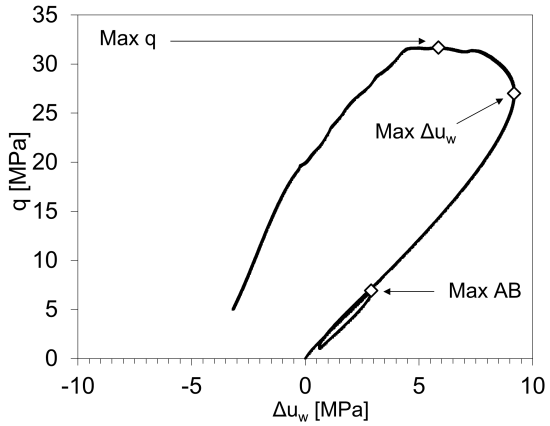

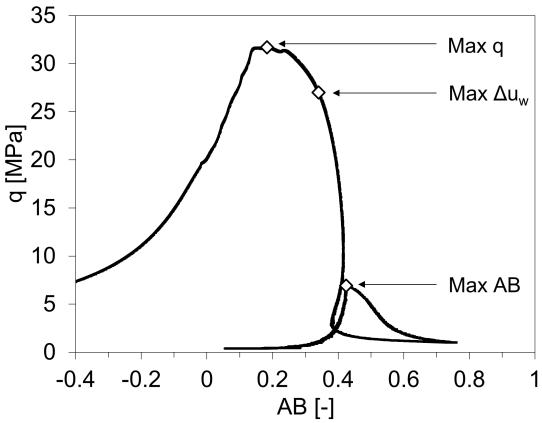

B10_TRU1_1_875_84Z13CTCU

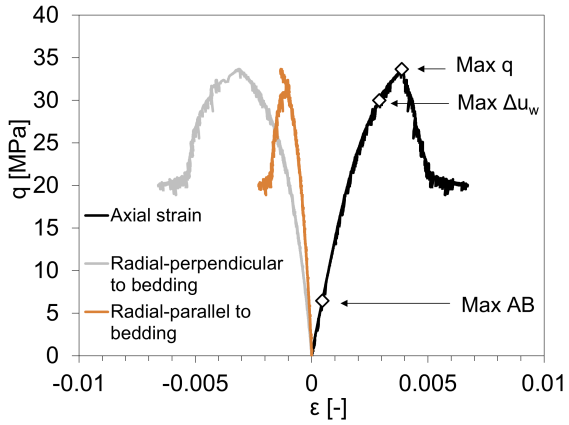

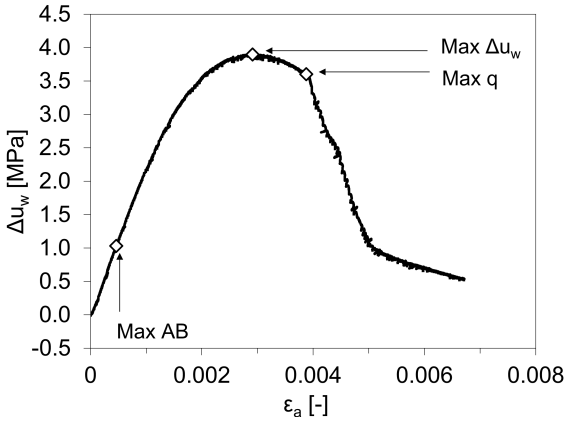

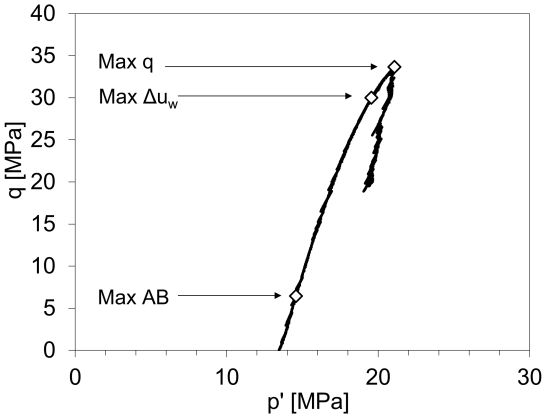

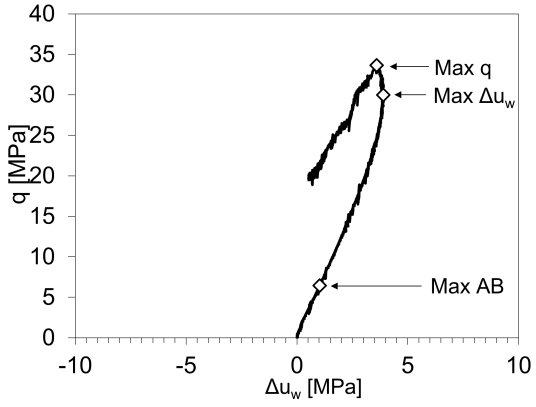

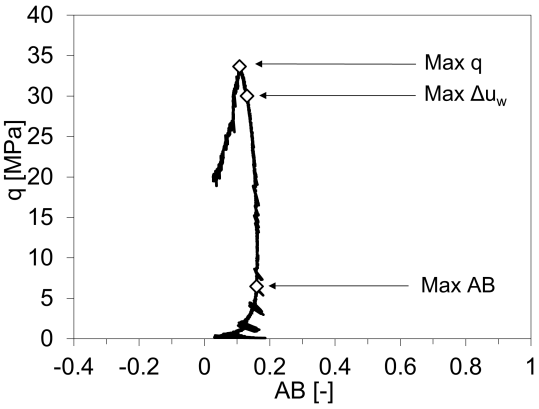

B11_TRU1_1_875_84Z7CTCU

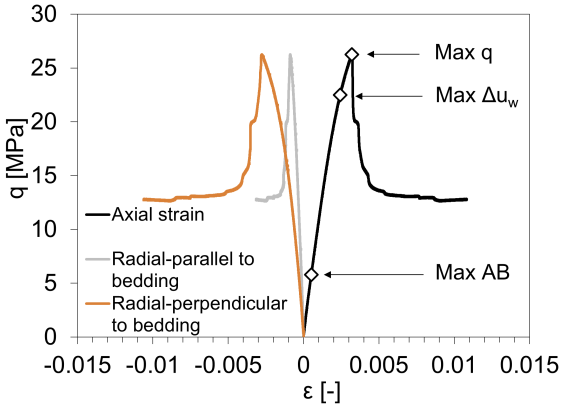

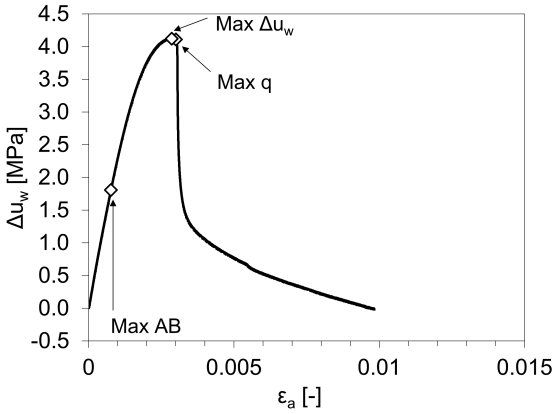

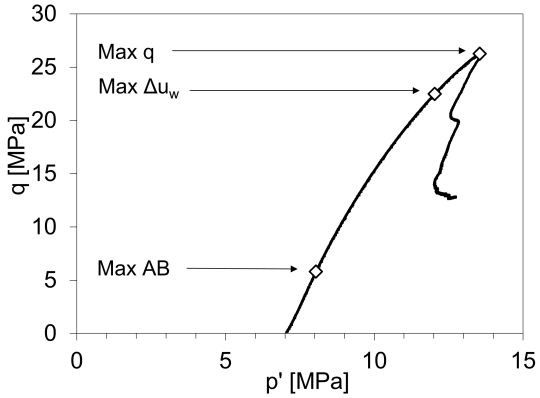

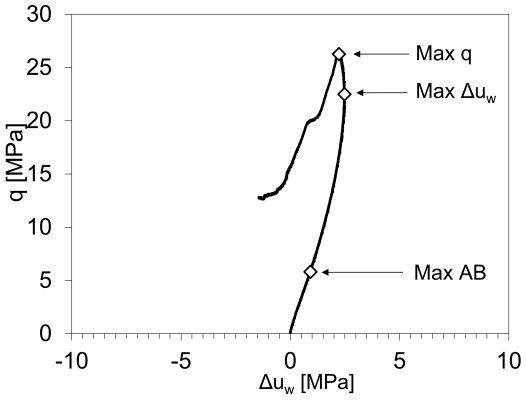

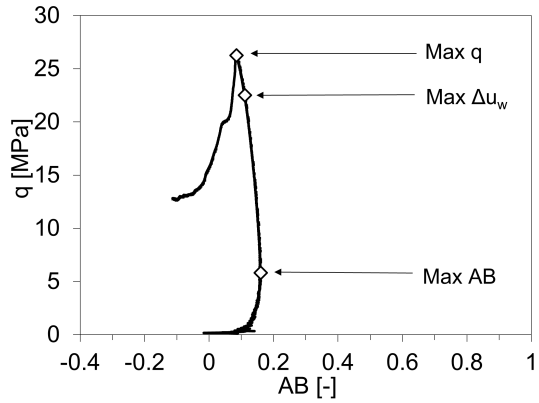

C1_TRU1_1_895_08P13CTCU

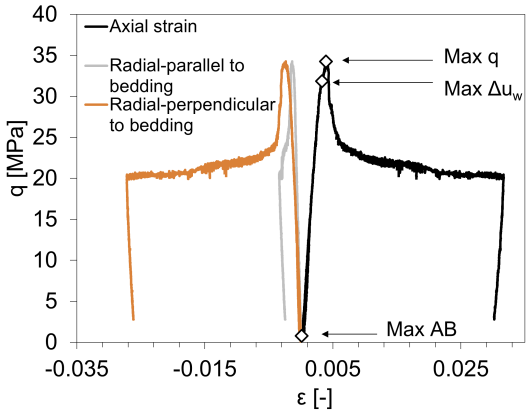

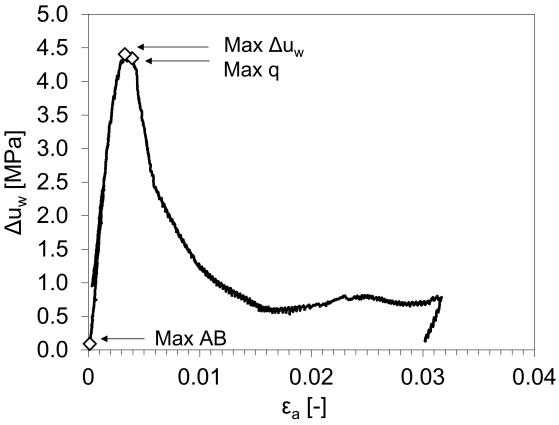

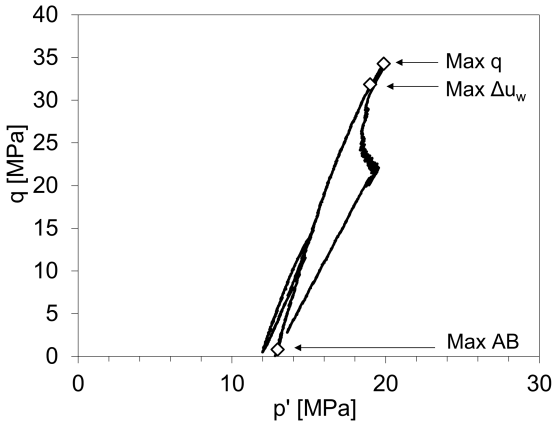

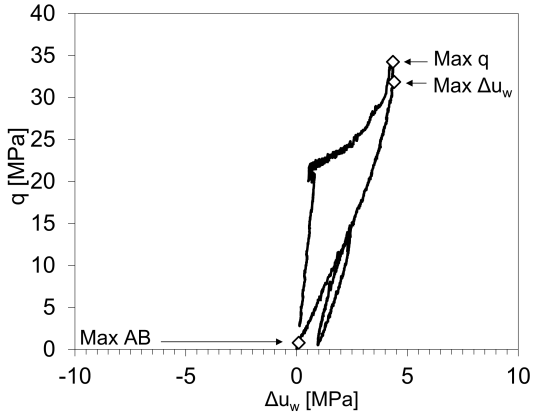

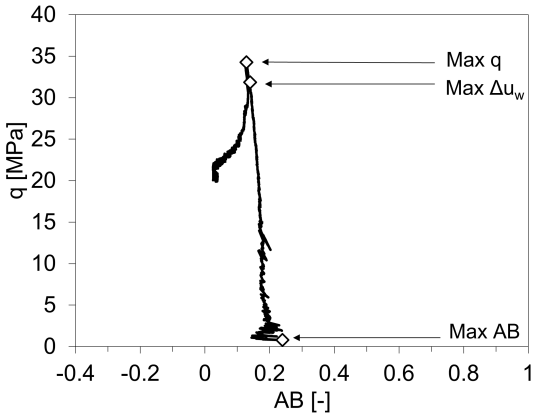

C2_TRU1_1_895_08P5CTCU

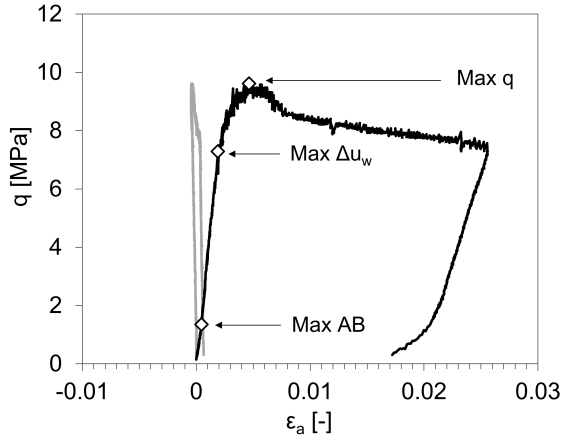

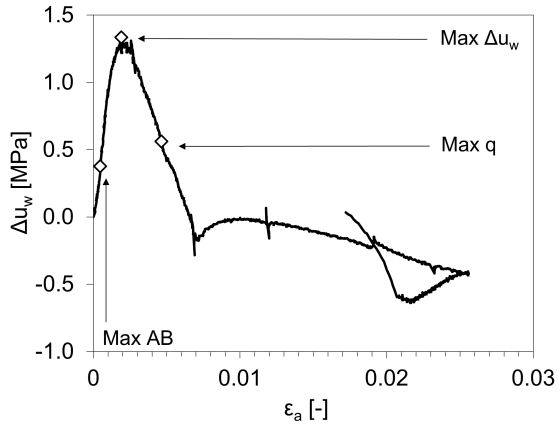

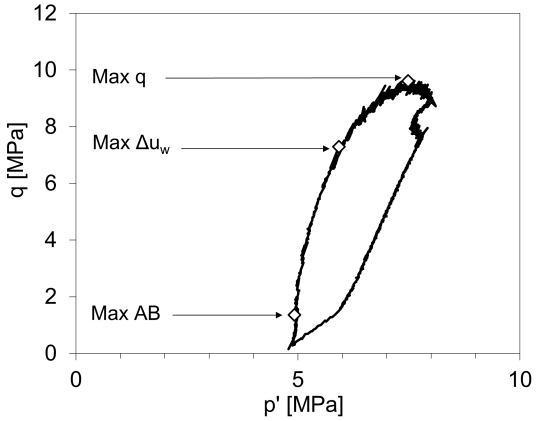

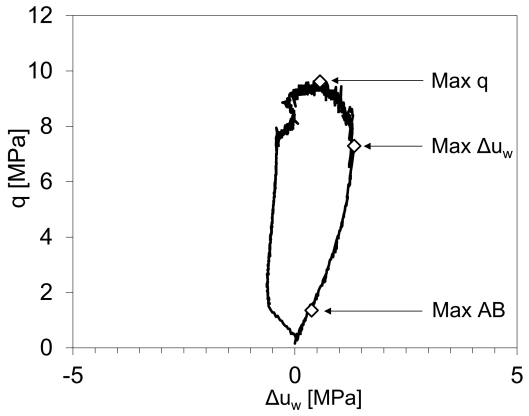

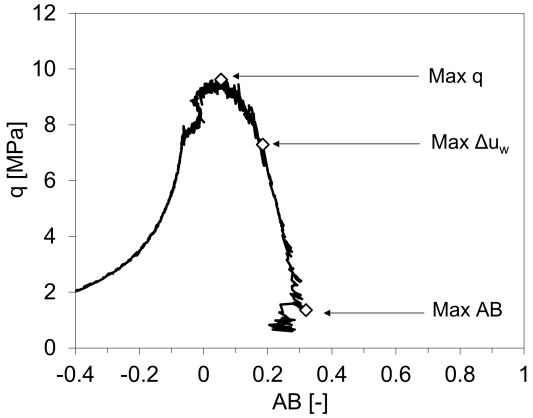

C4_TRU1_1_895_08S4CTCU

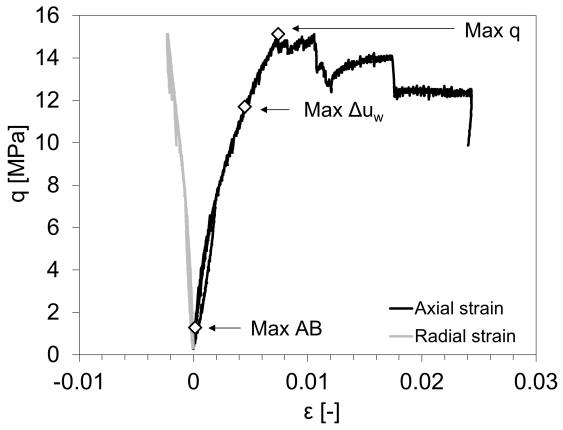

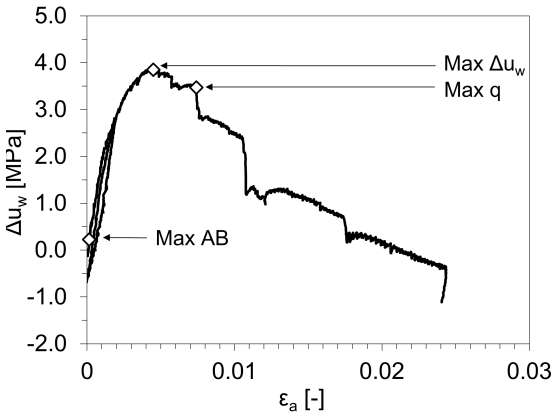

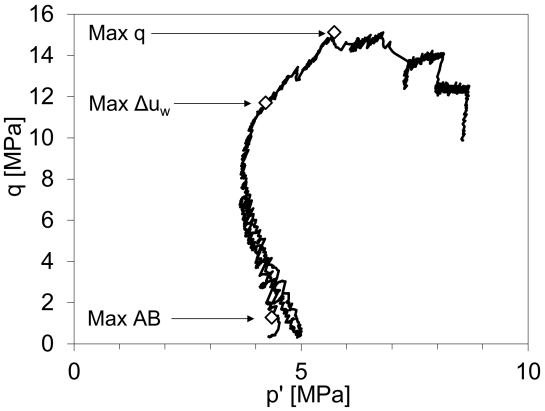

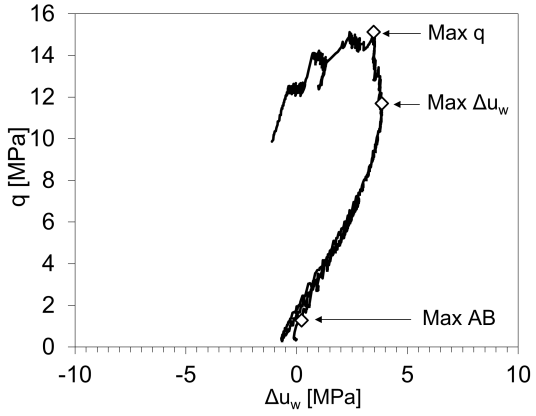

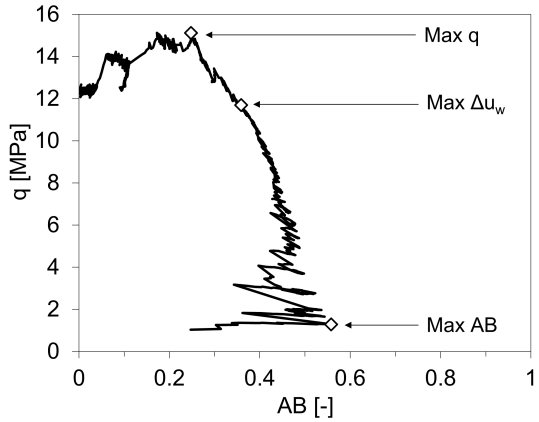

C5_TRU1_1_895_08S13CTCU

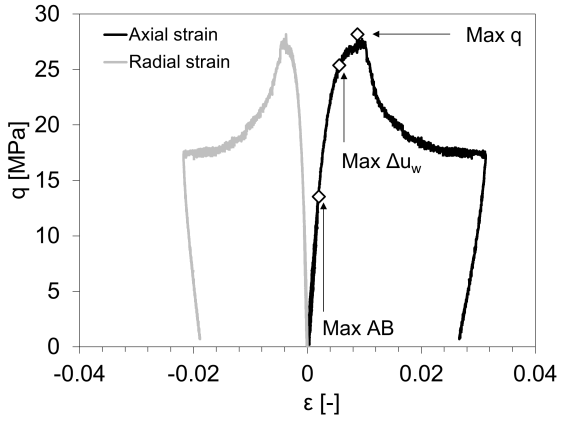

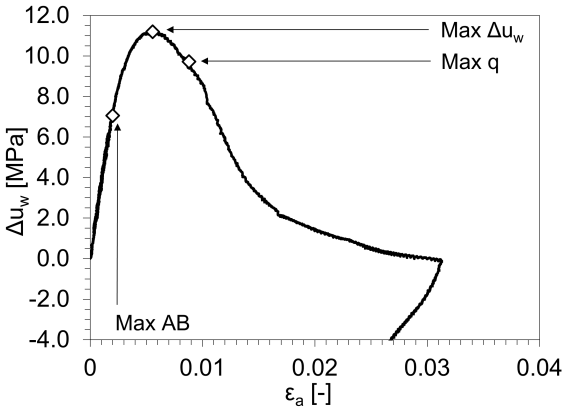

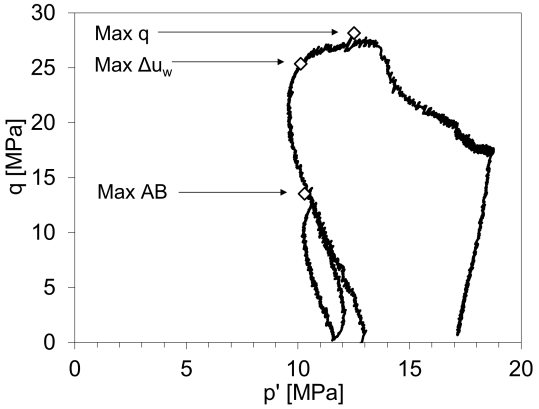

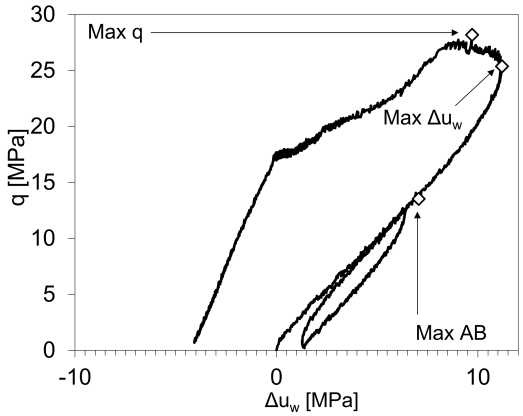

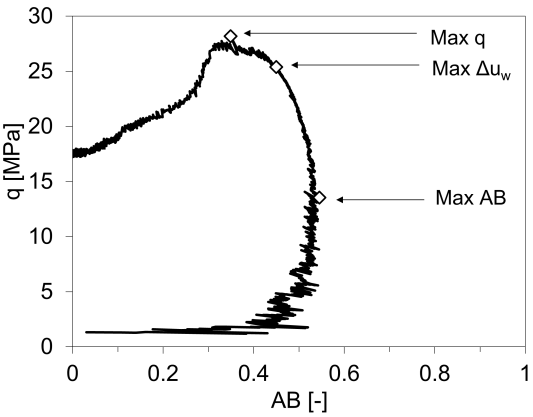

C3_TRU1_1_895_15Z5CTCU

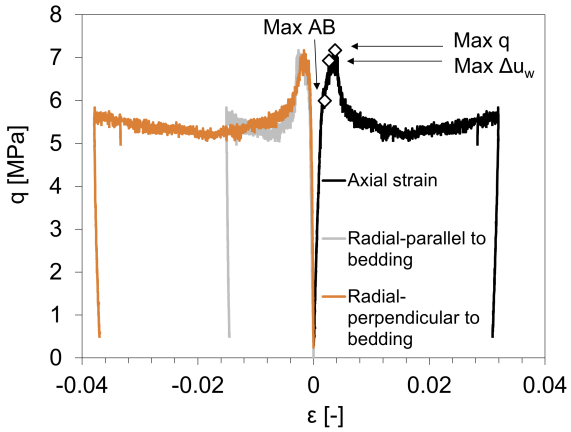

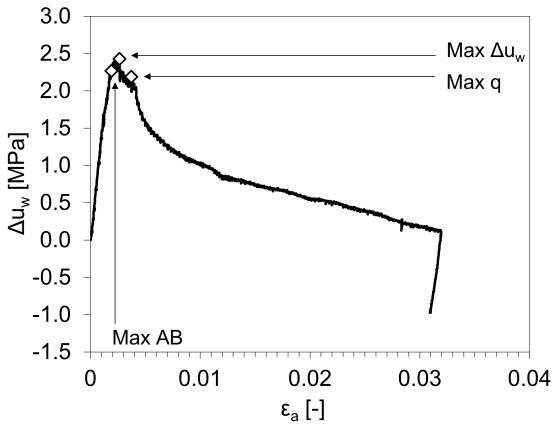

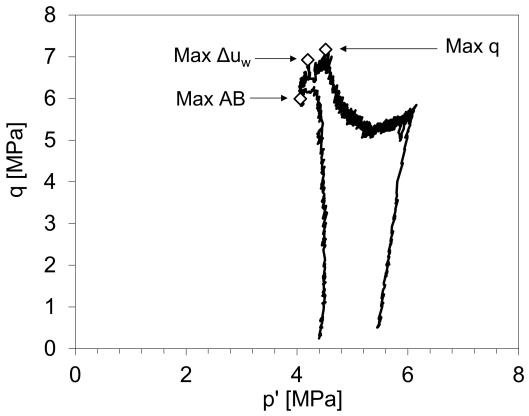

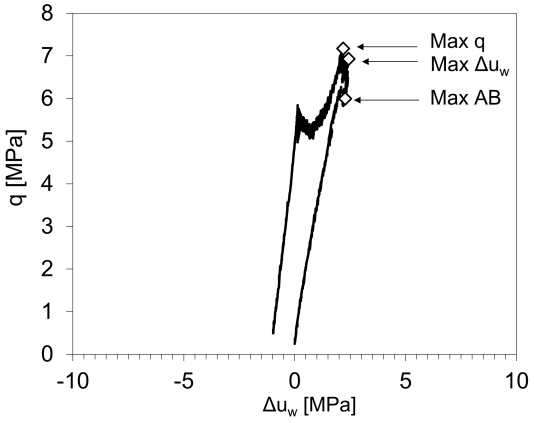

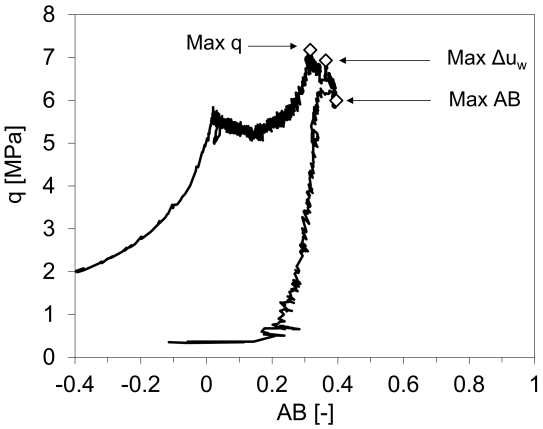

A12_TRU1_1_903_32P5CTC

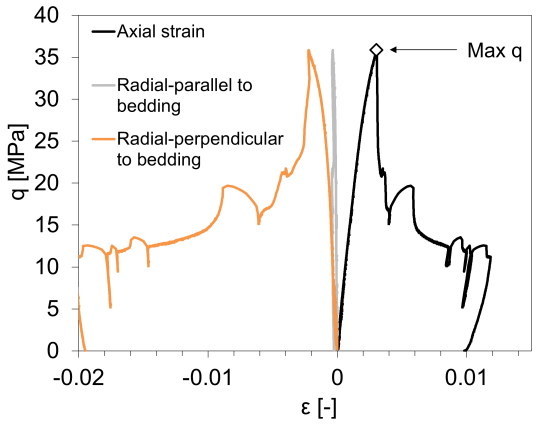

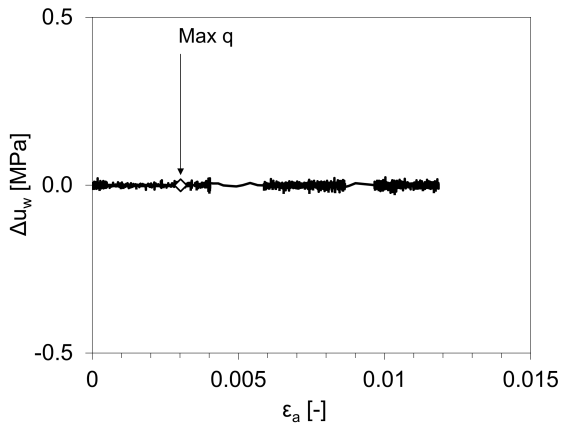

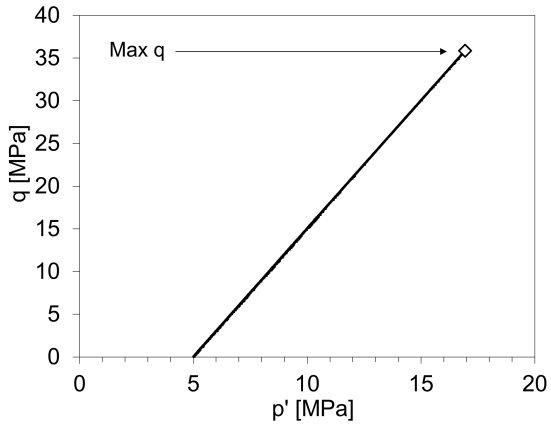

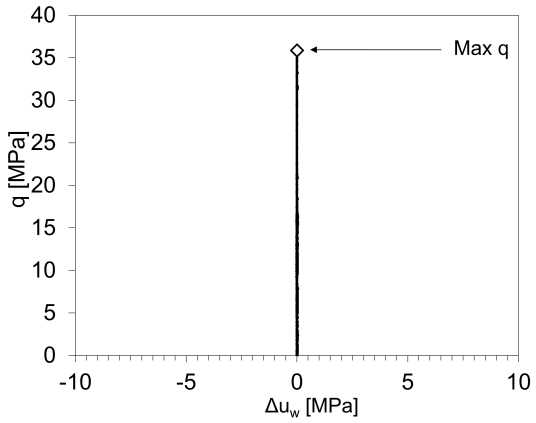

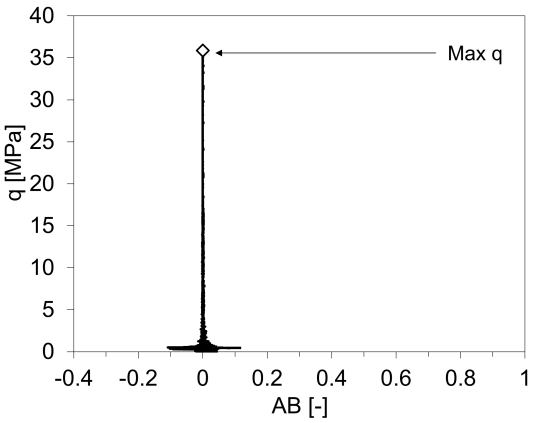

A11_TRU1_1_903_4S5CTC

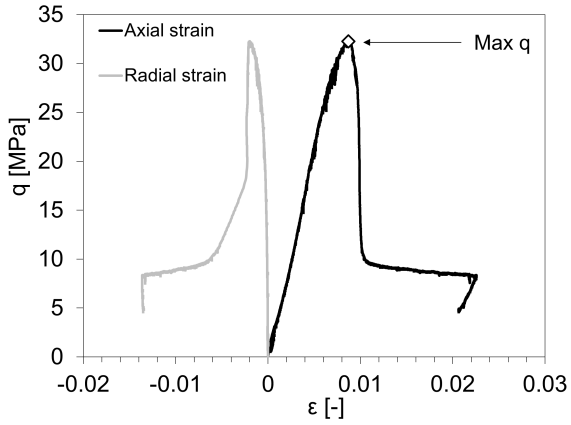

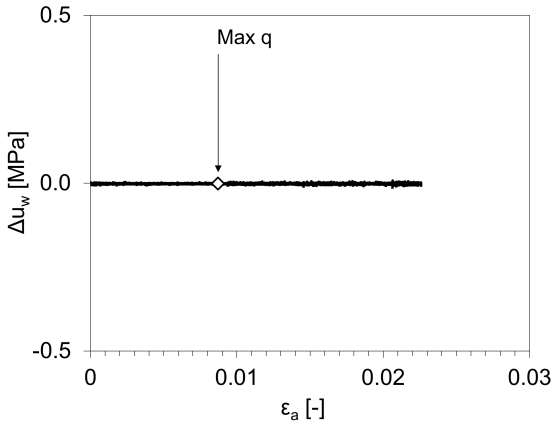

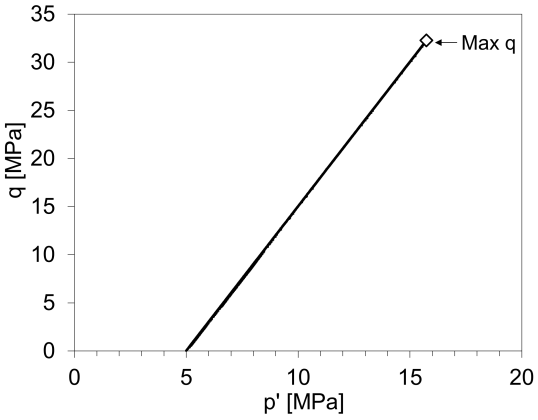

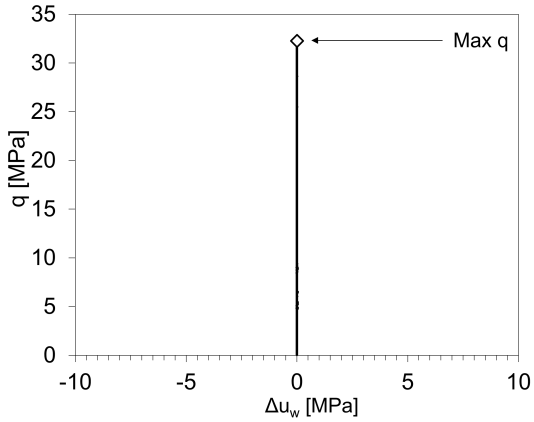

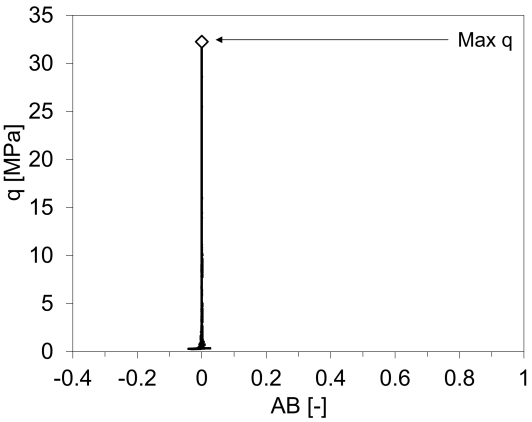

A7_TRU1_1_903_43S13CTCU

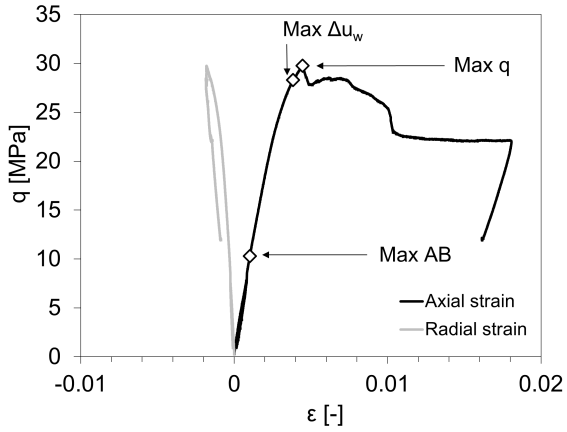

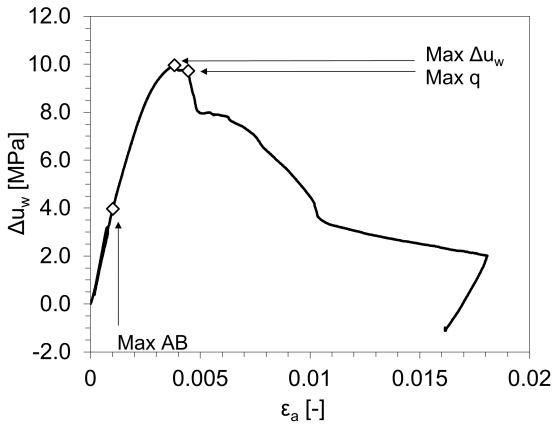

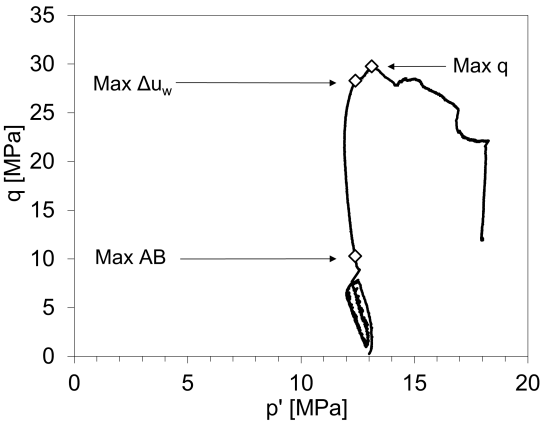

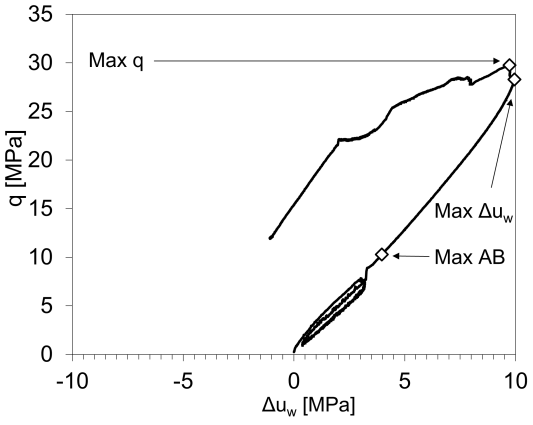

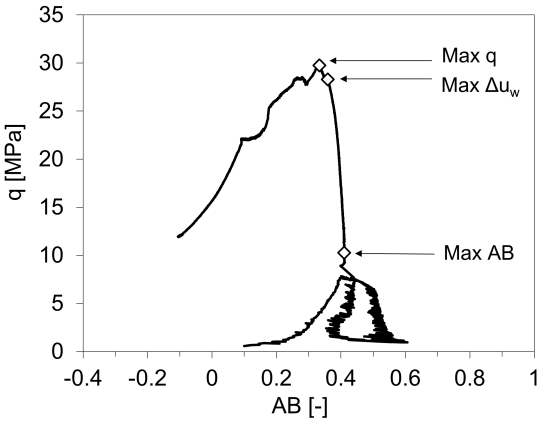

A8_TRU1_1_903_43S8CTCU

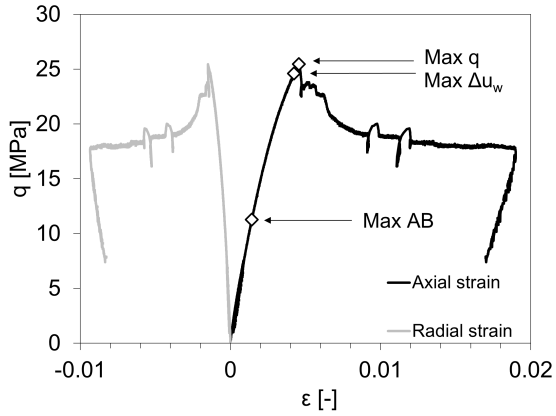

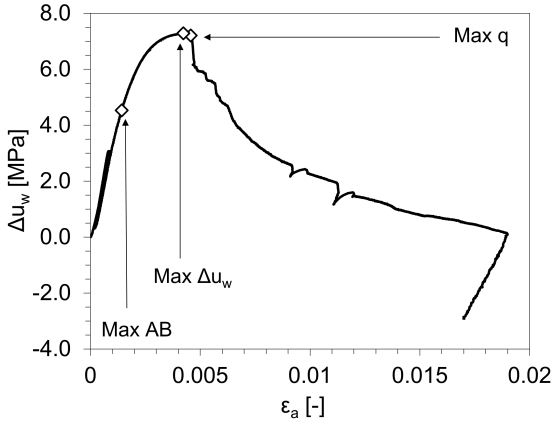

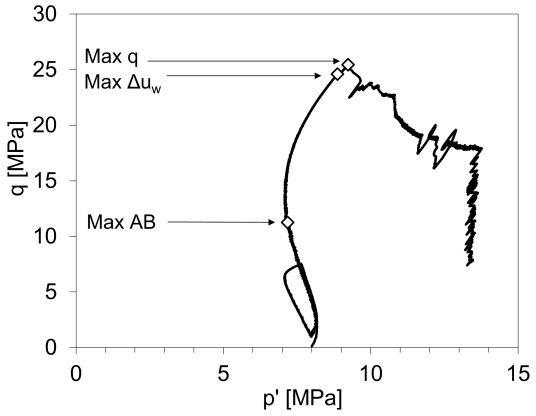

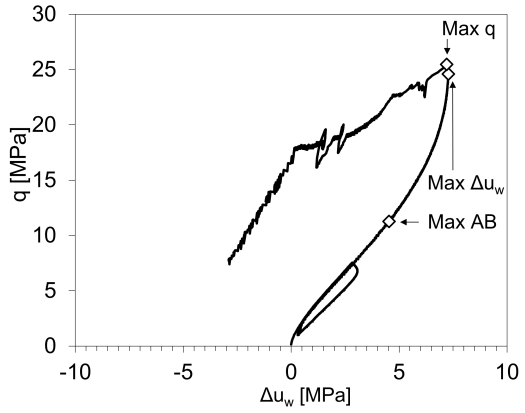

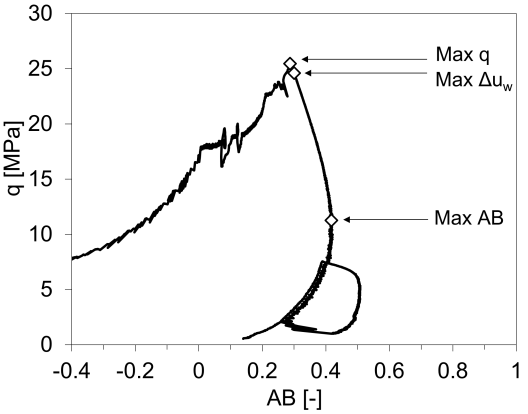

A5_TRU1_1_903_49P4CTCU

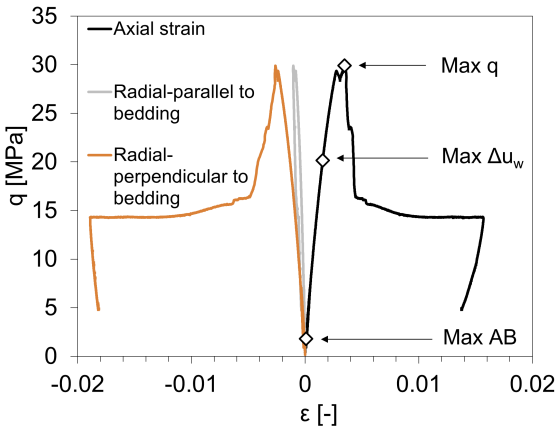

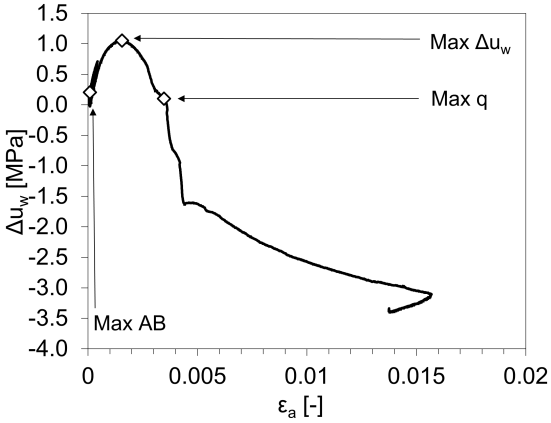

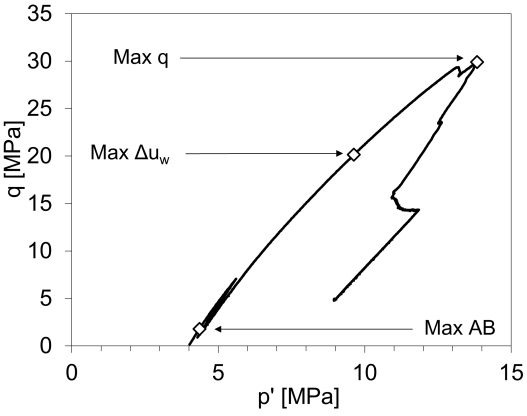

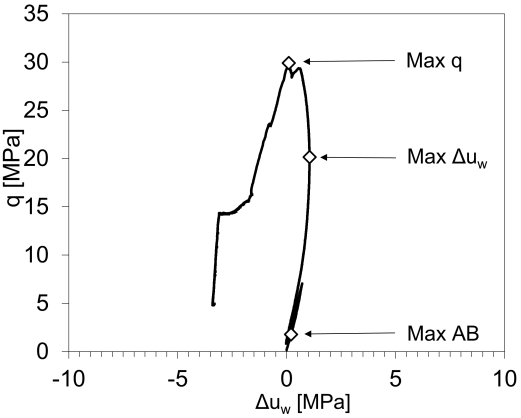

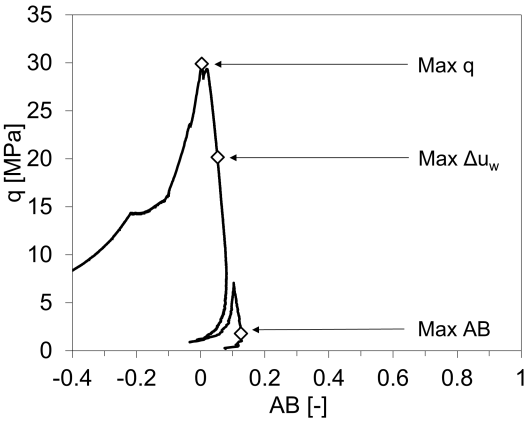

A6_TRU1_1_903_49P8CTCU

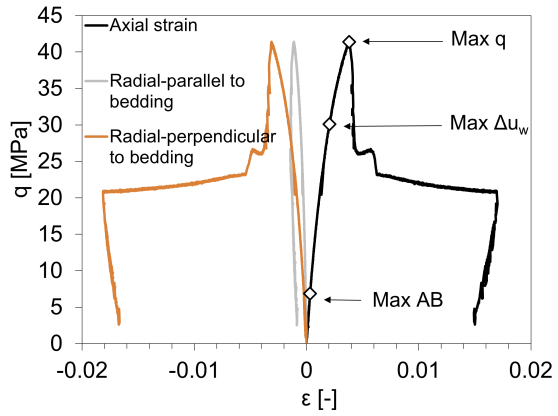

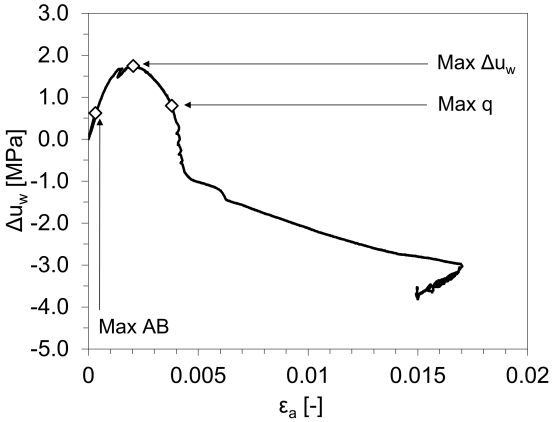

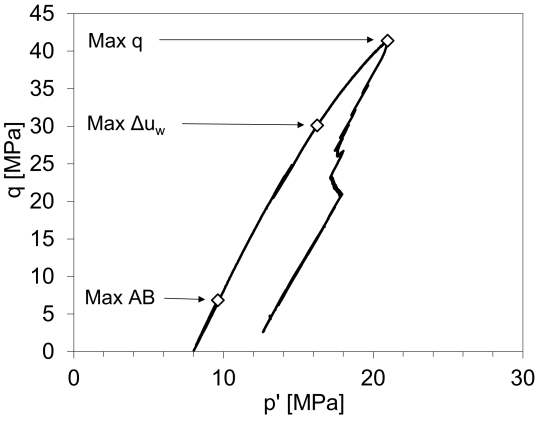

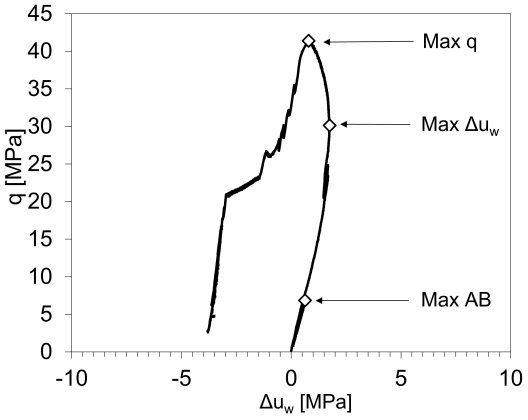

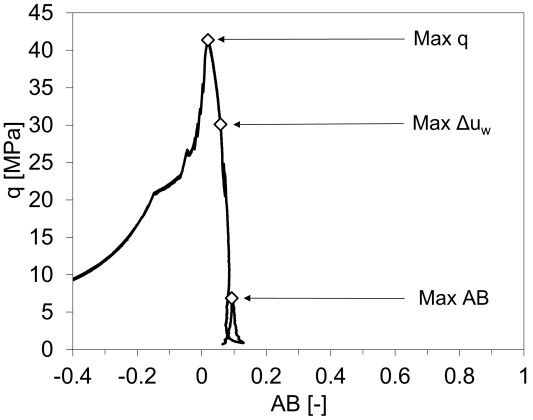

A9_TRU1_1_925_21_S13CTCU

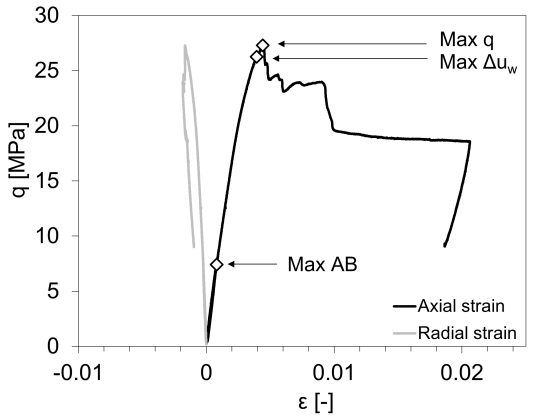

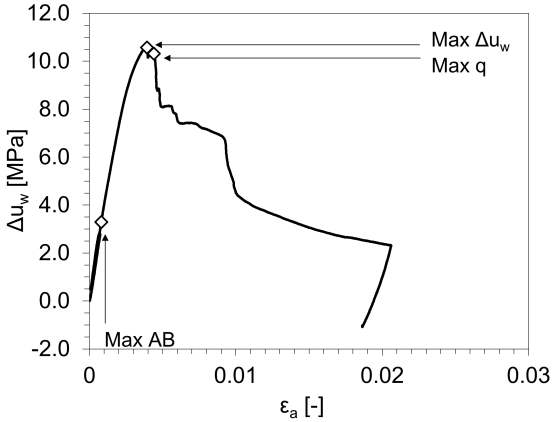

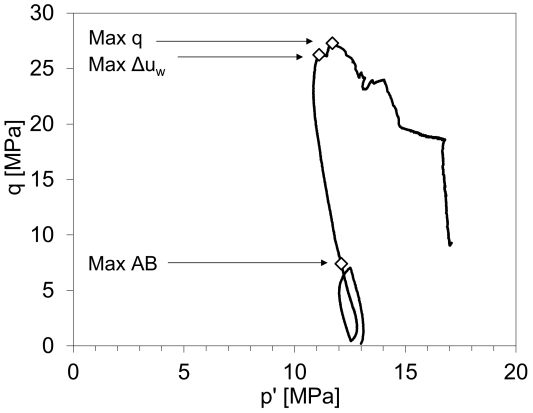

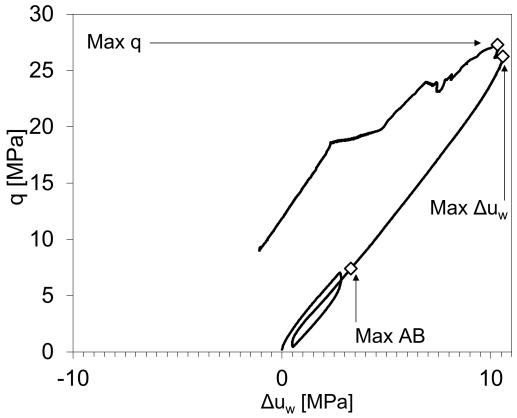

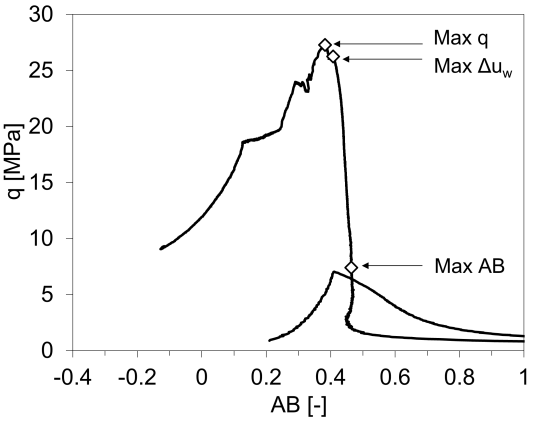

A10_TRU1_1_925_21S8CTCU

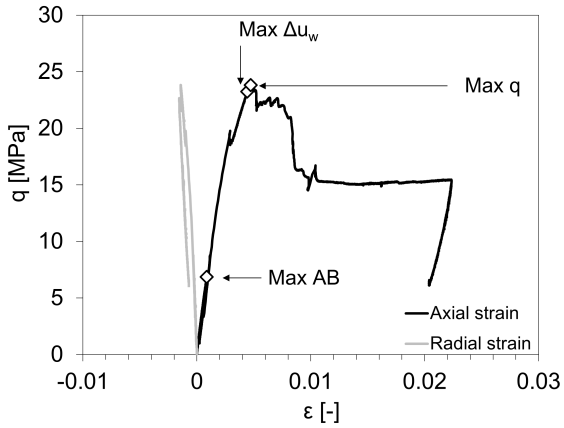

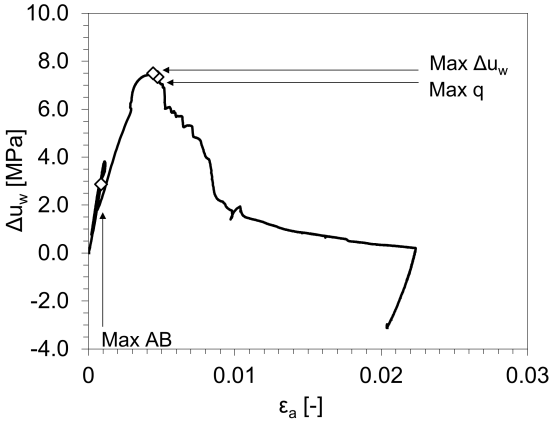

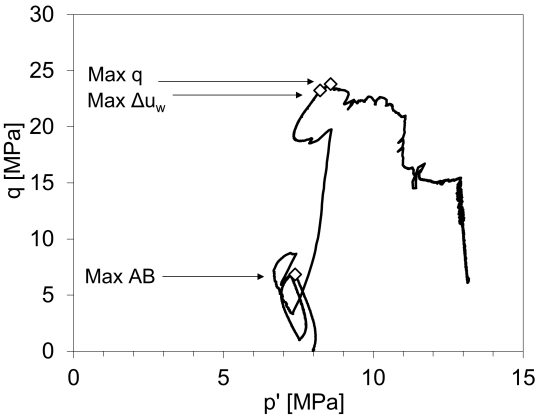

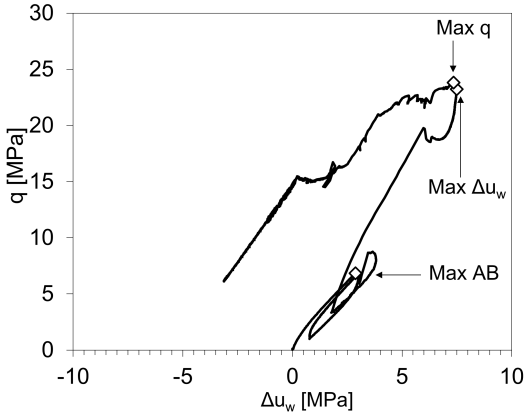

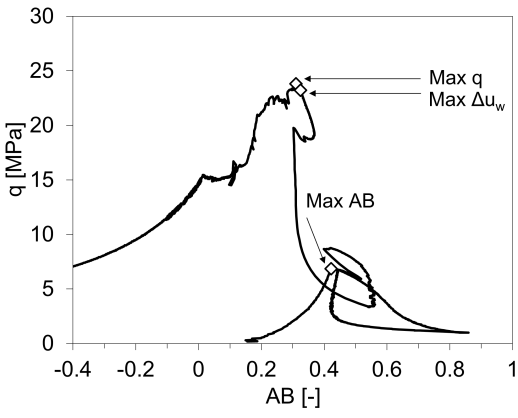

Appendix D Mineralogical analysis of the tested samples

Mineralogical analysis and grain density performed by the University of Bern on a series of specimens previously mechanically tested in triaxial or oedometric conditions; *a* indicates mineralogical analysis is performed on a specimen that was not used in the mechanical programme. The specimens used for mineralogy-only are considered representative for the mineralogical composition of the portion of core from which it was extracted (i.e. lateral variability is negligible). The ID of one of the specimens sourced at the same depth is reported.

Specimen ID	**S** [wt.-%]	**C(inorg)** [wt.-%]	**C(org)** [wt.-%]	**Quartz** [wt.-%]	**K-feldspar** [wt.-%]	**Plagioclase** [wt.-%]	**Calcite** [wt.-%]	**Dolomite/Ankerite** [wt.-%]	**Siderite** [wt.-%]	**Pyrite** [wt.-%]	**Clay minerals** [wt.-%]	**Grain density** [g/cm^3]	**Grain density STDEV** [10^{-4}/cm^3]
D01OED_TRU1_1	0.9	2.2	0.6	26.4	5.4	2.2	18.4	0.0	0.0	1.6	45.3	2.716	8
D01_OS_TRU1_1	0.8	2.3	0.6	26.2	5.4	2.5	19.0	0.0	0.0	1.5	44.9	2.712	9
D05OED_TRU1_1	0.9	2.3	0.6	25.7	5.3	2.7	18.9	0.0	0.0	1.7	45.2	2.720	8
A15_TRU1_1_798_21S10CTCU[a]	0.0	4.7	0.4	38.5	5.4	3.1	39.3	tr	0.0	0.1	13.2	2.682	4
A16_TRU1_1_811_05S10CTCU[a]	0.2	2.3	0.5	45.5	5.9	3.4	19.6	0.0	0.0	0.5	24.7	2.671	4
A01OED_TRU1_1	0.4	1.1	1.0	19.8	5.3	3.8	5.6	0.0	3.9	0.7	59.8	2.691	4
A02OED_TRU1_1	0.4	1.1	1.0	25.5	5.4	3.7	9.5	0.0	0.0	0.7	54.2	2.677	5
A2_TRU1_1_836_5P11CTCU	0.4	1.1	1.2	22.8	5.4	2.9	5.6		3.7	0.8	57.6	2.690	3
A1_TRU1_1_836_5P5CTCU	0.4	1.2	1.0	24.9	6.9	3.4	10.1	0.0	0.0	0.8	52.9	2.699	4
A4_TRU1_1_836_55S8CTCU	0.3	1.2	0.9	23.6	5.7	3.6	7.0	0.0	3.6	0.6	54.9	2.697	5
B4_TRU1_1_851_86P13CTCU[a]	0.4	1.3	2.0	24.3	4.7	2.6	7.7	0.0	3.5	0.7	54.4	2.639	7
B1_TRU1_1_851_94S13CTCU[a]	0.3	1.3	1.1	24.2	6.8	3.0	11.0	tr	0.0	0.5	53.4	2.680	2
B9_TRU1_1_875_56P8CTC[a]	0.2	1.7	1.0	21.7	4.4	3.2	9.3	tr	5.2	0.3	54.8	2.686	3
B13_TRU1_1_875_65P9TC[a]	0.2	1.5	1.0	23.7	5.3	2.2	8.8	tr	4.1	0.3	54.5	2.680	9
B8_TR1_1_875_56_P13CTCU	0.2	1.6	1.0	22.8	5.0	3.2	9.1	0.0	4.9	0.4	53.6	2.698	7
B6_TRU1_1_875_77S13CTCU[a]	0.2	1.4	1.1	25.2	5.7	3.5	8.1	0.0	3.8	0.4	52.2	2.678	5
B10_TRU1_1_875_84Z13CTCU[a]	0.3	1.4	1.3	22.3	4.4	2.9	7.6	0.0	4.8	0.6	55.9	2.668	9
D03OED_TRU1_1	0.2	1.5	1.0	24.2	4.7	3.4	9.5	0.0	3.6	0.3	53.3	2.680	64
D02OED_TRU1_1	0.6	1.5	0.9	23.8	5.2	3.1	9.5	0.0	3.9	1.0	52.6	2.700	7
D04_OS_TRU1_1	0.7	2.2	0.8	24.0	4.4	3.3	10.7	0.0	8.8	1.3	46.7	2.743	13
D04OED_TRU1_1	0.2	1.9	0.9	21.7	3.2	2.9	9.4	tr	7.6	0.3	53.9	2.712	9
C3_TRU1_1_895_15Z5CTCU[a]	0.1	0.8	1.3	23.1	5.1	2.7	5.0		2.2	0.2	60.4	2.655	4
A04OED_TRU1_1	0.2	1.5	0.9	22.7	5.4	3.0	7.1	0.0	6.5	0.3	54.1	2.697	4
A8_TRU1_1_903_43S8CTCU	0.2	1.5	1.0	24.0	5.3	3.3	7.3	0.0	5.8	0.4	53.0	2.691	4
A12_TRU1_1_903_32P5CTC	0.2	1.2	1.1	21.6	5.1	3.0	6.3	0.0	4.6	0.3	58.0	2.691	8
A5_TRU1_1_903_49P4CTCU	0.1	1.3	1.0	23.8	4.2	4.1	6.9	0.0	4.5	0.2	55.2	2.693	4
A03OED_TRU1_1	0.1	1.5	0.9	23.2	6.0	3.4	12.8	0.0	0.0	0.3	53.5	2.707	4
A02_OS_TRU1_1	0.1	1.2	1.2	20.7	5.6	3.2	9.9	0.0	0.0	0.2	59.2	2.668	4
A03_OS_TRU1_1	0.1	1.9	1.0	21.2	4.0	3.3	7.1	0.0	10.4	0.3	52.7	2.722	13
A05OED_TRU1_1[a]	0.3	1.2	0.9	14.6	5.3	2.9	6.9	0.0	3.3	0.5	65.6	2.700	3
A05OED_TRU1_1	0.4	1.2	0.8	14.9	3.9	2.4	6.8	tr	3.9	0.8	66.5	2.702	9
A01_OS_TRU1_1	0.4	1.4	0.8	15.1	4.5	2.6	8.3	tr	3.7	0.8	64.2	2.708	10
A9_TRU1_1_925_21S13CTCU[a]	0.4	1.3	0.8	15.3	4.0	3.2	7.7	0.0	4.0	0.7	64.4	2.704	5
A10_TRU1_1_925_21S8CTCU	0.5	1.4	0.8	15.8	4.9	2.2	8.4	0.0	3.3	0.9	63.7	2.710	7
A06OED_TRU1_1	0.2	1.4	0.8	25.2	5.5	2.5	8.1	tr	3.7	0.4	53.8	2.714	10

Appendix E Triaxial test results

Tab. E-1: Wave velocities recorded at the beginning of the shearing phase

Specimen ID, specimen geometry, mean effective and deviatoric stress (if applicable) at which the measurements were performed, P and S waves in the cylinder axis direction (Vp, Vs), P wave in the direction perpendicular to the axis direction (Vph). For specimen geometry see Fig. 4-1.

Specimen ID	Specimen geometry	p' [MPa]	q [MPa]	Vp [m/s]	Vs [m/s]	Vph [m/s]
A15_TRU1_1_798_21S10CTCU	S	10		3'958	2'278	
A16_TRU1_1_811_05S10CTCU	S	10		3'429	1'939	
A1_TRU1_1_836_5P5CTCU	P	5		3'988	2'053	
A2_TRU1_1_836_5P11CTCU	P	11		4'269	2'488	
A4_TRU1_1_836_55S8CTCU	S	8		3'243	1'979	
A3_TRU1_1_836_55S13CTCU	S	13				
A13_TRU1_1_836_64Z13CTCU	Z	13		3'912	1'981	
A14_TRU1_1_836_64Z7CTCU	Z	7		3'538	1'744	
B4_TRU1_1_851_86P13CTCU	P	13		4'224	2'271	3'445
B5_TRU1_1_851_88P7CTCU	P	7		4'158	2'110	3'696
B1_TRU1_1_851_94S13CTCU	S	13		3'343	1'495	4'285
B2_TRU1_1_851_94S10CTCU	S	10		3'173	1'399	4'255
B3_TRU1_1_851_70S7CTCU	S	7		3'142	1'236	4'246
B8_TRU1_1_875_56_P13CTCU	P	13		4'350	2'572	
B9_TRU1_1_875_56P8CTC	P	8		4'128	2'489	
B13_TRU1_1_875_65P9CTCU	P	9		4'159	1'617	
B12_TRU1_1_875_69Z13CTCU	Z	13		3'940	2'384	
B7_TRU1_1_875_76_S7CTCU	S	7		3'303	1'703	
B6_TRU1_1_875_77S13CTCU	S	13		3'460		
B10_TRU1_1_875_84Z13CTCU	Z	13		3'827	2'253	
B11_TRU1_1_875_84Z7CTCU	Z	7		3'744	2'099	
C1_TRU1_1_895_08P13CTCU	P	14.2	8.7	4'121	2'267	
C2_TRU1_1_895_08P5CTCU	P	5.9	6.3	3'943	1'997	
C4_TRU1_1_895_08S4CTCU	S	3.9	5.5	3'037	1'507	
C5_TRU1_1_895_08S13CTCU	S	11.6	8.3	3'199	1'554	
C3_TRU1_1_895_15Z5CTCU	Z	4.5	4.4	3'561	2'148	
A12_TRU1_1_903_32P5CTC	P	5		4'133	2'427	
A11_TRU1_1_903_4S5CTC	S	5		3'067	1'889	
A7_TRU1_1_903_43S13CTCU	S	13		3'275	1'635	
A8_TRU1_1_903_43S8CTCU	S	8		3'343	1'835	
A5_TRU1_1_903_49P4CTCU	P	4		4'043	2'338	
A6_TRU1_1_903_49P8CTCU	P	8		4'473	2'426	
A10_TRU1_1_925_21S8CTCU	S	8		3'096	1'595	
A9_TRU1_1_925_21_S13CTCU	S	13		3'059	1'230	

Specimen ID and corresponding initial characteristics are reported in Tab. 6-2, along with the results from the triaxial tests from the pre-shearing phases. Tab. E-2 includes:

- Specimen ID
- Core depth
- Formation
- Specimen geometry
- Bulk modulus ρ_{bulk} [g/cm^3]
- Initial void ratio, *computed using a reference solid density of 2.70 g/cm^3
- Initial and final water content
- Results of the Skempton's B check (B value and average mean effective stress at which it was obtained
- Swelling pressure obtained at the end of the saturation (radial and axial)
- Consolidation coefficient, obtained during the consolidation phase, and corresponding mean effective stress

Tab. E-3 presents the results from the shearing phases, including:

- Undrained elastic properties: Elastic modulus [GPa], Small Strain elastic modulus [GPa], Ratio of radial to axial strain [-], Ratio of radial (parallel to bedding) to axial strain [-] (only for P samples), Mean effective stress at which the elastic properties were computed [MPa]
- Drained elastic properties: Young's modulus E [GPa], Poisson's ratios $\nu_{\perp}$ (ratio of radial to axial strain) [-] and $\nu_{//}$ (ratio of radial (parallel to bedding) to axial strain) [-], and mean effective stress at which the elastic properties were computed
- Peak strength: Mean effective stress and deviatoric stress at peak
- Maximum AB value: Mean effective stress and deviatoric stress at the maximum AB value
- Maximum pore pressure: Mean effective stress and deviatoric stress attained at the maximum pore pressure
- Post peak strength: Mean effective stress and deviatoric stress

Tab. E-2: Triaxial test results (part 1)

For specimen geometry see Fig. 4-1.

Specimen ID	**Specimen geometry**	**ρ_{bulk}**	**e_0**	**Water content**		**B check**		**Swelling pressure**		**Consolidation phase**		**Strain rate**	**Stress path**
		[g/cm^3]	[-]	Initial [%]	Final [%]	p' [MPa]	B [-]	Axial [MPa]	Radial [MPa]	p' [MPa]	c_v [mm^2/s]	$\dot{\varepsilon}$ [s^{-1}]	
A15_TRU1_1_798_21S10CTCU	S	2.56	0.079	2.33	3.14	13.3	0.65	13.0	3.2	10	1.4E-03	5E-07	CTCU
A16_TRU1_1_811_05S10CTCU	S	2.52	0.117	4.18	5.29	6.0	0.80	5.5	1.7	10	2.0E-03	5E-07	CTCU
A1_TRU1_1_836_5P5CTCU	P	2.53	0.118	4.65	5.07	27.0	0.69	26.7	15.5	5	7.2E-04	1E-07	CTCU
A2_TRU1_1_836_5P11CTCU	P	2.50	0.132	4.71	5.33	29.0	0.70	29.0	19.0	11	9.9E-04	1E-07	CTCU
A4_TRU1_1_836_55S8CTCU	S	2.51	0.127	4.72	5.31	29.5	0.65	29.0	8.0	8	1.1E-03	1E-07	CTCU
A3_TRU1_1_836_55S13CTCU	S	2.52	0.123	4.70	4.86	23.9	0.63	23.8	7.8	13	1.1E-03	1E-07	CTCU
A13_TRU1_1_836_64Z13CTCU	Z	2.52	0.118	4.42	4.66	20.0	0.72	19.3	7.9	13	9.9E-04	1E-07	CTCU
A14_TRU1_1_836_64Z7CTCU	Z	2.51	0.122	4.51	5.11	18.5	0.74	17.6	6.6	7	6.4E-04	1E-07	CTCU
B4_TRU1_1_851_86P13CTCU	P	2.54	0.105	3.88	-	16.9	0.71	16.8	16.1	13	8.8E-04	7E-08	CTCU
B5_TRU1_1_851_88P7CTCU	P	2.55	0.105	4.28	4.57	19.6	0.83	18.8	17.8	7	4.9E-04	7E-08	CTCU
B1_TRU1_1_851_94S13CTCU	S	2.54	0.112	4.44	4.68	7.6	0.80	16.8	9.0	13	1.9E-03	9E-08	CTCU
B2_TRU1_1_851_94S10CTCU	S	2.51	0.130	4.96	5.18	10.0	0.77	19.5	11.1			9E-08	CTCU
B3_TRU1_1_851_94S7CTCU	S	2.52	0.121	4.86	5.06	9.8	0.79	19.6	12.4			9E-08	CTCU
B8_TRU1_1_875_56_P13CTCU	P	2.55	0.108	4.59	4.59	26.0	0.77	26.3	21.7	13	5.9E-04	7E-08	CTCU
B9_TRU1_1_875_56P8CTC	P	2.55	0.108	4.56	4.71	27.0	0.80	27.3	25.0	8	7.1E-04	1E-08	CTC
B13_TRU1_1_875_65P9TC	P	2.54	0.109	4.49	4.99	30.0	0.80	30.0	27.9	9	8.9E-04	1E-08	TC
B12_TRU1_1_875_69Z13CTCU	Z	2.53	0.114	4.48	4.75	33.0	0.77	33.2	31.2	13	1.0E-03	7E-08	CTCU
B7_TRU1_1_875_76_S7CTCU	S	2.53	0.119	4.89	4.93	25.3	0.80	24.9	17.7	7	9.9E-04	9E-08	CTCU
B6_TRU1_1_875_77S13CTCU	S	2.54	0.115	4.83	4.71	27.3	0.78	27.1	21.8	13	1.1E-03	9E-08	CTCU
B10_TRU1_1_875_84Z13CTCU	Z (70°)	2.53	0.122	4.96	4.99	23.4	0.78	23.9	20.6	13	6.5E-04	9E-08	CTCU
B11_TRU1_1_875_84Z7CTCU	Z (70°)	2.53	0.117	4.85	4.58	25.0	0.77	24.6	22.0	7	7.1E-04	7E-08	CTCU
C1_TRU1_1_895_08P13CTCU	P	2.52	0.125	5.00	4.85	10.0	0.91					1E-07	CTCU
C2_TRU1_1_895_08P5CTCU	P	2.50	0.130	4.80	5.04	2.0	0.95					1E-07	CTCU
C4_TRU1_1_895_08S4CTCU	S	2.50	0.136	5.06	4.83	3.5	0.93					1E-07	CTCU
C5_TRU1_1_895_08S13CTCU	S	2.49	0.135	4.78	4.77	6.5	0.88			13.0	2.6E-04	1E-07	CTCU
C3_TRU1_1_895_15Z5CTCU	Z	2.50	0.133	5.01	5.06	2.5	0.93					1E-07	CTCU
A12_TRU1_1_903_32P5CTC	P	2.52	0.124	4.86	5.28	29.0	0.65	28.7	25.0	5	3.1E-04	2E-08	CTC
A7_TRU1_1_903_43S13CTCU	S	2.53	0.114	4.36	4.66	27.0	0.74	27.0	7.6	13	1.0E-03	1E-07	CTCU
A8_TRU1_1_903_43S8CTCU	S	2.53	0.115	4.51	5.10	27.0	0.72	27.0	15.0	8	7.3E-04	1E-07	CTCU
A11_TRU1_1_903_4S5CTC	S	2.53	0.112	4.37	4.94	28.0	0.64	28.0	9.0	5	6.1E-04	2E-08	CTC
A5_TRU1_1_903_49P4CTCU	P	2.52	0.122	4.74	5.10	27.0	0.63	26.0	13.0	4	7.9E-04	1E-07	CTCU
A6_TRU1_1_903_49P8CTCU	P	2.51	0.125	4.79	5.27	23.0	0.71	22.0	16.0	8	4.9E-04	1E-07	CTCU
A9_TRU1_1_925_21_S13CTCU	S	2.53	0.122	5.18	5.23	21.0	0.72	20.8	5.0	13	1.1E-03	1E-07	CTCU
A10_TRU1_1_925_21S8CTCU	S	2.53	0.123	5.25	5.41	25.8	0.68	25.4	11.6	8	7.4E-04	1E-07	CTCU

Tab. E-3: Triaxial test results (part 2)

[d] Drained elastic modulus

Specimen ID	**Undrained elastic properties**					**Drained elastic properties**				**Peak strength** [MPa]		**Max. AB value** [MPa]		**Max. pore pressure** [MPa]		**Post peak strength** [MPa]		**Post peak elastic properties**	
	p' [MPa]	Elastic modulus [GPa]	Small Strain modulus [GPa]	Ratio radial to axial strain [-]	Ratio radial (parallel to bedding) to axial strain [-]	p' [MPa]	E [GPa]	$\nu_{\perp}$ [-]	$\nu_{//}$ [-]	q [MPa]	p' [MPa]	q [MPa]	p' [MPa]	q [MPa]	p' [(MPa]	q [MPa]	p' [MPa]	p' [MPa]	E [GPa]
A15_TRU1_1_798_21S10CTCU	11.4	21.9	25.4	0.34						91.2	45.4	10.2	12.1	48.8	20.6	45.2	30.1	30.0	9.2
A16_TRU1_1_811_05S10CTCU	10.4	12.8	17.1	0.42						67.1	38.3	8.2	10.3	33.6	15.8	52.0	35.5	35.4	8.7
A1_TRU1_1_836_5P5CTCU	6.5	14.2	17.9	0.64	0.17					26.8	12.1	2.0	5.4	25.1	11.4	15.8	13.0	13.4	8.7
A2_TRU1_1_836_5P11CTCU	12.7	20.0	23.4	0.59	0.12					38.0	20.8	10.8	13.5	36.0	19.9	21.0	20.9	20.6	
A4_TRU1_1_836_55S8CTCU	7.7	8.8	11.4	0.32						23.8	9.5	7.8	7.5	23.1	8.8	13.7	11.8	13.1	7.1
A3_TRU1_1_836_55S13CTCU	12.8	10.1	12.4	0.32						30.6	15.3	8.3	12.5	27.7	13.1	19.8	20.4	20.4	4.3
A13_TRU1_1_836_64Z13CTCU										26.6	17.6	14.1	15.2	26.0	17.3	17.0	18.1	18.2	9.0
A14_TRU1_1_836_64Z7CTCU										18.7	10.1	4.6	7.5	17.9	9.8	10.8	10.7	12.8	4.4
B4_TRU1_1_851_86P13CTCU	14.7	23.8	24.8	0.41	0.25					50.0	28.5	6.9	14.7	37.0	23.1	28.0	25.9	25.9	15.4
B5_TRU1_1_851_88P7CTCU	8.6	17.5	23.0	0.43	0.23					40.9	20.3	5.9	8.4	25.0	13.9	26.4	21.0	20.7	14.7
B1_TRU1_1_851_94S13CTCU	11.9	10.0	11.6	0.26						28.8	13.4	10.3	11.8	27.6	12.1	18.3	15.6	15.6	7.0
B2_TRU1_1_851_94S10CTCU	9.0	9.2	13.3	0.35						24.8	10.6	5.8	9.4	24.4	10.2	13.5	13.0	12.9	5.8
B3_TRU1_1_851_94S7CTCU												4.8	6.6						
B8_TRU1_1_875_56_P13CTCU	14.5	18.6	20.4	0.42	0.27					46.1	26.8	7.0	14.5	34.9	21.4	21.3	22.2	22.2	10.2
B9_TRU1_1_875_56P8CTC						10.3	15.7	0.38	0.30	38.7	20.9					13.9	12.6	12.6	8.6
B13_TRU1_1_875_65P9CTCU										22.3	9.0					12.1	9.0		
B12_TRU1_1_875_69Z13CTCU										29.7	18.8	10.3	14.6	29.0	18.6	14.0	17.6		
B7_TRU1_1_875_76_S7CTCU	6.8	8.2	10.0	0.35						24.5	9.6	4.1	7.1	22.7	8.6	12.7	12.1	12.1	5.0
B6_TRU1_1_875_77S13CTCU	12.4	11.0	12.7	0.31						31.7	17.6	6.9	12.4	27.0	12.7	19.4	19.7	19.7	5.4
B10_TRU1_1_875_84Z13CTCU										33.7	21.0	6.5	14.6	30.0	19.5	19.6	19.4		
B11_TRU1_1_875_84Z7CTCU										26.3	13.5	5.8	8.0	22.5	12.1	12.7	12.5		
C1_TRU1_1_895_08P13CTCU	15.2	14.9	22.0	0.46	0.34					34.3	19.8	1.8	13.1	31.8	19.0	21.8	19.5		12.0
C2_TRU1_1_895_08P5CTCU										9.6	7.4	1.4	4.9	7.3	5.7	7.5	7.8		
C4_TRU1_1_895_08S4CTCU	3.7	4.3	5.7	0.33						15.1	5.6	1.3	4.4	11.7	4.2				
C5_TRU1_1_895_08S13CTCU	10.7	7.5	10.5	0.33						28.2	12.4	13.5	10.3	25.4	10.2	16.8	18.6	18.7	4.4
C3_TRU1_1_895_15Z5CTCU										7.2	4.6	6.0	4.1	6.9	4.2	5.5	6.0		
A12_TRU1_1_903_32P5CTC						7.7	16.2	0.50	0.13	35.9	16.9					11.1	8.7		
A11_TRU1_1_903_4S5CTC						6.0	3.6	0.10		32.3	15.7					8.4	7.8	7.7	2.2
A7_TRU1_1_903_43S13CTCU	12.3	10.0	12.9	0.26						29.8	13.1	10.3	12.4	28.3	12.4	22.1	18.4	18.3	5.7
A8_TRU1_1_903_43S8CTCU	7.6	9.1	11.9	0.27						25.5	9.2	11.3	7.1	24.6	8.9	17.7	13.7	13.8	4.6
A5_TRU1_1_903_49P4CTCU	5.6	16.8	20.8	0.65	0.17					29.9	13.8	1.8	4.4	20.2	9.6	13.8	11.7	11.8	6.3
A6_TRU1_1_903_49P8CTCU	9.7	21.5	22.5	0.57	0.15					41.4	20.9	6.9	9.7	30.1	16.2	20.8	17.8	17.9	7.8
A10_TRU1_1_925_21S8CTCU	7.4	8.6	10.8	0.32						23.8	8.6	6.8	7.4	23.2	8.3	15.1	12.0	12.9	5.2
A9_TRU1_1_925_21_S13CTCU	12.5	10.0	12.0	0.29						27.3	11.7	7.4	12.1	26.2	11.1	19.0	15.7	16.7	4.6

Appendix F Test results in oedometric conditions

Results of the oedometric test results are here reported in terms of oedometric curves (void ratio at the end of the primary consolidation) obtained for each test. In each graph the void ratio (e) versus the vertical effective stress (σ'_v) are reported. In each graph, it is highlighted the initial void ratio, the swelling pressure attained at the end of the resaturation phase (S_p), the yield stress (σ'_y) obtained through the Casagrande's construction, the compressibility (C_c) and the unloading (C_s) indexes.

A01OED_TRU1_1

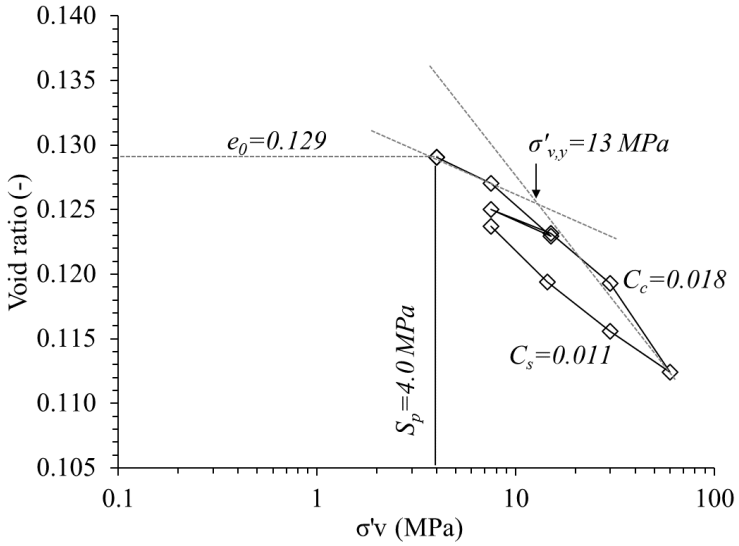

A02OED_TRU1_1

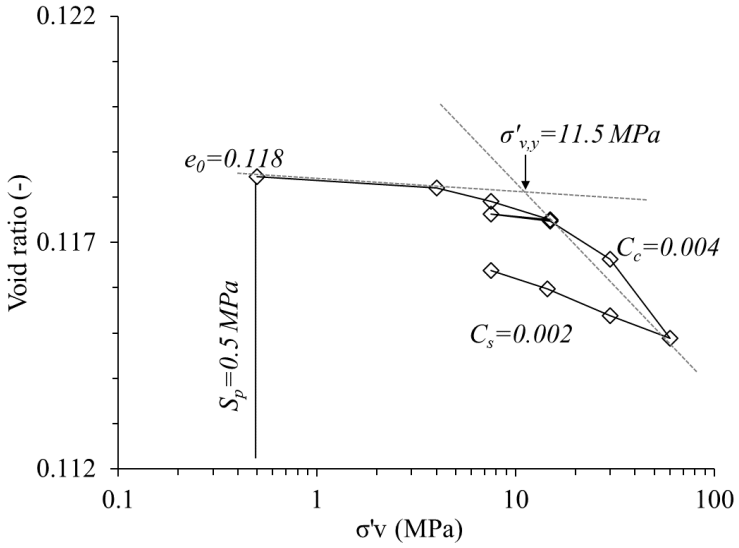

A03OED_TRU1_1

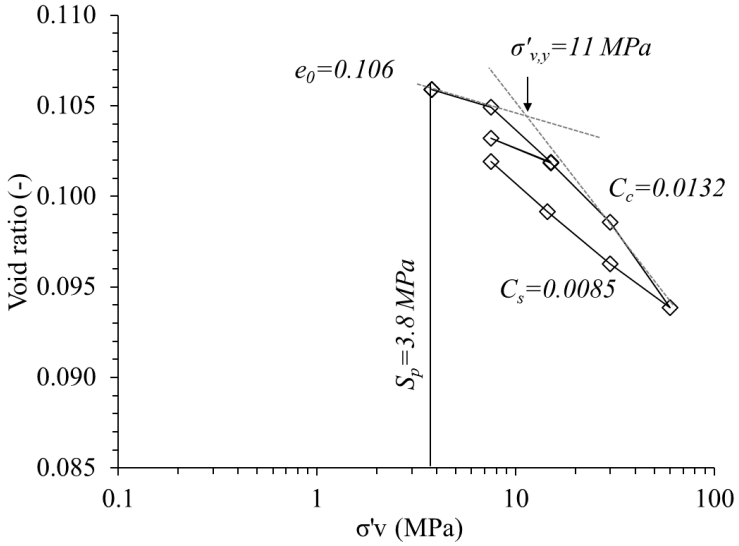

A04OED_TRU1_1

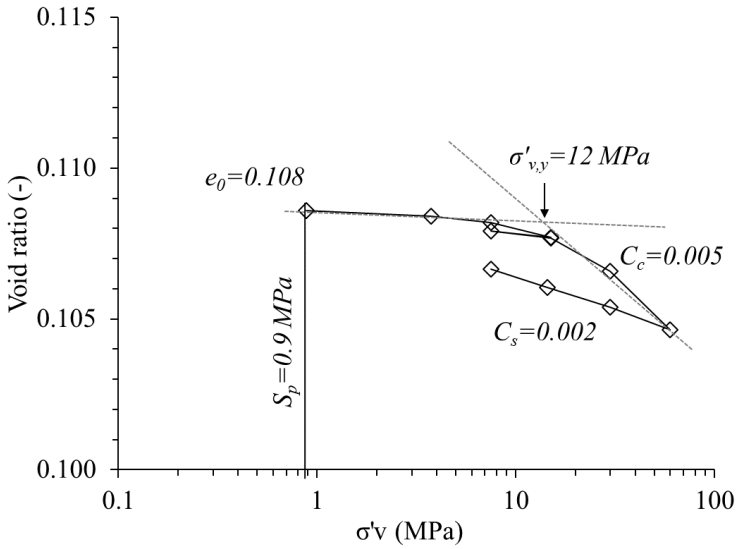

A05OED_TRU1_1

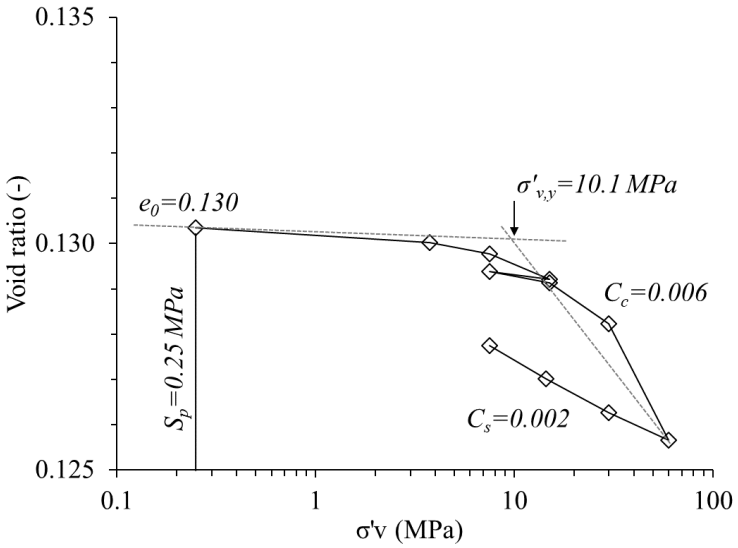

A06OED_TRU1_1

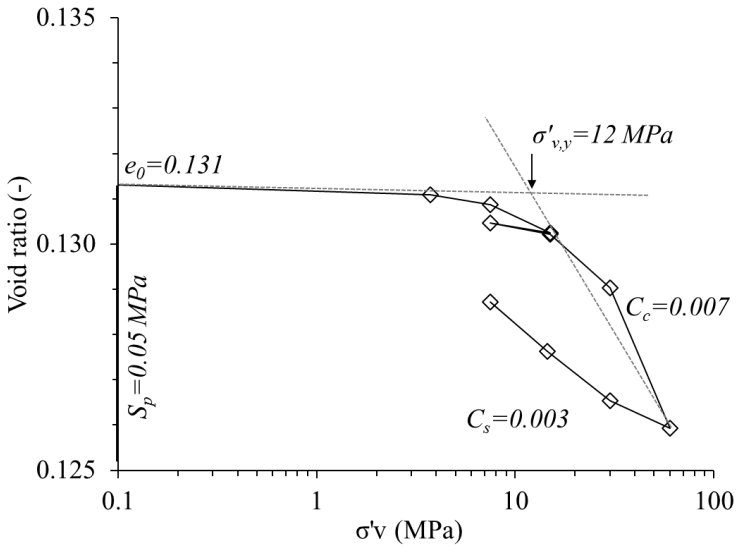

D01OED_TRU1_1

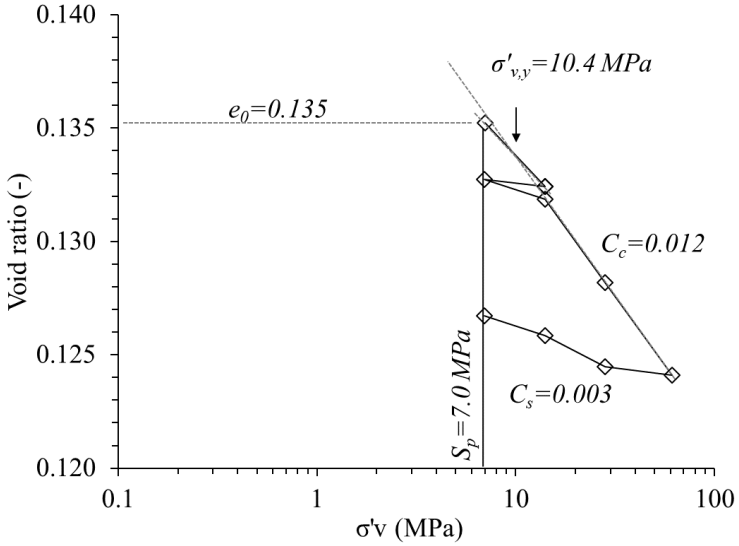

D02OED_TRU1_1

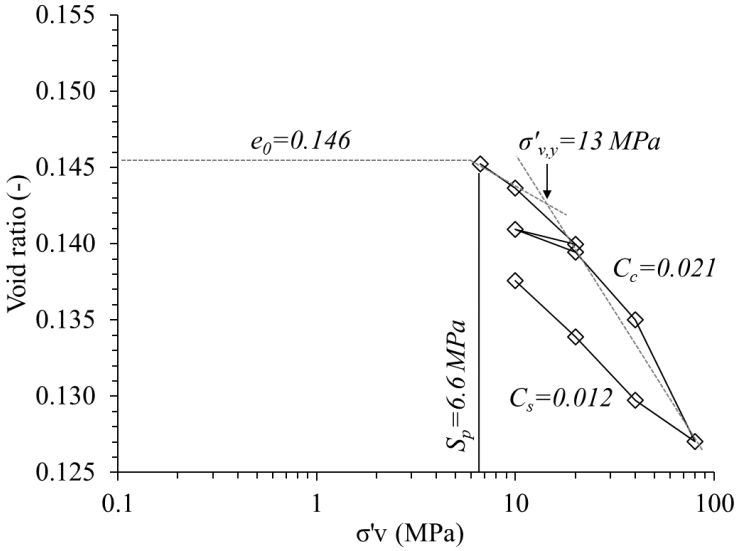

D03OED_TRU1_1

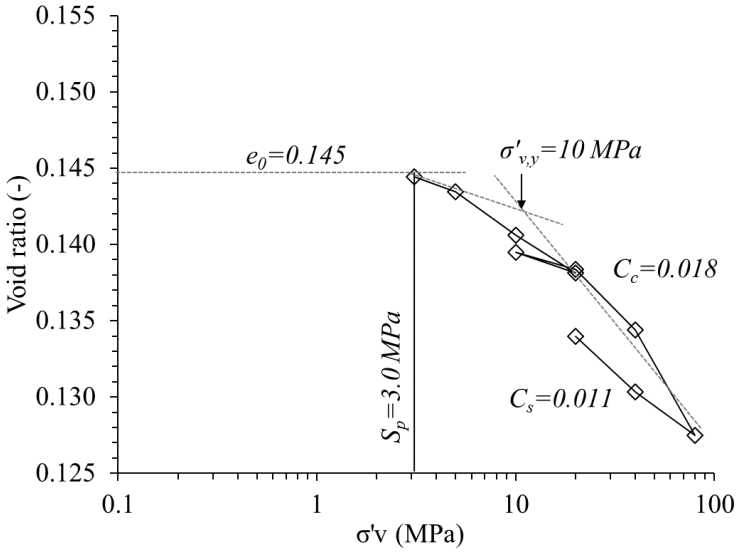

D04_OED_TRU1_1

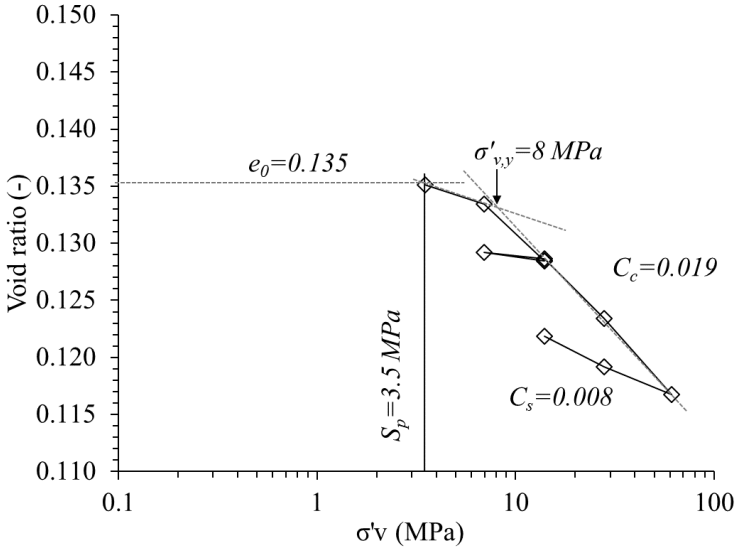

D05OED_TRU1_1

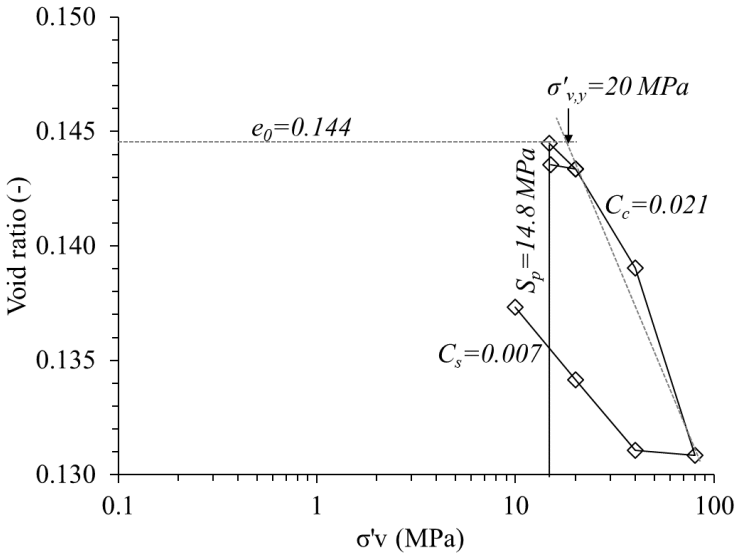

D06OED_TRU1_1

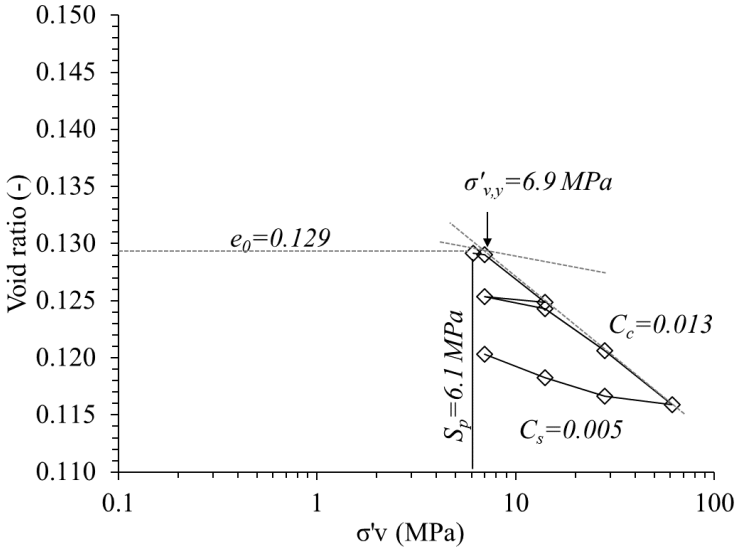

The results of the one-dimensional swelling tests are reported below.

A01OS_TRU1_1

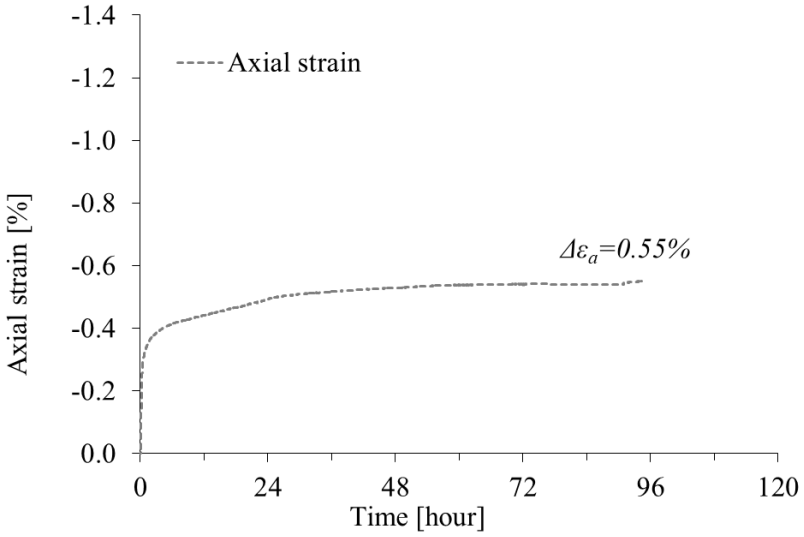

A02OS_TRU1_1

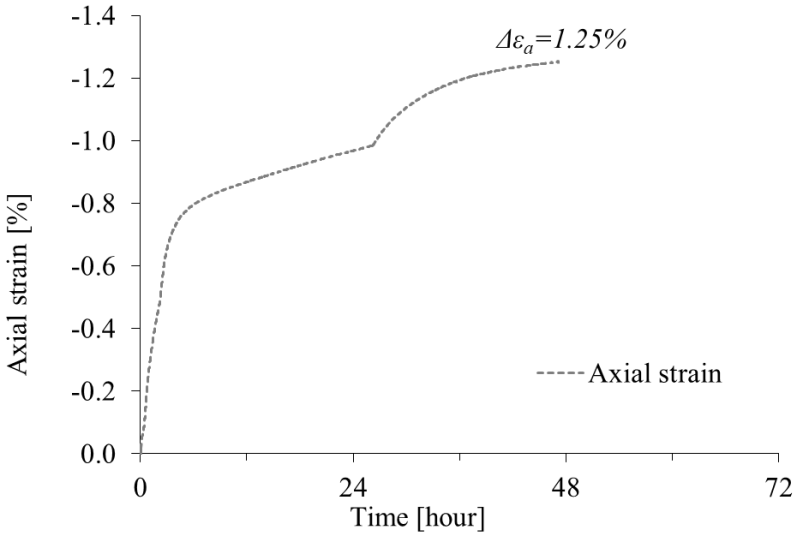

A03OS_TRU1_1

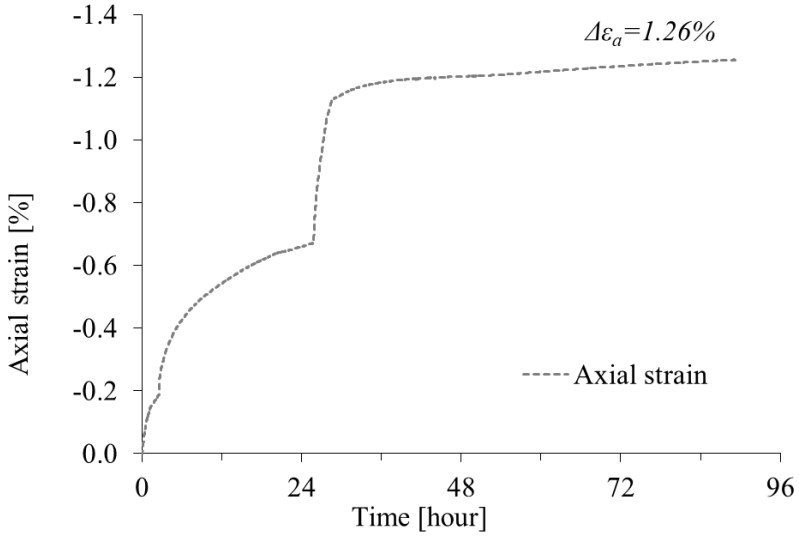

D01OS_TRU1_1

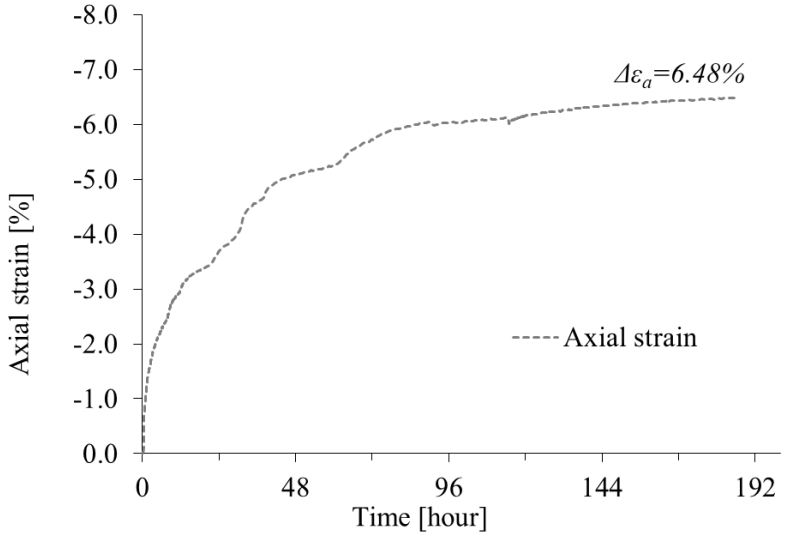

D02OS_TRU1_1

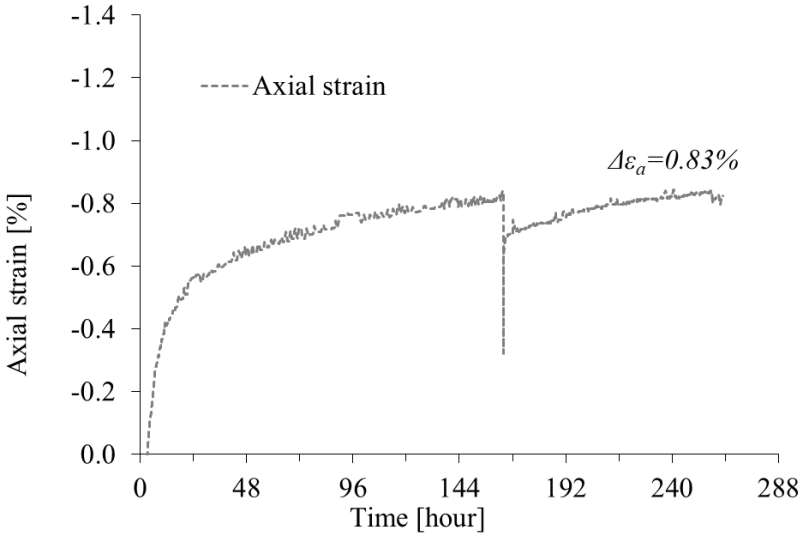

D03OS_TRU1_1

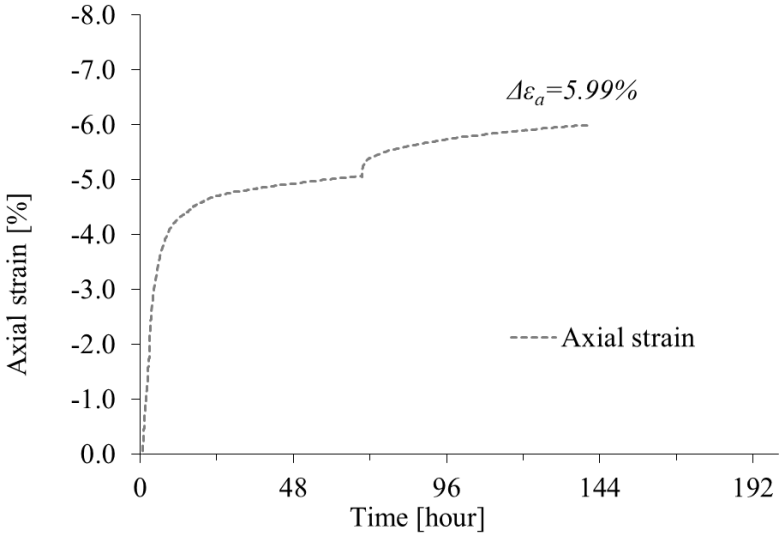

D04OS_TRU1_1

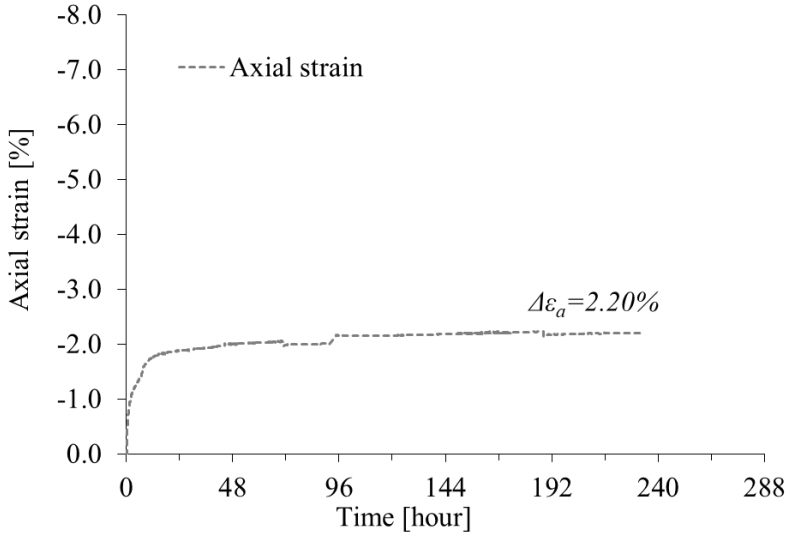
-8.0
-7.0
-6.0
-5.0
-4.0
-3.0
-2.0
-1.0
0.0
Axial strain [%]
Axial strain
$\Delta\varepsilon_a$=2.20%
0
48
96
144
192
240
288
Time [hour]